INVESTIGATION OF SOOT PROCESSES IN AN OPTICAL DIESEL ENGINE

A thesis submitted for the degree of Doctor of Philosophy

By

BARBARA MENKIEL

School of Engineering and Design
Brunel University
United Kingdom

January 2012

Abstract

This study is dedicated to investigation of soot formed during combustion in diesel engine. Measurements were performed in a high speed direct injection optical diesel engine. Initially soot particle size, size distribution and soot volume fraction were investigated using time resolved laser induced incandescence (TR-LII) technique. For this study standard diesel fuel was used and measurements were performed for various injection timing and two different engine loads. Investigation showed that TR-LII is a powerful tool that can be used for characterization of in-cylinder soot in the engines. Subsequently TR-LII technique was developed to measure in-cylinder soot in two dimensional plane (planar laser induced incandescence PLII) and technique was combined with high speed imaging to investigate soot processes for ultra-low sulfur diesel (ULSD) and bio-fuel (RME). Two injection strategies of single and double injection were applied during these measurements. A high speed imaging technique was used to study the soot formation and oxidation during the combustion process within the cylinder and PLII was applied later in the stroke to study qualitatively the relative amount of un-oxidised soot that was left in the combustion chamber. In addition to PLII, TR-LII technique was used simultaneously to explore crank angle resolved variation of primary soot particle size and their size distribution during the expansion stroke. The same measurements were repeated for fuels with different composition investigating the relationship between the fuel properties and soot emission. Finally mathematical model for soot particle size and distribution width was modified by introducing assumption of multi-lognormal in-cylinder soot particle size distribution.

The investigation leads to conclusion that optical diagnostics can be successfully used for in-cylinder soot processes characterisation. It was as well demonstrated that the fuel composition can influence significantly soot emission. The TR-LII measurements revealed a general trend of the soot particle sizes decreasing with crank angle due to oxidation and later in expansion stroke a well-defined soot particle size distribution was observed. Results obtained during PLII and high speed imaging measurements show that oxygen content and aromatics content influence the soot processes in combustion chamber. Moreover results show that soot particles in combustion chamber can be distributed in a multi-lognormal manner.

Acknowledgments

The financial and technical support provided by Shell Global Solutions is acknowledged.

I would like to thank to my supervisor Dr. Lionel Ganippa whose patience and academic experience have been invaluable to me and who has supported me throughout my doctorate.

I would like to thank to Dr. Roger Cracknel for advice and help during last four years.

I would also like to thank to my friends Dr. Arjan Donkerbroek and Dr. Saumyabrata Banerjee who have always been very helpful sharing knowledge and giving assistance during many hours of experiments.

I would like to express my appreciation to Andy Selway for all the time that he spent rebuilding the engine, Ken Anstiss and Clive Barrett for their incessant support and advice.

And finally I would like to thank to my family: Paul and Rosita who are my joy, my guiding lights and my pillars in life. I would like to thank to Paul without whose love, encouragement and editing assistance, I would not have finish this thesis.

Abbreviations

2D	Two-dimensional
AC	Alternating current
AR	Anti-reflection
BDC	Bottom dead centre
BTL	Biomass to liquid
CAD	Crank angle degree
CFU	Control flow unit
CI	Compression Ignition
CIDI	Compression -ignition direct-injection
CMD	Count median diameter
CN	Cyano Compound
CN	Cetane number
CO	Carbon monoxide
CPC	Condensation particle counter
CxHx	Hydrocarbons
DC	Direct current
DMA	Differential mobility analyser
DPF	Diesel particulate filter
ECU	Electronic control unit
EGR	Exhaust Gas Recirculation
EMS	Electromobility spectrometer
FAME	Fatty-acid methyl ester
FCE	Faraday cap electrometer
FLoL	Flame lift off length
FT	Fisher-Tropsch
FWHM	Full width half maximum
GTL	Gas to liquid
H_2O	Water
HCCI	Homogeneous charge compression ignition
HCN	Cyano Compound
HRR	Heat release rate
HSDI	High speed direct injection
ICCD	Intensified charge coupled device
ID	Ignition delay
IMEP	Indicated mean effective pressure
IVC	Inlet valve closure
LED	Light-emitting diode
LII	Laser induced incandescence
LPG	Liquefied petroleum
LTC	Low temperature combustion
NIR	Near infrared light
NO_x	Nitrogen Oxides
OH*	Hydroxyl Radical

PAH	Polyaromatic hydrocarbons
PC	Personal computer
PCCI	Premixed charge compression ignition
PLII	Planar laser induced incandescence
PM	Particulate Matter
PMT	Photomultiplier
PPM	Parts per million
RME	Rapeseed methyl ester
S	Sulphur
SI	Spark Ignition
SLoL	Soot lift-off length
SNL	Soot natural luminosity
SO_2	Sulphur Dioxide
SOC	Start of combustion
SOI	Start of injection
SVF	Soot volume fraction
TC TR-LII	Two colour time-resolved laser induced incandescence
TDC	Top dead centre
TEM	Transmission Electron Microscopy
THC	Total hydrocarbons
TR	Time resolved
TR-LII	Time resolved laser induced incandescence
UV	Ultraviolet light
VCR	Compression ratio
VIS	Visible light
VVL	Variable valve lift
VVT	Variable valve timing
XTL	Anything to liquid

Nomenclature

C_P	specific heat of soot particle
C_v	specific heat at constant pressure
c	speed of light
D	diffusion coefficient of vapour into the ambient gas
d_{cmd}	count median diameter
d_{mono}	mono-disperse particle diameter
d_p	diameter of soot particle
d_p^0	initial soot particle diameter
$E(m_1)$	soot absorption function at 415 nm
$E(m_2)$	soot absorption function at 665 nm
E_{int}	internal energy of soot particle
$f_c(Kn_c)$	empirical function of Knudsen number for conduction
$f_{ev}(Kn)$	empirical function of the Knudsen number for evaporation
f_v	soot volume fraction
$f_v(x)$	local soot volume fraction
G	geometry dependent heat transfer factor
G_{cal}	gain of the photomultiplier (1 or 2) during experiments
G_{exp}	gain of the photomultiplier (1 or 2) during calibration
ΔH_V	specific heat of vaporisation per unit mass carbon
h	Planck's constant
h_f	sensible enthalpy of the injected fuel
h_i	enthalpy of flux i;
Δh_v	soot evaporation enthalpy
I_a	mean free path in the ambient environment
K	constant for a given detection system
$K(\lambda)$	calibration constant
Kn	Knudsen number
k_B	Boltzmann's constant, $1.380662 \cdot 10^{-23}\ J/K$
k_*	reference value for thermal conductivity
$LII(\lambda)$	signal measured at 415 nm or 665 nm
LII_{cal}	signal measured during calibration
LII_{exp}	measured LII signal

LII_{theo}	calculated LII signal
M_g	molar weight of the ambient gas
$\dot{m}_f$	mass flow of the fuel
$\dot{m}_i$	mass flow rate into system at location i
m_p	mass of soot particle
p_g	in-cylinder gas pressure
Q_{abs}	Mie absorption efficiency
$\dot{Q}_{cond}$	heat flux due to conduction
$\dot{Q}_{cond,fm}$	heat flux due to conduction in free molecular regime
$\dot{Q}_{cond,c}$	heat flux due to conduction in continuum regime
$\dot{Q}_{rad}$	heat flux due to radiation
$\dot{Q}_{sublim}$	heat flux due to sublimation
$\dot{q}_{abs}$	heat rate due to absorption
$\dot{q}_{cond}$	heat rate due to conduction
$\dot{q}_{laser}$	laser fluence
$\dot{q}_{rad}$	heat rate due to radiation
$\dot{q}_{vap}$	heat rate due to evaporation
R	gas constant
r_{cmd}	count median radius
S	measured soot natural luminosity
S_k	Sutherland constant for thermal conductivity
T	absolute temperature
T_g	temperature of ambient gas
T_p	soot particle temperature
T_*	reference temperature
U	sensible internal energy of the in-cylinder charge
$\dot{U}_{evap}$	evaporation rate
U_s	sensible enthalpy of injected fuel
V	in-cylinder volume

Greek letters

α_T	translational energy accommodation coefficient
α_v	accommodation coefficient for evaporation
γ	ratio of specific heat at constant volume and pressure
ε_{pt}	particle total emissivity
θ	crank angle
λ	wavelength
λ_{cond}	thermal conductivity
$\lambda_{detect}, \lambda_1, \lambda_2$	detection wavelength, detection wavelength (415 nm), detection wavelength (665 nm)
$\lambda_{mfp,a}$	mean free path
ξ	divisible factor
ρ_p	soot particle density
ρ_∞	carbon vapour density at infinite distance from the soot particle
σ_{SB}	Stefan-Boltzmann constant, $5.670 \cdot 10^{-8} \frac{W}{m^2 K^4}$
σ_{col}	collisional cross-section of the soot particles with the surrounding air
$\sigma,\ \sigma_g$	standard deviation $\sigma = \ln(\sigma_g)$, geometric standard deviation
σ_{ini}	initial distribution width
ω_b	laser sheet thickness

Contents

List of Figures

List of Tables

1.Chapter 1 - Introduction

1.1 Introduction

During recent years, diesel engines have become a popular alternative to the gasoline engines in modern passenger cars and have started to dominate the European car market. However, imposed emission regulations restrict emission levels and introduce a challenge for engine designers to apply the new techniques and processes that may reduce pollutions and lead to further development of engines. The mechanism of pollutant formation was broadly studied and is well understood. Current work focuses mostly on soot which is one of the most unwanted products of combustion. Combustion processes are strongly influenced by fuel injection strategies and fuel-air mixture formation in the combustion chamber. It is therefore necessary to study in-cylinder soot processes and find the link between in-cylinder and exhaust soot emission. Optical diagnostics is an attractive alternative to physical probing and is based on measurements of interaction between light and an atom or a molecule. It gives as well possibility to measure emission at the early stage in combustion chamber that would not be possible using physical probing. However, application of optical techniques in highly turbulent environment like diesel engine is challenging and only limited data is available in the literature. Lately interest in alternative fuels increased and subsequently need of studding the correlation between fuel composition and pollutants formation emerged. Optical diagnostics enables to obtain useful information that can support development of mathematical models for various fuels and help to understand link between fuel and soot emission.

The work presented here was undertaken in Brunel University as a part of project sponsored by Shell. Measurements were done in single cylinder diesel engine with optical access using laser diagnostics and high speed imaging techniques. Soot processes were studied using time resolved laser induced incandescence (TR-LII) and planar laser induced incandescence (PLII). Additionally combustion processes were studied via high speed imaging where soot incandescence and radicals chemiluminescence were measured. Standard ultra-low sulphur diesel (ULSD), bio-diesel (RME – rapeseed methyl ester) and fuels of different compositions were used in this investigation.

1.2. Structure of thesis

Chapter 2 gives the background and literature review related to the diesel combustion and in-cylinder optical diagnostic techniques. In this chapter operating principle of diesel engine is

explained. Subsequently combustion processes based on Dec's conceptual model are presented and main emissions from diesel engine are discussed. Afterwards mechanism of soot formation is presented in details and modern methods of diesel combustion optimisation are briefly introduced. In the last two sections of the chapter fuel properties, additives and alternative fuels are described as well as soot measurements techniques applied in diesel engine are presented.

Chapter 3 introduces the theoretical background for in-cylinder combustion and soot processes. In this chapter theory behind the in cylinder pressure analysis is presented. Subsequently mathematical models applied for soot particle size evaluation based on measured LII signals, available in literature, are presented and the detailed model used in current investigation is described.

Chapter 4 explains experimental set up and facility employed during this study and provides detailed description of the single cylinder optical diesel engine, laser and detection system.

Chapter 5 presents the measurements of in-cylinder soot particles, their distribution and soot volume fraction in optical diesel engine using TR-LII technique. The difficulties in uncertainties related to measurements are discussed and influence of changes in injection timing and quantities of injected fuel are investigated.

In chapter 7 soot processes for ULSD and RME in diesel engine are characterised using TR-LII, PLII and high speed imaging for single and double injection strategy. The study focused on investigation of differences in soot processes between these fuels.

Chapter 8 presents results obtained during measurements in diesel engine using TR-LII technique. In this chapter assumption of multi-lognormal soot particle size distribution in combustion chamber was introduced and investigated.

In chapter 9 conclusions are summarised and recommendation for future work is stated.

2.Chapter 2 – Literature Review

2.1. The Diesel engine classification, components and operating cycles.

The cost of steam engines in the 19th century caused an increase in the need of designing more affordable motors, leading to the production of the first internal combustion engine. The design of the internal combustion engine was based on the steam engine. The fundamentals of the engine were developed at the end of the 19th century and subsequently lead to the rapid expansion of the motor vehicle industry, [1]. The main purpose of the internal combustion engine is production of mechanical power from chemical energy contained in fuel. The fuel's energy is released by oxidizing the fuel inside the engine. There are many different types of internal combustion engine and for example Rajput [2] proposed classification according to:

1. **Cycle of operation:**
    a. Two stroke cycle engines;
    b. Four stroke cycle engines;
2. **Cycle of combustion:**
    a. Otto cycle engine (combustion at constant volume);
    b. Diesel cycle engine (combustion at constant pressure);
    c. Dual combustion or semi-diesel engine (combustion partially at constant volume and partially at constant pressure);
3. **Arrangement of cylinders (see Fig 2.1):**
    a. Single cylinder;
    b. Inline or straight;
    c. V-engine – most larger vehicles use 8-cylinder, V-engine;
    d. Opposed cylinder – common for small aircrafts;
    e. W-engine – developed mainly for racing applications
    f. Opposed piston – single combustion process causes two power strokes, at the same time;
    g. Radial engine – many medium and large size aircraft, large aircrafts two or more banks of cylinder are mounted together;

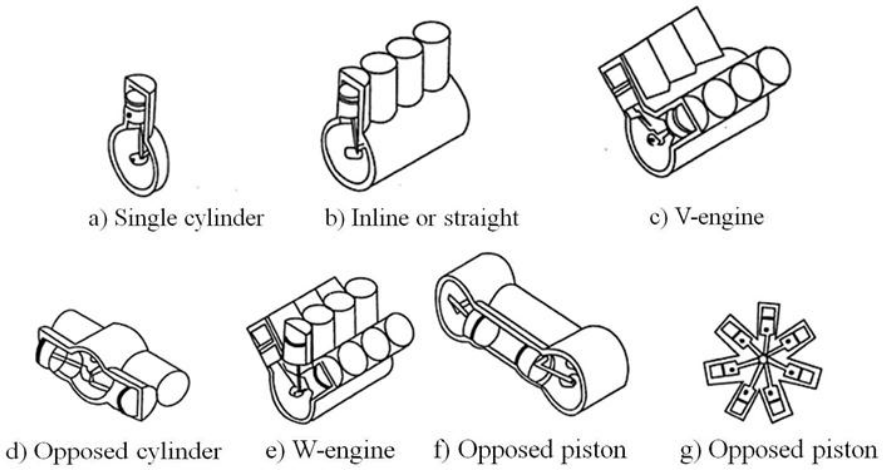

Figure 2.1. Engine classification according to arrangement of the cylinders

4. **Speed of the engine:**
    a. Low-speed engines;
    b. Medium-speed engines;
    c. High-speed engines;
5. **Method of ignition:**
    a. Spark ignition engines;
    b. Compression ignition engines;
6. **Method of cooling of cylinders:**
    a. Air-cooled engines;
    b. Water-cooled engines;
7. **Method of governing:**
    a. Hit and miss governed engines;
    b. Quantity governed engines;
    c. Quality governed engines;
8. **Valve arrangement:**
    a. Overhead valve engine;
    b. T-head valve engine;
    c. L-head type engine;
    d. F-head type engine;
9. **Number of cylinders:**
    a. Single-cylinder engines;
    b. Multi-cylinder engines;
10. **Intake process:**
    a. Naturally aspirated;
    b. Supercharged;

c. Turbocharged;

d. Crankcase compressed;

11. Fuel employed:

a. Oil engines;

b. Gas engines;

c. LPG engines;

d. Duel fuel engine;

e. Petrol engine;

f. Kerosene engine;

g. Alcohol-methyl, ethyl engine;

h. Gasohol engine;

2.1.1. Engine components

In Fig. 2.2. the cross section of V-type diesel engine with its main components is presented.

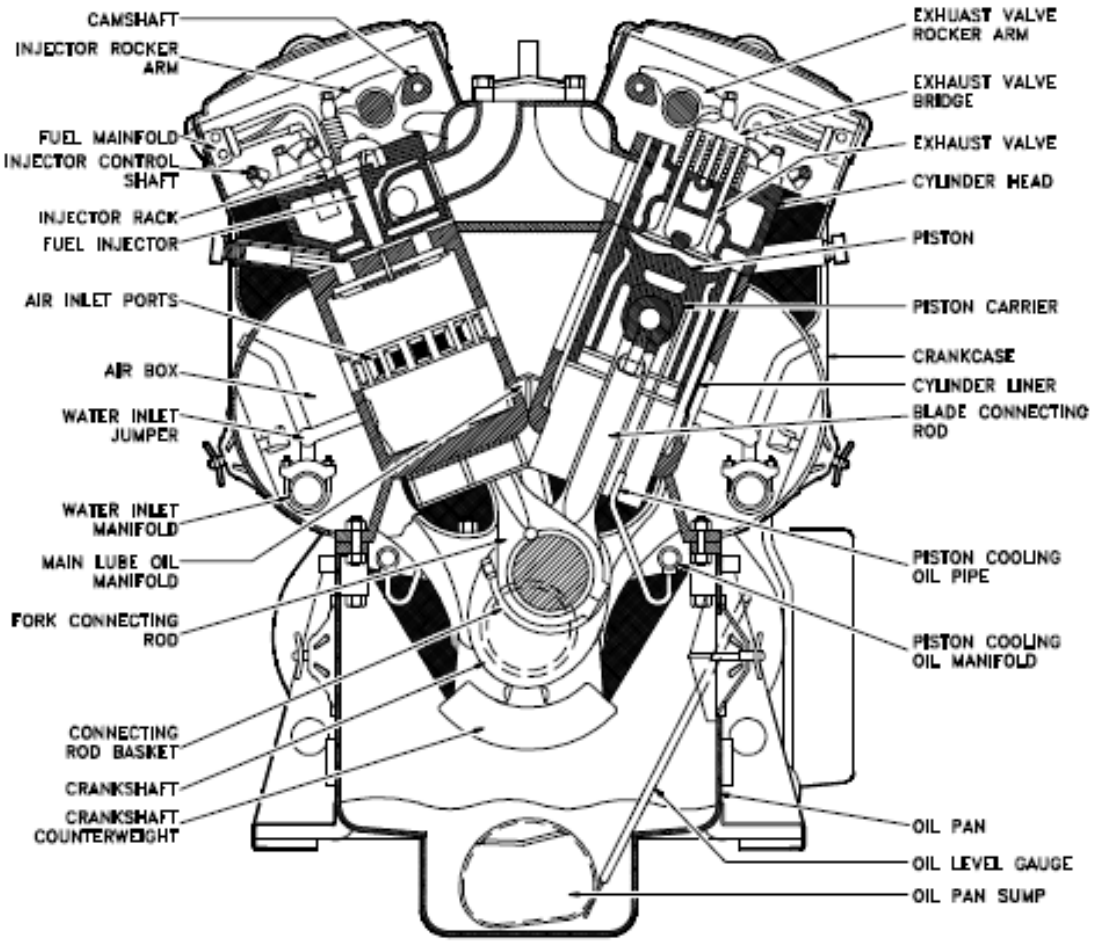

Figure 2.2. Cross section of V-type diesel engine, [3].

The main components of a diesel engine are, [4, 5]:

- **Cylinder block**: usually made of grey cast iron (low cost and high resistance to wear). It houses both the cylinders and pistons.
- **Cylinder head**: is made from iron and aluminium, is connected to the top of cylinder block and forms top of combustion chamber. In diesel engines the cylinder head contains the fuel injectors and valves. The In-line engine has one cylinder head for all the cylinders.
- **Valves and valve trains**: are usually made from forged alloy steel. Sometimes steel is mixed with chromium or silicon to make them more resistant to corrosion. Exhaust valves are frequently made from nickel based alloy. Valves are located in the cylinder head.
- **Camshaft and drives**: made of hardened iron alloy or steel, the camshaft is usually cast or machined. Its main function is driving the valves and is supported by the main bearings. The number of bearings depends on number of cylinders and typically is one more than number of cylinders.
- **Crankshaft**: is made of alloy steel of great mechanical strength. Is attached to the connecting rod in areas called throws - where the downward power pulses change into rotating motion.
- **Crankcase**: is often integrated with the cylinder block and is sealed at the bottom with a pressed steel or cast aluminium oil pan.
- **Piston**: is made of aluminium and its design depends on the engine type. Pistons transfer the gas energy into the crank through connecting rods. The piston is fitted with rings used to seal the cylinder and prevent both heat and pressure from escaping. Upper rings are called compression rings and lower oil rings. Oil rings scrape the oil from the cylinder wall and returns it to crankcase.

2.1.2. Engine operating cycles

Most engines operate on a four-stroke cycle. To complete the sequence of events, the piston has to complete four strokes that correspond to two crankshaft revolutions. Four strokes are schematically presented in Fig. 2.2 and are composed of [4]:

1. **An intake stroke** starting at TDC and ending at with piston at BDC. In this stroke air mixture enters the combustion chamber. The intake valves open just before the stroke starts and close after it ends.

2. **A compression stroke** when all valves are closed and the mixture inside the cylinder is compressed to a small volume while piston moves towards TDC. Towards the end of compression stroke, the combustion is initiated and the cylinder pressure rapidly rises.
3. **A power stroke** (expansion stroke) starting at TDC and ends at BDC. High-temperature and high-pressure gases push down the piston and force the crank to rotate. While the piston approaches BDC the exhaust valves open and the in-cylinder pressure drops.
4. **An exhaust stroke** in which gases remaining after combustion exit the cylinder. The piston in this time moves towards TDC and just after the exhaust valves close, the intake valves open and the cycle begins again.

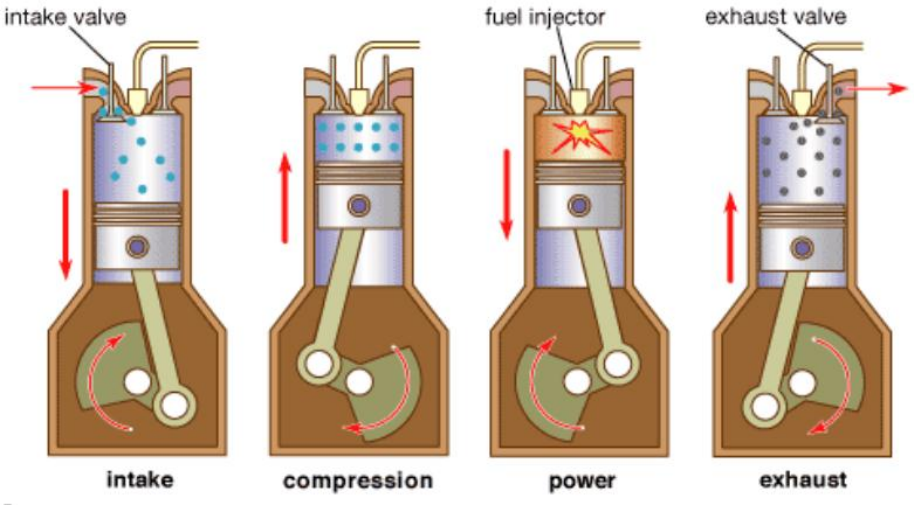

Figure 2.3. The four stroke operating cycle, [6].

2.1.3. Advantages and disadvantages of diesel engine

An increase in the popularity of diesel engines over recent years is a result of their numerous advantages over gasoline combustion engines. The advantages and disadvantages of diesel combustion engines are as follows

Advantages:

- High efficiency (higher compression ratio than petrol engine);
- Low volumetric fuel consumption;
- High reliability: absence of electrical ignition system;
- Longer lifetime in comparison to petrol engines;
- High torque;
- Lower maintenance cost;

- Can run with bio-fuels;

Disadvantages:

- Higher manufacturing cost in comparison to petrol engine;
- High emission of NOx, PM and noise;
- Expensive exhaust gas after treatment system;

2.2. Diesel combustion process

The combustion process in a diesel engine is a combination of complex chemical and physical mechanisms. The process starts from the injection of fuel under high pressure near the end of the compression stroke. A high speed fuel jet enters the combustion chamber through the injector nozzles and its liquid core quickly brakes up into small droplets. A turbulent environment together with the swirl of the intake air improves the mixing process of air and fuel. The time available for mixing in a diesel engine is limited and it is therefore imperative to achieve the best possible atomization. While the piston moves towards TDC, the in-cylinder pressure and temperature increases and the injected fuel quickly evaporates. Combustion is initiated while the temperature reaches the level sufficient for spontaneous auto-ignition and this temperature is one of the most important parameters in combustion process. Auto-ignition depends on in-cylinder temperature (pressure), concentration of air, fuel and its chemical composition. Fuel auto-ignition is characterized by cetane number and may occur simultaneously in different locations of combustion chamber. The production of soot and compounds like nitrogen oxides, carbon monoxides, carbon dioxides and unburned hydrocarbons are correlated with combustion process and are known as pollutants, [1].

2.2.1. Combustion process, Dec's conceptual model

Emissions of soot and nitrogen oxides are related and were extensively studied in the optical engines. The conceptual model was published in 1997 by Dec in [7] and eventually extended by Flynn in [8], who studied kinetic modelling. In his work, the model was compared with experimental data. The developed, integrated model is presented in Fig. 2.4 and shows thermal and chemical processes present inside the burning fuel plume.

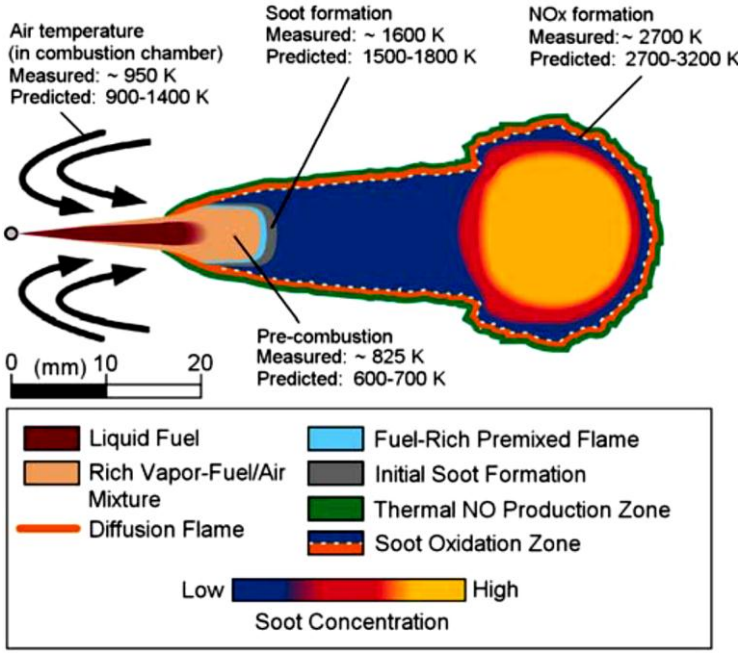

Figure 2.4. Dec's conceptual model integrated with chemical kinetics proposed by Flynn, [8].

Cold fuel (350 K), which is entering combustion chamber atomizes, mixes with hot air and finally vaporizes. As the formed air/fuel mixture moves downstream the jet and its temperature increases. Fuel molecules brake down resulting in formation of different compounds, but combustion does not take place yet. When the temperature is sufficient, the fuel ignites, exothermic reaction of oxidation occurs and a rapid release of energy, known as premixed combustion phase, takes place. The premixed combustion phase is very short and is associated with high heat release rate, (Fig. 2.5).

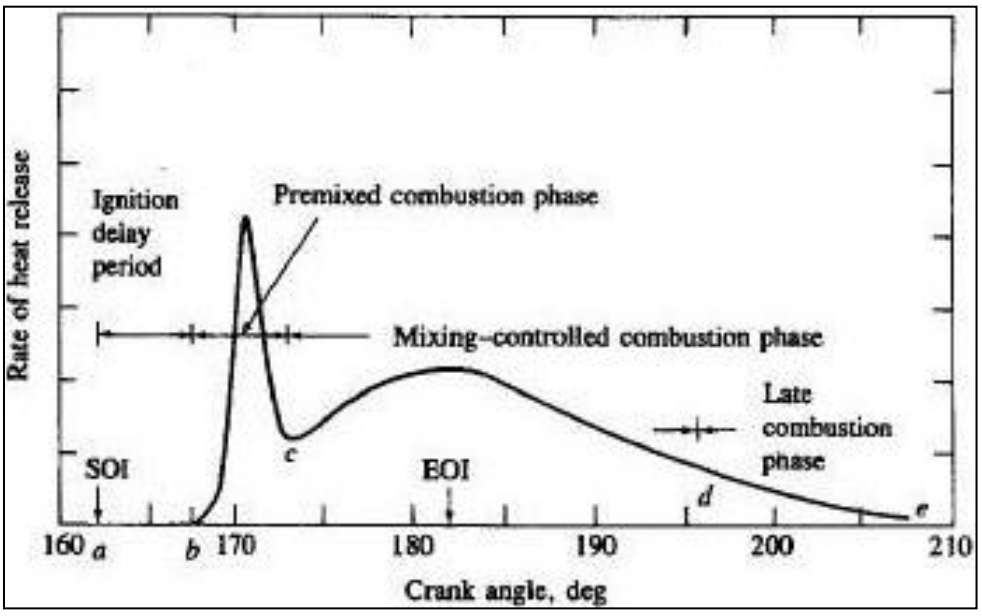

Figure 2.5.Typical heat release rate diagram illustrating different combustion phases for DI [4].

When all oxygen in this phase is consumed, gas products of CO, H_2O and compounds like C_2H_2, C_2H_4, C_3H_3 combine and form PAH structures that eventually create small soot particles. PAH are distributed across the jet and temperatures present there reach 1600 K (see Fig.2.4), [8]. Small soot particles are formed downstream to the location of first PAH formation. The fuel, which is still injected, pushes products of the reaction towards the sides of jet where fresh oxygen is available. Around the periphery of jet, the diffusion flame begins to form and temperatures reach approximately 2700 K, while the equivalence ratio is around 1. Heat generated during oxidation causes a reduction in the length of the liquid fuel and shifts towards the injector. The shortest distance from the diffusion flame to the injector is called the flame lift off length (FLoL). FLoL is strongly related to air entrainment in the core of the fuel spray. Longer FLoL corresponds to a greater quantity of oxygen available in the spray and it is directly related to soot formation and oxidation, [7]. Simultaneously growth of the soot particles takes place, until they reach diffusion flame, where their oxidation occurs. High temperatures at the boarder of diffusion flame cause thermal NO formation. Eventually combustion shifts to mixing controlled phase where the burning rate is controlled by the fuel vapour-air mixing process. The heat release rate reaches a second, lower peak as shown in Fig. 2.5, [4]. In parallel, soot particles are constantly growing until they reach the diffusion flame, where they are oxidised. Figure 2.4 shows jet at the time when the fuel is still injected and combustion is in the mixing controlled phase. Late, an increase in soot size and concentration is observed. The high temperature field shifts towards injector resulting in early fuel ignition in the core of the jet. In the final stages, the rate of heat release decreases during the expansion stroke as the kinetics of the final processes slows down as the temperature decreases.

The model presents the conceptual model of combustion in diesel engine without swirl or spray-wall interactions, which will lead to turbulences and a subsequent change in the shape of the jet cross section presented in Fig. 2.4.

2.2.2. Emissions

Generation of soot and compounds like nitrogen oxides, carbon monoxides, carbon dioxides and unburned hydrocarbons is correlated with the combustion process and these combustion products are known as pollutants. European emission legislations are focused on reducing both soot and nitrogen oxides (NO_x). Standards for these two pollutants for passenger cars are presented in Fig. 2.6. Euro 6 is forcing a limit of 0.005 g/km for soot emission which must be achieved by September 2014. The directive also specifies a particle number limit which is

$6 \cdot 10^{11}$ #/km [9, 10]. Recently new legislation was released that introduces particle number limits for gasoline engines.

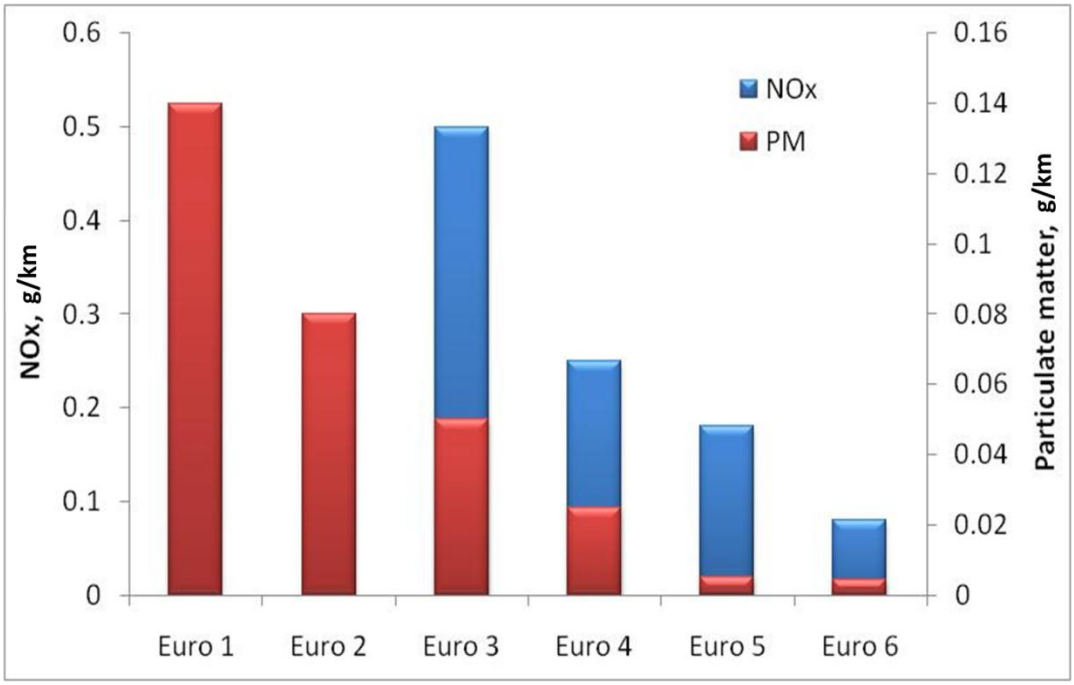

Figure 2.6. Euro 6 emission standards for NO_x and PM, [9, 10].

As a result of these recent legislations, research has focused at providing further understanding of pollutant formation. The following subsection presents a description of the mechanisms behind the formation of these pollutants.

2.2.2.1. Nitrogen oxide NO_x

Nitrogen oxides are one of the most unwanted pollutants formed during combustion in diesel engines. Nitrogen oxides present in exhaust gases are composed of nitrogen oxide (70% to 90%) and nitrogen dioxide (10% to 30%). Thermal formation of NO was extensively studied and it was found that NO is formed mainly by extended Zeldovich mechanism [4, 7], according to the following equations:

$$O + N_2 \leftrightarrow NO + N \quad (2.1)$$

$$N + O_2 \leftrightarrow NO + O \quad (2.2)$$

$$N + OH \leftrightarrow NO + H \quad (2.3)$$

An atom of nitrogen, which is in an excited state, reacts with available oxygen forming NO. OH radicals, which appear during combustion, may also react with the atom of nitrogen as shown in Eq. 2.3. It was reported that thermal NO formation occurs in the fuel lean region and is strongly dependent on the temperature due to high activation energy of reaction rates [4].

Fuel contains nitrogen, which may also be a source of NO. The mechanism of its formation however is not fully understood. Thermal decomposition of fuel in the combustion zone may lead to the release of nitrogen-containing compounds (cyano compounds: HCN, CN). These compounds are likely to react with oxygen and generate nitrogen oxides, [4]. NO in the flame zone can rapidly react according to:

$$NO + HO_2 \rightarrow NO_2 + OH \qquad (2.4)$$

And conversion of this NO_2 to NO occurs as follows:

$$NO_2 + O \rightarrow NO + O_2 \qquad (2.5)$$

However, information and understanding of the processes taking place at this point is limited. Another reported NO formation mechanism is called prompt NO formation. It is believed that prompt NO are formed in the width of the flame and following reactions are responsible for its formation, [11]:

$$CH + N \text{ « } HCN + N\,2 \qquad (2.6)$$

$$C + N \text{ «} CN + N\,2 \qquad (2.7)$$

Quantity of formed NO usually remains low in comparison to thermal NO formation. Prompt NO formation will be more significant in low temperature.

2.2.2.2. Soot processes

Soot emission from the engine reflects poor combustion and loss of engine efficiency. This issue initialised studies aiming in the reduction of soot generation and improvement of soot oxidation. Although the soot formation process has not been fully understood, it has been acknowledged that the process has negative impact on both the environment and human health. The epidemiology and toxicology of particulate matter present in ambient is a very active area of research. The first epidemiological observations in 1775 were provided by Sir Percival Pott, a London physician, who suggested that incidence of the scrotal cancer in chimney sweeps, was due to the exposure to soot, [12]. In 1936 Kuroda and Kawahata reported high occurrence of lung cancer in men working for steel company and in men involved in carbonization for coal gas production, [13]. Research conducted by Kotin (1954), [14], provided evidence of carcinogenicity of various soot and soot extracts through animal testing and suggested that soot as well is carcinogenic for human. It was reported by Mauderly [15], that mass concentration of soot particles is not the best indicator of health hazards and it is necessary to consider different soot properties including number, size, morphology and chemical composition. The development of strategy of soot measurements

and elimination as a result of combustion (not only in diesel engines) is therefore very crucial and requires good understanding of processes hidden behind soot formation and oxidation.

Mechanism of soot formation

The development of solid soot particles from liquid or vapour phase hydrocarbons mainly involves the following processes: pyrolysis, nucleation, coalescence, surface growth, agglomeration and oxidation, [16, 17]. The schematic of soot formation process is presented in Fig. 2.7. Simultaneously at each point of soot formation, soot oxidation occurs and both processes are constantly competing. The rate of these two processes depends on fuel composition, oxygen content, in-cylinder temperature, pressure and engine operating conditions.

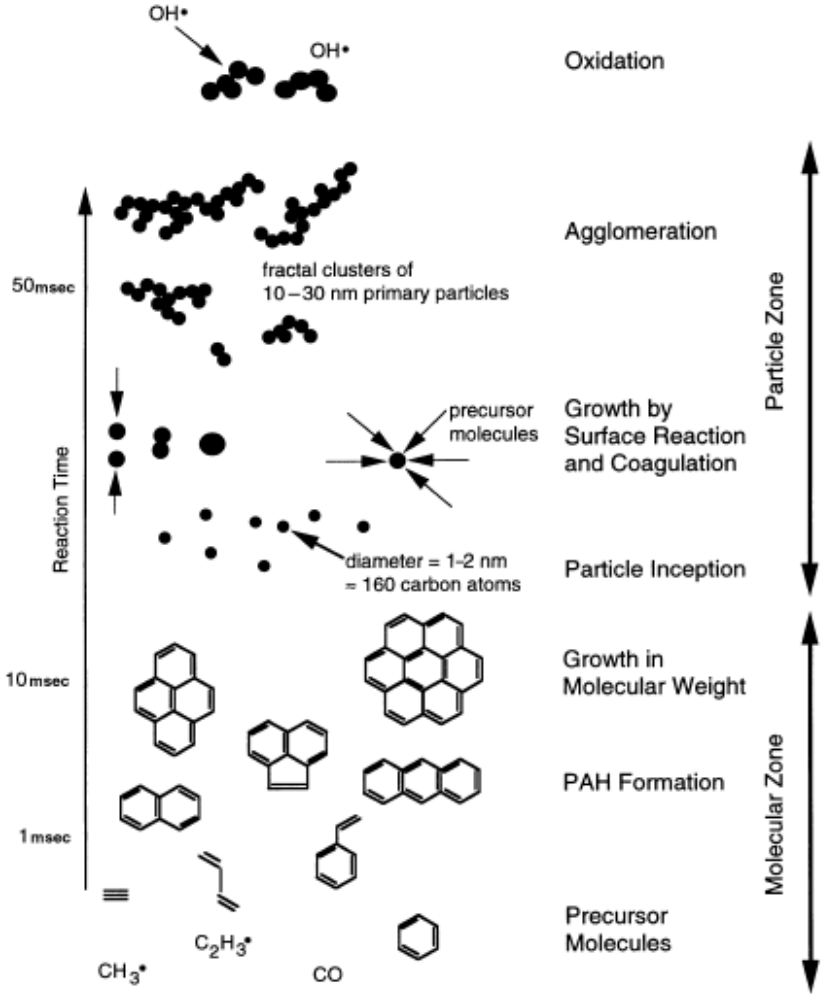

Figure 2.7. Schematics of soot formation process, [16].

The process of decomposition of organic material in high temperatures and in the absence of oxygen is called pyrolysis. High in-cylinder temperature alters the molecular structure of fuel and endothermic reactions take place. Rates of reactions are highly dependent on the

temperature and as a result, the formation of compounds, which are precursors of soot, takes place. Soot formation depends on fuel pyrolysis and rate of fuel and precursor oxidation by the hydroxyl radical (OH*), [17]. The processes of soot formation and oxidation are strongly related to the in-cylinder temperature. While the temperature increases, soot oxidation is increasing at a faster rate than soot formation. Fuels which are pyrolised produce species like: unsaturated hydrocarbons, polyacetylens, polycyclic aromatic hydrocarbons and acetylene. The decrease of the residence time in pyrolysis zone reduces soot formation was also reported in [18].

Nucleation, particle inception

Nucleation or particle inception is the process of small particle formation from gas phase reactants. Small particles generated in this process are called nuclei and their diameter is in the range from 1.5 nm to 2 nm, [17, 19, 20]. The nuclei have significant influence on the final soot formation since they provide the site for surface growth. Nucleation occurs mainly in the locations where temperatures are high in both premixed and diffusion flames. It is believed that there are mechanisms of soot formation which do not include the step of soot nucleation. Soot formation depends on the growth rate of the initial aromatic ring. Then formation of the structures creating polyaromatic hydrocarbons (PAH) is faster and is similar for all fuels. PAH grow in the presence of acetylene and nucleate when large enough. At this point nuclei contain large amount of hydrogen.

Surface growth

Surface growth is the process of adding mass to formed nuclei. The process of soot nucleation and surface growth are occurring simultaneously and it is difficult to distinguish between them. During surface growth, gas–phase hydrocarbons and acetylenes are connecting to the surface of the soot particle, [17]. The mass of the soot increases and the process continues as the particle shifts to cooler regions. The rate of the process is faster for smaller particles since they contain more reactive radical sites. The duration of surface growth is reflected in the size of the final primary particle. The size of primary particles may vary and depends on engine operating conditions, sampling technique and the method used to determine particle size. Usually primary particle sizes are reported to be in the range from 20 to 70 nm, [17].

Coalescence and agglomeration

Coalescence is sometimes called coagulation and takes place when two particles collide to form a single larger particle, Fig. 2.8. Due to the process of coagulation, the number of particles decreases but their mass remains constant. Agglomeration occurs when two particles stick together to form groups of primary particles which usually look like chains.

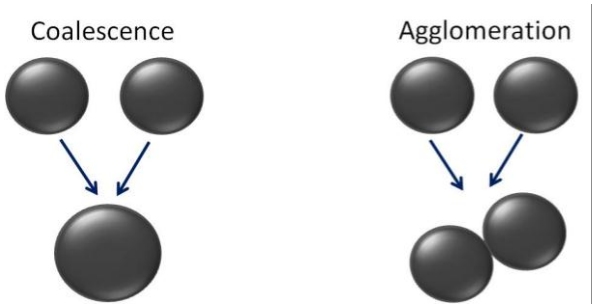

Figure 2.8. Soot processes: coalescence and agglomeration

Reduction of NO_x and PM can be obtained mainly by two approaches: after-treatment approach through the application of filters, which will remove pollutants from exhaust gasses or by preventing formation of pollutants. In current work, the after-treatment approach was not considered. Combustion researched aimed at reducing pollutant emissions whilst simultaneously increasing engine efficiency has been the subject of recent works. Significant improvement in the development of future engines was completed by application of computational fluid dynamics and simulations, [21]. Experimental work conducted on laminar and turbulent flames, constant volume chambers enhanced the knowledge and understanding of formation, behaviour and oxidation of pollutants. Additionally broad research has been conducted focusing on advance combustion models. Complex engine optical diagnostics provided methods of validating theoretical models. Simultaneously significant work was has been done to investigate the influence of fuel composition on soot emissions (see section 2.3).

2.2.3. Optimisation of diesel combustion

A significant reduction in engine emissions by optimisation of diesel combustion is required, together with after treatment systems currently present in all modern diesel engines in order to meet future emission regulations. There is a significant interest in combustion technologies that maintains the efficiency of the diesel engine whilst reducing both NO_x and PM emissions. Emissions of NO_x and soot from diesel engines have decreased significantly during recent years. The main reasons for this reduction are improvements in fuel injection system, which allowed fuel injection at very high pressure and application of cooled exhaust gas

recirculation system (EGR). However, simultaneous reduction of NO_x and soot is challenging since the emissions of both pollutants is related. Recently new low temperature combustion concepts: HCCI and PCCI have been proposed as an alternative route.

2.2.3.1. Homogeneous charge compression ignition (HCCI)

It was reported that the HCCI combustion process can provide efficiencies as high as compression-ignition direct-injection (CIDI), an advanced version of the commonly known diesel engine that generates low nitrogen oxides and soot emission [22]. The principle of HCCI is to obtain a lean, well mixed charge that reacts and burns homogeneously throughout the cylinder volume. Lean charge can be formed by using EGR or a dilute homogeneous air-fuel mixture. Dilution may be quite high since the flame propagation is not required. HCCI combines quality of spark ignition (SI) and compression ignition (CI) engines. In comparison to SI, HCCI efficiency is improved by eliminating throttling losses, using high compression ratios (similar to a CIDI engine) and shorter combustion duration, [22]. Another advantage of HCCI combustion is that it can be used in combination with various fuels, [23]. The main difficulties of HCCI combustion are: attain cold start, controlling of ignition timing over wide range of different speeds and loads, decreasing combustion rate at higher loads, improving smooth operation in transient condition and meeting emission standards (particularly hydrocarbons (HC) and carbon monoxide (CO)). The most difficult to control is ignition since it takes place after injection and is governed by the chemical kinetics. SI engines are easier to control but they suffer from knocking and misfire. Recently, research has focused on the improvement of injection control systems by variable valve timing (VVT), compression ratio (CR), fuel additives and EGR.

There are few approaches which enable HCCI combustion to be achieved. Early injection will lead to formation of well mixed charge, reduce emission of NO_x and PM, but due to the wall wetting will result in higher emission of HC and increase fuel consumption, [20]. In work presented Odaka [24], HCCI was obtained by application of split injection, addition of EGR and late inlet valve closure (IVC) or variable valve lift (VVL). Reduction of HC was obtained for low load but controlling the injection timing was challenging. It was suggested in [22] that engines with HCCI combustion systems may be commercialized in light-duty passenger vehicle by 2010 and that current diesel versions of vehicles use 40 percent less fuel than gasoline. As it was reported in [25] two engines are already in production: Nissan in Japan produces light truck engine and Honda with 2-stroke gasoline engine for motorcycles. However, optimisation of the conventional combustion process is still required since it is questionable if these new strategies will have application at higher loads.

2.2.3.2. Premixed charge compression ignition (PCCI)

PCCI concept was introduced to improve the control of early ignition, since diesel fuel is very reactive and avoid walls wetting. In PCCI combustion, fuel is injected closer to TDC by early or late injection. For early injection the combustion in coupled with injection. This strategy prevents wall wetting since fuel is in a high pressure and high temperature environment leading to quick fuel evaporation. In order to obtain a satisfactory level of premixing, cooled-EGR is normally added to in-cylinder air, [26]. EGR maintains a low temperature and additionally extends ignition delay that is beneficial for this strategy as it results in decoupling of injection and combustion. Separate injection and combustion prevent from soot formation in diffusion burn period. As with HCCI combustion various approaches were applied to extend ignition delay: late intake valve closing (IVC) or use of fuels with low auto-ignition feature fuel.

Properties of the PCCI concept are very similar to HCCI since HCCI may be treated as a case of (early injection) PCCI. The main advantages of PCCI are: low soot and NO_x emission, low combustion temperature which result in lower heat losses to the chamber walls, short combustion period. The disadvantages are: misfire and incomplete combustion, high emission of HC and CO, problems with ignition timing control which may lead to misfire or 'knock' combustion, [27].

2.2.3.3. Low-Temperature Combustion (LTC)

Another route parallel to HCCI and PCCI combustion is low temperature combustion (LTC). The idea of this combustion is to achieve low temperature with relatively low equivalence ratio, [28].The lean air/fuel mixture used in LTC may lead to an increase in CO and HC emissions. To prevent this problem, good mixture stratification (premixing) has to be achieved to aid in controlling ignition and heat release rate, [29]. Extended premixing is obtained by application of different injection strategies.

Frequently, especially for higher loads, high levels of EGR are used to reduce in cylinder temperatures, [30]. Application of EGR however may lead to poor fuel consumption and high levels of CO, HC and soot emissions. LTC concepts and injection strategies are still under development.

2.3. Fuels

Increased interest in diesel powered vehicles has enhanced the sale of diesel fuel. Diesel fuel used in high speed diesel engines is obtained in refineries and contains approximately 3000 different hydrocarbons [1]. Fuel production in recent years has developed significantly to fulfil the demands of engine manufacturers and emission legislations. There are number of additives which provide significant improvement in the properties of fuels. As an alternative to petroleum based fuels, synthetic fuels that can be used for combustion in diesel engines have gained substantial interest. In 1925 Fischer-Tropsch synthesis was discovered [1]. Synthetic gas, which was generated from coal or natural gas, was used to produce synthetic hydrocarbons that were eventually refined to diesel fuel or gasoline (GTL). Nowadays as it was reported in [31] most of the materials containing carbon can be converted to liquid fuel. However, because of the high production cost of these fuels they are mainly used as a blend component.

2.3.1. Properties

Diesel and bio-diesel requirements are listed in three existing specification standards: EN590, DIN 51606 and EN14214. EN590 describes physical properties for fuel which is introduced to the market in EU, Iceland, Norway or Switzerland. DIN 51606 is the German standard for bio-diesel and EN14214 is a recent standard for bio-diesel in Europe. Diesel fuel requirements are listed in DIN EN 590 and the most significant fuel properties are: density, ignition quality (cetane number), boiling curve, resistance to cold and sulphur content, [32]. The effects of the aforementioned properties are as follows:

- Increase in fuel density results in an increase in energy content injected into cylinder but volumetric fuel consumption increases while density decreases.
- Ignition quality of fuels depends on the cetane number (CN) which is define as a volumetric percentage of cetane (C16H34, n-hexadecane), where CN=100 and the reference fuel, where cetane number is low CN~15. Fuel ignition quality has a significant influence on the combustion process and exhaust emissions. Increase in CN can be achieved through the addition of organic nitrates to the fuel. Calculation of cetane index is based on the fuel density and boiling behaviour and does not represent ignition accelerators.
- Boiling or distillation curves indicate where the fuel starts and stop evaporating. High final boiling point causes an increase in the size of fuel droplets during injection and leads to longer ignition delay, which may be disadvantageous. Low boiling point is

beneficial for cold start but too low boiling point causes fuel evaporation at the injection nozzle and reduces distribution of the fuel in combustion chamber.

- Viscosity generally increases with fuel density. Too high viscosity leads to generation of large fuel droplets and too low viscosity can cause insufficient lubrication of injection system.
- Another property is flash point which describes the temperature at which fuel vapours are ignited by external ignition.
- Sulphur content of fuel depends on the origin of the fuel and during combustion is converted to SO_2. The desulphurisation process applied in refineries has significantly reduced the sulphur content although the process does not eliminate 100 % of sulphur. Many researches have focused on the influence of sulphur on particulate emissions as this area still remains a problem in countries where fuel is of a lower quality.

2.3.2. Additives

Additives are used to improve the properties of fuels, reducing engine emissions, solve the problems and meet requirements necessary for efficient diesel engine operation without side effects. Usually, the concentration of additives added to fuel is very low (ppm, parts per million). Additives may solve problems related to the combustion process including low cetane improvement through ignition accelerators, nozzle coking reduction with the addition of detergents and to prevent corrosion in the fuel system usually corrosion inhibitors are applied. To decrease the pump wear caused by low sulphur diesel, wear protection lubricates are added and to eliminate the foam, antifoaming agents prevent them from their generating. The smell of diesel fuel can be reduced by aromatic odour improvers. Some additives which aid in the regeneration of particle filters are also widely used.

2.3.3. Alternative fuels

Sun-fed primary energy sources like plants can be converted to secondary energy such as alcohols or oils which are well known alternative fuels. The first diesel engine was design to run using peanut oil. Recently, the utilisation of bio-fuels and alternative fuels has gained significant interest.

Alcohols

An attractive alternative to standard diesel are alcohols, mostly methanol, ethanol and bio-alcohol. Their main advantage is reduction of exhaust emission, [33]. Alcohols like methanol contain more oxygen which allows for more effective soot oxidation. Its vaporization heat is

high and leads to temperature reduction and reduced NO_x formation. The main drawback of this fuel is that its aldehyde, CO and HC emissions are high. Application of alcohol requires improvement of the self-ignition property of fuel. The effect of diesel-alcohol blends on engine performance and emission was studied. In [34, 35] it was reported that alcohol-diesel blend lead to an increase in fuel consumption. However, measured exhaust emission of NO_x, CO and soot were reduced.

Vegetable oils

A wide range of vegetable oils like soybean, peanut, cocoanut, palm oil may be use in diesel engines and are widely available on markets all over the world. Recently biodiesels produced from biomass (e.g. rapeseed oil) gained attention because of the increasing oil prices, political instabilities of oil producing countries and increasing concerns over greenhouse gas emissions. The European Union supports biofuel production primarily through tax deduction. It is also well known that closed a CO_2 loop does not raise the concentration of CO_2 in atmosphere. However, farming and converting crop to biomass requires energy and must be considered when evaluating the process. Figure 2.9 shows bio-diesel production in European countries in 2009, with France and Germany dominating production when compared with the rest of Europe.

Table : Production of fuel-biodiesel in the EU-27 and Switzerland in 2009

Countries		Production [Ml/yr]
AT	Austria	349
BE	Belgium	468
BG	Bulgaria	28
CY	Cyprus	10
CZ	Czech Republic	185
DE	Germany	2'859
DK	Denmark	151
EE	Estonia	27
EL	Greece	87
ES	Spain	967
FI	Finland	248
FR	France	2'206
HU	Hungary	150
IE	Ireland	19
IT	Italy	830
LT	Lithuania	110
LU	Luxembourg	0
LV	Latvia	50
MT	Malta	1
NL	Netherlands	364
PL	Poland	374
PT	Portugal	282
RO	Romania	33
SE	Sweden	112
SI	Slovenia	10
SK	Slovakia	114
UK	United Kingdom	154
EU-27	**EU 27**	**10'187**
CH	**Switzerland**	**8**

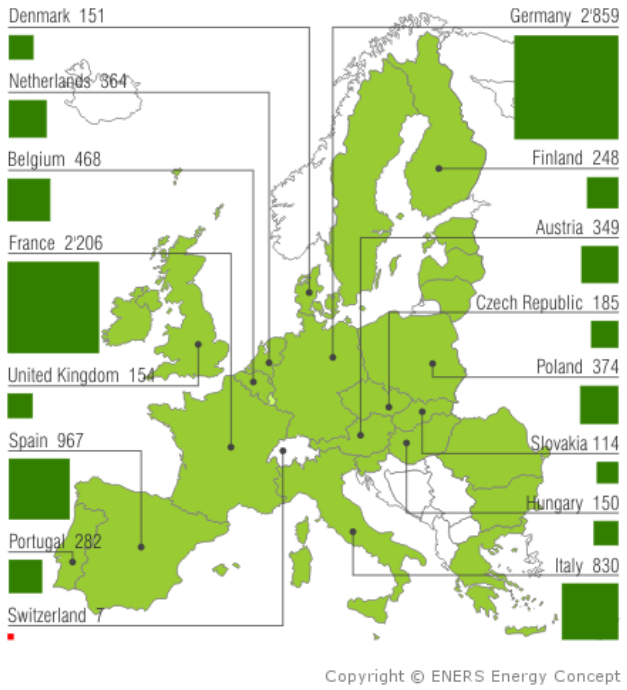

Figure 2.9. Bio-diesel production in Europe in 2009, [36].

The evolution of bio-diesel and bio-ethanol fuel consumption is presented in Fig. 2.10 and clearly shows an exponential increase in demand for these fuels.

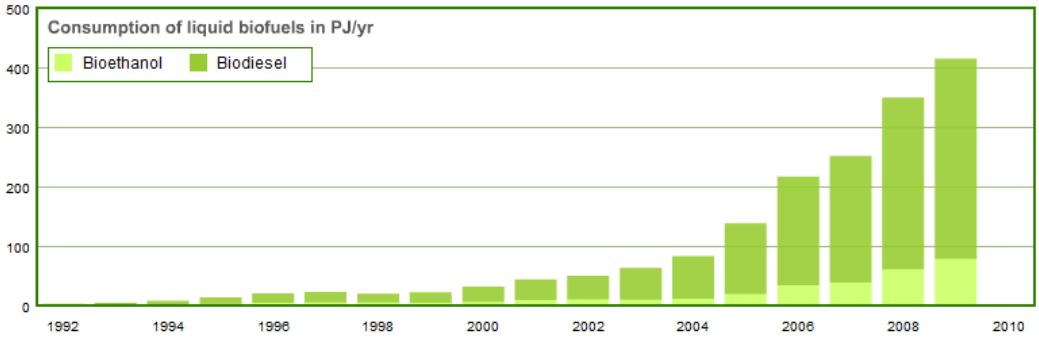

Figure 2.10. Bio-ethanol and bio-diesel consumption evolution, [36].

Despite the fact that these fuels are attractive alternative considering environment issues, especially CO_2 emission, it was proved that pure oils cannot be used because of technical problems. The high viscosity leads to poor fuel atomization, inefficient oxidation, an increase in exhaust emissions and carbon deposits on the injector [1, 33]. It was concluded that pure oils require modification to be useful for diesel engine applications, achieved by the process of transesterification which improves fuel viscosity, lubricating properties and thermal stability. One of the most popular fuels obtained in this process is RME (rapeseed methyl ester). It was reported in literature that application of RME is advantageous since it produces lower particulate, CO, HC emissions, [31]. However, the process of fuel conversion requires additional energy and a subsequent increase in production costs. For example, RME production is approximately six times greater than diesel fuel, [36]. Distribution of biodiesel blends with conventional diesel is common and is given a B rating which states the amount of biodiesel present in fuel mixture. For example B20 corresponds to 20 % of biodiesel in mixture.

During recent years extensive study was conducted on the combustion of diesel fuel containing oxygenated hydrocarbons. It was reported that a beneficial influence of oxygen content on soot emission may be caused by a reduction of the carbon atoms which are replaced by oxygen atoms in the fuel structure. A reduced number of carbon atoms would lead to a decrease in soot precursors formation. In review paper [17] numerous studies were analysed with respect to fuel composition and emissions. They reported that oxygen content in fuel causes a reduction in soot emission. However, it was emphasised that the reduction in measured soot may be related to reduced soot formation rather than oxidation. It was also emphasised that the effects of molecular structure and fuel composition on soot formation is not fully understood.

Numerous alternative fuels have also been used in diesel engines including: algae based fuel, hydrogen, gas to liquid (GTL), bio-mass to liquid (BTL), anything (any carbonaceous material) to liquid (XTL), liquefied petroleum gas (LPG).

GTL is a paraffinic fuel generated from natural gas during Fisher-Tropsch (FT) synthesis using CO and H_2 which are generated from raw material. The main advantage of GTL is that it does not contain polyaromatic hydrocarbons and sulphur, which is detrimental to after-treatment systems, [37]. BTL fuel is generated during thermal process of bio-mass gasification resulting in formation of "syngas" (mixture of CO and H_2). Usually as feedstock, forestry and mill residues, straws and energy grasses are used, [38]. This concept enables the possibility of fuel formation from anything (any carbonaceous material) (XTL) and is a promising concept.

2.4. Soot measurement techniques

This section gives a general overview of in-cylinder optical diagnostics applied for visualisation of combustion and soot characterization and explains the physical principle of measurement techniques used in this study. The last subsection presents techniques applied for soot particle measurements in exhaust gasses.

2.4.1. In-cylinder soot measurements - optical diagnostics

An understanding of diesel combustion processes has become crucial, especially during recent years when severe emission regulations were developed and imposed. The need of defining a phenomenological model for diesel combustion and emissions was critical and at this point, laser diagnostics for in-cylinder measurements gained interest. Experimental studies of combustion and emission processes were performed by number of researchers. The main challenge was to apply these various techniques and simultaneously run the engine under realistic conditions. Optical diagnostics are an attractive alternative to physical probing and are based on the measurements of interactions between light and atoms or molecules. Optical techniques are difficult to apply and analyse. Therefore knowledge regarding physics, properties of light and construction of instruments for its detection is necessary. Additionally, the relationship between emission of optical signal and factors like temperature, pressure, state of molecules has to be understood.

2.4.1.1. Shadowgraphy

Shadowgraphy is one of the techniques employed for visualisation of the fuel jet where the spray breakup process can be investigated. It is a non-intrusive optical, line-of-sight visualisation technique. Incident light with certain intensity illuminates the flow from the back side and the light intensity which is transmitted through the spray is photographed. A

decrease of the light will be observed and will depend on the composition of medium. Part of the light may be absorbed by the medium and part may be scattered. Scattering and absorption efficiency is dependent on the size of fuel droplets and the differences in optical density of the species in the cross-section, [39]. Based on these measurements, information about droplet size and position of the fuel spray can be obtained.

2.4.1.2. Laser diagnostics

To perform optical measurements in the engine, optical access to the engine combustion chamber has to be granted. Usually it is achieved by installing flat optical pistons with small optical windows in combustion chamber walls. Possible changes in geometry, heat transfer and temperature distribution in the combustion chamber caused by optical components also have to be considered and have been discussed at depth in previous work [40]. Once the optical access is achieved, care has to be taken during measurements to ensure components are clean to provide optimal signal.

Despite all difficulties, optical diagnostics has been successfully applied and enhanced the understanding of the basic processes occurring during combustion in the engine, [7]. Laser diagnostics have several advantages over common physical probing since they are considered as non-intrusive and non-disturbing. Continuous improvements in detection system technology allow for signal acquisition in extremely high temporal and spectral resolutions and enable a detailed investigation of in-cylinder processes to be undertaken. However, to perform any measurements, optical access is required and this is the main disadvantage of these techniques, [41].

2.4.1.2.1. Laser induced incandescence (LII) and time resolved laser induced incandescence (TR-LII)

LII potential of particle sizing was reported in 1974, [42] when an incandescence signal from soot was detected during the application of spontaneous laser Raman diagnostics. Subsequently, Melton and Dash built up theoretical background of LII, [43, 44, 45]. Laser induced incandescence (LII) is a technique that operates in real time and can therefore be applied for *in-situ* measurements. The technique gave the possibility to obtain spatially and temporally resolved measurements of soot in a simple way. Soot, which is irradiated by the high energy laser beam with a short duration of few nanoseconds, absorbs the energy and its temperature increases from surrounding temperature to approximately 3000 to 4000 K. The incandescence signals from the laser heated soot particles are captured using photo detectors

(like PMT) in combination with collection optics. The collected data is further analysed to derive the soot particle temperature, size, distribution width and the soot volume fraction [46, 47, 36, 48, 49, 50, 51, 52, 53]. Frequently LII signal is measured by two PMTs which collect signal emitted at two different wavelengths. This method is called Two Colour Time Resolved LII (TC TR-LII) and allowed for initial soot particle temperature determination which is one of the initial parameters for the mathematical model.

Dec and co-workers for example conducted study of soot formation in diesel engines [52, 53]. Quantitative measurements of soot volume fraction were conducted by several groups [54, 55, 56, 57, 58] and further improvement of mathematical model was completed [56, 59, 60]. Application of LII is very wide, measurements in laminar and turbulent flames are common [59, 61, 62, 63]. LII technique was successfully applied for soot volume fraction measurements in different types of flames: ethane flame with various additives such as methane, methanol, ethanol [64], acetylene/air flame [65], ethylene flame at pressures between 5 and 20 bar [66] and ethylene-nitrogen flame [67]. It was also found that various fuels generate different sizes of primary particles, which eventually resulted in different soot quantity [68]. The engine environment is much more complex due to the turbulent nature of combustion, higher in-cylinder temperature and pressure fluctuations. Nevertheless, several groups have conducted in-cylinder measurements [49, 50, 69, 70] and have found that the particle size increases initially with crank angle and then reduces during the expansion stroke [49, 50, 63, 70]. These investigations revealed that the size of soot particles is dependent on engine operating conditions, variation in air to fuel ratio, engine speed, load and fuel injection pressure. A decrease in the air to fuel ratio resulted in an increase in the particle size [71], whilst higher engine speeds resulted in the generation of smaller particles. Application of higher injection pressure caused a reduction in particle size (approximately 3 times smaller) [51]. Very limited work has been carried out on the measurement of in-cylinder soot particle size and their distribution width in an automotive high speed direct injection diesel engines. LII technique has been used in conjunction with other measurement techniques such as scanning mobility particle sizing techniques [46], scattering and extinction measurements [47] and transmission electron microscopy TEM [72, 73, 59], to validate the measured particle sizes and to extract information about soot volume fraction. The LII technique was also applied to soot volume fraction measurements within the flames in constant volume chambers, engine exhaust systems and in a high pressure in-cylinder engine environment.

2.4.1.2.2. Planar laser induced incandescence (PLII)

Formation of laser beam to laser sheet allows for application of this technique for two dimensional visualisation of soot: Planar Laser Induced Incandescence (PLII) was successfully applied for soot characterisation [61, 63, 74]; however, few results have been published based on engine measurements, [63]. This technique allows for relatively easy measurement of soot volume fraction and particle sizes in combustion chamber (once laser alignment and detection system synchronization with engine is achieved), not only during the initial part of fuel injection but during fully developed combustion and subsequently later in the expansion stroke. The laser beam is usually expanded by utilising cylindrical lenses and focused by a spherical lens. The laser dimensions depend on application and window dimension when PLII is applied to an engine. Usually beam thickness is set to few hundred μm (for example 350 μs), but greater values can also be applied. LII images are taken by an intensified CCD camera equipped with a lens. In front of the camera, a broadband filter may be placed to reduce interference from scattered light. Additionally, to reduce scattering the camera is gated just after the laser pulse. Usually a short gate with is applied (~ 20-30 ns).
In [63], PLII and two-colour time resolved LII were used simultaneously to estimate spatial soot distribution and local mean primary particle diameters. Soot volume fraction and particle diameters were estimated for several crank angle degrees and showed the development of soot processes in the combustion chamber. PLII was used in [63] to study the differences in soot processes between different fuels (diesel and mixture n-heptane/alpha-methylnaphthalene).

2.4.1.2.3. Laser Induced Fluorescence (LIF), Rayleigh, Mie and Raman scattering

Laser Induced Fluorescence (LIF)

The temperatures present in the combustion chamber during turbulent combustion in a diesel engine can be extreme and difficult to measure, especially with use of thermocouples. Application of thermocouples may affect flow and flame behaviour, their working range is limited and may be difficult to interpret since number of corrections for radiation, convection and conduction must be applied. Non-intrusive techniques for in-cylinder temperature including Laser Induced Fluorescence (LIF) and Rayleigh scattering became popular and frequently used. In Laser Induced Fluorescence, molecules are excited and return to their background state emitting radiation. The main difficulty in applying LIF is electronic quenching which is influenced by local temperature and pressures as well as concentration of species present in combustion chamber. This may lead to ambiguous results since quenching effects are difficult to estimate.

LIF can be used for temperature measurements when the laser beam which is irradiating molecules is changed to a frequency which causes combustion of a radical or molecule (like NO or OH) to fluoresce. The intensity of a signal will be dependent on specie density. For temperature measurements, two different transitions are probed and the ratio of measured intensities can be related to temperature using the Boltzman relationship, [41]. It provides non-intrusive temperature measurement technique, together with information regarding species concentration, velocity, pressure and density.

Rayleigh scattering

The elastic scattering by molecules and particles is called Rayleigh scattering and is observed when light scattered by small molecules or particles does not change its wavelength. The in-cylinder temperature can be calculated based on Rayleigh scattering. This method however is limited to flames with relatively low soot levels.

Mie scattering

Another important elastic scattering process due to aerosol particles is Mie scattering. This method was developed in 1908 by Gustav Mie [75] and occurs when a particles size is comparable to wavelength near the infrared band. The intensity of the scattered light is determined by the ratio of the droplet size to wavelength of the illuminating light and the refractive index of the sphere.

Raman scattering

The inelasting photon scattering occurs when photons scattered from an atom or a molecule changes its state and was first measured by Raman in liquids. The main disadvantage of this scattering is that is much weaker than the Rayleight scattering. Spectral measurements of Raman scattering allows for molecular species identification.

2.4.1.3. Combustion imaging

Combustion imaging has been widely applied for in-cylinder diagnostics to observe and characterise soot emitted in its early stages. Application of a high speed camera (HS) or intensified camera (ICCD) provides detection of spatially resolved flame natural luminosity. Chemiluminosence from radicals emitted at different wavelengths (eg. OH*, CH*) can be measured using spectrally resolved combustion imaging, `[63, 61, 76, 77]. For this purpose, an image intensifier utilising a series of filters is required. The soot processes of diesel fuel were studied widely in constant volume chambers for different sets of engine operating conditions including: ambient temperature, ambient density, injection pressure, [77, 78] as well as in diesel environment [79, 80, 81]. Owing to in-cylinder imaging techniques,

development of the fuel spray from the point of injection was studied. Research demonstrated that there are characteristic properties of jet which may be related to soot emission at a later stage. A wide range of studies has been completed on spray lift-off length (more details can be found in section 2.2.1 and chapter 7) [82] with findings indicating a strong relationship between the soot processes and flame lift-off length. It is believed that diesel combustion and emission processes are affected by the air-fuel premixing, just before the mixture enters combustion zone in diesel spray. Depending on the amount of premixed air, soot emission may be significantly reduced at the later stage. The influence of oxygen content on lift-off length and its effect on in-cylinder soot formation were as well investigated [81, 82, 83]. Subsequently, the correlation between lift-off length and ignition delay was frequently studied to further understand the mechanism behind flame lift-off length stabilisation.

2.4.1.3.1. Soot luminosity

Soot natural luminosity signal is a combination of incandescence signal from hot soot and chemiluminesence signal from excited gaseous species. Luminous radiation from soot can be recorded by camera and natural luminosity imaging is a valuable tool for characterising in-cylinder processes like soot formation and oxidation. Natural flame luminosity (radiation from soot) has been widely used for characterising in-cylinder combustion, soot formation and oxidation processes [31, 80]. The intensity of flame luminosity is strongly dependent upon the temperature of the burning soot, thus interpretation of high luminosity regions as regions of high soot may be misleading. Hence, natural flame luminosity should not be directly related to the amount of soot produced during the combustion process. The luminosity detected by a camera depends upon many factors, such as quantum efficiency of the image intensifier, detection system and its gain, adiabatic flame temperature, in-cylinder temperature and optical thickness. All these factors have to be taken into consideration when evaluating experimental data. Detailed discussion regarding all these factors is provided in section 6.3.2. Measurements are simple to obtain but interpretation of recorded signals can be challenging. Frequently, combustion imaging is performed in combination with the light source, for example copper vapour laser (CVL). Elastic laser light scattering from fuel droplets (Mie scattering) enables recording of the fuel injection, which is captured together with flame luminosity.

2.4.1.3.2. OH* chemilminesence

Chemiluminescence is a part of the natural luminosity signal and represents radiation from excited molecules. OH* is created during reaction and is interpreted as an indicator of high temperature reactions, which are initiated at a certain temperature level. An excited molecule can relax from excited to ground level by many different mechanisms, [84]. Usually, transmission between energy levels called radiative transition involves either the adsorption or the emission of radiation. Transition that takes place without adsorption or emission of radiation is called non-radiative transition.

The lifetime of radicals considered here is very short and once formed, is quickly consumed primarily during soot oxidation. Radiation, which is emitted by OH* occurs in a very narrow spectral range of approximately 310 nm, but the signal is quite easy to capture. Since the chemiluminescence signal is weak measurements require application of a high speed camera in combination with an image intensifier and adequate filter cantered around the spectral range of OH*. The radical's intensity level is an indication of the combustion which takes place within the lean portion of the mixture and as it was reported, radicals may appear in the centre of the spray and are surrounding soot but they do not coexist with soot, [76]. Among all radicals generated during reactions taking place in combustion chamber, OH* has an number of advantageous: OH* plays an important role in soot oxidation, [74, 85] is relatively easy to detect due to its strong signal when compared with different radicals and it is usually present in large concentrations.

2.4.1.4. Two colour method

Soot particles emit light which show a black-body spectrum. Depending on temperature, absolute intensity of emission and the shape of spectrum can change. The intensity ratio of the emission at two wavelengths contains information about soot particle temperature and the principle of its determination is called two-colour method. Soot is not an ideal black body (grey body radiator) but its radiation can be related to black body radiation by inclusion of apparent temperature. Apparent temperature is defined as the temperature at which the radiation of black body is equal to a non-black-body radiation at a certain temperature. Radiation can be measured at two different wavelengths from which, after calibration of the measurement system, apparent temperatures can be calculated and flame temperature and soot concentration can be determined. The theory and technique for two-colour measurements is presented in [86] and has been successfully applied for measurements in diesel engines.

2.4.2. Soot measurements in exhaust gases

Current work focuses on the in-cylinder soot characterisation and therefore, techniques for exhaust soot measurements are just briefly described. In the following section, electrostatic classification of soot particles and transmission electron microscopy techniques will be discussed.

2.4.2.1. Electromobility spectrometer

Implication of particulate limit of $6 \cdot 10^{11}$#/km by Euro5 B directive raised need of developing a device capable of monitoring particulate number emission. Interest in system using electrostatic mechanism for soot particles classification increased. Developed systems are capable of measuring the number of soot particles (considering that particle diameter is represented by mobility diameter) in the broad range from 1000 nm to few nanometres. It was reported that soot particles formed in diesel engines are distributed in a bimodal manner with nucleation and accumulation mode [87, 88]. Nucleation mode is composed of soot particles in the range from few to ~ 20 nm. The mass of particles present in this mode is in the range from 1 to 20 % with nearly 90% of particle number. In accumulation mode, particle sizes from ~ 60 nm to 500 nm are present and most of the particle mass with low particle number is observed here. Soot particle size distribution was proposed by Kittelson [89] and is presented in Fig.2.11:

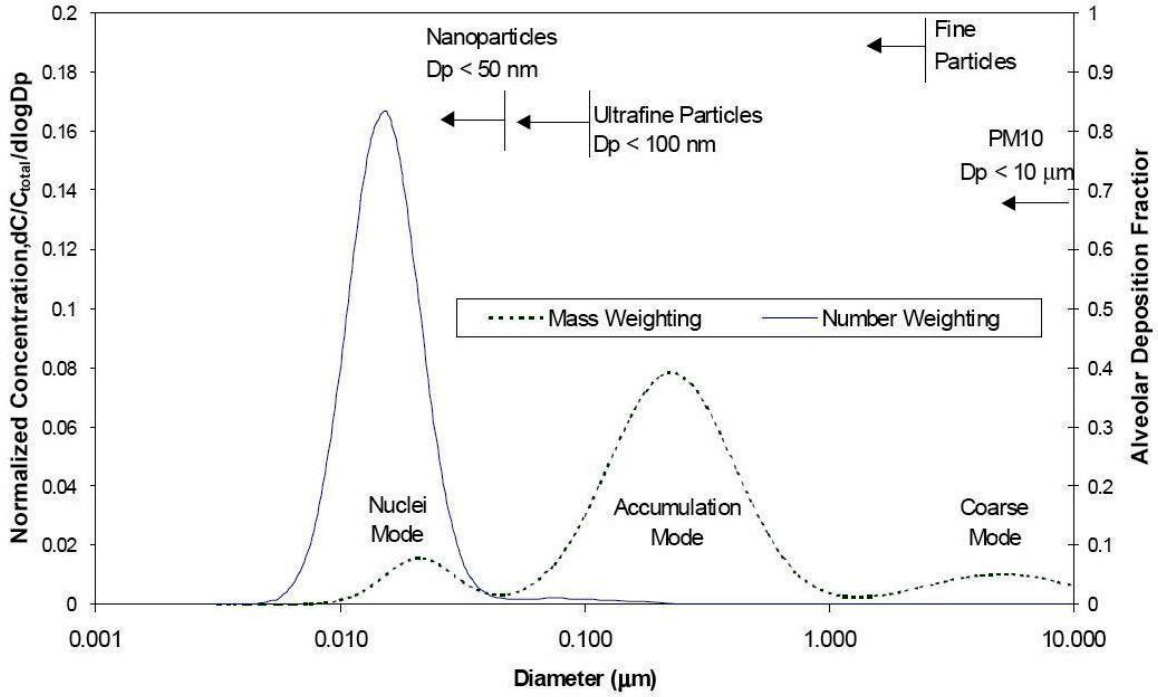

Figure 2.11. Soot particle size and mass distribution in diesel engine, Kittelson [89].

During measurements, sampled exhaust gasses are diluted to simulate the mixing with ambient gas. Dilution ratio and temperature are one of the most important parameters which may influence soot particle distribution. Exhaust gasses after diluting, pass through the neutraliser and a differential mobility analyser (DMA) coupled with a faraday cup electrometer (FCE), where soot particles are counted. A detailed description of experimental set-up is presented in section 4.6.

Several groups [87, 88, 90, 91], have used a combination of DMA and condensation particle counter (CPC) to investigate the effects of engine operating parameters, fuel and lube oil composition, engine duty cycle, speed and load on the exhaust particle size distribution. It was observed that in general, the exhaust soot size distribution is dependent on the engine operating conditions. Kittelson *et al.* [87] and several others have shown that the soot particles emitted from engines have exhibited a bi-modal size distribution. Particles measured with diameters less than 30 nm are referred to as nucleation mode particles whilst particles measured with diameters greater than 30 nm are referred as accumulation mode particles.

2.4.2.2. Transmission electron microscopy (TEM)

To obtain information of soot present in exhaust gasses, thermophoretic sampling is applied. A sampling probe is inserted for a short time into the exhaust pipe and soot particles are collected on the surface of a grid. The sample is then analysed with help of transmission electron microscopy (TEM). TEM allows for measurements of morphological properties of soot and actual dimensions and shape of soot and soot aggregates. As a result, primary particle size, aggregate size, structure and size distribution can be obtained. The optical properties of soot may be analysed and comparison between soot obtained from different sources is possible. Application of this technique provides important data which is necessary for the development of a soot formation and oxidation model as well as gives possibility to compare results obtained based on in-cylinder measurements, [63, 70, 92]. Typical images obtained from TEM are presented in Fig. 2.12.

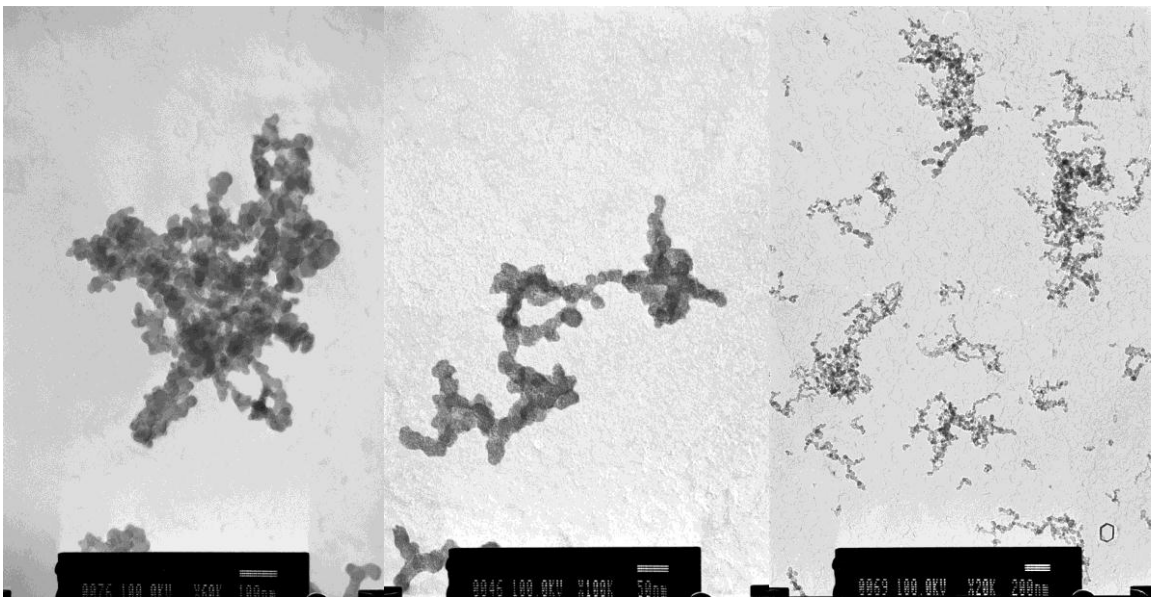

Figure 2.12. TEM images of soot measured in the exhaust pipe.

3. Chapter 3 - Theoretical background

In this chapter in cylinder pressure analysis is described and subsequently detailed discussion regarding mathematical model for LII measurements is presented. Section 3.2 provides general overview of mathematical models applied for soot particle sizing and highlights main differences between them. Section 3.3 gives detailed description of mathematical model used during this study.

3.1. In-cylinder pressure and heat release rate calculation

Based on in-cylinder pressure data combustion can be characterized by calculating indicated mean effective pressure (IMEP), heat release rate and ignition delay. In current work Microsoft Excel and Matlab R2008b were used for all calculations.

3.1.1. Indicated Mean Effective Pressure (IMEP)

Indicated mean effective pressure (IMEP) is valuable measure of engine's work that is related to engine displacement. IMEP is calculated based on pressure-volume diagram, [1]. Gross IMEP is calculated from area enclosed between the compression and expansion strokes where negative work is done during the exhaust and intake strokes. To calculate net IMEP negative work has to be subtracted from gross IMEP. Subsequently IMEP is calculated by integrating the pressure over the changes in volume of combustion chamber, using Eq. (3.1).

$$IMEP = \frac{1}{V}\int p_g dv \tag{3.1}$$

where V corresponds to in-cylinder volume and p_g pressure. The step interval in Eq. (3.1) was 0.2°CA.

3.1.2. Heat release rate

Based on in-cylinder pressure data heat release rate can be determined. HRR is based on first law of thermodynamics and is calculated from the energy balance of combustion chamber:

$$\frac{dQ}{dt} - p_g \frac{dV}{dt} + \sum \dot{m}_i h_i = \frac{dU}{dt} \tag{3.2}$$

where:

$\frac{dQ}{dt}$ - is a rate of transfer into system across boundary; $p_g \frac{dV}{dt}$ - rate of work transfer by system; $\dot{m}_i$ - mass flow rate into system at location *i*; h_i - enthalpy of flux *i*; U - internal energy.
While intake and exhaust valves are closed mass flow consist of mass of fuel injected into the combustion chamber, mass flow through the crevice and all other mass flow through the system boundary. In optical engine leakage through the optical components sealing may be observed and is very difficult to estimate how big it may be. The effect of this leakage was not taken into consideration in current work. Eq. (3.3) can be therefore expresses as:

$$\frac{dQ}{dt} - p_g \frac{dV}{dt} + \dot{m}_f h_f = \frac{dU}{dt} \tag{3.3}$$

U is defined as sensible internal energy of the in-cylinder charge, h_f is the sensible enthalpy of the injected fuel and h_f is neglected. Subsequently $\frac{dQ}{dt}$ becomes net heat release rate $\frac{dQ_n}{dt}$ which is defined as a difference between the heat generated during combustion of fuel and heat exchanged between system and ambient:

$$\frac{dQ_n}{dt} = \frac{dQ_{ch}}{dt} - \frac{dQ_h}{dt} = p_g \frac{dV}{dt} + \frac{dU_s}{dt} \tag{3.4}$$

Considering that in-cylinder gas behaves as an ideal gas Eq. (3.4) can be expressed as:

$$\frac{dQ_n}{dt} = p_g \frac{dV}{dt} + mc_v \frac{dT}{dt} \tag{3.5}$$

Where c_v is specific heat at constant pressure; T is absolute temperature. Taking into consideration ideal gas law and assuming that gas constant R is constant we can rearrange equation (3.5) to:

$$\frac{dQ_n}{dt} = \left(1 + \frac{c_v}{R}\right) p_g \frac{dV}{dt} + \frac{c_v}{R} V \frac{dp_g}{dt} \tag{3.6}$$

Substituting ratio of specific heats $\gamma = \frac{c_p}{c_v}$ into equation we will obtain:

$$\frac{dQ_n}{dt} = \frac{\gamma}{\gamma-1} p_g \frac{dV}{dt} + \frac{1}{\gamma-1} V \frac{dp_g}{dt} \quad (3.7)$$

Heat release rate in diesel engine can be calculated using Eq. (3.7). During engine operation specific heat ratio constantly changes. For air usually γ =1.35 are used and for burned gases γ of approximately 1.28-1.30 were used, [4].

The cumulative heat release rate can be calculated from the heat release rate:

$$CHR_n = HR_{n-1} + (HR\Delta\theta) \quad (3.8)$$

where HR is heat release rate and $\Delta\theta$ corresponds to crank angle degree.

3.1.3. Ignition delay (ID)

Based on the in-cylinder pressure ID can be determined. ID in current study is defined as the time from the start of injection (SOI) to the start of combustion (SOC). SOI is determined from the trigger signal for injector. SOC is evaluated from apparent heat release rate data in terms of CAD when the heat release curve becomes positive after SOI.

3.2. The mathematical models for soot particle size calculation

In order to extract particle size information from the measured LII data, a theoretical model was developed to simulate TR-LII signal and fit to the experimental data. The LII model is based on the energy and mass balance of soot particle, when it is irradiated by a high energy laser beam. Heated soot particles exchange energy with surrounding gases through the mechanism of conduction, sublimation, radiation and several other processes like annealing and oxidation. The presence of high pressure environment in the combustion chamber of diesel engine favours conduction as a dominant mode of heat exchange.

The base for all models was introduced by Melton [43] and represented by energy balance was for single, spherical soot particle:

$$\frac{d}{dt} E_{int} = \dot{q}_{abs} - \dot{q}_{cond} - \dot{q}_{vap} - \dot{q}_{rad} \quad (3.9)$$

The right side of equation stands for heat rate due to absorption of the energy from the laser beam and heat losses due to conduction, evaporation and radiation respectively. Schematic of mathematical model is presented in Fig.3.1.

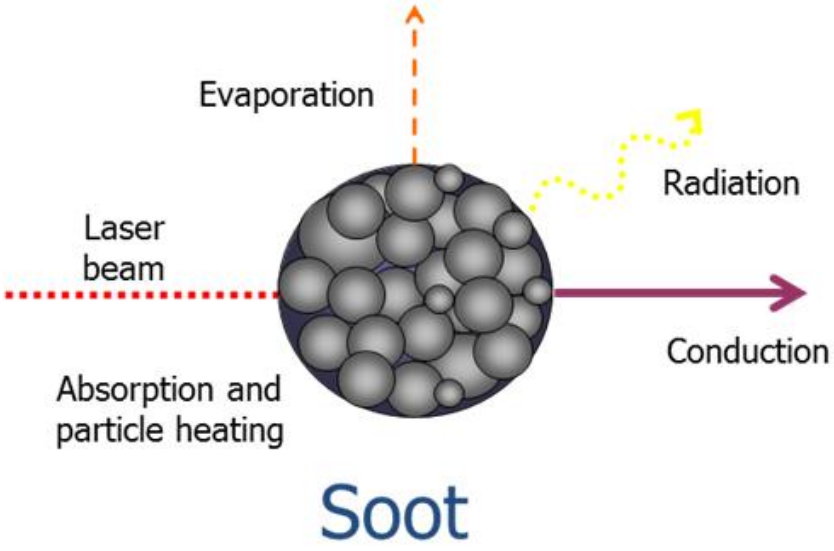

Figure 3.1. Schematic of mathematical model proposed by Melton.

High energy laser beam heats up soot particle and then cooling by conduction, evaporation and radiation is taking place.

Melton described the internal energy of single soot particle at certain temperature as:

$$E_{int} = \frac{4}{3}\pi r_p^3 \rho_p C_p T_p \tag{3.10}$$

where ρ_p is density, C_p is the heat capacity of soot particle. Majority of the models assume that primary particle has spherical geometry, they do assume as well that soot material properties are as graphitic carbon. As it was reported in [50] specific heat capacity of soot in most of the models is assumed as constant. Thus in models proposed by Kock, Michelsen and Liu temperature dependent heat capacity was used, [50].

In Melton model absorption term is expressed as:

$$\dot{q}_{abs} = Q_{abs}\pi r_p^2 \dot{q}_{laser} \tag{3.11}$$

where Q_{abs} is Mie absorption efficiency, $\dot{q}_{laser}$ is the laser fluence and $d_p = 2r_p$. Most of the models include absorption of the laser energy that is a function of laser fluence as well as wavelength and complex refractive index, which is discussed later. As mentioned soot particles absorb the energy from the laser beam and reach its peak temperature towards the end of the laser pulse. This temperature is one of the inputs to the mathematical model and is almost independent of particle size in the Rayleigh limit. It has been shown that for laser fluences up to 0.2 J/cm^2 the LII signal increases linearly and then reaches a plateau in the range about 0.2 to 0.4 J/cm^2 [93, 61]. In the plateau region the LII is independent of laser fluence. The analysis of the heat transfer due to absorption of energy from laser has not been considered in modelling for deriving primary particle size in current work.

In the Melton model, conduction cooling was dependent on thermal conductivity of air, ambient temperature and the Eucken factor which accounts for energy transfer between translational energy and internal energy [93]. The conduction cooling term proposed by Melton is dependent on Knudsen number, which allows for classification of the regime in which heat conduction occurs. Knudsen number is a dimensionless number and it is determined from the ratio of mean free path and characteristic length scale (soot particle diameter).

$$Kn = \frac{\lambda_{mfp,a}}{d_p} \tag{3.12}$$

The mean free path is defined as the average distance a particle travels between subsequent collisions and it is calculated as discussed in [62]. Number of mathematical models for heat conduction were developed based on Knudsen number. For large Knudsen numbers (greater than 10), mean free path is much larger than the radius of soot particle [62]. Heat conduction in this case is considered to be in the free-molecular regime. While Knudsen number is small (0.01), heat conduction between the soot particle and environment is considered to be in continuum regime [62].

The main issue related to heat losses due conduction is lack of agreement between the models regarding heat transfer coefficient. For free molecular regime heat losses due conduction can be described as proposed by Williams and Loyalka in [94].

$$\dot{q}_{cond} = f_c(Kn_c)\, \dot{q}_{cond} \tag{3.13}$$

For elevated pressures (transition regime) Knudsen-number-dependent interpolation function between free molecular and continuum regime based as well on William and Loyalka theory was used, [94]. For continuum regime heat conduction can be defined as:

$$\dot{q}_{cond} = 4\pi r_p \lambda_{cond}\left(T_p - T_a\right) \tag{3.14}$$

where λ_{cond} is thermal conductivity. Thermal conductivity can be calculated using Eq. (3.15):

$$\lambda_{cond} = \frac{1}{3} I_a c_{ta} C_v \frac{p_g}{R_m T_g} \tag{3.15}$$

where I_a is the mean free path in the ambient environment.

Knudsen number Kn_c is calculated based on the mean free path in the ambient environment according to the equation presented in [94]:

$$\lambda_{mfp,a} = \frac{1}{\sqrt{2}\sigma_{col}} \frac{k_B T_g}{p_g} = \frac{1}{\sqrt{2}\sigma_{col}\rho_g} \tag{3.16}$$

where σ_{col} is the collision cross section of the soot particles with the surrounding air.

There are several models which use McCoy and Cha theory for heat conduction which says that soot particle may collide with object or air molecule present in combustion chamber, [95, 96, 97, 98, 99]. In [100] heat transfer coefficient is calculated using Sutherland approximation and is expressed as:

$$h = \frac{1}{1+G\cdot Kn} k_* \left(\frac{T_p}{T_*}\right)^{3/4} \frac{T_*+S_k}{T_*+S_k} \tag{3.17}$$

where S_k is Sutherland constant for thermal conductivity, k_* is reference value for thermal conductivity and T_* is corresponding temperature. The power law of the temperature in the Suterland approximation is used to determine heat transfer coefficient. Fuchs in his model [101], considered heat conduction within two layers: in the boundary layer close to the particle, free-molecular regime was assumed, and outside the heat transport is assumed to be in continuum regime. The heat transfer coefficient in this model is calculated according to following Eq. (3.18):

$$h = \alpha_T \frac{p_g}{2} \sqrt{\frac{8k_B}{\pi M_g T_g}} \frac{\gamma+1}{\gamma-1} \tag{3.18}$$

where p_g and T_g are ambient pressure and temperature respectively, M_g is the molar weight of the ambient gas and k_B Boltzman constant. The values of accommodation coefficient α_T are discussed in section 3.3.1.

The heat loss due to vaporisation in Melton model is written as a product of mass loss rate and heat of vaporisation of carbon according to Eq. (3.19):

$$\dot{q}_{vap} = \Delta H_V \frac{dm_p}{dt} \tag{3.19}$$

where ΔH_V is specific vaporisation heat per unit mass carbon. Most of the available models consider evaporation/sublimation as a one of the governing mechanism. Vaporization from the surface of soot particle occurs at high laser fluence and the details associated with evaporation of soot are not well understood. Lasers with high incident energy may also lead to formation of molecular carbon species like C_2 and C_3. Care has been taken to eliminate the interference of swan band emission (438.3, 473.7, 516.5 and 563.6 nm) by exciting soot using the fundamental wavelength of Nd:YAG and using shorter detection wavelengths [50, 70]. In order to avoid uncertainties associated with this complex phase change processes low laser fluence was used in this work. According to Clausius-Clapeyron equation, particle vaporization temperature increases with pressure [61] so under high pressure engine

applications vaporisation will not be of major concern. Heat losses due to radiation not always are incorporated in the model since this heat exchange mechanism was considered as negligible.

Significant change in the particle size may be caused by sublimation of carbon species. Some of the models consider as sublimation as well as melting of soot particles [95]. Due to sublimation significant mass loss may be observed. Most of the models determine mass loss based on model proposed by Melton. Some of the models use expression which corrects for evaporation efficiency [96, 97]. This efficiency is comparable to accommodation coefficient in conduction term. In [49, 47] Knudsen-number dependent function for the mass flow was rate determination was used. Knudsen number there is determined from the ratio of mean free path of the vapour and into the ambient gas.

Heat exchange due to radiation in Melton model was determined based on the Stefan-Boltzmann law. Most of the models include cooling process due to radiation despite the fact that its influence is negligible.

3.3. Soot particle size and size distribution modelling-theoretical approach and simulations applied in current study

In current work, the mathematical model describes heat losses from an isolated spherical soot particle of diameter d_p, heated up by a pulsed high energy laser beam, is expressed based on the energy and mass balance equations (model does not include soot particle heating mechanism):

$$\frac{(m_p \cdot C_p \cdot dT_p)}{dt} = -\dot{Q}_{cond} - \dot{Q}_{sublim} - \dot{Q}_{rad} \tag{3.20}$$

$$\frac{dm_p}{dt} = -\dot{U}_{evap} \tag{3.21}$$

where the left side of equation relates to change of the internal energy of soot particle and the right side of the energy balance equation are: $\dot{Q}_{cond}$ - the heat losses due to conduction from the particle to the surrounding gas, $\dot{Q}_{sublim}$ - the heat losses due to sublimation and $\dot{Q}_{rad}$ - heat losses due to radiation; and the left side is the change in the internal energy of soot particles. Other cooling mechanisms like annealing, soot oxidation and photo-desorption that are discussed in Michelsen model [50] are not taken into consideration in this work. To account for temperature dependence a polynomial expression for specific heat capacity of

soot that is presented in [50] was used. In the temperature range $T_p = (0 - 1200)K$, C_p was calculated as:

$$C_p = \left(-9.7768 \cdot 10^{-4} + 2.7943 \cdot 10^{-4} + 1.4554 \cdot 10^{-5} \cdot {T_p}^2 - 3.4432 \cdot 10^{-8} \cdot {T_p}^3 + 3.6700 \cdot 10^{-11} \cdot {T_p}^4 - 1.9485 \cdot 10^{-14} \cdot {T_p}^5 + 4.1802 \cdot 10^{-18} \cdot {T_p}^6\right) \cdot 10^{-3} \quad (3.22)$$

and in the temperature range $T_p = 1200K$ to $5500K$

$$C_p = \left(2.9497 \cdot 10^{-1} + 2.9614 \cdot 10^{-3} \cdot T_p - 2.1232 \cdot 10^{-6} \cdot {T_p}^2 + 8.1901 \cdot 10^{-10} \cdot {T_p}^3 - 1.7516 \cdot 10^{-13} \cdot {T_p}^4 + 1.9628 \cdot 10^{-17} \cdot {T_p}^5 - 8.9817 \cdot 10^{-22} \cdot {T_p}^6\right) \cdot 10^{-3} \quad (3.23)$$

It has been suggested in [62] that neglecting the temperature dependence of heat capacity ratio will lead to underestimation of heat conduction rate by as much as 18% when the local gas temperature is around 400 K. In the flame the local gas temperatures are significantly higher (the difference between soot temperature and flame temperature are not that large) and temperature dependency can be neglected leading to the underestimation of conduction rate of approximately 3%. In this work particularly when soot measurements are carried out after the end of visible luminous combustion large temperature difference exists between the surrounding gas and laser heated soot. Thus it is very important to account for temperature dependence on specific heat ratio under these conditions.

In the current study, the mathematical model is based on the formulations used in [70]. Most of the LII models that are published in literature are based on the simple assumption that soot primay particles are not influenced by aglomeration process, which means the soot primary particles are loosely attached to form aggregates. This assumtion introduces uncertainities in soot sizes estimation. In this model the measured decay rate is linked directly to the surface area of the primary soot particles, which in turn leads to the diameter of soot primary particle. However, there are concerns with the assumption of spherical soot particle as the published literature on soot using TEM techniques in flames have shown that the primary soot particles are not exactly spherical. Due to coagulation process they are more of rotational ellipsoid shape. The surface area to volume ratio of these rotational ellipsoidal shapes are relatively larger than spherical shapes, which can lead to higher cooling rates due to conduction and underestimation of particle size. Additionally aglomeration tends to reduce the heat exchanging surface. All these deviations in shape of primary soot particale from spericity can in result reduce heat transfer rate which leads to overestimation of soot particle sizes.
In this model the assumptions were made that the considered particles are single, spherical and are distributed in a log-normal manner within the probed measurement volume.

3.3.1. Conduction

Since the in-cylinder pressures are higher, the heat exchange process between soot particles and the gas in the combustion chamber is dominated by heat conduction. The in-cylinder pressure varies with crank angle, therefore it is important to account for these pressure variations to the LII model. The effects of pressure variation are taken into consideration through the non-dimensional Knudsen number, which is introduced into conduction model through an empirical function $\mathrm{fh} = f_c(Kn_c)$ in [70]. The operational in-cylinder pressure range of the engine, their corresponding Knudsen numbers and their effects on heat loss rate due to conduction are presented in Fig 3.2.

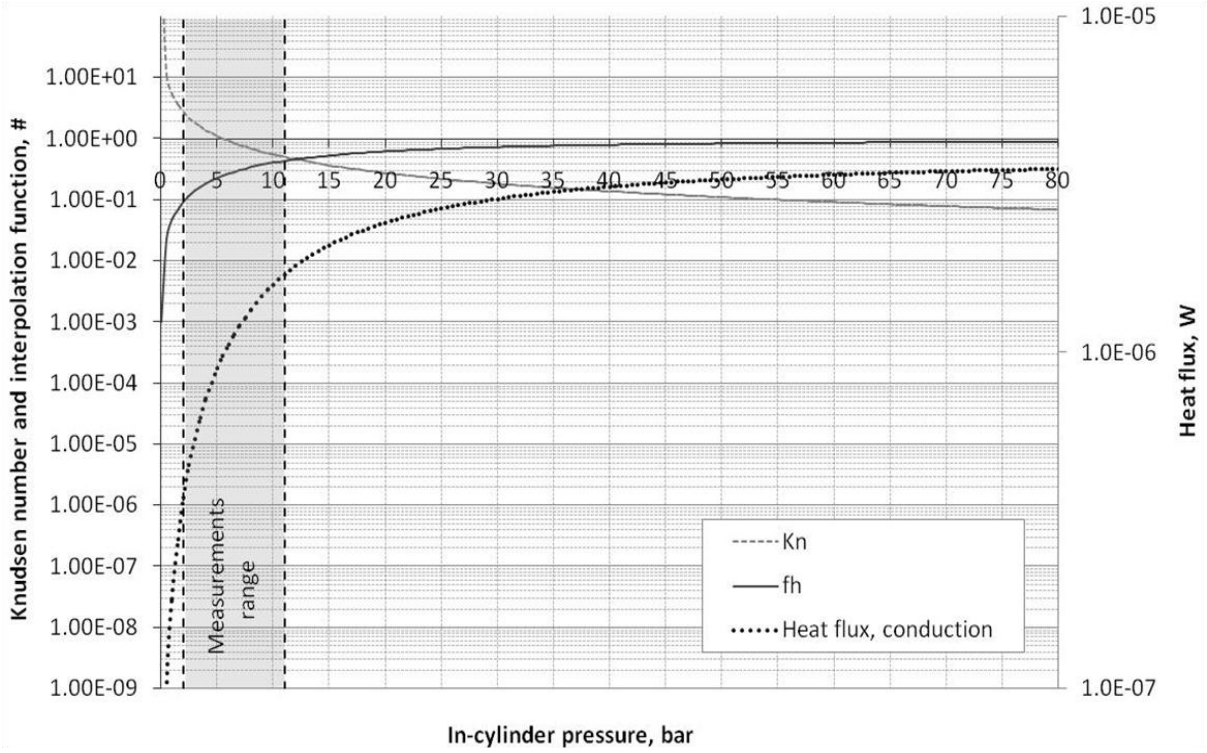

Figure 3.2. Variations of Knudsen number interpolation function and heat flux due to conduction at different cylinder pressures.

It can be seen that the considered measurement range falls in the transition regime which is between free molecular and continuum regime. Heat transfer due to conduction in the current study is approximated by the inclusion of Knudsen number interpolation function, which was originally introduced by Williams and Loyalka as shown in Eq. (3.24), [19, 8]:

$$\dot{Q}_{cond} = 2\pi d_p \lambda_{cond} \left(T_p - T_g\right) f_c(Kn_c) \tag{3.24}$$

$f_c(Kn_c)$ is an empirical function that corrects the continuum heat flux for pressure effects and is calculated according to eq. (3.25), [15]:

$$f_c(Kn_c) = \left[1 + \frac{1.9234A + 1.3026}{1.9234Kn_c + 1}\right] \tag{3.25}$$

where

$$A = \frac{\dot{Q}_{cond,c}}{\dot{Q}_{cond,fm}} = 5\frac{\sqrt{\pi}}{\alpha_T}\left(\frac{\gamma-1}{\gamma+1}\right)Kn_c \tag{3.26}$$

where: $\dot{Q}_{cond,c}$ is the heat flux due to conduction in continuum regime $\dot{Q}_{cond,fm}$ is the heat flux due to conduction in free molecular regime, α_T is the translational energy accommodation coefficient and γ is the heat capacity ratio.

The translational energy accommodation coefficient (α_T) is an important parameter that provides details about how much energy is transferred during collision between particle and environment. This parameter is used in the Knudsen number interpolation function. In the case of full accommodation $\alpha_T = 1$, gas molecules leave the soot particle with temperature of the particle. When $\alpha_T = 0$, gas molecules which leave soot particle after collision retains the gas temperature. This parameter is essential for heat conduction modelling but unfortunately it has not been completely understood and it introduces an uncertainty to LII model. Information concerning the values of thermal accommodation coefficient obtained through experiments is limited. Recently Snelling [102] have experimentally derived the value of α_T and it was found to be 0.37 in an atmospheric laminar ethylene diffusion flame. In literature [62, 102, 60] a wide range of values ranging from 0.07 to 1 have been used for various conditions. For transition regime, values from α_T=0.26 to α_T=1, were used in [50, 62, 60]. Under intermediate ambient pressure conditions most of the values reported in literature for transition regime were about 0.3, [50, 62, 95, 63]. The LII measurements in engines were performed under transition regime conditions, so in this work the value of thermal accommodation coefficient was assumed to be 0.3. Heat capacity ratio for in cylinder gasses generally is assumed to be constant and its values are in range from 1.3 to 1.4, Michelsen *et al*. [50]. In model presented here following equation was used, Michelsen *et al*. [50]:

$$\gamma = 1.4221 - 1.863 \cdot 10^{-4}T_g + 8.0784 \cdot 10^{-8}T_g^2 - 1.6425 \cdot 10^{-11}T_g^3 + 1.2750 \cdot 10^{-15}T_g^4 \tag{3.27}$$

Since the cylinder pressure and temperature vary with crank angle, this pressure and temperature influences the heat conduction and it is important to take this into consideration during modelling of TR-LII. Number of collisions between the particles and the ambient gas molecules increases with pressure and it enhances conductive cooling mechanism. Subsequently shielding effect changes the heat transfer (mainly conductive cooling) between

the particle and environment due to agglomeration of primary particles (to form aggregates). The influence of shielding effect on the presented particle size was not considered in current work. This effect of shielding was investigated by considering the aggregate as an equivalent sphere [62, 103]. It has been shown that shielding can reduce heat losses due to conductive cooling by several tens of percent for a typical soot structure. This slower heat transfer rate will result in an overestimation of soot particle sizes. For a 10% decrease to the conductive cooling behaviour of our measured data we have found the size of particles to increase by 6%. This effect can be partially accounted for by using appropriate mean thermal accommodation coefficient.

TEM images from the engine exhaust normally show a complex aggregate structure but not much of this information is known or available in the literature regarding the structure of soot in a complex high pressure turbulent in-cylinder environment. If the aggregates would be loosely spaced in the probing volume then it would be possible to measure soot primary particle size. On the contrary if the aggregates would be densely packed in the probing volume, the signal decay rate from densely packed aggregates would be slower than that from primary particle. This would be mainly due to reduction in surface to volume ratio for collision with surrounding gas of the aggregate compared to primary particle. This results in measuring a larger size particle (over-estimation of primary size particle – when the decay is measured from an aggregate).

3.3.2. Evaporation

The phase change processes like sublimation and evaporation are a source of uncertainty in LII modelling, as not much is known about the structure of soot under these conditions. Thus in this work experiments were carried out at low laser fluence. The difficulties associated with the modelling of sublimation process is to sufficiently account for cooling immediately after the laser pulse, where the soot incandescence decay rate is nearly linear and has a large slope. It is not yet well defined which species are evaporating from particle surface, in the current work only C_3 molecules were taken into consideration. Lack of information regarding which evaporating species are formed leads to uncertainties in the soot particle temperature calculation, since the heat of vaporization of these molecules are significantly different. The heat flux due to evaporation was calculated as a product of evaporation rate $\dot{U}_{evap}$ and enthalpy of evaporation of the soot particle Δh_v.

$$\dot{Q}_{sublim} = \dot{U}_{evap} \Delta h_v \tag{3.28}$$

The evaporation rate was calculated as proposed in [15]:

$$\dot{U}_{evap} = 2\,\pi d_p D(\rho_s - \rho_\infty) f_{ev}(Kn_{ev}) \tag{3.29}$$

where D is the diffusion coefficient of the soot vapour into the ambient gas and it is calculated according to the theoretical equation proposed in [94, 104]. As the in-cylinder pressure increases the diffusion process slows down causing a decrease in heat transfer rate due to sublimation. Density of the soot vapour ρ_s in (Eq. 3.29) is treated as carbon vapour at the particle surface and it was determined from Clausius-Clapeyron equation by assuming that soot vapour behaves like an ideal gas in thermodynamic equilibrium. The carbon vapour density ρ_∞ at infinite distance from the soot particle will be low and therefore in this analysis the assumption of $\rho_\infty = 0$ was made. Evaporation rate $\dot{U}_{evap}$ of the soot particle in the transition regime was approximated by the interpolation function $f_{ev}(Kn_{ev})$ expressed by:

$$f_{ev}(Kn_{ev}) = \left[1 + Kn_{ev}\frac{1.3333B+1.0161}{1.3333Kn_{ev}+1}\right]^{-1} \tag{3.30}$$

Where:

$$B = \frac{\dot{U}_{sublim,c}}{\dot{U}_{sublim,fm}} Kn_{ev}\frac{\sqrt{\pi}}{\alpha_v} \tag{3.31}$$

Calculation of this function requires information regarding thermal accommodation coefficient for evaporation, which in this study was assumed to be $\alpha_v = 1$ that corresponds to full accommodation as discussed in [70].

3.3.3. Radiation

Assuming that soot is a black body radiator, heat losses from soot was calculated from the Stefan-Boltzman equation:

$$\dot{Q}_{rad} = \pi {d_p}^2 \sigma \varepsilon_{pt}\left(T_p^4 - T_g^4\right) \tag{3.32}$$

The total emissivity was assumed as $\varepsilon_{\mathrm{pt}} = 1$. The influence of radiation on the soot particle cooling process is negligible compared to conduction [70, 105].

3.3.4. Solution

The energy and the mass balance equations were solved using fourth order Runge-Kutta method to obtain the soot particle temperature and its size as a function of time. Temporal incandescence of laser irradiated soot was calculated based on Planck's law at the detection wavelength of 415 nm. The signal intensity of soot incandescence can be expressed as:

$$LII(t) \propto \left\{ d_p(t)^3 \left[exp\left(\frac{hc_0}{\lambda_{detect} k_B T_p(t)} \right) - 1 \right]^{-1} - \left(d_p^0 \right)^3 \left[exp\left(\frac{hc}{\lambda_{detect} k_B T_g} \right) - 1 \right]^{-1} \right\} \tag{3.33}$$

Within the probing zone (in atmospheric flames as well as in exhaust gasses) there are particles of various sizes [70, 71, 106], a similar behaviour of particles of various sizes tend to exhibit in the combustion chamber of diesel engines under high pressure operating conditions. For this reason particle size distribution was approximated using a lognormal distribution function $P(d_p)$.

$$P(d_p) = \frac{1}{\sqrt{2}\pi d_p \sigma} exp\left\{ - \frac{[ln(d_p) - ln(d_{p,cmd})]}{2\sigma^2} \right\} \tag{3.34}$$

The experimentally measured LII data and the theoretical by derived LII signals were compared using the least squares fitting procedure to get: count median diameter (called particle diameter in this work) and the distribution width. Figure 3.3 illustrate the method of soot particle size and distribution width determination.

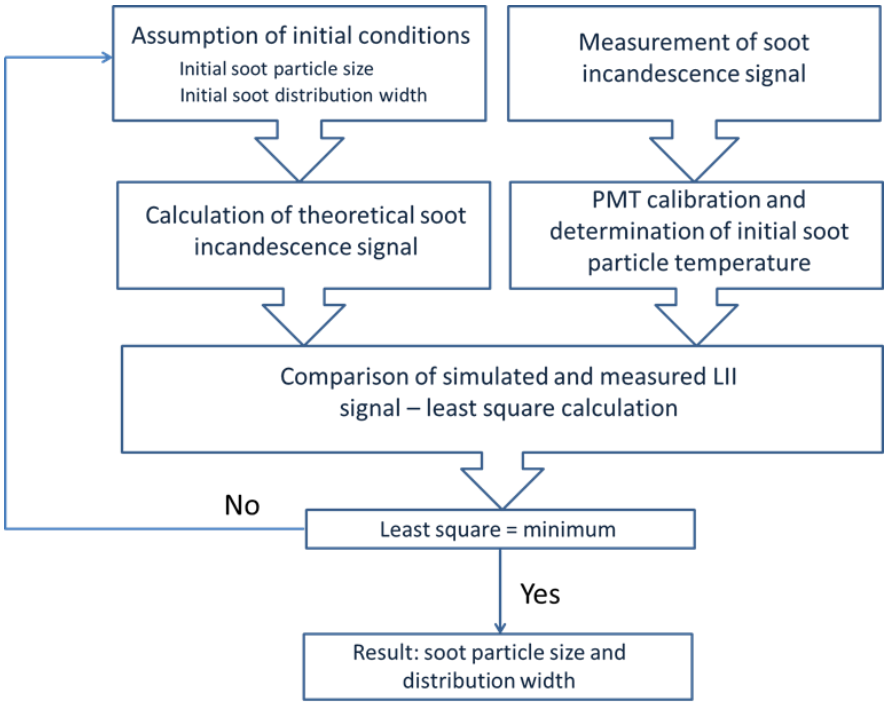

Figure 3.3. Flow diagram for soot particle size and distribution width determination.

3.4. Initial soot temperature

Time resolved two colour laser induced pyrometry technique was used to estimate the temperature of the laser-heated soot particle just after the laser pulse. The initial soot

temperature is one of the input parameters for LII model and was derived from the ratio of LII signals measured by PMTs at 415 nm and 665 nm. In order to calculate initial soot temperature detection system has to be calibrated. The calibration may be performed with various light sources of known incident irradiance on a diffuser of known scattering efficiency and angular distribution. In this study detection system is calibrated using a Tungsten Light Source (HL-2000) of known spectral output from 300 to 1050 nm presented in Fig. 3.4.

Figure 3.4. Ocean Optics Tungsten Light Source (HL-2000), [107].

Before calibration fibre optics was fitted into the lamp and flux at different wavelengths was measured using integrating sphere (Labsphere). Labsphere system is composed of spectrometer coupled with application based software and it allows for measurements of total spectral flux of small light sources. The spectrometer used in the set-up is of low spectral noise with broad spectral range through UV-VIS-NIR. With help of integrating sphere total light emitted by the lamp in all direction can be measured. The assumption has to be made that light output is isotropic that means that spectral radiant intensity $\frac{W}{sr \cdot m}$ in all directions is the same. The spectral radiance of the lamp can be calculated by dividing measured flux by solid angle and detection area, which in this case is a detection area of PMT. After determining spectral radiance of the lamp, PMTs calibration was performed. Since the PMTs are not gated, a light chopper was used between light source and the detection system during calibration. Known spectral intensity from the calibration lamp was detected by the PMTs and was used for determining the calibration constants K(λ). Calibration constant was determined from the ratio of signals detected by PMT during calibration, spectral radiance and PMT gain as described in [96]. The ratio of the incandescence signal obtained from experiments can be related to the ratio of incandescence signals obtained during calibration [96, 63], and it is expressed as:

$$\frac{\lambda_2{}^6 E(m_1)}{\lambda_1{}^6 E(m_2)} exp\left[-\frac{hc}{k_B T_p}\left(\frac{1}{\lambda_1}-\frac{1}{\lambda_2}\right)\right] = \frac{LII(\lambda_1)}{LII(\lambda_2)}\frac{K(\lambda_2)}{K(\lambda_1)}\frac{G_{exp2}}{G_{exp1}} \quad (3.35)$$

where $E(m_1)$ and $E(m_2)$are soot absorption functions at 415 nm and 665 nm. These functions depend on soot refractive index, which vary with wavelength. Several values were reported in literature depending on the source of soot and this variation may introduce an uncertainty in LII modelling. The values of wavelength dependent soot absorption function obtained from different experimental conditions are presented in [60, 108, 109]. In the current work, soot absorption function was calculated according to linear expression proposed by Snelling [96], which was obtained based on the experimental studies of Krishnan et al. [110].

$$E(m,\lambda) = 0.232 + 1.254 \cdot 10^{-4}\lambda \quad (3.36)$$

The gain for two PMTs were kept at the same level during all measurements, therefore the ratio of the gains will be eliminated. Subsequently after re-arranging Eq. (3.35), the temperature of the soot particle was calculated using Eq. (3.37).

$$T_p = \frac{hc}{k_B}\left(\frac{1}{\lambda_2}-\frac{1}{\lambda_1}\right)\frac{1}{ln\left(\frac{LII(\lambda_1)K(\lambda_2)\lambda_1^6 E(m_2)}{LII(\lambda_2)K(\lambda_1)\lambda_2^6 E(m_1)}\right)} \quad (3.37)$$

The temperature of soot particles that are heated up by laser pulse is related to the ratio of absolute light intensities measured at two wavelengths. Assumptions were made that soot particles were heated up by laser with spatially uniform fluence that results in uniform soot particle temperature in the laser probing volume. In the Rayleigh limit all particles have the same initial temperature. The absolute intensities of incandescence signal were calculated by dividing experimental signal by calibration constant and the temperature decay of soot particle was obtained from Eq. 3.37

3.5. Soot volume fraction (SVF) calculation

Using the derived initial soot particle temperature data it is possible to obtain soot volume fraction without any external calibration [96]. The corresponding soot volume fraction relation is based on the measured absolute soot incandescence:

$$f_v = \frac{LII}{K(\lambda_1)\omega_b G_{exp}\frac{12\pi c^2 h}{\lambda_1^6}E(m_{\lambda_1})\left[exp\left(\frac{hc}{k_B\lambda_1 T_p}\right)-1\right]^{-1}} \quad (3.38)$$

where the notation *LII* in Eq. (3.38) is the measured soot incandescence signal, $G_{exp}$is the gain of photomultiplier tube and $E(m_{\lambda_1})$ the soot absorption function calculated as described in section 3.4. $K(\lambda_1)$ is the calibration constant and it is obtained as shown in Eq. (3.39):

$$K(\lambda_1) = \frac{LII_{cal}}{R(\lambda,T)\cdot G_{cal}} \tag{3.39}$$

where $LII_{cal}$is the spectral intensity measured at 415 nm during calibration, R is spectral radiance of the lamp, which is a function of temperature and wavelength and G_{cal} is the gain of the photomultiplier tube that was used during calibration. Results obtained from SVF measurements are presented in chapter 6.

4. Chapter 4 - Experimental set-up

In this section experimental set-up and facilities used for measurements are presented. Chapter is divided into three sections: in first single cylinder optical engine is described, subsequently detection systems and laser. Figure 4.1 shows basics of experimental test facility used during measurements.

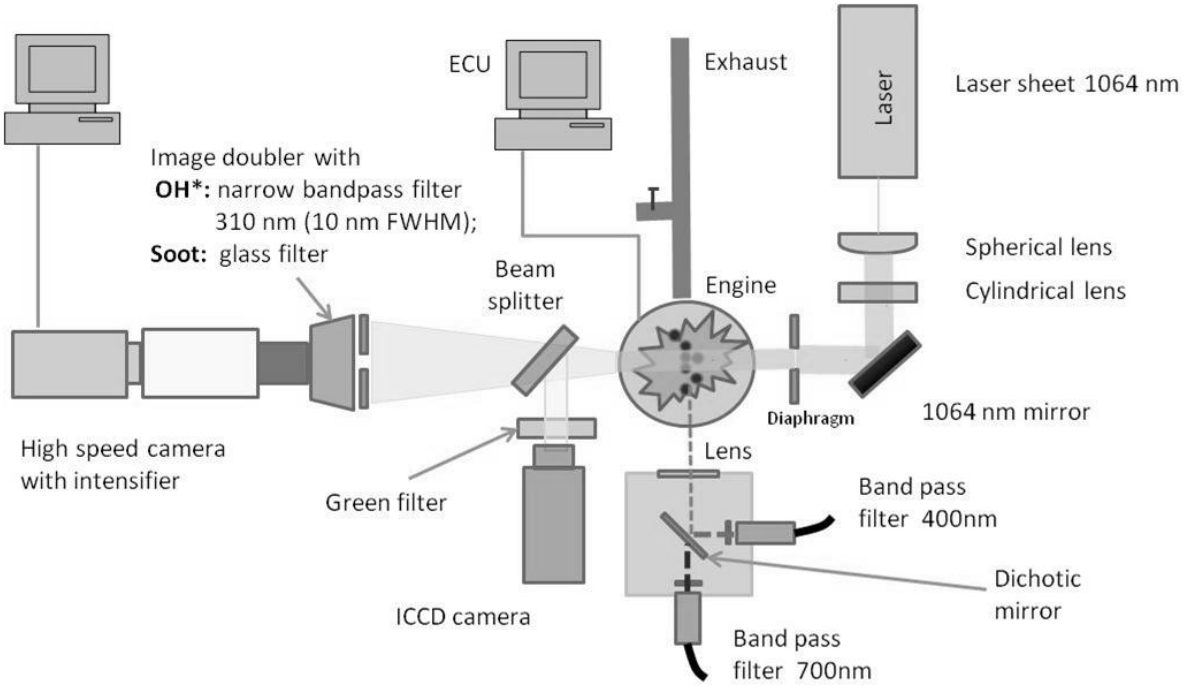

Figure 4.1. Experimental test facility.

4.1. Single cylinder optical high speed direct injection (HSDI) diesel engine

All the measurements presented in this study were performed in a single cylinder Ricardo Hydra optical diesel engine presented in Fig. 4.2.

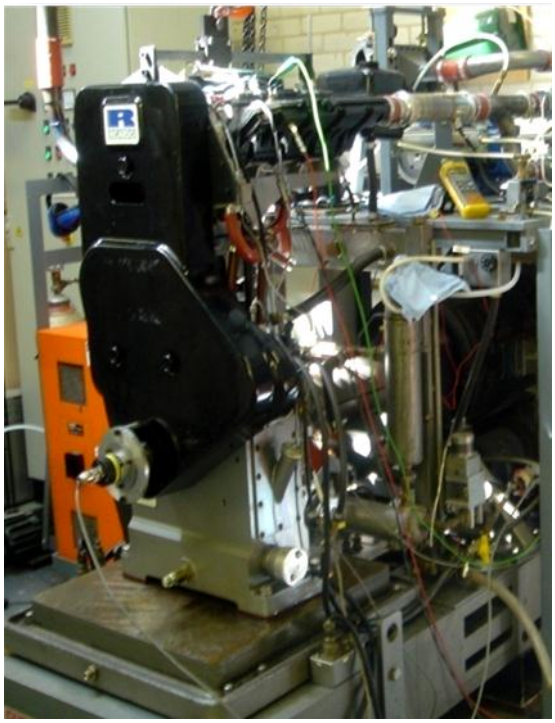

Figure 4.2. Ricardo Hydra optical diesel engine.

The specifications for the optical engine are detailed in Table 4.1.

Type	Engine details
Bore	86 mm
Stroke	86 mm
Swept volume	499 cm^3
Compression ratio	16.0:1
Swirl ratio	1.4

Table 4.1. Engine specification.

Engine was mounted on engine test bed produced by Cussons Technology. Test bed consists of a seismic mass engine mounting, 30 kW DC dynamometer, engine coolant and engine oil circuits. The 30 kW DC dynamometer motors the engine as well as acts as a brake when the engine is firing.

The coolant and lubricant temperature were heated up before measurements to approximately 80°C and were kept constant during the engine run to achieve steady state conditions, similar to those in standard diesel engine. The coolant system is composed of electric pump and a heater controlled by thermostat. The oil in lubrication system is pumped by a gravity-fed pressure pump driven by electric motor from the wet sump trough a filter to the main oil gallery in crankcase. The main oil gallery supplies the crankcase and cylinder head. The oil which is distributed by the action of crankshaft lubricates lower piston and cylinder wall. To

prevent contamination of optical surfaces in the upper cylinder block and piston lubrication by oil was avoided and was substituted by two carbon rings made of Le Carbone Lorraine grade 5890 carbon. For sealing two conventional steel compression rings were fitted and these rings were as well lubricated by carbon deposited on the cylinder wall by carbon rings in combination with lubrication paste applied during each rebuild of engine.

4.1.1. Cylinder head and windows

The cylinder head is from a production Ford 2.0 litre ZSD 420 Duratorq turbocharged engine. The injector is located centrally and cylinder head is equipped in four valves. The glow plug was replaced by Kistler 6125 piezoelectric transducer for measuring in-cylinder pressure.
The optical access was provided by fused silica window located in the base of the piston bowl. The piston and cylinder block were extended and a mirror of 45° angle with aluminized front surface was mounted between the upper and lower part of the piston (see Fig. 4.3). The width of the optical window is 43.5 mm and the high is 13.5 mm.

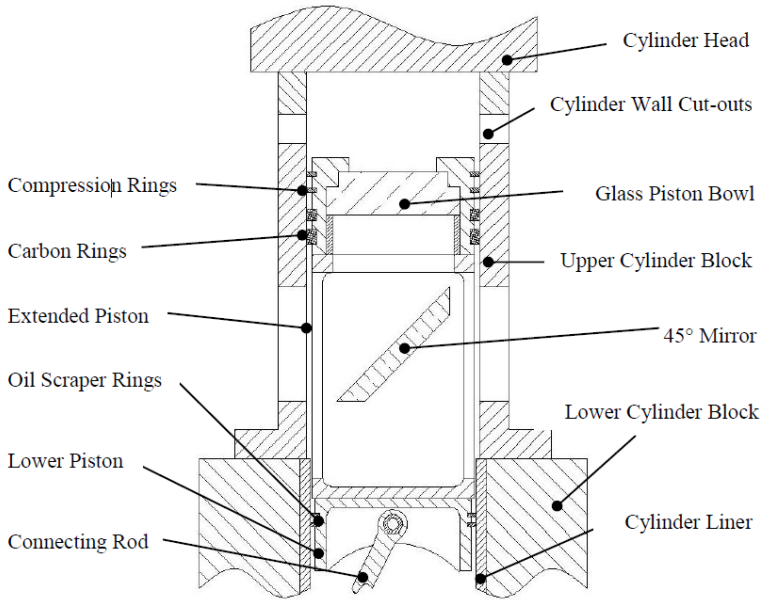

Figure 4.3. Engine's optical access.

In upper part of cylinder block three rectangular windows made of fused silica were mounted. Two side rectangular windows are visible in Fig. 4.3 (cylinder wall cut-outs), third window was placed perpendicularly. Depending on the measurement technique applied different windows were used. Usually trough the top windows, which are in plane laser sheet was directed. The laser beam was positioned to pass through the top part of combustion chamber, approximately 10 mm from the tip of injector towards the bottom of combustion chamber and

about 11 mm from the injector tip towards the side window (where the detection system was placed). In front of third perpendicular window or 45° mirror detection system was placed.
A glass window made of fused silica was mounted at the bottom of the piston. A graphite gasket was fitted between upper piston and the window and carbon gasket between the window and spacing ring that is sealed against extended piston (see Fig. 4.4). Set of these gaskets allowed for good seal and provided protection for glass components.

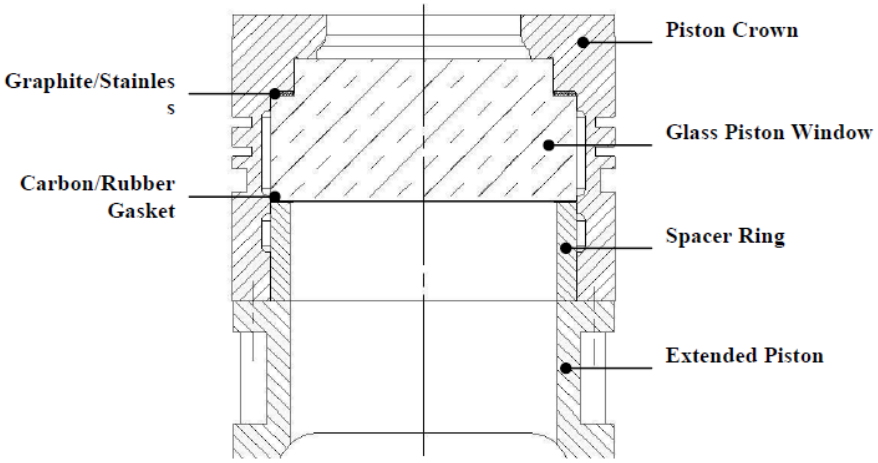

Figure 4.4. Piston window schematic view.

4.1.2. System for angular position detection

A shaft encoder was used to determine the angular position of the crank shaft. The shaft encoder transmits signals outputs of one pulse per revolution and 1800 pulses per revolution. Electronic control unit (ECU) uses these signals to control injection system and data acquisition system. Additionally single signal is used to illuminate LED which visualise occurrence of TDC and is mostly used during high speed imaging.

4.1.3. Fuel injection system

The main components of fuel injection system are: high pressure pump, common rail system, injector and electronic control unit.
The high pressure pump continuously supplies pressurised fuel into common rail. Delphi common rail injection system was used during this study. The fuel supplied to common rail using a single thick-wall steel pipe. The common rail injection system used in this study may generate a maximum injection pressure of maximum 1350 bar; however, peak pressure will be reduced due to the losses inside the pipe. Since in current study fuels of different properties were used, in order to maintain the fuel injection characteristics a pneumatic pump pneumatic PowerStar 4 pump which converts air inlet pressure to hydraulic output pressure up to 1200

bar and does not require lubrication (see Fig. 4.5 and 4.6) was used. The first generation Bosh high pressure pump outlet was blanked off and connected directly to the common rail.

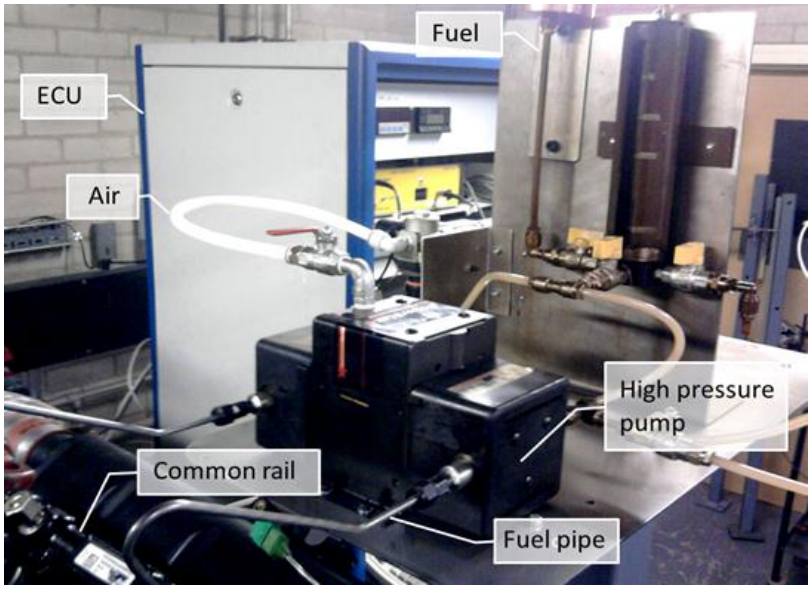

Figure 4.5. Injection system.

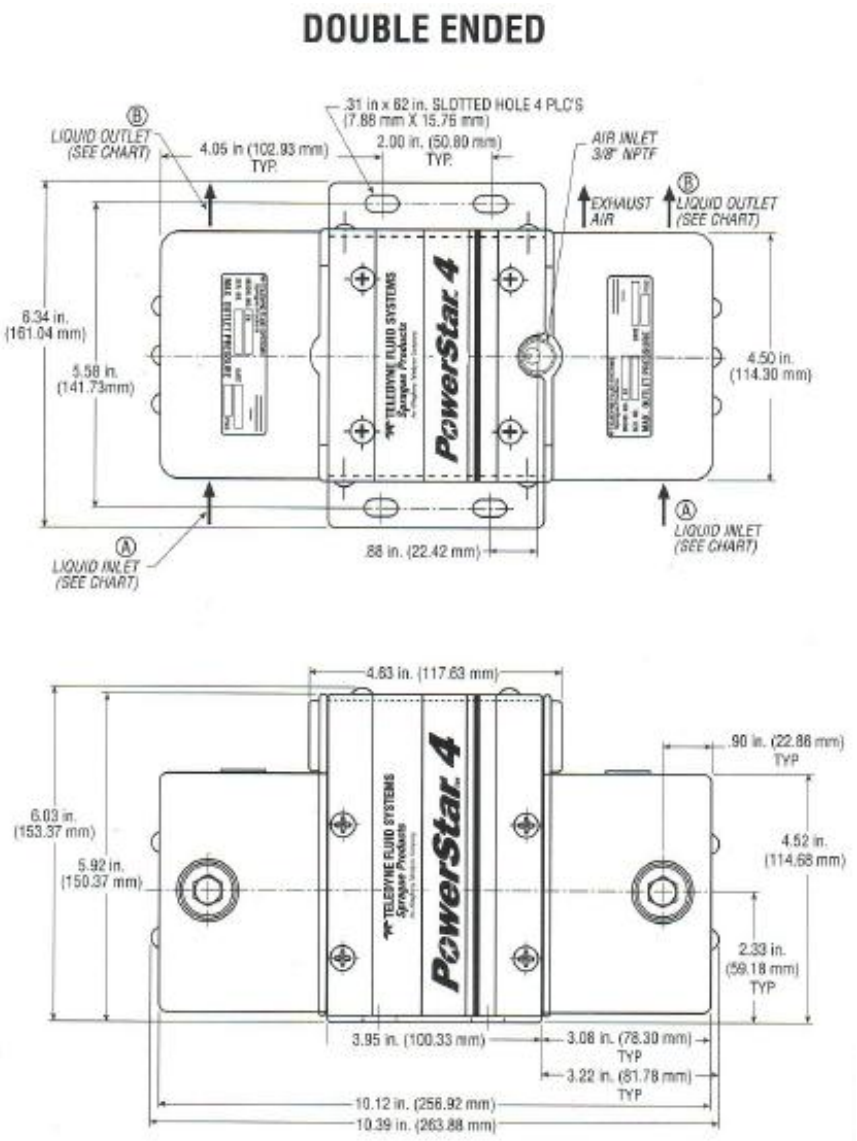

Figure 4.6. Drawing of PowerStar 4 pneumatic pump.

The advantage of common rail is that fuel injection pressure is independent on engine speed. This gives flexibility in injection timing and rate as well as improves jet quality. To control injection pressure, Delphi rail pressure sensor was fitted and its signal was sent to ECU where the pressure was controlled. Three of the common rail outlets were blanked off and remaining one was connected to injector. Common rail injection system fuel was coupled with the standard injector for Ford Mondeo, injector specifications are provided in Tab. 4.2. Injection was controlled by EmTroniX system (EC-GEN 500A), which gives possibility to precise control of injection timing and quantity of injected fuel.

Injection System	
1st Generation Common Rail System Delphi Standard Injector	
Maximum Injection Pressure	1350 bar
Number of Holes	6
Hole Size	0.154 mm
Cone Angle	154°
Flow Rate	0.697 l/min
Type	VCO

Table 4.2. Injection system specifications.

4.1.4. Intake system

The intake air can be either naturally aspirated or supercharged to engine. The possibility of connecting EGR as well exists. Experimental rig for supercharged intake system is presented in Fig. 4.7. Intake air can be boosted by Eaton M45 supercharger which is connected to the intake. This is compact supercharger which is driven by an AC motor at 2600 rpm and therefore do not affect fuel economy. The supercharger is a positive displacement type blower and it has a built-in bypass valve which helps to reduce the maximum boost pressure.

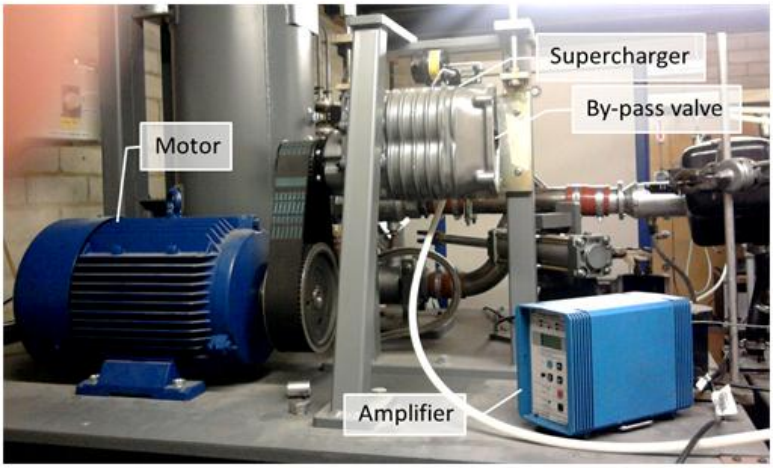

Figure 4.7. Intake system - supercharger

The intake manifold pressure is measured with a Kistler 4045A5 piezo-resistive pressure transducer connected to Kistler 4618A2 piezo-resistive amplifier. Pressure data can be recorded by a digital oscilloscope. Boost pressure can be controlled by opening or closing the bypass valve and the maximum boost pressure of 0.5 bar gauge can be obtained.
System for naturally aspirated intake air is visible in Fig.4.8, there intake air is directed to manifold trough the heater.

Figure 4.8. Intake system- naturally aspirated

For heating the intake air 3kW heater fitted before intake manifold is used. For measuring the intake air temperature thermocouple mounted in to the intake is used. Signal from thermocouple is send to a home-built heater control box which can turn the heater on or off and keeps it at a constant temperature. Intake heater is presented in Fig. 4.9.

Figure 4.9. Intake air heater.

4.1.5. System for in-cylinder pressure acquisition

In order to gain information about processes taking place in the combustion chamber, in-cylinder pressure analysis has to be performed. On the base of in-cylinder pressure heat release rate can be calculated which enables to characterise combustion process in diesel engine. In-cylinder pressure is acquired with help of Kistler 6125A piezoelectric transducer

visible in Fig. 4.10 connected to a Kistler 5011 charge amplifier, which sends an amplified signal to the data acquisition system.

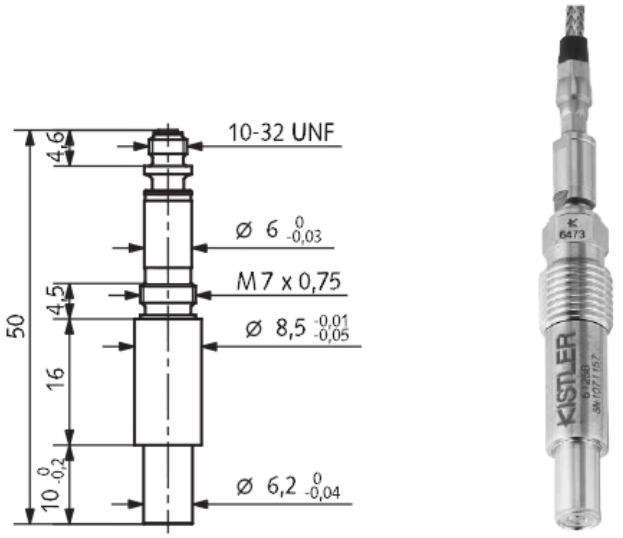

Figure 4.10. Piezoelectric transducer for in-cylinder pressure measurements.

The data acquisition system is composed of acquisition card, provided by National Instruments, software written in LabWIEV by John Williams at Brunel University and interface board. The signal from shaft encoder is provided together with amplified signal from charge amplifier which is connected to National Instruments BNC-2110 board. The board subsequently is connected to the National Instruments PCI-MIO-16E data acquisition card installed on computer. The data is recorded with intervals of 0.2 crank angle that corresponds to 1800 pulses per revolution which are sent from shaft encoder. Measured values of in-cylinder pressure are used afterwards for heat release rate, IMEP and ignition delay (ID) calculation.

4.1.6. Engine preparation procedure

The optical engine can be operated for short durations followed by shut down to cool optical engine components, and this process was repeated throughout the work. To simulate adequate real engine conditions one hour prior to start of the measurements cooling and lubricating systems were enabled to reach sufficient engine's temperatures. Before each test low pressure pump was turned on to make sure that the high pressure pump was lubricated. Subsequently the engine was motored at low speed (~ 800 rpm) and intake air heater was enabled. Once the temperatures were sufficient the speed of engine was increased and measurements were taken. During all measurements engine speed of 1200 rpm was maintained. Injection was controlled via PC using EC-Lab software and pressure data was acquired. Motoring pressure was

recorded at the beginning of each session to make sure that engine conditions were comparable, the piston window seals are in good conditions and check if the engine needs rebuilding

4.2. Detection system

Depending on technique applied for in-cylinder measurements detection system was divided in three sections:

- Time resolved laser induced incandescence (TR-LII) system for in-cylinder particle size, size distribution and soot volume fraction measurements (SVF);
- Planar laser induced incandescence (PLII) for two dimensional soot volume fraction measurements;
- High speed imaging for soot incandescence and OH* chemiluminescence measurements.

4.2.1. Time-resolved laser induced incandescence (TR-LII)

Laser induced incandescence (LII) is a technique that operates in real time and can therefore be applied for in-situ measurements. In order to detect soot incandescence high energy laser beam is sent through the top section of combustion chamber. Soot, which is irradiated by the high energy laser beam with a short duration of few nanoseconds, absorbs the energy and its temperature increases from surrounding temperature to approximately 3500 to 4000 K. The incandescence signals from the laser heated soot particles are captured using photo detectors (like PMT) in combination with other collection optics. Detection system is placed perpendicularly to the laser beam in front of third window in top section of combustion chamber. The collected data are further analysed to derive the soot particle temperature, size, distribution width and the soot volume fraction. Experimental test facility for TR-LII is presented in Fig. 4.11.

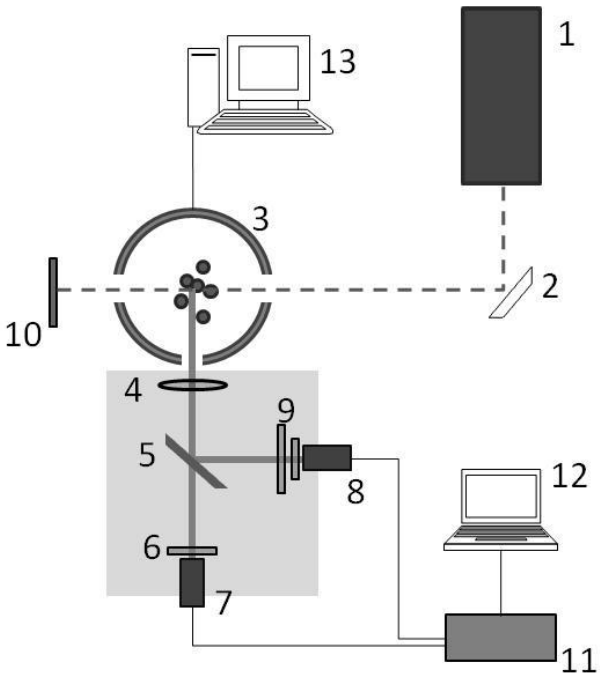

Figure 4.11. Schematic of experimental set-up: 1- laser; 2- 1064 nm mirror; 3- engine; 4- lens; 5- dichroic mirror (DMLP425) ; 6 - longpass filter (FGL665); 7 and 8 – photomultipliers; 9- green filter (BG39) and longpass filter (FGL400); 10- beam dump; 11- oscilloscope (TDS 2000B); 12- computer; 13- engine control unit.

The main components of TR-LII system are (PMT) and collection optics. Photomultipliers are devices designed to detect the light of very low intensity. It amplifies the light, so that even the weakest signal can be detected. Photons which are entering PMT are absorbed and electrons are emitted. The electrons generated by a photocathode which is exposed to photon flux are amplified, [111]. The principle behind PMT is visualised in Fig. 4.12.

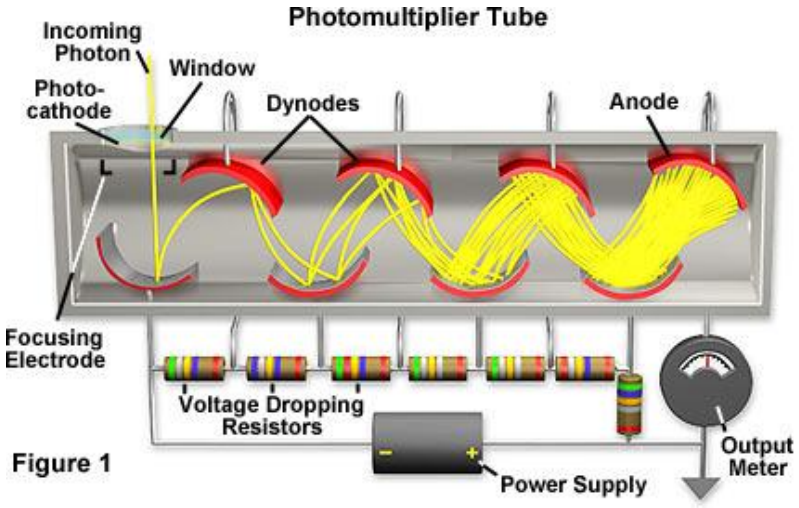

Figure 4.12. Photomultiplier tube principle, [111].

To collect broadband incandescence emission and directs it to the detection system the antireflection (AR) lens of 159 mm focal length was used. The signal passing through the dichroic mirror (DMLP425) was detected by two high response photomultipliers (rise time approximately 0.78 ns) provided by Hamamatsu Photonics, one with peak sensitivity at 400 nm (H6780-04) and the other at 630 nm (H6780-20) wavelength. The schematics and photography of experimental set-up for PMTs is presented in Fig. 4.13.

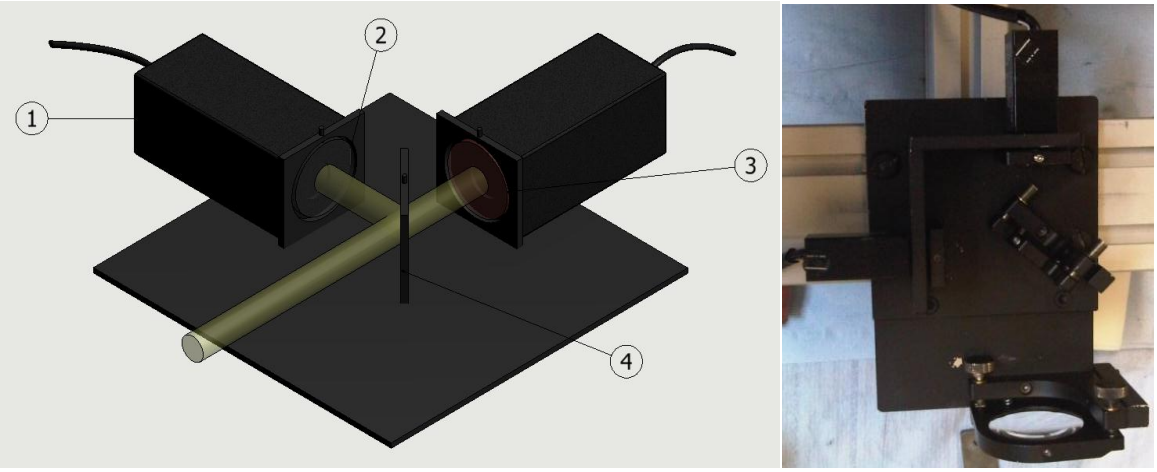

Figure.4.13. Right side: photomultipliers set-up: 1. PMT; 2. Narrow band pass filter or combination of filters with wavelength centred at 415nm; 3. Narrow bandpass filter or combination of filters with wavelength centred at 665 nm; 4. Dichroic mirror. Image on right side shows experimental set-up.

The first PMT measured the LII signal at 415 nm, this was achieved through a combination of dichroic mirror DMLP425 (reflects wavelengths between 380 nm to 425 nm), FGL400 filter (transmits everything above 400 nm), and BG39 filter (that eliminates wavelengths above 700 nm). Combination of these filters, together with the sensitivity of PMT leads to the detection wavelength centred at 415 nm with a FWHM of approximately 20 nm. Regarding the second PMT, combination of the dichroic mirror (transmits the light in range 440 nm to 700 nm) and FGL 665 (transmits wavelengths above 665 nm) in combination with the sensitivity of PMT resulted in a detection wavelength centred at 665 nm with a FWHM of about 30 nm. The example of LII signal measured during experiments, taken directly from oscilloscope is presented in Fig. 4.14.

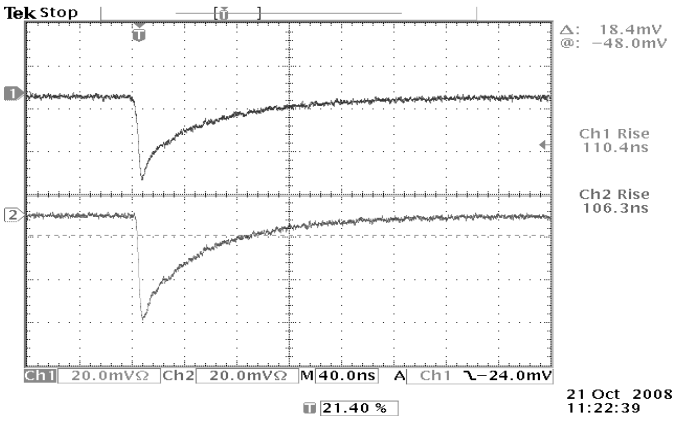

Figure 4.14. LII signal measure by two PMT during experiments

Since the spectral region for LII emission is wide, selection of spectral response of detection system is important especially to eliminate the interferences caused by Swan band emission. Collection of signal from wider spectral range may lead to overestimation of soot particle diameters or may lead to collection of signal caused by photochemical interferences and underestimation of soot particle diameters.

Both PMTs were set at the same gain and the soot emissions detected by the two PMTs were simultaneously acquired through a digital storage oscilloscope (TDS 2000B). The data was transferred to the computer through LabVIEWSignalExpress software supplied by National Instruments. For particle size evaluation, the PMT data corresponding to the wavelength centred at 415 nm was used.

4.2.2. Planar laser induced incandescence (PLII)

For PLII measurements laser was formed in laser sheet and was directed trough the top section of combustion chamber. Experimental test facility for PLII measurements is presented in Fig. 4.15. The principle of PLII is the same as LII with this difference that LII is a single point measurement and PLII provides two dimensional information of soot present in the measurements volume.

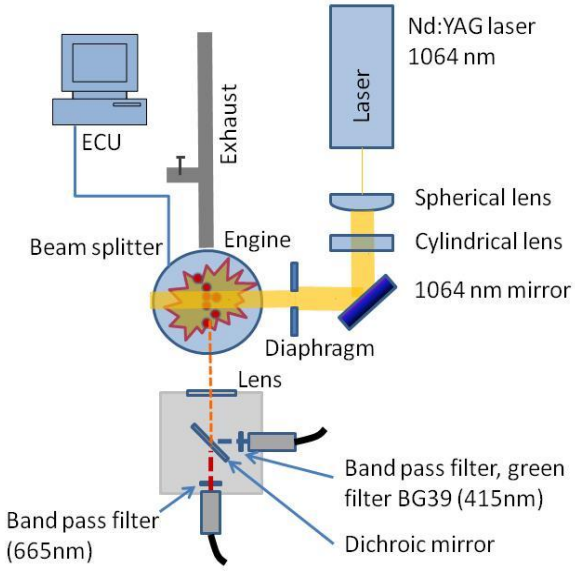

Figure 4.15. Experimental test facility for PLII measurements.

Emitted soot incandescence was directed though the piston window, 45° mirror, beam splitter BSW16 (45°, 50:50, transmission: from 300 nm to 400 nm, reflection from 400 nm to 700 nm) to the AndorInstaSpec V ICCD camera. The camera was equipped with a Nikkor 50 mm, 1:14 lens. The camera contains a monochrome CCD sensor. Triggering of camera is possible through the control unit and recorded images are transferred to PC using data acquisition card. Camera's gain can be adjusted (from 0 to 9) by a switch which is on top of camera. Collected data can be managed by Andor MCD software provided by Andor Technologies. For aligning camera is triggered manually, during measurements external trigger for approximately 60-70 ns is used (for PLII measurements). The ICCD image acquisition is quite long, the rate is limited to 0.2 Hz. The experimental set-up for PLII measurements is presented in Fig.4.16.

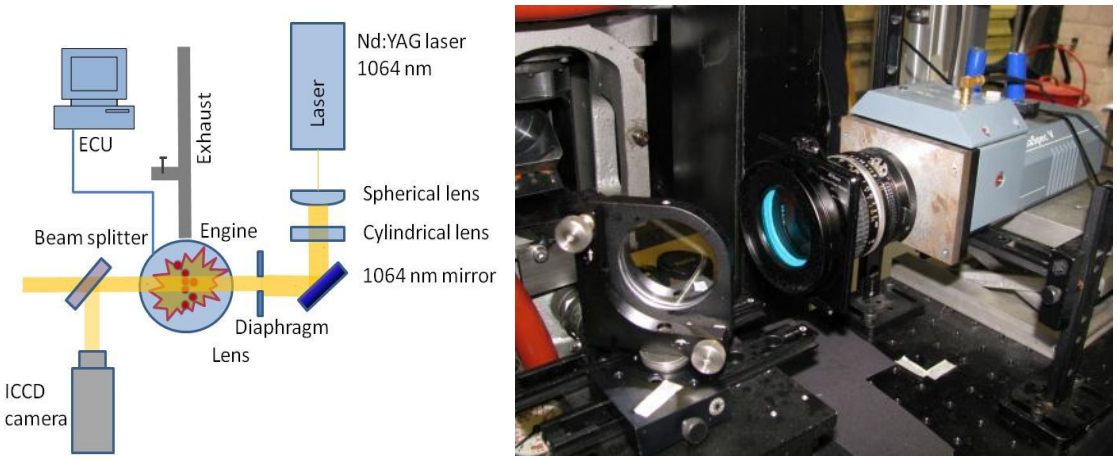

Figure 4.16. Left side: experimental set-up for PLII measurements. Right side: ICCD camera with beam splitter.

During PLII measurements engine was operated in a skip firing mode and the PLII images were recorded once per 60 cycles. PLII and TR-LII measurements were made possible only after the side windows were uncovered by the piston to allow the laser sheet to pass through, so the measurements were carried out after 45°aTDC.

4.2.3. High speed imaging

For high speed movies acquisition Memrecam FX 6000 coupled with DRS intensifier ILS-3-11 equipped with UV-Nikkor 105 mm , 1:4.5 lens was used. All movies were captured trough the piston window as it is visible in Fig. 4.17.

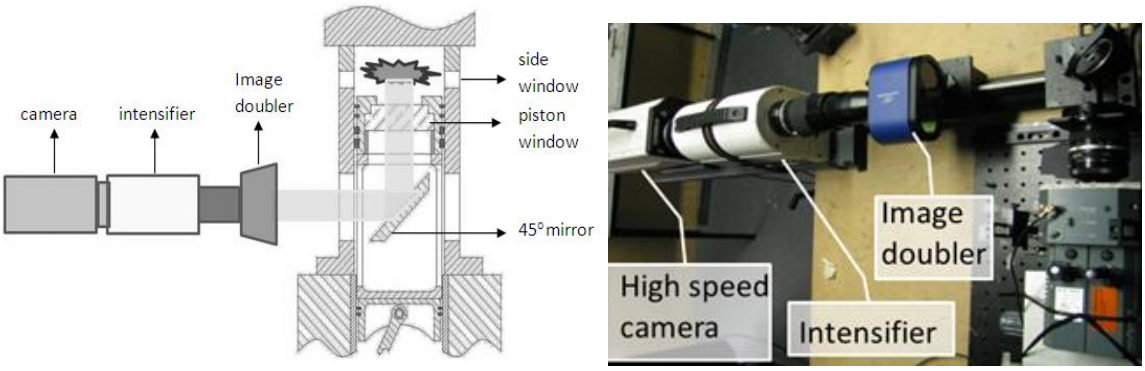

Figure 4.17. Left side: schematics of experimental set-up for high speed movies acquisition. Right side: photography of experimental set up for sigh speed imaging.

The spectral response of the intensifier is in the range from 214 – 900 nm. The high speed camera was operated at 10,000 frames per second, the corresponding pixel resolution was 512 × 248, and each frame corresponds to ~ 0.72° crank angle resolution. The spectral response of intensifier is in the range from 214 to 900 nm and is presented together with quantum efficiency in Fig. 4.18.

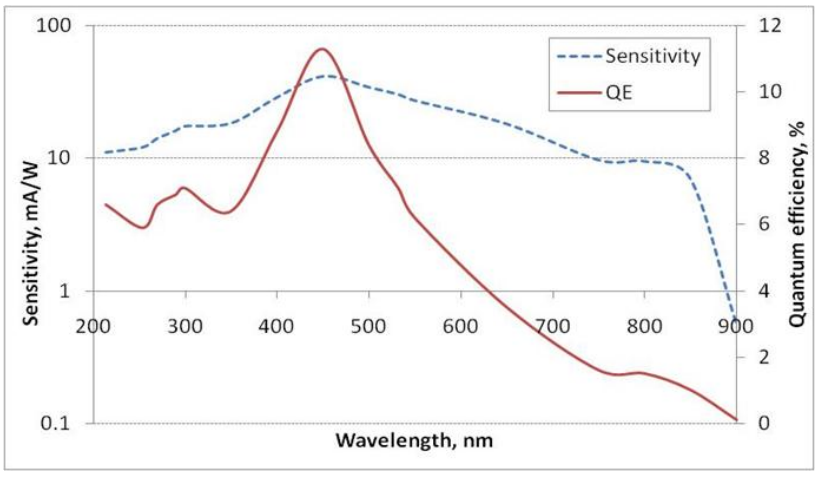

Figure 4.18. Spectral response and quantum efficiency of intensifier

High speed camera is equipped with image doubler which enabled simultaneous measurements of soot luminosity and OH* chemiluminescence. Image doubler was supplied by La vision and is presented in Fig.4.19 together with schematics of its working principle.

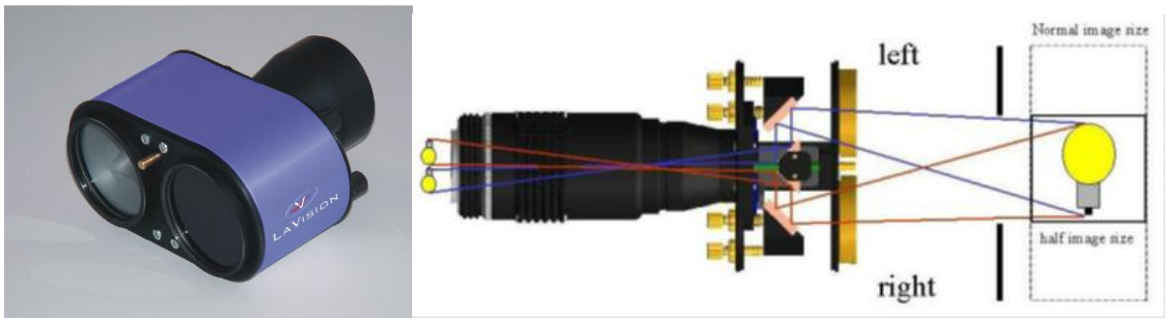

Figure 4.19. Image doubler and working principle.

The camera was triggered at a start of injection and images were acquired over duration of ~11 ms (approximately 80 CAD). During one engine run about 10 to 12 injection events are captured, and each injection event is composed of ~ 110 frames. For measuring OH* chemiluminescence a narrow band pass filter centred at 310 nm with a FWHM of 10 nm and 15 % peak transmission was used. For soot emission measurements, glass plate was used as a filter in front of the high speed camera to block OH* chemiluminescence and other UV emissions.

4.3. Laser

For TR-LII and PLII measurements Q-switched Nd:YAG laser (Continuum-Surelite) operating at fundamental wavelength of 1064 nm. Laser generates high energy pulses with the pulse width of 8ns (FWHM) and pulse repetition of 10 Hz. Laser was externally triggered once per each cycle. Figure 4.20 shows the laser used during experiments. Laser beam was directed through the combustion chamber with two 1064 nm mirrors (NB1J13) provided by Thorlabs.

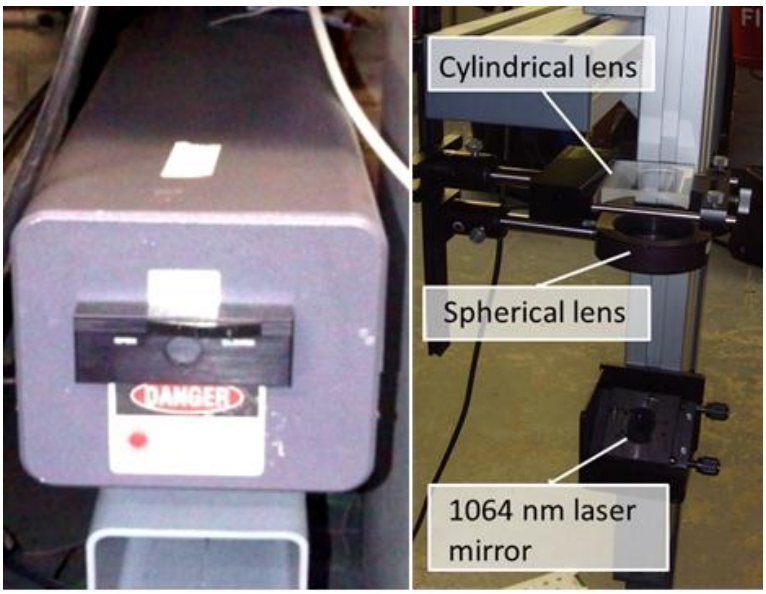

Figure 4.20. Experimental setup for Nd:YAG Laser. Left side: Nd:YAG laser. Right side: lenses set up for PLII measurements.

The laser generated a beam of approximately 6 mm diameter which for PLII measurements was passing through the cylindrical and LA1417-A plano-convex spherical lens (f=150mm, ARC 350-700nm) and was shaped to the laser sheet of 3 mm thickness and 21 mm. The laser fluence for TR-LII measurements was set at 0.21 (J/cm^2) and for PLII was approximately 0.38 (J/cm^2) taking into consideration of energy loses on the lenses and mirrors.

4.4. Synchronization

Detection system was synchronized with the engine and laser via an engine control unit and synchronisation scheme is presented in Fig. 4.21.

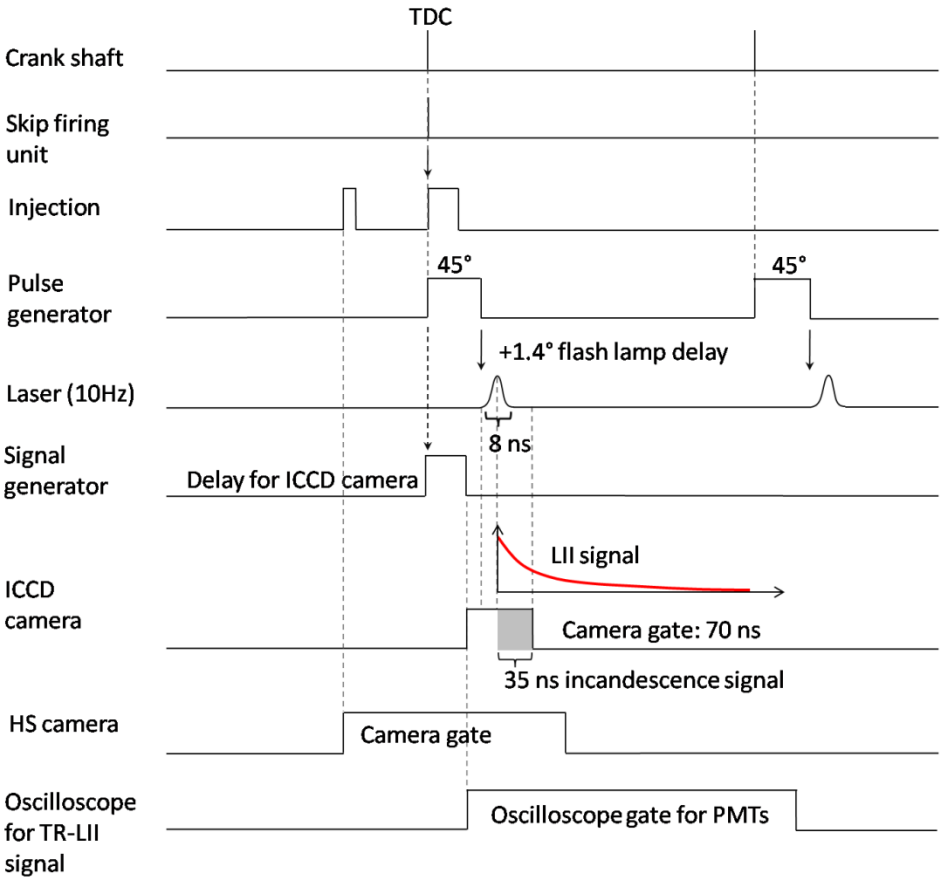

Figure 4.21. Engine and detection system synchronisation scheme.

For high speed imaging measurements, the crank angle signal from TDC probe was fed to the pulse generator to trigger a skip firing unit, which in turn triggered the fuel injection system. A signal from fuel injection system was sent to trigger the high speed camera. The top dead centre location for the high speed images were also determined from a TDC probe coupled to a LED fixed in front of high speed camera, signal from LED on the high speed detector provides additional confirmation of TDC location and this reference was used for further characterisation of acquired data. For PLII measurements, synchronisation between the engine and the Nd:YAG laser operating at 10 Hz was obtained by operating the optical engine at a constant speed of 1200 rpm. Signal from the skip firing unit was used to trigger simultaneously the flash lamp of the Nd:YAG laser and the ICCD camera after sufficient delay to measure prompt PLII data. The centre of camera gate (gate width of 70 ns) was set at a point where laser was fired to capture incandescence signal during and after the laser pulse for about 35 ns. In order to synchronize laser and camera, before each experiment camera delay was checked and adjusted. For this purpose photodiode was placed near the detection system together with plate acting as a beam dump and scattered light was directed into detector. Signal from photodiode and trigger for camera were fitted to oscilloscope for gate delay monitoring. The centre of camera gate (gate of 70 ns) was set at a point where laser was

fired that allowed for capturing incandescence signal promptly after the laser pulse for about 35 ns. Since the ICCD camera required about 5 to 6 s to download the image, the engine was operating in skip-firing mode that resulted in injection taking place once per 60 cycles, about 10-12 incandescence images were collected for each crank angle. For TR-LII measurement, PMTs were operated continuously together with a storage oscilloscope to acquire and store the TR-LII data.

Photomultipliers where transferring the signal to oscilloscope which was as well triggered. For this purpose the same signal which was fitted to ICCD camera was used, with this difference that oscilloscope was triggered for about 500 ns.

4.5. Multi-cylinder diesel engine

Measurements of particle size number and distribution in exhaust gasses were performed in multicylinder Ford's Duratorq (Puma) diesel engine which was the prototype, four cylinder, engine supplied by Ford. The main engine specifications are listed in table 4.3. The engine is equipped with a turbocharger but during measurements intake air was naturally aspirated. The injection system is composed of Delphi direct injection common rail system with six hole injectors of 0.154 mm diameter and angle of 154°. The engine prior to measurements was wormed up and engine temperature (~50°C) together with coolant temperature (~ 70°C) was monitored during experiments. The cooling system is equipped with safety cut-off which stops the engine when temperature of cooling water increases to 100°C.

HSDI diesel engine	
Displacement, cm3	1998.23
Cylinder numbers	4
Compression ratio	18.2 : 1
Bore, mm	86
Stroke, mm	86
Cod-Rod length, mm	155

Table 4.3. The engine specification.

The engine was coupled with W130 Schenck's eddy - current dynamometer to control the engine load and speed. The dynamometer modes are used to control the engine:

- constant torque where the engine torque is fixed by dynamometer and increase in the quantity of injected fuel causes increase in the engine speed;
- constant speed where engine speed is fixed and torque can be changed by injecting different quantities of fuel.

The engine failures are detected by the dynamometer controller and forwarded to safety circuit which stops the engine. The engine parameters like injection timing, pressure, EGR are controlled by ECU software (Gredi).

4.6. Electromobility spectrometer (EMS)

The electromobility spectrometer system EMS VIE-11 for soot particle size and distribution width measurements in exhaust gases is composed of neutralizer, differential mobility analyser (DMA) and Faraday cup electrometer (FCU). The EMS system is capable of providing an absolute standard to measured particle size as well as particle concentration, details about the measurement principle of EMS system are discussed elsewhere Reischl (2006). The exhaust gasses from diesel engine are sampled through the perforated probe fitted in the exhaust tail pipe presented in Fig. 4.22.

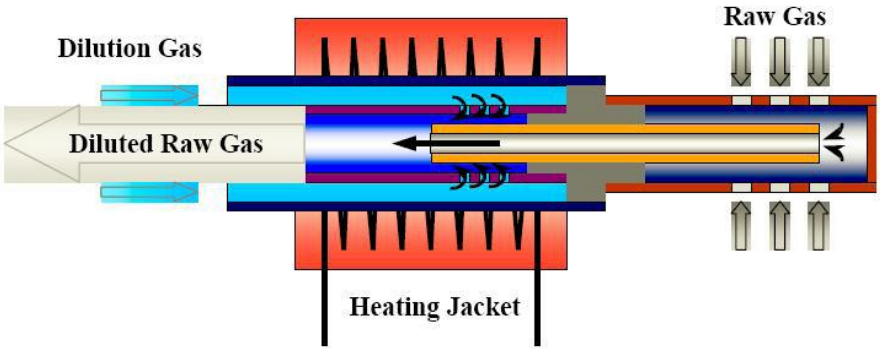

Figure 4.22. Schematic drawing of dilution probe.

The probed gasses are simultaneously diluted and heated up (maximum temperature of 300°C can be applied). The dilution system is closed loop and schematic of system is presented in Fig. 4.23.

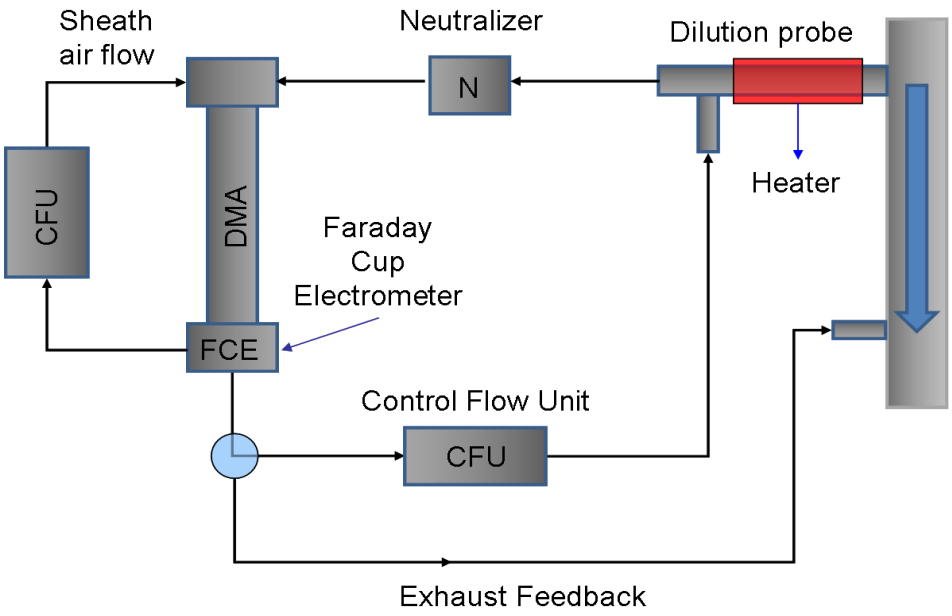

Figure 4.23. Schematics of closed loop dilution system

The pump generates stable flow of approximately 2.6 l/min which circulates through the DMA, FCE, system of orifices and dilution probe. Gases used for dilution are passing through the absolute filter where all contamination is eliminated. There are generally three reasons why the aerosols are diluted:

- The aerosols are diluted to simulate the condition of how an aerosol will mix with atmospheric environment as it is emitted from the engine exhaust.
- The aerosols are diluted close to the sampling location to avoid any further alteration of particle sizes either due to condensation or nucleation.
- The aerosols are diluted to lower the aerosol concentration and to reduce their temperature to such an extent that it could be handled by the measuring device.

Neutraliser

Diluted aerosol passes through Am-241 neutraliser presented in Fig. 4.24 with alpha activity of 60 MBq to obtain uniform charge distribution.

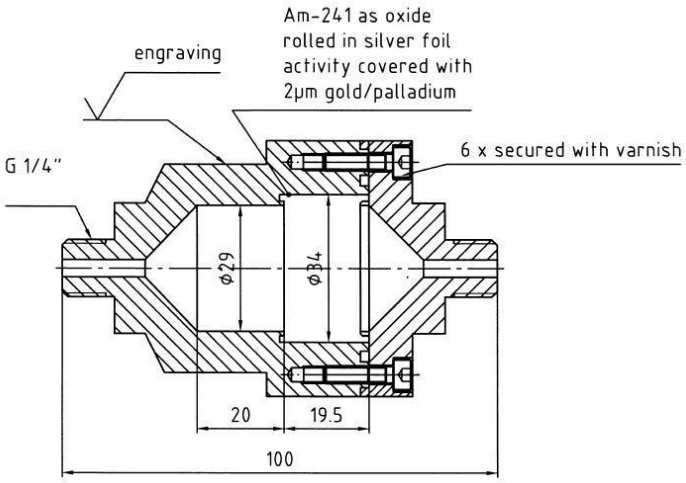

Figure 4.24. Neutraliser (from user manual).

Differential mobility analyser

Charged gas enters subsequently DMA which schematic picture is presented in Fig. 4.25. A stainless steel DMA600 of 600 mm length was used during these experiments and allowed to measure the soot particle diameters in the range from 5 to 650 nm. The inner and outer electrodes are of 16 mm and 22.5 mm diameter respectively. The size classification of aerosols (sampled and diluted exhaust soot) is based on the principle of electrical mobility and the effect of electric field between the inner and outer electrodes of the DMA. The charged particles are directed towards the inner electrode through the flow of clean sheath air along the DMA. The particles of well-defined mobility are extracted through a slit that is designed in the inner electrode which is positioned at the lower end of DMA. Larger particles are carried by the sheath flow, while the smaller particles are transported into the inner electrode.

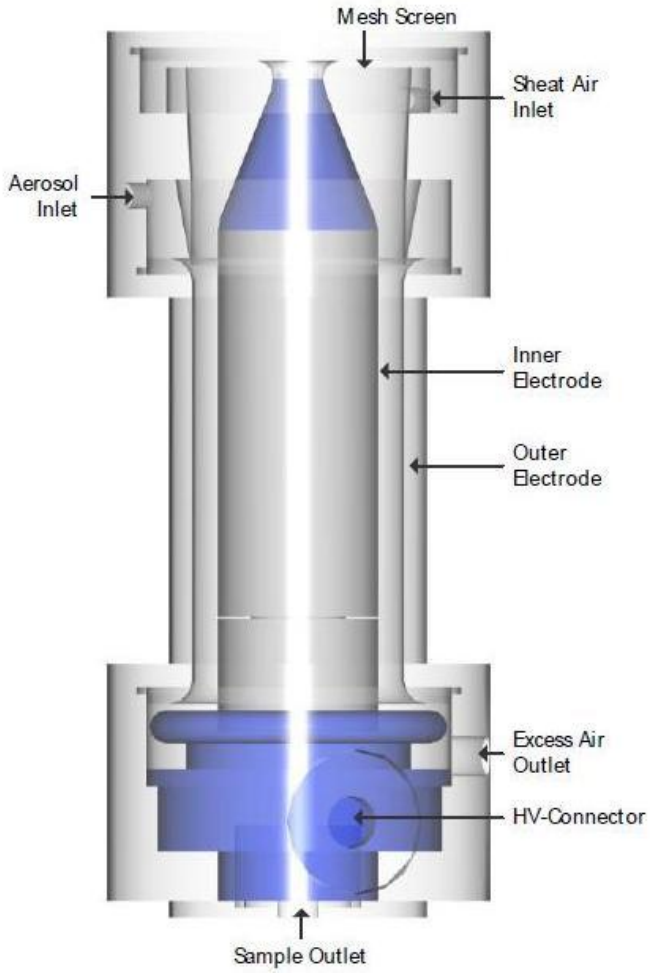

Figure 4.25. Schematics of DMA.

Faraday cup electrometer (FCE)

The soot particles were counted in 11/A FCE which enables to measure number of particles of certain sizes. The measurements range of FCE is from 1.0e-15 to 0.5e-10 A. The principle of FCE is based on Faraday cage where sampled aerosol carries charge to the cage and the charge is compensated by a current to the outside of the Faraday Cup, which is measured.

The EMS system is controlled by software (see Fig. 4.26) which allows for monitoring of measured particle size and number. The screenshot shows interface of software where bars represent concentration number of soot particles (in $1/cm^3$) measured for different particle sizes. It is possible to change the measurement resolution from low (20 channels with the shortest measurement time) through medium to high (100 channels).

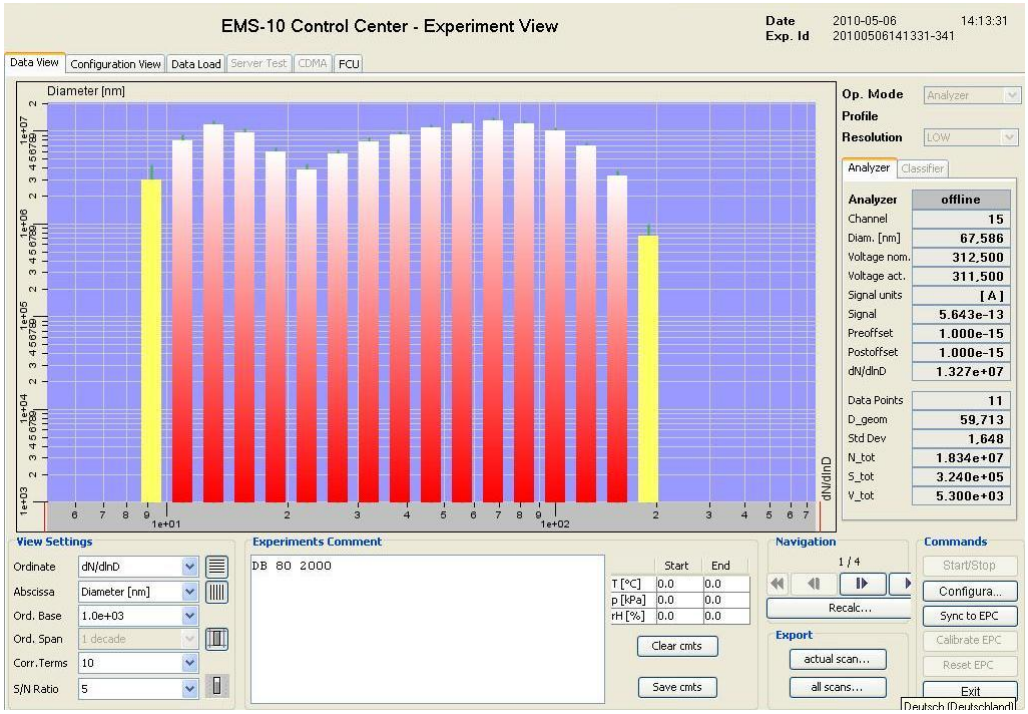

Figure 4.26. EMS system control software

EMS system is fixed with an integrated mixing tube diluter in the sampling probe, which is located at a distance of about 45 cm from the engine exhaust to facilitate sampling and dilution at the sampling location close to the engine exhaust.

5. Chapter 5 - Measurement of in-cylinder soot particles and their distribution in an optical HSDI diesel engine using Time Resolved Laser Induced Incandescence (TR-LII)

5.1. Introduction

Reduction of soot, an unwanted product generated during combustion in diesel engines, is a challenging task. The European Union has imposed limits on vehicle exhaust emissions by introducing new emission standards. Current and future emission legislations: Euro 5 and Euro 6 aim to reduce PM emission to 0.005 g/km for passenger cars and the future legislation introduces a limit on particle number emissions [9]. Currently diesel powered vehicles require particulate filters (DPF) to reduce soot emissions to acceptable levels. Over time, however, the filter requires regeneration which directly corresponds to higher fuel consumption. DPF filters are very efficient in trapping large soot aggregates whilst the harmful smallest particles are emitted into the atmosphere. There are several strategies of particulate matter reduction: the aforementioned exhaust gas treatment by application of DPF, altering fuel composition, application of alternative fuels with high oxygen content, improvement of combustion by varying engine operating conditions and engine design modifications [31, 80]. A detailed review about the soot processes in diesel engines are provided in [112]. Soot is generally produced from the combustion of fuel rich mixtures. Its formation is mainly based on the following processes: pyrolysis, nucleation, coalescence, surface growth, agglomeration and oxidation described in section 2.2.2.2. In order to control and reduce the soot particles more efficiently, soot formation and oxidation have to be fully understood. Details of TR-LII technique are presented in section 2.4 and 3.3.

Several measurements have been carried out in atmospheric flames to understand the principle of LII, and several challenges and developments were addressed in [59, 61, 62, 63]. LII technique was successfully applied for soot volume fraction measurements in different types of flames: ethane flame with various additives such as methane, methanol, ethanol [64], acetylene/air flame [65], ethylene flame at pressures between 5 and 20 bar [66] and ethylene-nitrogen flame [67]. It was also found that various fuels generate different sizes of primary particles, which eventually resulted in different soot quantity [68]. LII technique has been used in conjunction with other measurements techniques such as scanning mobility particle sizing techniques [113], scattering and extinction measurements [114] and transmission electron microscopy TEM [65, 47, 115], to validate the measured particle sizes and to extract information about soot volume fraction. The LII technique was also applied for soot volume

fraction measurements within the flames in constant volume chambers, engine exhaust systems and in in-cylinder engine environment. The engine environment is much more complex due to the turbulent nature of combustion, temperature and pressure fluctuations. Nevertheless several groups have conducted in-cylinder measurements [49, 69, 70] and have found that the particle size increases initially and then reduces during the expansion stroke [63, 49, 69, 70]. These investigations revealed that the sizes of soot particles are dependent upon the engine operating conditions, variation in air to fuel ratio, engine speed, load and fuel injection pressure. A decrease in the air to fuel ratio resulted in an increase in the particle size, whilst higher engine speeds resulted in smaller particles [71]. Application of higher injection pressure caused a reduction in particle size (approximately 3 times smaller) [51]. Very limited work has been carried out on the measurement of in-cylinder soot particle size and their distribution width in an automotive high speed direct injection diesel engines. Thus in order to gain an understanding of the in-cylinder soot processes and to enhance the existing database, TR-LII was applied to study the effects of fuel injection quantity and fuel injection timing on the in-cylinder soot particle size, their distribution and the soot volume fraction in a high speed direct injection diesel engine. TR-LII signals were acquired simultaneously at two different wavelengths for crank angles in the range from 48.4° to 111.4° after top dead centre (aTDC) and for various engine operating conditions. Particle sizes were found to be dependent on the engine load but no significant change in particle sizes were observed for different fuel injection timings. The average sizes of the primary particles measured over different crank angles were larger at higher engine loads compared to lower engine loads. A general trend of the soot particle diameter decreasing with crank angle was observed due to oxidation, but towards the end of the expansion stroke a marginal increase in size was noted. For all operating conditions the width of the particle size distribution was found to decrease with crank angle until 61.4°aTDC, and thereafter it increases to reach a well-defined size distribution for a given fuel injection quantity despite the differences in the injection timing. The soot particles are randomly transported by the complex fluid motion present within the combustion chamber leading to strong cycle to cycle fluctuations of the measured time resolved LII data. The in-cylinder soot volume fraction derived from TR-LII data revealed that for different fuel injection timings, relatively higher amount of soot was produced for shorter ignition delay compared to larger ignition delays.

5.2. Experimental set-up

The experimental test facility presented in Fig. 5.1 consists of an engine, laser and detection system.

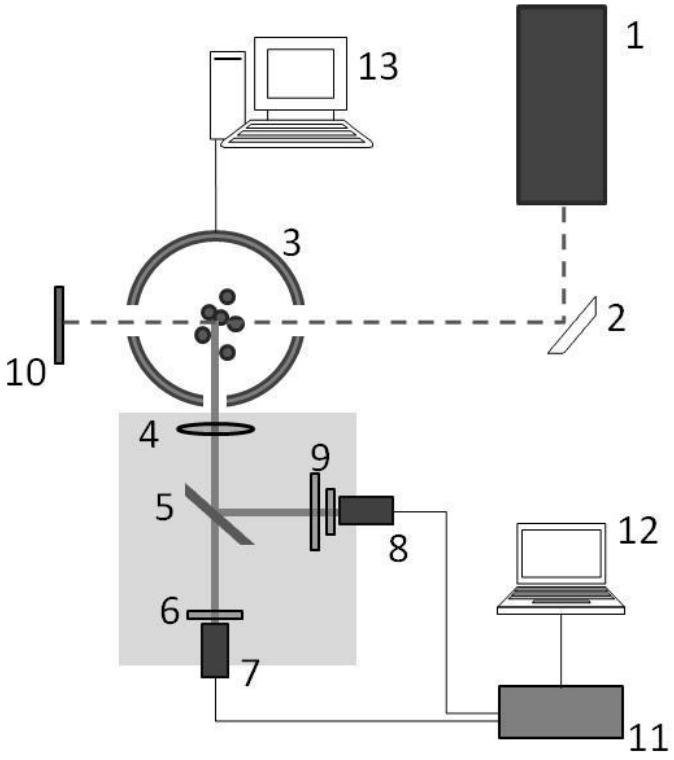

Figure 5.1. Schematic of experimental set-up: 1- laser; 2- 1064 nm mirror; 3- engine; 4- lens; 5- dichroic mirror (DMLP425) ; 6 - longpass filter (FGL665); 7 and 8 – photomultipliers; 9- green filter (BG39) and longpass filter (FGL400); 10- beam dump; 11- oscilloscope (TDS 2000B); 12- computer; 13- engine control unit.

The measurements were performed in a single cylinder Ricardo Hydra optical engine (specification provided in chapter 4.1) using diesel fuel. The air temperature at the intake was raised to approximately 85°C to obtain adequate and realistic engine operating conditions. The intake air was supercharged (1.4 bar) to compensate for losses through the optical components.

In the current study a metal, flat piston replaced the piston with optical window and the three upper windows were used during measurements (see Fig. 5.1). The laser beam was allowed to pass through the two side windows to heat up the in-cylinder soot particles and the PMTs were placed orthogonally to the laser beam in front of the third window to detect incandescence signals.

A Q-switched Nd:YAG laser (Continuum-Surelite) operating at fundamental wavelength of 1064 nm with the pulse width of 8 ns (FWHM) was used during measurements. The laser

generated a top hat beam of 6 mm diameter with a pulse repetition rate of 10 Hz. Top hat spatial profile of the beam was achieved by the output coupler in the laser which has a graded reflectivity across its surface. The laser beam was positioned to pass through the top part of combustion chamber, approximately 10 mm from the tip of injector towards the bottom of combustion chamber and about 11 mm from the injector tip towards the side window, where the detection system was placed. To enable synchronisation between the engine and laser, the engine speed was maintained at 1200 rpm and the engine control unit (ECU) was used to trigger the flash lamp of the laser. The laser fluence was set at 0.21 (J/cm^2) taking into consideration energy loses on the side window and mirrors.

The detection system during these experiments was as described in section 4.2.1.

Since the spectral region for LII emission is wide, selection of spectral response of detection system is important especially to eliminate the interferences caused by Swan band emission. Collection of signal from wider spectral range may lead to overestimation of soot particle diameters or may lead to collection of signal caused by photochemical interferences and underestimation of soot particle diameters.

5.3. Experiments

In this investigation two sets of experiments were carried out. The first experiment was focused on exploring the influence of fuel injection timing on primary soot particle size, their distribution and the soot volume fraction. The second experiment was focused on exploring the influence of fuel injection quantity (engine load) on the above mentioned quantities.

In the first strategy, experiments were carried out by maintaining a constant fuel injection quantity of 20 mg/stroke, whilst the fuel injection timings were varied: 10°bTDC, 5°bTDC, TDC and 2°aTDC.

In the second strategy, experiments were carried out by fixing the fuel injection timing at 5°bTDC and by varying the fuel injection quantities: 20 mg/stroke, 15.4 mg/stroke and 11.6 mg/stroke and the corresponding IMEP are 3.42, 2.46 and 1.5 bar respectively. In order to prevent excessive thermal load on the optical components of the engine, the maximum fuel injection quantity was limited to 20 mg/stroke.

The fuel injection pressure was maintained at 1000 bar for all conditions. For both injection strategies, the TR-LII signal was collected for the following detection crank angles: 48.4°aTDC, 54.4°aTDC, 61.4°aTDC, 71.4°aTDC, 91.4°aTDC and 111.4°aTDC. The design features of optical engine limited the measurement of soot particle size and its distribution width closer to TDC where most of soot processes are taking place. However, measurements

carried out during the latter part of the expansion stroke provide information concerning changes the soot may undergo just before leaving combustion chamber. Later in the stroke chemistry slows down due to decreasing temperatures; however, in-cylinder temperatures are still high enough to cause oxidation of soot. Soot processes occurring at these crank angles have the most significant effect on the number and size of soot particles that are emitted out of the engine.

5.4. Initial conditions

The solution for the differential equations (Eq. 3.20 and Eq. 3.21 in section 3.3) leading to calculation of soot particle size and distribution width can be attained by providing appropriate initial conditions and parameters, such as initial soot particle temperature, diameter, size distribution, ambient gas temperature and pressure.

Determination of the initial soot temperature is quite challenging amongst all the initial conditions. The initial particle diameter has to be assumed. Ambient gas pressure and temperature can be determined directly from the in-cylinder pressure data. Chapter 3 describes the procedures adapted for determining these initial conditions.

Results of the initial soot particle temperature derived from two-colour pyrometry technique as described in section 3.4 and from the experimental fitted simulated data are presented in Fig. 5.2.

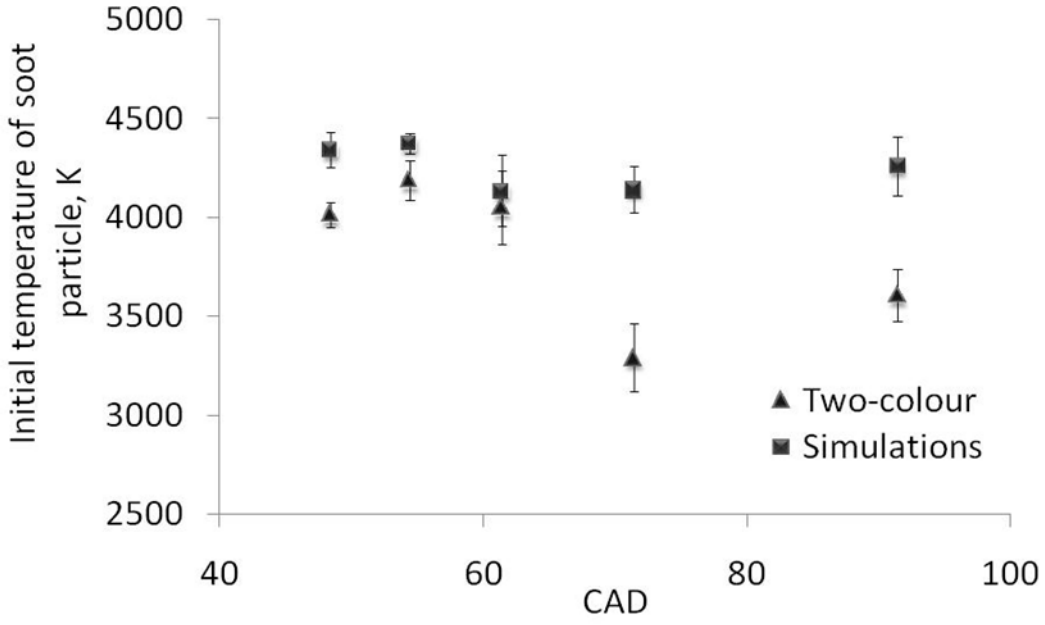

Figure 5.2. Initial temperature of soot obtained from two-colour pyrometry (triangles) and from simulations (squares). Solid symbols represent averaged value and error bars indicate standard deviation.

The filled square show the temperatures calculated from simulations and the filled triangle indicates the temperature calculated from two colour method, and error bars represent the standard deviation from the average number of evaluations. Initial soot particle temperature derived from two-colour pyrometry depends mainly on the assumption of soot absorption function, ratio of detection wavelengths and the ratio of the measured LII signal. Selection of soot absorption function and detection wavelengths introduced an overall uncertainty to the derived initial soot particle temperature for all crank angles. The origin for the variation to the measured initial soot particle temperature for each crank angle comes from the measured LII signal at each crank angle. The measured peak of the LII signal is influenced by soot attenuation at each crank angle, in particular the wavelength dependent attenuation leads to variations to the measured signal ratio LII(λ_1)/ LII(λ_2).This ratio variation due to attenuation of LII signal leads to strong differences to the measured initial soot temperature at different crank angles.

The application of laser fluence of 0.21 J/cm^2 during current measurements led to an initial soot temperatures in the range from 3300 K to 4400 K. Similar magnitudes of high temperature have been measured and reported in [63, 93]. A laser fluence of 0.15 J/cm^2 was used to obtain initial temperatures up to 4000 K [64]. Interesting results regarding relation between laser fluence and soot temperature were presented in [106], for a laser fluence of 0.2 J/cm^2 temperatures up to 4000 K were measured. It had been shown that soot vaporization occurs for laser fluence greater than 0.5 J/cm^2, [65]. Application of 0.21 J/cm^2 in our case leads to high soot temperatures according to Clausius–Clapeyron relation, but signal transients did not show any occurrence of soot vaporization.

The LII model requires in-cylinder pressure (ambient gas pressure) and ambient temperature; these values are established from the pressure data acquired during measurements. In-cylinder pressure data for different injection timings and for different fuel injection quantities are presented in Fig. 5.3 A and 5.3 B respectively.

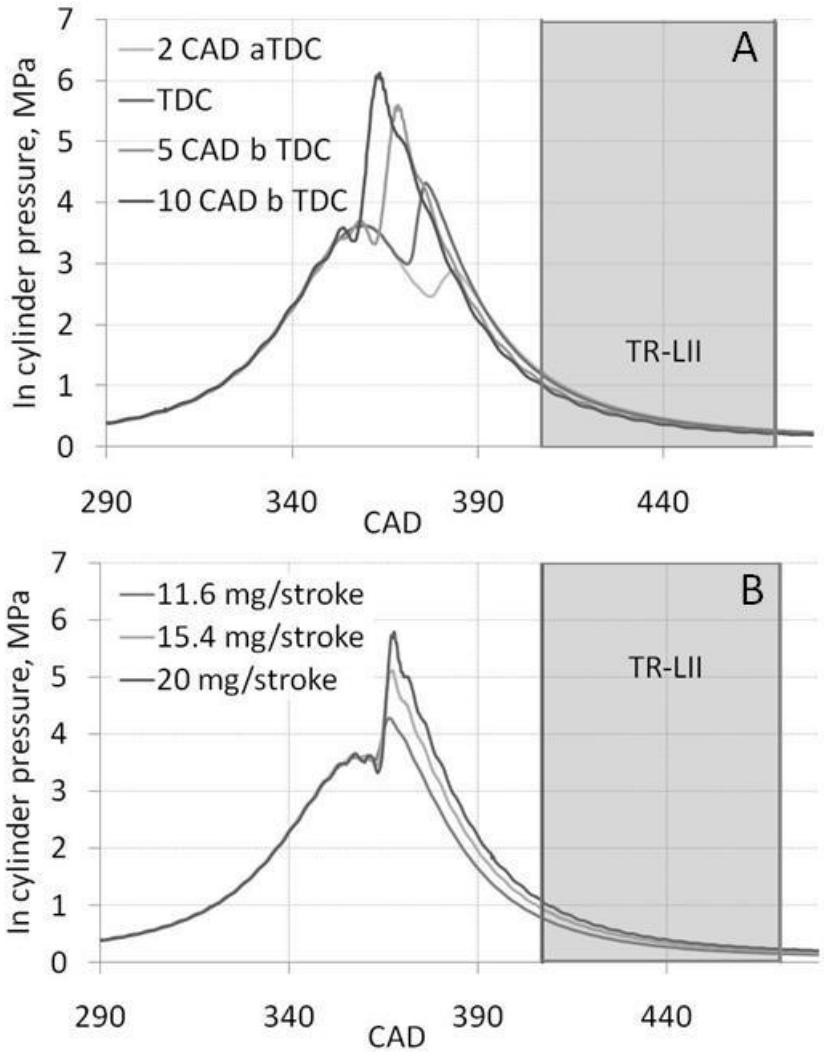

Figure 5.3. A) In-cylinder pressure measured at different start of fuel injection timings; B) at different fuel injection quantities. Grey area indicates the crank angle range were TR-LII measurements were performed.

The engine design limitations prevented measurements of TR-LII signals near TDC. The grey area in the plot starting form 48.4°aTDC represents the measurements range where the TR-LII readings were obtained. Based on the in-cylinder pressure, Indicated mean effective pressure and ignition delay were calculated as described in section 3.1. IMEP, ID and peak pressure for all measured conditions are listed in Tab. 5.1.

Injection timing	Fuel quantity mg/stroke	IMEP	Ignition delay, CAD	Peak pressure, bar
2 CAD aTDC	20	3.62	14.0	36.13
TDC		3.87	11.2	43.22
5 CAD bTDC		3.42	8.8	56.01
10 CAD bTDC		3.03	8.0	61.22
5 CAD bTDC	11.6 mg/stroke	1.50	7.2	42.86
	15.4 mg/stroke	2.46	8.0	51.17
	20 mg/stroke	3.42	8.8	61.22

Table 5.1. In-cylinder pressure analysis.

Shorter ignition delay and higher peak in cylinder pressure were observed for injection timing of 10° and 5°bTDC. For injection timing at TDC and 2°aTDC longer ignition delays were observed with lower in-cylinder pressures. Longer ignition delay and higher in-cylinder peak pressures were observed while increasing quantities of injected fuel.

5.5. Results and discussion

5.5.1. Analysis of LII signal

Figure 5.4 shows experimentally measured soot incandescence detected at 415 nm and 665 nm when 20 mg/stroke of fuel was injected at 5°bTDC.

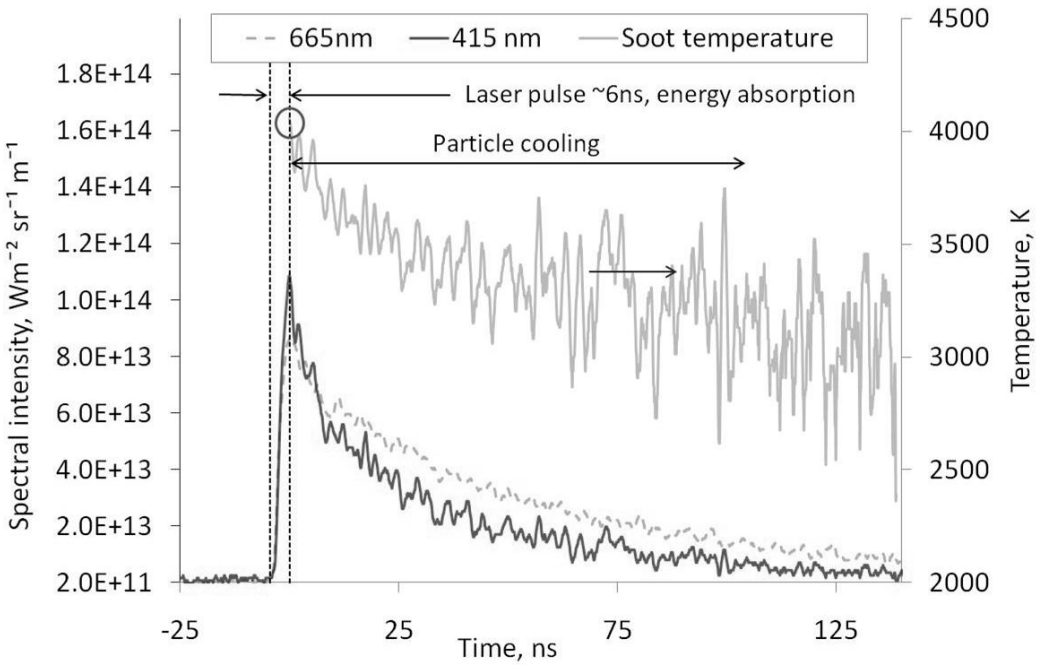

Figure 5.4. Absolute LII signal intensities recorded at 415 and 665 nm and soot temperature calculated based on two colour pyrometry at 48.4°aTDC, 5°bTDC injection timing.

First part of the curve, where the signal is rising (for approximately 6 ns), indicates absorption of energy during the laser pulse. During and after the laser pulse the process of heat transfer from soot to environment takes place and eventually the high temperature soot particles cool down to surrounding conditions. The initial part of the decay illustrates the contribution of incandescence signals from both small and large particles, while the final part of decay is dominated by cooling of larger particles. In order to extract information regarding the contribution from various sizes of soot particles to the experimentally measured LII signal at different time instants of the LII decay rate, the LII data was analysed in segments of shorter time intervals. Section 5.6.3 contains details concerning fitting in intervals and their results.

5.5.2. Signal characterization

Since the in-cylinder environment is strongly turbulent, a number of measurements are necessary to obtain information about soot diameters. Figures 5.5 A and 5.5 B illustrate typical cycle to cycle variations of the LII signal strength and the decay rate detected during one engine run.

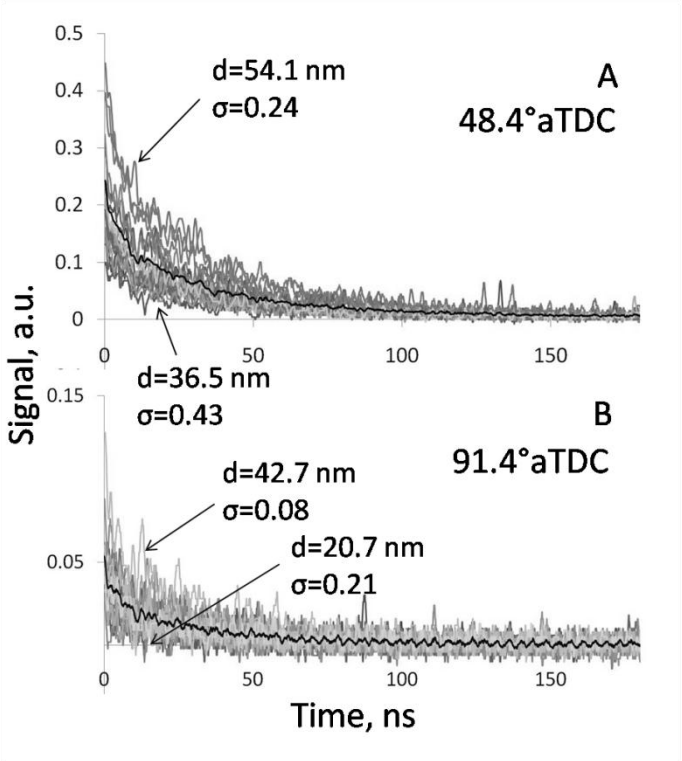

Figure 5.5. Several single shots and averaged (black line) TR-LII signal decays recorded at 48.4°aTDC (A) and 91.4°aTDC (B) together with calculated diameters and distribution

widths for extreme cases. This data was measured at the fuel injection timing of 5°bTDC injection timing, 20 mg/stroke injected fuel.

Figure 5.5 is composed of approximately 15 single shot readings of LII signals that were measured at 48.4°aTDC and 91.4°aTDC at 415 nm detection wavelengths and the average of all these measurements are shown as a solid black line.

The signal strength at 48.4°aTDC was approximately four times higher than that at 91.4°aTDC (Fig. 5.5 A and 5.5 B). Difficulties were encountered for measuring soot emissions during the later part of the expansion stroke. Those data which were weak in its signal intensity and of poor signal to noise ratios were not taken into consideration for data analysis. It is known that signal decay time and shape contains information about the size and distribution of particles in the combustion chamber. For each set of incandescence data, particle size and distribution width were calculated, but here only results for extreme cases are shown. For the strongest and the weakest signals at 48.4°aTDC, the diameters were determined to be 54.1 nm and 36.5 nm, whilst their distribution widths are 0.24 and 0.43 respectively. For the 91.4°aTDC, the derived diameters for the strongest and the weakest signals are 42.7 nm and 20.7 nm respectively, whilst the obtained distribution widths were 0.08 and 0.21 respectively. The variations in the observed particle size at 48.4°aTDC and 91.4°aTDC are about 39% and 70% respectively. Considering the distribution width, the variations observed at 48.4°aTDC and 91.4°aTDC are about 57% and 89% respectively.

The particle diameter and distribution width calculated based on the strongest and the weakest signal show the level of fluctuations during measurements in engine. Laser pulse to pulse fluctuations were measured to find out if the observed signal fluctuations are due to the turbulent engine environment or due to the laser pulse to pulse fluctuations. A variation in laser intensity of up to 4% was observed from shot to shot. The fluctuations shown in Fig. 5.5 A and 5.5 B could not be solely caused by laser pulse to pulse variations. Observed behaviour may probably be attributed to the variations in soot distribution within the combustion chamber due to the transient nature of diesel combustion and complex in-cylinder fluid dynamics.

5.5.3. Decomposition of experimental signal

An attempt was made to fit the theoretical and experimental signal in time intervals to extract the information regarding the contributions to the incandescence signal from different size particles, during signal decay. In the first approach the experimentally measured LII data was analysed in segments, by fixing the initial starting point of the data from peak (i.e. at 0 ns) and

varying the decay time only for a specified time interval of 10 ns, 20 ns, 30 ns and so on until 170 ns. Diameters determined from this analysis are ploted at the time corresponding to the end of the considered time interval. In the second approach the experimentally measured LII data was analysed in segments by varying only the initial starting point of the entire LII data from the peak in steps of 10 ns, 20 ns, 30 ns and so on until 80 ns. Obtained results were plotted at the time corresponding to the beginning of the fitting interval. In order to make the analysis simpler a monodisperse particle size distribution was assumed for this part of investigation.

The initial conditions for simulations were determined as described in section 3.4 and 5.5. The decay of LII signal last for approximately 180 ns therefore in-cylinder pressure and temperature will not change significantly in that short time period.The values of pressure and temperature at 54.4°aTDC and 91.4°aTDC were taken as the initial condition for each considered segment. Similarly the initial soot particle temperature determined from two colour method was also used as an intial condition for this analysis. Paricle sizes calculated from the segmented fitting are presented in Fig. 5.6.

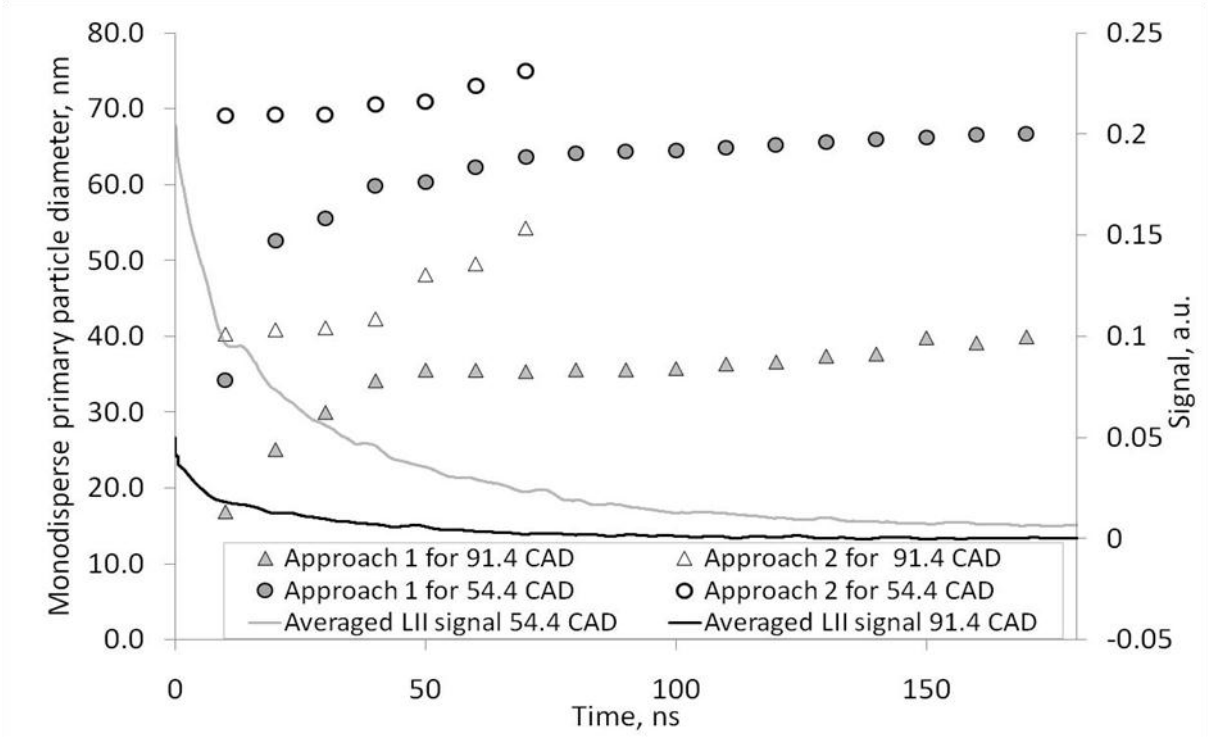

Figure 5.6. Monodisperse particle sizes obtained as a result of segmented fitting of experimental and theoretical curves at 54.4°aTDC and 91.4°aTDC (for 5°bTDC injection timing). Solid symbols represent approach 1 and empty symbols represent approach 2 of segmented fitting. Solid lines show averaged raw incandescence signals recorded at 54.4°aTDC and 91.4°aTDC, which were used for fitting.

Results obtained at 54.4°aTDC show that initially (for time interval τ =1-10 ns) soot particle diameters of approximately 34 nm were observed. In the second time step (τ =1-20 ns), an increase in particle size was observed from 34 nm to 53 nm. Subsequently for larger time intervals, the resultant particle sizes increased, and they were in the size range from ~ 60 nm to 67 nm. When the same fitting procedure was applied to the signal decay measured at 91.4°aTDC, significantly smaller size soot particles of about 17 nm was observed for the first time interval (τ =1-10 ns). In the next step the soot particle size increased to about 25 nm. Further analysis of data at larger time intervals followed the trends observed for 54.4°aTDC. For the last step (τ =1-170 ns) i.e., for the complete measured data, the derived soot particle sizes were in the range from 35 nm to 40 nm. The monodisperse particle diameter derived during the fitting of the complete decay rate for 54.4°aTDC and 91.4°aTDC were 67 nm and 40 nm respectively. Results for both crank angles show that immediately after the laser pulse the soot incandescence is dominated by smaller particles. The smallest calculated soot particle diameters were 34 nm for 54.4° and 17 nm for 91.4°aTDC. These values, however, will be overestimated since monodisperse particle size distribution was assumed in model, moreover the initial part of the signal represents contributions from both small and large particles [116]. These results confirm the findings presented in [60], where it was shown that later part of LII signal is biased by the contributions from larger size particles. The second approach focused mainly on determination of soot particle size which contribiutes to the later part of incandescence signal. Soot particle diameters of aproximately 69 nm were calculated for the initial time interval (τ =10-170 ns) for 54.4°aTDC. Fitting the later part of incandescence signal resulted in slightly larger particle sizes of approximately 70 nm. Finally for the last step (τ =80-170 ns) the analysis resulted in a particle size of 75 nm. In the second approach difficulties in fitting were encountered towards the later part of the LII signal because of decreasing signal strength. Thus the last time interval taken into consideration was τ=80-170 ns. Smaller soot particle diameters were observed for 91.4°aTDC, starting from approximately 40 nm for the first time interval (τ =10-170 ns). Fitting the later part of incandescence decay (τ =80-170) resulted in particle sizes of approximately 57 nm. The obtained results revealed that later part of LII decay is affected mainly by larger soot particles. Temperature of small soot particles at this point will be close to temperature of ambient since they cool down faster and their contribution to signal will be marginal.

Preformed analysis provides insight on the size of particles which contribute to LII decay at different time intervals. Results show that mainly smaller particle contribute to initial decay of the incandescence signal and larger size particles contribute to later part of the LII signal.

5.5.4. Experimental signal fitting issues

Since the theoretical model is very sensitive to initial conditions, care must be taken when determining the initial values for deriving the theoretical LII signals. The standard procedure used in LII involves fitting experimental data with the theoretical model using least square fitting algorithm. However, due to the presence of noise in the measured LII data there are possibilities for the non-linear curve fitting algorithm to get trapped in to a local minimum rather than the absolute minimum. Similar fitting difficulties were encounter under high pressure LII measurements in constant volume chamber [51], where it was highlighted that least square results should be interpreted with care, if some of the parameter used in the model are assumed. The initial conditions must therefore be carefully defined. The effects of initial conditions on the fit parameters are investigated in this section.

The best fit values of the soot particle diameter and their distribution widths are dependent on the initial guess for these parameters. Numerous tests were carried out to establish appropriate initial conditions for the LII model. The purpose of this compilation was to find whether the change in initial conditions *viz.*, soot particle temperature, soot particle diameter and soot particle size distribution widths affect the solution, and still have a good agreement between modelled and measured LII signal. The minimum value of least square indicates the solution. Figure 5.7 illustrates least square map determined by fitting a single shot experimental data obtained at 54.4°aTDC, when 20 mg/stroke of fuel was injected at 5°bTDC, with a theoretically simulated LII curve.

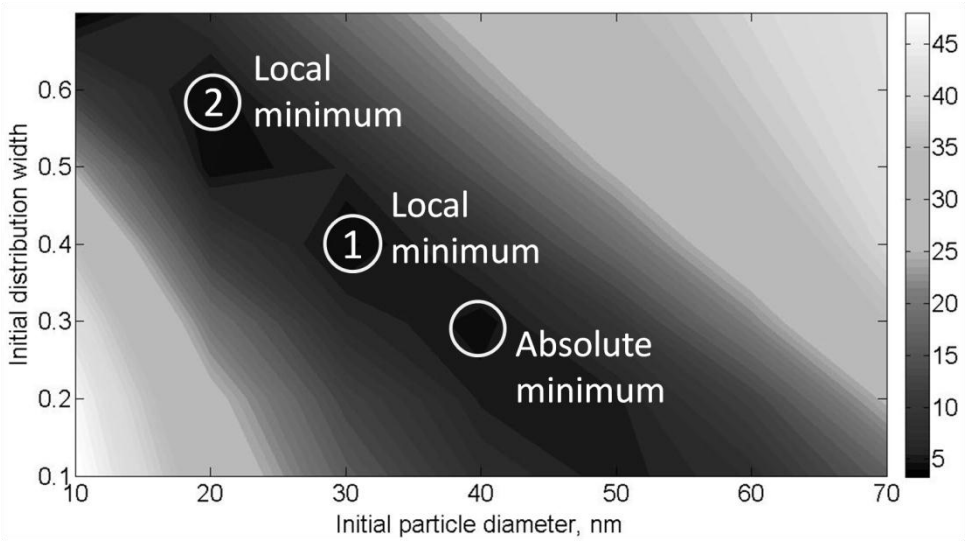

Figure 5.7. The least square map obtained from fitting of the signal obtained at 54.4°aTDC, (fuel injection at 5°bTDC), for the range of initial soot diameters, distribution widths and fixed initial temperature of 4400 K.

In this case the least square minimum map was computed for a constant initial temperature of 4400K and for varying initial particle size and distribution width. The minimum valley in Fig. 5.7 stretches diagonally, and the absolute minimum was obtained for the following initial conditions: d_{ini}=40 nm and σ_{ini} =0.3. However, two local minima can be observed in the least square map topology for the following initial fitting parametrs of d_{ini}=20 nm and σ_{ini} =0.57 and d_{ini}=30 nm and σ_{ini} =0.4, which also results in good fitting between theoretical and experimental data in Fig. 5.8.

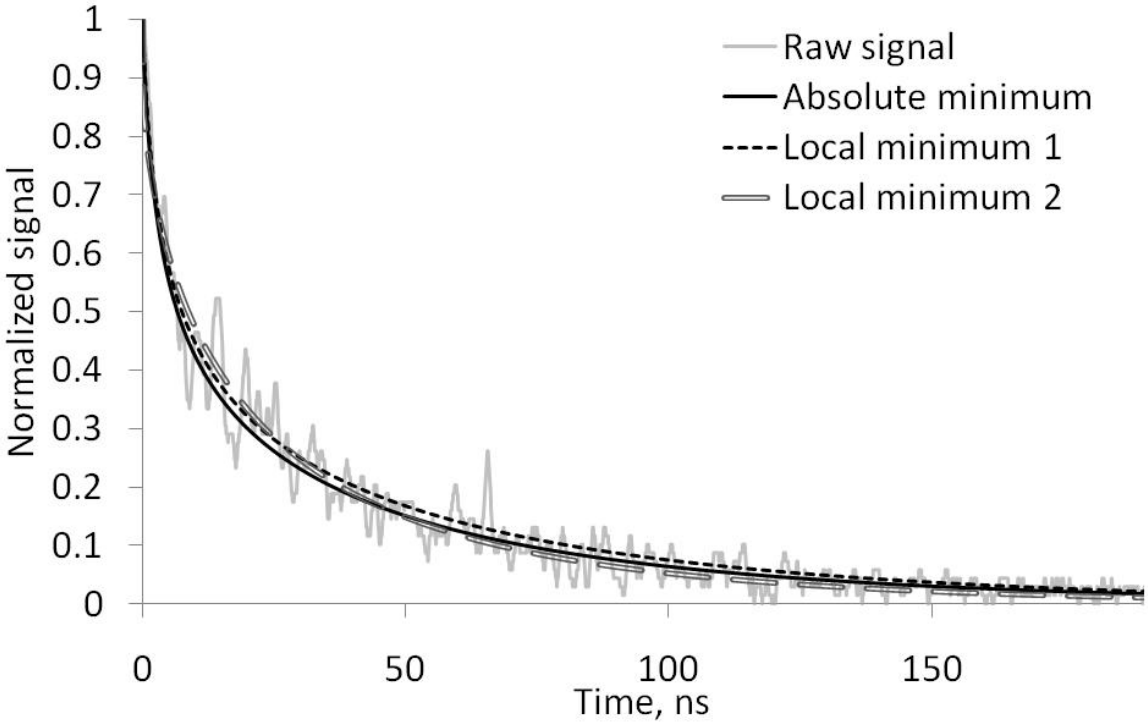

Figure 5.8. Experimental curve recorded at 54.4°aTDC (5°bTDC injection timing) plotted together with curves obtained in fitting, representing absolute minimum and local minima.

This suggests that the use of any of these initial parameters will not lead to a solution corresponding to the absolute minimum of the least square function, particularly when the measured TR-LII data are noisy as shown in Fig. 5.5. A small change in the shape of the experimental curve, caused for example by the presence of noise, may lead to the shift of absolute minimum and the related solution.

Knowledge regarding experimentally determined soot temperatures can narrow down the area of search and improved the computational time as these temperatures can be used as initial value. The analysis revealed that careful selection of the initial conditions is crucial since the least square topology is complex and it contains a number of local minima, particularly due to the nature of the experimentally measured TR-LII data. Hence it is essential to check the

solution with several initial values of $T_{p,ini}, d_{ini}, \sigma_{ini}$ to confirm whether the obtained minimum is local or absolute.

5.5.5. Particle diameters and size distribution

Figure 5.9 shows the histogram of best-fits for particle diameters obtained from the least square regression analysis for all the measured LII data that corresponds to fuel injection quantity of 20 mg/stroke at an injection timing of 5°bTDC.

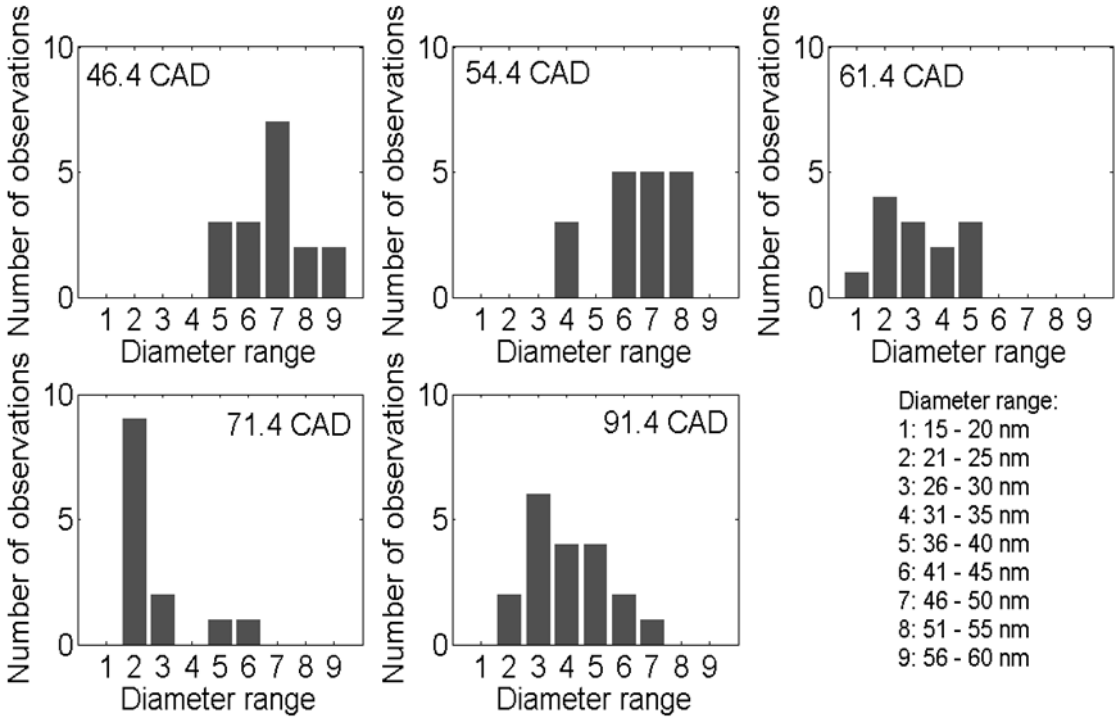

Figure 5.9. Histogram showing number of particles of certain diameters obtained at different crank angle degrees for the case of fuel injection at 5°bTDC.

The result provides information regarding the variations in particle size obtained during single shot time resolved measurements. For the first two measured crank angles (48.4° and 54.4°aTDC) more number of particles with larger diameters (41 nm to 50 nm) were detected. For 61.4° and 71.4°aTDC, particle diameters decreased and they were in the range 15 nm to 30 nm. Then for 91.4°aTDC the particle diameters were mostly in the range 26 nm to 30 nm, but particles of larger diameters were also observed.

Crank angle resolved average primary particle size and size distribution for varying fuel injection timings are presented in Fig. 5.10 A and B, each point corresponds to averaged value and the error bar indicates the standard deviation.

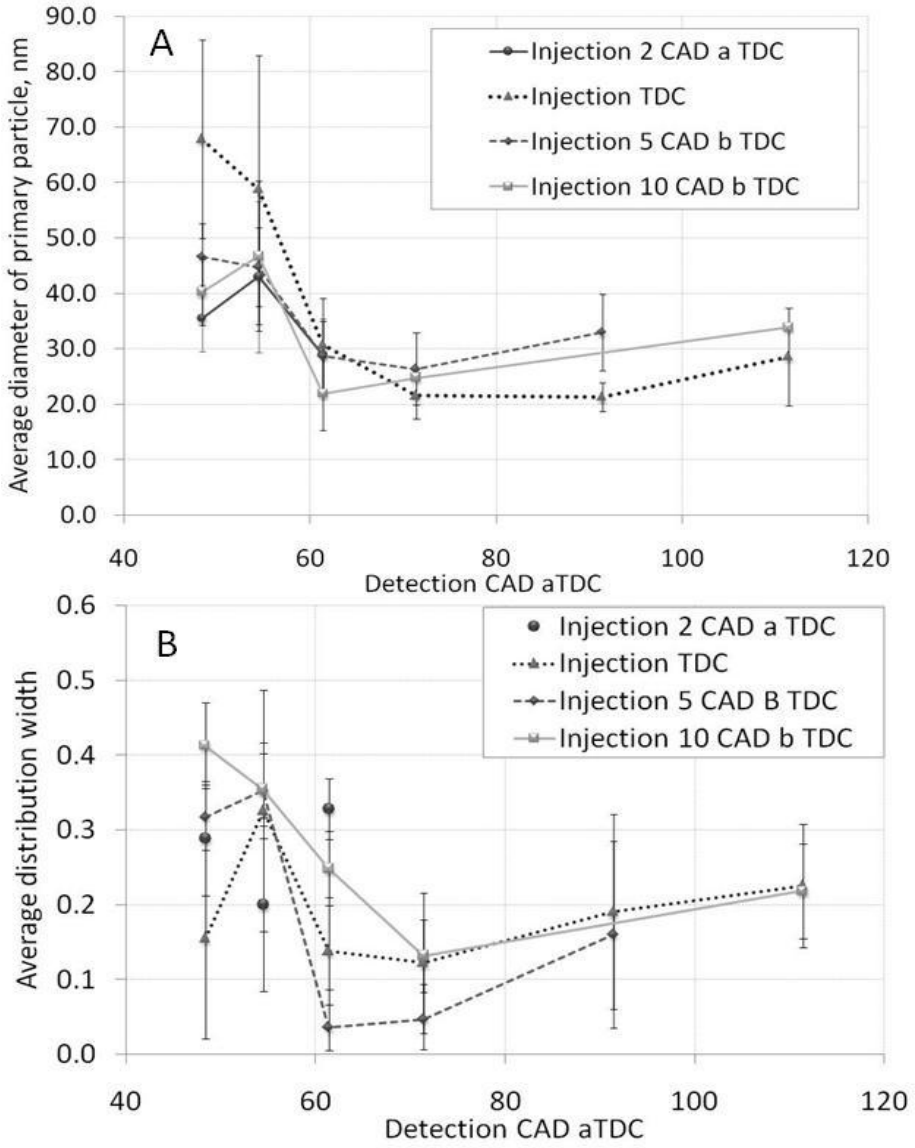

Figure 5.10. Primary particle size (A) and distribution width (B) obtained for different injection timing and 20 mg/stroke injected fuel. Error bars indicate standard deviation and the symbols indicate average value of calculated particles and distribution widths at measured crank angles.

The average values of the soot particle diameter and size distribution for a given crank angle are based on the diameters derived from 15 and more single shot TR-LII data measured during one engine run. For all cases the average soot particle size decreased up to 61.4°aTDC, and thereafter the average value of soot particle size remained nearly constant before increasing slightly during the latter part of the expansion stroke. The initial reduction in particle sizes are caused mainly by oxidation due to high in-cylinder combustion temperatures and similar observations have been reported in [69, 70].

In the later part of the expansion stroke i.e., after 71.4°aTDC a slight increase in particle size was observed and this may be caused by the processes of aggregation and coagulation. Larger aggregates can reduce the heat exchange rate due to lower surface to volume ratio. Cooling rate of soot particles may be as well affected by shielding effect and the slower cooling rates are related to larger particle sizes. These processes alter the structure and size of soot present within the combustion chamber [69, 70, 117].

Results in Fig. 5.10 B show an initial decrease in particle size distribution from approximately 0.41 at 48.4°aTDC to a distribution width of 0.13 at 71.4°aTDC for the case of fuel injection at 10°bTDC. Subsequently an increase in the distribution width was observed and the average value of the distribution width at 111.4°aTDC was approximately 0.22. The geometric distribution width for the case of fuel injection at 5°bTDC was observed to be lower than all other fuel injection timings at all measured crank angles. The corresponding initial distribution width for the fuel injection timing of 5°bTDC was about 0.32 at 48.4°aTDC, which then decreased to 0.035 at 61.4°aTDC and thereafter increased to 0.16 at 91.4°aTDC. Similar trends were observed for rest of the injection timings. For all considered cases the in-cylinder soot particle size distribution decreased initially up to 61.4°aTDC - 71.4°aTDC and then increased towards the end of measurement. The derived size distributions for all the considered fuel injection timings indicate that later in the stroke a well-defined size distribution can be attained for a given engine load.

Figures 5.11 A and B present the average diameter of primary particle and averaged particle distribution measured from 48.4°aTDC to 111.4°aTDC, for three different fuel injection quantities (loads).

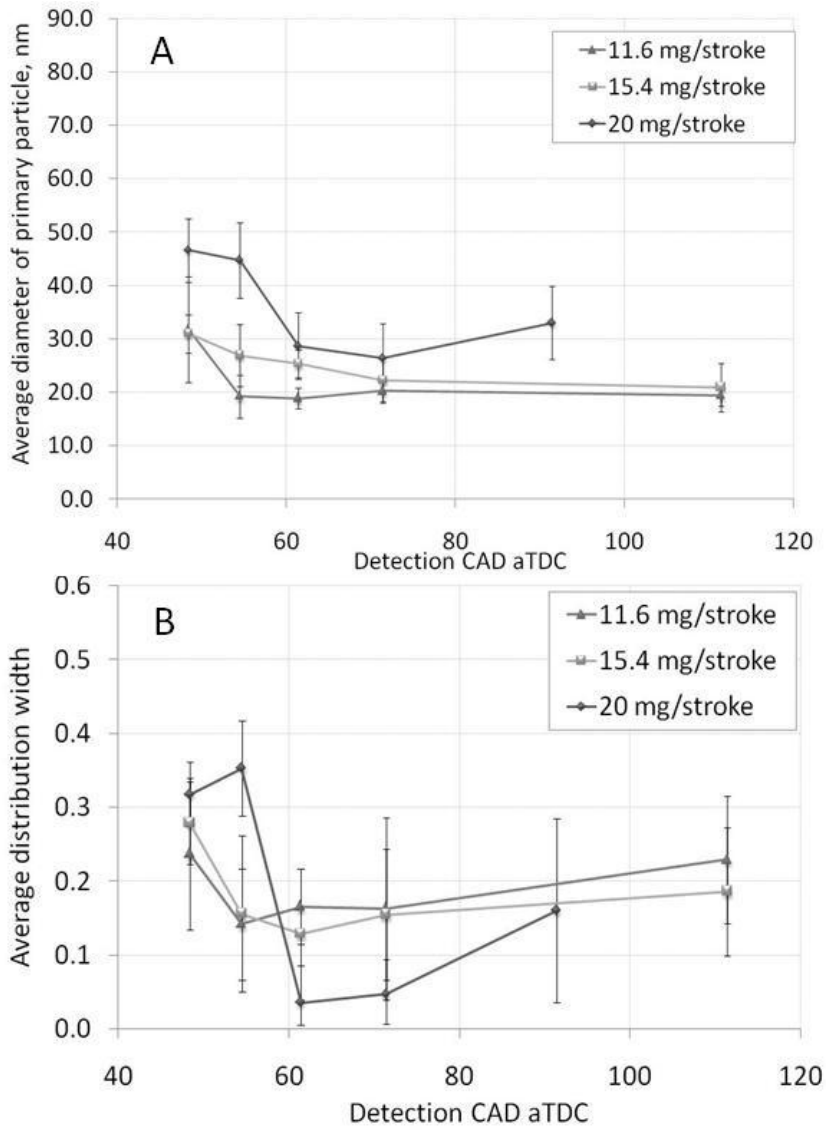

Figure 5.11. Primary particle size (A) and distribution width (B) obtained for different loads for the case of fuel injection at 5°bTDC. Error bars show standard deviation and symbols indicate average value of calculated particles and distribution widths at the measured crank angles.

Acquiring the LII data for later crank angles in the expansion stroke (i.e. after 111.4°aTDC) was particularly difficult due to reduction in signal intensity as well as absence of LII signal for many cycles. For all three engine loads the soot diameters decreased with crank angle, moreover the engine load itself has an effect on the particle size. For the case of 20 mg/stroke of injected fuel the particle diameter of approximately 48 nm was obtained at 48.4°aTDC and later in the stroke the particle size reduced to 26 nm at 71.4°aTDC. For lower engine loads: 15.4 mg/stroke and 11.6 mg/stroke, smaller particle diameters of approximately 30.9 nm and 31.7 nm were measured respectively at 48.4°aTDC. Later in the stroke at 71.4°aTDC soot particle sizes of approximately 22 nm and 20 nm were detected (for 15.4 mg/stroke and 11.6

mg/stroke respectively). The energy release rate is higher for 20 mg/stroke of injected fuel and this result in an increase in cylinder pressure and temperature. Despite higher in-cylinder temperatures the start of combustion was still delayed with increasing fuel injection quantity due to increased time required for evaporation. Thus for the case of 20 mg/stroke of injected fuel, richer fuel-air mixture results in insufficient oxygen for soot oxidation, which provokes nucleation, coagulation and surface growth and this is reflected in an increase in particle size. Similar trends were observed in [70, 71] where soot particle diameters increased with load.

Decreasing the quantity of fuel injected into the cylinder reduces both in-cylinder pressure and temperature, whilst the combustion starts earlier due to the quicker evaporation of the fuel. Availability of more oxygen tends to minimise regions of rich mixtures locally within the combustion chamber, this leads to an efficient oxidation of soot particles under partially premixed combustion conditions and the soot particle diameter decreases in all cases from 61.4° to 71.4°aTDC.

Figure 5.11 B shows the average geometric size distribution, each point corresponds to an average value of distribution width and the error bar indicates the standard deviation. The global trends of the crank angle resolved size distribution widths are similar to that which was observed in Fig. 10 B. Maximum width of the soot particle size distribution was about 0.35 and it was observed at 51.4°aTDC for the case when 20 mg/stroke of fuel were injected. The distribution width then decreased with crank angle and at 61.4°aTDC nearly a mono-disperse distribution of 0.04 was observed. For later crank angles at 71.4°aTDC and 91.4°aTDC the particle distribution width increased to 0.16. Results determined for 15.4 mg/stroke and 11.6 mg/stroke follow the same trend and the differences in the distribution width between these two conditions are not that significant.

Results obtained from the crank angle resolved, time resolved LII measurements show a general trend of particle size decreasing with crank angle during the expansion stroke. These findings are in agreement with previously published works, [63, 69, 70]. The main reason for the decrease in the average value of particle size is attributed to soot oxidation due to the presence of higher in-cylinder temperatures under these conditions. However, the motion of soot clouds within the combustion chamber also contributes fluctuation to the obtained results and this random effect cannot be separated from the normal oxidation process in such a complex environment like diesel engine. As mentioned previously, after the end of visible \luminous spray combustion the soot that was formed in the spray flame mixes with surrounding gases and occupies the entire volume of the combustion chamber. At these later crank angles it is expected to have a relatively uniform soot distribution, but there can also be

in-homogeneities in the in-cylinder soot distribution. These in-homogeneities tend to cause random fluctuations to the measured soot if they pass through the probing zone. This effect will be significant when the overall soot concentration is very low. However, in order to overcome this effect more number of data was acquired for each crank angle. Therefore we would expect that the influence of soot cloud motion on obtained results will be not that significant at following crank angles: 48.4°aTDC, 54.4°aTDC, 61.4°aTDC. Further in the expansion stroke it was difficult to measure LII signal due to lower concentration of soot in the probing volume. Particularly at later crank angles of 71.4°aTDC, 91.4°aTDC and 111.4°aTDC the effect of random motion of soot clouds can be more pronounced.

5.5.6. Soot volume fraction (SVF)

The in-cylinder crank angle resolved SVF was derived from TR-LII data measured from a very small region of the whole combustion chamber of the optical diesel engine. Thus the obtained results cannot be considered to be a representative of the total soot emitted from the engine at that particular crank angle.

The ratio of LII signals measured at two different wavelengths allowed for temperature determination according to Eq. (3.37) and the SVF is derived based on measured initial soot particle temperature, as described in Eq. (3.38). Soot particle concentration derived promptly after the laser pulse was considered. During the first 20 ns the SVF remains nearly constant where mostly contributions from small particles are observed, eventually the SVF decreases with time. Similar trends of SVF that was calculated based on the measured LII decay are reported in [63].The error induced in calculated soot temperature may strongly affect the estimated SVF. As it was reported in [63] error corresponding to 2.5% in estimated soot equivalent temperature may lead to 15% error in calculated SVF. It is evident that the observed variations in the measured initial soot temperature could have led to the discrepancy to the derived crank-angle resolved SVF. The origin for the variation to the measured initial soot particle temperature comes from the measured LII signal. The measured peak of the LII signal is influenced by soot attenuation at each crank angle, in particular the wavelength dependent attenuation leads to variations to the measured signal ratio $LII(\lambda_1)/LII(\lambda_2)$. This ratio variation can lead to strong differences to the measured initial soot temperature, which subsequently causes discrepancy to the derived crank-angle resolved SVF.

The presence of dense soot cloud between laser sheet and measuring device leads to attenuation of LII signal intensity. Attenuation of laser beam as well as attenuation of LII signal by soot is an undesirable effect and this leads to uncertainties for the soot volume

fraction measurements. The degree of LII signal trapping depends on soot concentration and wavelength since soot radiative properties are changing with wavelength. Soot intensities will be high mainly during the combustion process, which takes place close to TDC where the processes of soot formation and oxidation are taking place within a small chamber volume. As the piston moves towards BDC, the volume of combustion chamber increases and the local soot densities will decrease. Probability of signal trapping at this point will be lower than in case when piston is close to TDC, but possibility of its occurrence cannot be neglected. LII signal trapping by soot was not quantified during this experiment but it is expected to be low: (i) at low engine loads the soot formation is less; (ii) the measurements were performed in the later part of the stroke where the volume of combustion chamber is larger and the corresponding local soot volume fraction is lower. Additionally during measurements, the location of laser beam and detection system was chosen to minimise signal trapping or attenuation for this engine. Care was taken to avoid window fouling by cleaning the side windows regularly after each run.

The average value of SVF obtained for different fuel injection timings are plotted against different crank angle in Fig. 5.12.

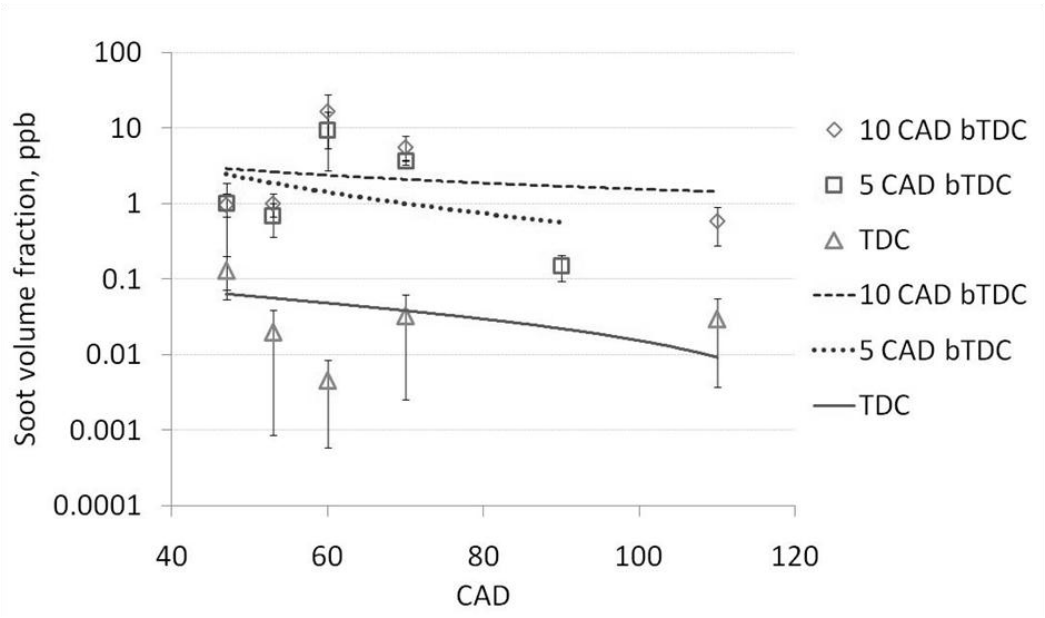

Figure 5.12. Soot volume fraction derived for different fuel injection timings versus crank angle degree for 20 mg/stroke of injected fuel. Error bars show standard deviation and symbols indicate average value of calculated SVF at following crank angles. Lines correspond to trend lines for each set of data.

Error bars correspond to standard deviation. The average values of SVF for the fuel injection time of 10°bTDC increases initially from 1 ppb at 54.5°aTDC to 16.7 ppb at 61.4°aTDC.

Subsequently for later crank angles the SVF decreases and reaches a value of approximately 0.59 ppb. Results obtained for the fuel injection timing at 5°bTDC follow a similar trend but of lower concentration compared to the fuel injection at 10°bTDC. Relatively less amount of soot was observed when the fuel was injected at TDC, and hardly any signals were detected at 2°aTDC. In many cases the soot emissions at this fuel injection timing were detected only by one PMT. Since the incandescence signals were very weak only limited number of measurements were obtained during this condition, and these data were not taken into consideration for data analysis. In-cylinder pressure analysis show that the ignition delay for the case of fuel injection at 10°bTDC and 5°bTDC was relatively short compared to the case of fuel injection at TDC. Shorter ignition delay results in poor mixing of fuel and air, which leads to formation of fuel rich regions and higher soot emissions. Longer ignition delay that was observed for the case of fuel injection at TDC results in more time for mixing of fuel and air. This leads to improved distribution of local oxygen concentration and a favourable environment for oxidation of soot. The longest ignition delay was observed for the case of fuel injection at 2°aTDC. SVF derived for different quantities of injected fuel are presented in Fig. 5.13.

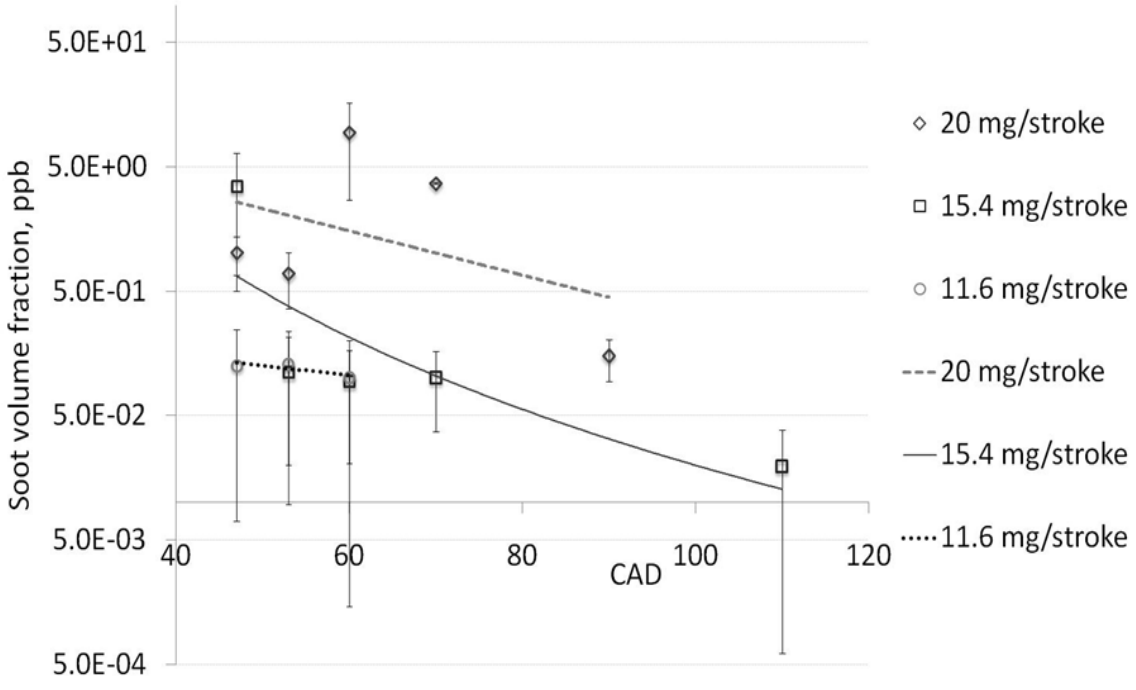

Figure 5.13. Soot volume fraction recorded for different engine loads versus crank angle degree for injection at 5°bTDC. Error bars represent standard deviation and symbols indicate average value of calculated SVF at following crank angles. Lines correspond to trend lines for each set of data.

The error bars corresponds to standard deviation from average value. A general trend of SVF decreasing with crank angle was observed in both Figs. 5.12 and 5.13. For the case when 20 mg/stroke of fuel was injected, relatively higher level of soot concentration was observed. When the fuel injection quantity was decreased from 20 mg/stroke to 15.4 mg/stroke, relatively less amount of soot was produced. Soot production was significantly reduced when the fuel injection quantity was further reduced to 11.6 mg/stroke.

Fuel injection quantity is related directly with the engine load. For increased loads the local available oxygen within the combustion chamber is inadequate to oxidise all the soot produced during the combustion process, so the in-cylinder SVF are relatively high over all the measured crank angles. For lower engine loads the fuel injection quantity is less and low amount of soot is produced. The oxygen present in the combustion chamber in relatively high quantities causes more efficient oxidation of soot under this condition and leads to an overall lower SVF for all the measured crank angles.

5.5.7. Uncertainties in soot particle diameter and SVF estimation

Crank angle resolved in-cylinder soot particle size measurements in an optical HSDI diesel engine require experimental determination of TR-LII and theoretical simulation of LII data. The theoretical simulation of LII signal involves assumption of many optical properties of soot, which are not well established and these parameters influence the calculated size of soot particles. In addition to this the input parameters fed into the theoretical model also influence the size of the measured soot particle. The main parameters that can directly influence the calculated soot particle size and their distribution width are: in-cylinder pressure, gas temperature and initial soot temperature; optical properties of soot such as soot absorption function and thermal accommodation coefficient. The derived soot volume fraction from TR-LII data depends mainly upon initial soot temperature and the assumed optical properties of soot. Uncertainty analysis was performed using sequential perturbation as described in [46]. The maximum uncertainty interval determined for in-cylinder pressure measurements in this optical engine, in the TR-LII measurement range (from approximately 10 bar to 2.2 bar) was ±5% (that includes error of 2% induced by charge amplifier, 1% introduced by pressure transducer and random uncertainty in pressure data), this leads to an uncertainty of ±0.5 nm during particle diameter calculation. The temperature of gas inside the engine cylinder is related to the measured in-cylinder pressure. The major contribution to temperature uncertainty estimation comes from the uncertainty of in-cylinder pressure. An uncertainty of 5% to in-cylinder pressure leads to temperature uncertainty of ±4.5°C which subsequently leads to soot particle diameter uncertainty of ±0.1nm. The thermodynamic calculation of in-

cylinder temperature provides global in-cylinder gas temperatures. In reality the temperature of gas may not be uniformly distributed inside the engine. The local in-cylinder gas temperatures variations can be in the order of up to ±200°C as proposed in [70], which can contribute to an uncertainty of ±1.6 nm to the measured soot particle size. The root-sum-square of uncertainties due to variation of in-cylinder gas temperature and pressure will result in an uncertainty of approximately 2% to the determined soot particle diameter.

Subsequently the size of soot particle diameter may be affected by uncertainty in the determination of initial soot particle temperature. Calculation of initial soot temperature from the two colour pyrometry depends on many parameters, such as choice of detection wavelength, soot absorption function, laser wavelength and laser fluence. Uncertainty in soot absorption function estimation will result in uncertainty to the calculated soot particle temperature, particle size and soot volume fraction. The soot absorption function was calculated based on expression presented in section 3.4. If assumption was made that in the considered range of wavelengths, the complex refraction index function is linear and its value is constant as suggested in [43], then the ratio of absorption function, $E(m_1)/E(m_2)$ would be equal to 1. This causes the difference to the calculated initial soot temperature by ±6% which introduces an uncertainty to the determined particle size by an order of ±6 nm. Inclusion of uncertainty of soot absorption function on top of previously determined uncertainties will lead to an uncertainty of approximately 19% to the derived soot particle diameter.

Additionally the choice of optical parameters in the theoretical simulation of LII signal influences the derived particle size. One of the main parameters which introduce uncertainty in LII modelling is thermal accommodation coefficient. Discussion regarding selecting appropriate value of thermal accommodation coefficients for high pressure applications is provided in section 3.1. In this study $\alpha_T$was assumed a value of 0.3 based on the published high pressure LII works [62, 63, 60, 97]. Moreover the in-cylinder pressure conditions of the optical engine were under conditions typical for transition regime. The assumption of thermal accommodation coefficient of 1 would lead to change in particle size diameter by approximately 19%. Including the uncertainty of thermal accommodation coefficient the overall uncertainty on the derived soot particle size will be approximately ±28%. Calculated soot volume fraction is dependent strongly on soot initial temperature. Change of soot absorption function, as described above, leads to an uncertainty of 40% to the derived SVF. SVF is also will be affected by the determined calibration constant, a difference of 5% in ratio of calibration constants will lead to an uncertainty of 9% to the calculated SVF.

From this analysis we can conclude that assumed parameters like thermal accommodation coefficient and complex refraction index function and calibration constant will have

significantly stronger effects on calculated soot particle size and volume fraction than the measured in cylinder pressure or temperature. Determination of the right values of soot absorption function and thermal accommodation coefficient are very crucial in reducing the uncertainty of the derived soot particle size and soot volume fraction.

5.8. Summary and conclusions

TR-LII is a powerful tool for characterization of in-cylinder soot in engines. In-cylinder diagnostics helps in gaining an understanding of soot processes inside the combustion chamber. Current work presents the results obtained from point measurements in a single cylinder optical diesel engine and it highlights the challenges and uncertainties encountered during measurements and data analysis. Quantitative in-cylinder information about particle sizes and their distribution are helpful in understanding the mechanisms of soot formation and oxidation under different engine conditions and even while applying different fuels. The main findings from current in-cylinder TR-LII measurements are concluded as follows:

- The information about in-cylinder primary particle sizes and their size distributions can be obtained through TR-LII measurements. The in-cylinder soot particles are randomly distributed and are transported within the combustion chamber by fluid motion as revealed by the strong cycle to cycle fluctuations of the measured time resolved LII data.
- Segmented analysis of time resolved laser induced incandesce data reveal that the early part of the LII signal is influenced by soot particles of smaller sizes and the later part of LII decay is influenced by larger particles.
- The analysis revealed that the least square map topology is complex and contains local minima due to the presence of noise in the measured time resolved LII data under complex engine operating conditions. The most commonly used non-linear curve fitting algorithm can get trapped in a local minimum, rather than the absolute minimum. This induces errors on the derived soot particle size and their size distribution, thus careful selection of the values of initial conditions are crucial in determining the location of absolute minimum or alternative fitting procedures such as genetic algorithms should be adopted.
- Crank angle resolved time resolved LII measurements revealed a general trend of the soot particle sizes decreasing with crank angle due to oxidation, and slightly larger particle sizes were observed later in the stroke due to soot agglomeration.

- In this investigation the change in the fuel injection timing did not have any effect on the measured primary particle size. However, the particle sizes were found to be dependent on injected fuel quantity, relatively larger particle sizes were observed for 20mg/stroke of injected fuel. In-cylinder particle size distribution results revealed that later in the expansion stroke a well-defined size distribution can be obtained for a given fuel injection quantity despite the differences in the injection timing.
- The in-cylinder soot volume fraction measured for different fuel injection timings show relatively higher amount of soot produced for shorter ignition delay for cases such as 10°bTDC and 5°bTDC injection timing. For the case of fuel injection at TDC the amount of soot produced was less as combustion tends to be partially premixed due to longer ignition delay.
- A general trend of decreasing SVF with crank angle was observed for most engine operating conditions.

6. Chapter 6 - Characterization of in-cylinder combustion and soot processes for RME and ULSD fuels in a single cylinder optical diesel engine

6.1. Introduction

Diesel engines account for a major percentage of passenger car market in Europe because of its higher thermal efficiency and lower fuel consumption. Fuels in Europe contain increasing amounts of bio-components up to 20% as supported by various EU incentives and mandates [118]. For automotive applications, it has been shown that bio-fuels in the form of pure plant oils cannot be effectively used in diesel engines because of technical problems arising from their high viscosity, corrosive nature and increase in exhaust smoke emissions [1]. However, these oils can be used in diesel engines after removing glycerol components and this can be achieved by transesterification, in which the plant oil is converted to Fatty Acid Methyl Ester (FAME) (or in some cases a Fatty Acid Ethyl Ester).The most commonly used bio-diesel in Europe is Rapeseed Methyl Ester (RME). RME contains more oxygen than ULSD, approximately 10% by weight. Most research recognizes that the presence of oxygen content in fuel is beneficial for the reduction of pollutants like CO, THC and soot. Recently it has been shown through laser extinction measurements that diesel fuels produce higher levels of in-cylinder soot compared to that of oxygenated fuels [79]. Similar results have been demonstrated in [80] where spatially integrated in-cylinder soot luminosity was lower for oxygenate fuels. The presence of chemically bonded oxygen in the fuel causes that number of carbon atoms in fuel is reduced and oxygen content in combustion chamber is improved leading to the reduction in formation of soot precursors and possibly improved oxidation. The emission formation is also strongly dependent on engine operating conditions. In order to understand and control the formation of these emissions a detailed insight into the spray development, combustion and soot processes in diesel engine.

Since soot is a major concern for diesel engine exhaust emissions, efforts are made to understand diesel spray combustion process at fundamental level in diffusion jet flames. To mimic the actual engine operating condition, measurements have been performed to study Combustion and soot processes in constant volume chamber at different ambient conditions [77, 78, 81] and also in a much complex optical diesel engines [79, 80, 31].

In-cylinder investigations have led to the proposal of several conceptual models that help in the understanding of diesel spray combustion process [8, 7, 119]. It has been shown that ignition takes place in the regions where the temperatures of the reactive fuel air mixtures are high with favourable equivalence ratio. Initiated flame consumes the fuel-vapour-air mixture surrounding the liquid core of the spray. The flame stabilizes at a distance from the nozzle tip, and the distance from the nozzle tip to the first appearance of flame is defined as lift off length (LoL). The mixture downstream of LoL is premixed and heat release in this region is quite rapid. Further downstream, the mixtures are rich where the initial soot formation occurs, which are diffused and transported towards the tip of the flame. At the periphery of spray flame the oxygen concentration is high where soot oxidation occurs, fast oxidation at the periphery minimises oxygen entrainment downstream of the LoL. Thus LoL is strongly related to the amount of oxygen in the fuel-rich core and revealed that knowledge regarding LoL and air entrainment upstream of the spray is necessary to fully understand in-cylinder soot processes in spray flames [112].

High speed imaging techniques are used to measure time resolved natural luminosity of flames for understanding in-cylinder combustion and soot process in optical engines [31, 76, 119]. Through the application of high (HS) speed camera along with an integrated image intensifier, severe useful insights can be gained on spray development, coupling between spray and flame, combustion and soot process with high temporal and spatial resolution. Detailed discussions concerning challenges associated with the measurement of natural flame luminosity, signal interpretations and their relation to in-cylinder soot concentration for different test-fuels are presented in [80]. These analyses concluded that oxygenated fuels tend to reduce the average in-cylinder soot volume fraction. The high temperature reaction processes in flames are normally characterised by the OH* radicals that are emitted from the flames. These radicals contribute to the oxidation of soot that is produced during the high temperature combustion process [83]. Chemiluminescence emitted from radicals that are formed during combustion process can be detected at their respective emission wavelengths through spectrally resolved measurements [31, 61, 63, 76]. HS imaging techniques provide time evolution of radicals formed during various stages of combustion. For this purpose image intensifier with a combination of set of filters are required. The OH* radicals are used for determination of flame lift-off length for diesel spray combustion systems [120]. From these investigations it has been found that the soot processes in spray flames are strongly linked to fuel injection parameters and the associated flame lift-off length. In diesel engines, the spray combustion and emission processes are influenced by the level of global air entrainment and the local equivalence ratio of the fuel air mixture in the region of flame lift-

off length. As reported in [23, 81], longer flame LoL allow more entrainment of the air into the fuel jet, which results in less fuel rich regions and reduced soot generation. In-cylinder soot formation and oxidation in optical diesel engines are investigated through non-intrusive laser diagnostics, alongside the use of HS cameras. Techniques like Laser Induced Incandescence (LII) and Time Resolved Laser Induced Incandescence (TR-LII) are generally used for measuring soot volume fraction, and primary soot particle sizes [63, 70, 112]. LII techniques have been successfully applied to study and understand soot processes in different kind of flames [60, 65, 102, 64] as well as in internal combustion engines [49, 51, 69, 70] Formation of laser beam to a laser sheet allows for application of this technique for measuring soot volume fraction in a two dimensional plane. Combined PLII and TR-LII techniques were used for characterisation of soot emitted during combustion of laminar diffusion flame at atmospheric pressure and in an optical diesel engine [63]. It has been shown that the soot volume fraction increased after the start of combustion and reached a maximum at about 10°aTDC and decreased thereafter with crank angle during the expansion stroke. The measured soot particle sizes also had a similar trend to that of soot volume fraction as reported in [70, 69]. Attempts were made to quantify the measured soot particle size and number density in an optical diesel engine by using LII and laser induced scattering (LIS) techniques simultaneously [55]. The same measurement technique (LII and LIS) was used to study the spatial distribution of particle size and its number density distribution in spray flames, in a rapid compression machine [121]. High number density of smaller size particles were detected in the central part of the spray flame, while the reduced particle number density and increased size particles were observed in the regions downstream of the jet. It can be seen that more physical parameters can be elucidated through the use of two or three measurement techniques simultaneously.

The study described here focuses on understanding of the in-cylinder combustion and soot processes for RME and ULSD. Combustion and soot processes for ULSD and RME are characterised using high speed imaging technique, which enabled the measurement of natural soot luminosity and OH* chemiluminescence simultaneously during the visible luminous combustion process. In addition to this, time resolved laser induced incandescence (TR-LII) and planar laser induced incandescence (PLII) techniques were used simultaneously to measure soot particle size, their distribution width and the soot volume fraction from the un-oxidised soot that was left within the combustion chamber after the end of high temperature luminous combustion. The details of the in-cylinder combustion and soot processes for RME are compared against ULSD. Experiments were carried out for single and double injection strategies. Acquired high speed images were used for determining the flame lift-off length

(FLoL), area occupied by flame, ignition delay (ID) and spatial distribution of OH* radicals and soot in spray flames. Spatially integrated data from the high speed soot luminosity images have shown that the intensities of soot emitted during combustion of RME are lower compared to ULSD. The soot formation rates are slower for RME and at the same time the formed soot are oxidised at a faster rate for RME compared to ULSD. The flame lift off length (FLoL) and the distance at which first soot luminosity (SLoL) occurs were longer for RME. Longer LoL for RME causes more air entrainment into the fuel jet that improves oxidation of soot. The early phase of combustion proceeds quicker for RME when compared to ULSD due to oxygen enrichment of the reactive mixture. PLII data confirmed that the amount of soot left in the cylinder after the end of visible luminous combustion is less for RME compared to ULSD and the measured in-cylinder primary soot particles are slightly smaller for RME compared to ULSD.

6.2. Experimental set-up and measurements

Specification of experimental set-up is discussed in chapter 4 (TR-LII section 4.2.1, PLII section 4.2.2) and schematic drawing is presented in Fig. 6.1. For this investigation TR-LII, PLII and high speed imaging were used.

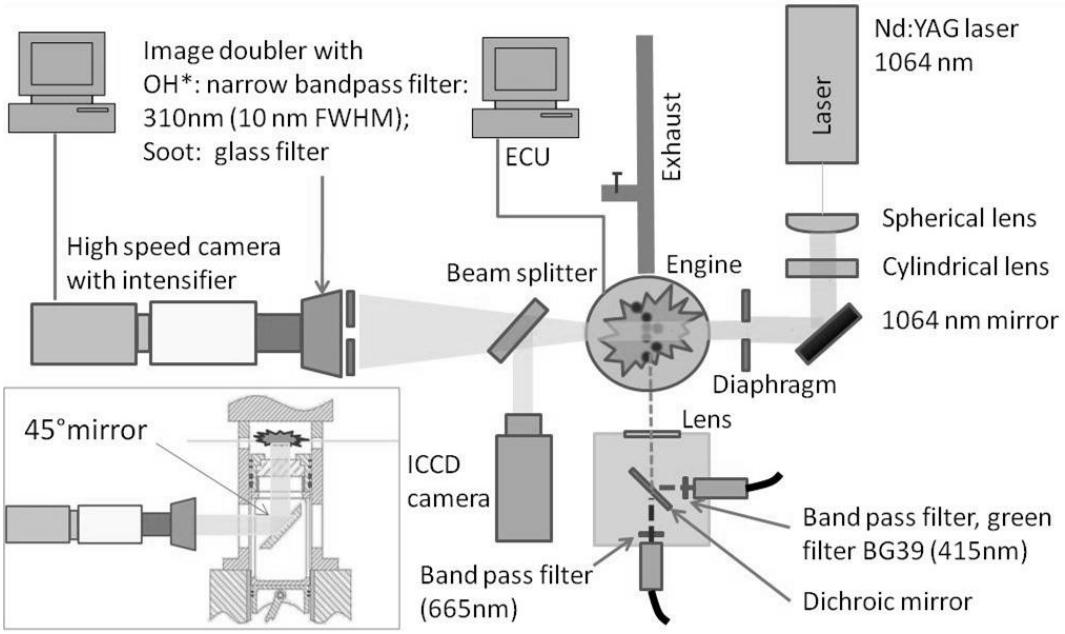

Figure 6.1. Schematics of experimental test facility, side view is presented in the left bottom corner.

Experiments were conducted to study in-cylinder combustion and emission performance for two fuels, RME and ULSD. Two injection strategies (single and double injections) were

considered. For the case of single injection 20 mg/stroke of fuel was injected at 5°bTDC; for the case of double injection 9 mg/stroke of fuel was injected first at 20°bTDC, and 19mg/stroke of fuel was injected at TDC for second injection. The fuel injection pressure was maintained at 1000 bar for both fuels. Multiple injection strategy usually uses a pilot injection, a main injection and a post injection. Application of pilot injection causes an increase in gas temperature inside the combustion chamber prior to the main injection, which leads to shorter ignition delay and reduced noise. Usually pilot injection is about few percent of the main injection. In this study double injection strategy was applied where the first injection was about 45% of main injection. The dwell between injections for the double injection strategy was set at 20 CAD, the injection timings and quantities were fixed in such a way to enhance soot formation. The fuel injection timings and quantities were not optimised, so the load under these conditions and the soot formation rates are higher when compared to a single injection strategy. Thus no comparison will be made between the single and double injection strategies but only the performance between RME and ULSD fuels within each injection strategies will be discussed. Soot luminosity and OH* chemiluminescence were recorded right from the start of injection until the end of visible luminous combustion and thereafter un-oxidised soot present within the combustion chamber after the end of combustion were characterised using PLII and TR-LII. During the engine run PLII and TR-LII data were acquired simultaneously for following crank angle degrees: 46.4ºaTDC, 51.4ºaTDC, 61.4ºaTDC, 71.4ºaTDC, 111.4ºaTDC. Engine limitation prevented LII incandescence measurements around TDC where most of the processes of soot formation and oxidation occur. Nevertheless, it is important to obtain information about soot process in the later part of the expansion stoke to understand the relation between in-cylinder soot processes and exhaust out emission.

6.3. Results and discussion

Results section is divided into three subsections; in the first subsection (6.3.1) in-cylinder pressure analysis is presented. The following subsection (6.3.2) presents results obtained from high speed imaging. Here, spray development, soot processes, distribution of soot and radicals from the time of injection for both fuels are considered. The goal of this analysis is to compare the differences in early soot processes for both fuels and understand how they affect further soot emission. In last two sections (6.3.3 and 6.3.4) results obtained from PLII and TR-LII are presented and the soot processes after the end of luminous combustion, late in the expansion stroke are discussed.

6.3.1. In-cylinder pressure analysis

In-cylinder pressure data acquired from a single cylinder optical engine during the combustion of ULSD and RME when operated under single and double injection strategies are presented in Fig. 6.2 together with the calculated cylinder temperatures.

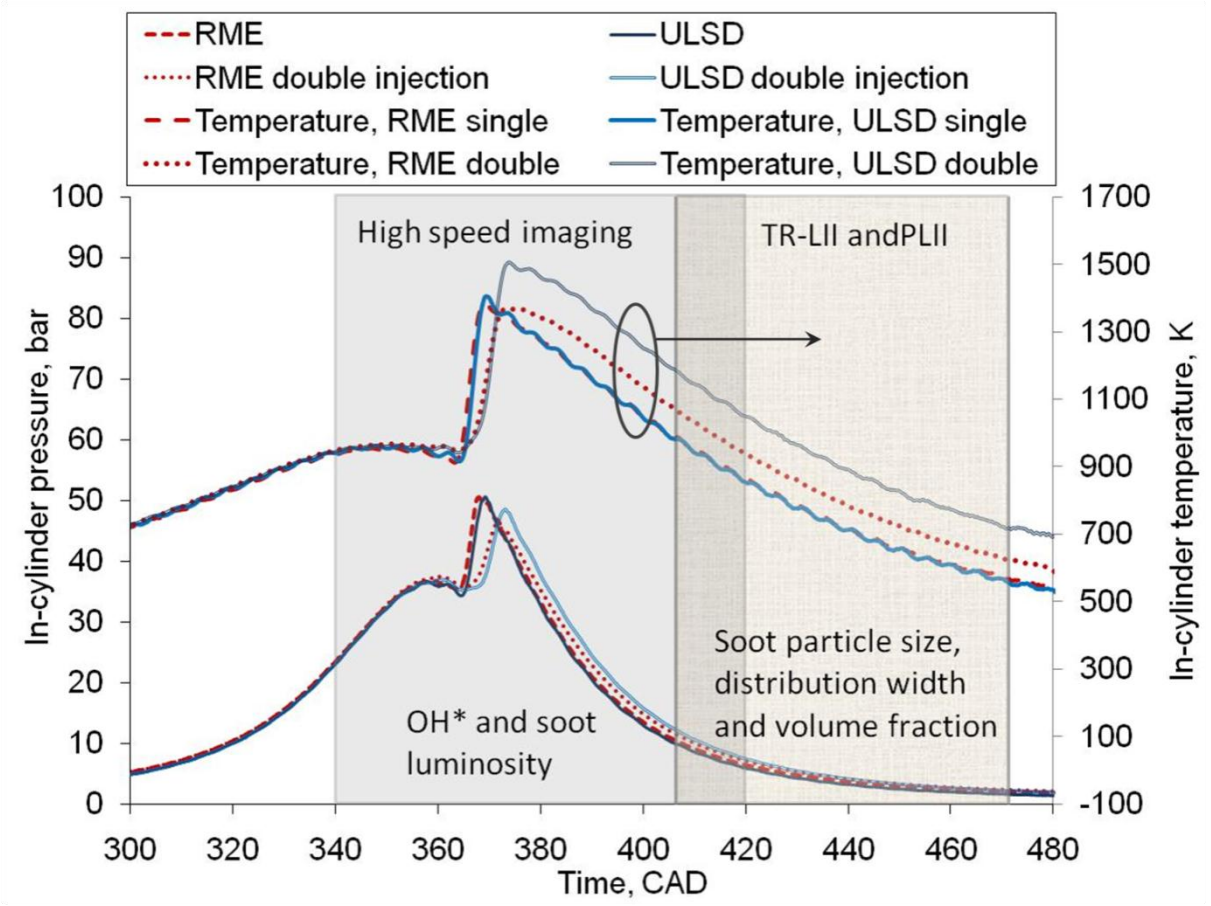

Figure 6.2. In-cylinder pressure recorded for ULSD and RME, for single and split injection and measurements range for OH*, soot luminosity and TR-LII and PLII indicated by grey areas.

The data was averaged over 20 firing cycles and filtered using fast Fourier transform algorithm to eliminate the noise. From the in-cylinder pressure data, gross heat release rate and in-cylinder temperatures were calculated using basic thermodynamic formulations discussed in chapter 3. The gross heat release rates for single and double injection strategy for ULSD and RME are presented in Fig. 6.9 and Fig. 6.10 respectively. The start of combustion (SOC) for ULSD and RME was determined as explained in section 3.1.

The grey area in Fig. 6.2 indicates the range of crank angles right from SOI until the end of visible luminous combustion where OH* chemiluminescence and soot luminosities were

measured using the high speed camera. The amount of un-oxidised soot left in the combustion chamber after the end of luminous flame was detected using Laser Induced Incandescence (LII) technique. Simultaneous application of Planar LII (PLII) and Time-resolved LII (TR-LII) techniques allowed for two dimensional soot volume fractions and primary soot particle size measurements. The primary particle sizes were obtained by comparing the measured TR-LII signal against the theoretical TR-LII data. Details regarding the application of TR-LII technique for measuring particle sizes in optical engines have been discussed in section 4.2.1. Calculated ignition delay and IMEP for ULSD and RME for single and double injection strategies are provided in Tab. 6.1.

Fuel	IMEP, bar	SOC, °aTDC	ID, (CA)
RME single inj.	2.8	2.6	7.6
ULSD single inj.	2.6	4.1	9.1
RME double inj.	3.2	3	3
ULSD double inj.	3.9	3.6	3.6

Table 6.1. IMEP, start of combustion and ignition delay for ULSD and RME, single and split injection.

The IMEP for single injection strategy was comparable between fuels but for double injection strategy, the IMEP for ULSD was slightly higher compared to that of RME. Taking single injection into consideration slightly longer ignition delay was observed for ULSD when compared to that of RME and similar trends were observed for the case of double injection. The observed shorter ignition delay for RME under both injection strategies could be related to higher oxygen content and improved mixing during injection (longer lift-off length) of oxygenated fuel compared to that of ULSD.

6.3.2. Soot luminosity and OH* chemiluminescence

This section presents the result of soot spatial distribution, lift-off length, ignition delay, spatial distribution of OH* chemiluminosence and spatially integrated results of soot luminosity and OH* chemiluminosence. The purpose of this analysis is to compare the differences in early soot processes for both fuels and to understand how they affect further soot emission. Emissions from flame are composed mainly of radiation from soot and chemiluminescence from various gaseous species. Natural flame luminosity (radiation from soot) has been widely used for characterising in-cylinder combustion, soot formation and

oxidation processes, [31, 80]. The intensity of flame luminosity is strongly dependent upon temperature of the burning soot, thus interpretation of high luminosity regions as regions of high soot may be misleading. Hence natural flame luminosity should not be directly related to the amount of soot produced during the combustion process. The luminosity detected by camera depends upon many factors, such as quantum efficiency of the image intensifier, detection system and its gain, adiabatic flame temperature, in-cylinder temperature and optical thickness, all these factors have to be taken into consideration while evaluating experimental data.

$$S = K f_v(x) g(T(x), m) \tag{6.1}$$

Equation 6.1 shows the simplified expression used for correcting the measured in-cylinder natural soot luminosity emission [80]. Where S is measured soot natural luminosity (SNL) and it is related to local soot volume fraction $f_v(x)$ and g function, K is constant for a given detection system, it was calculated by considering collection solid angle, measurement volume and proportionality constant of the detection system as suggested in [80].

The g function is dependent upon local temperature $T(x)$, soot refractive index m, detection wavelength λ and quantum efficiency of the detection system η .

$$g(T(x), m) = -\int_0^\infty \frac{\eta}{\lambda^6\left(e^{c_2/\lambda T}-1\right)} Im\left(\frac{m^2-1}{m^2+2}\right) d\lambda \tag{6.2}$$

$c_2$is second Planck's constant (1.4388 x 10^{-2}m·K). Values of refractive index were linearly interpolated between the values listed in [80]. By integrating Eq. (6.2) the variation of g function with temperature was obtained. The soot luminosity that was measured with the detection system in this work was proportional to ~ T^{10} for temperatures ranging from 1500 to 2700 K and this indicates that only the hottest soot will dominate the recorded signal. Similar magnitudes of temperature dependence $\sim T^{11}$ and $\sim T^{13}$ has been reported in [80] and [31] respectively. Acquired natural flame luminosity was corrected for the influence of adiabatic flame temperature and detection system effects (quantum efficiency of the intensifier).

6.3.2.1. Spatial distribution of soot luminosity

Figures 6.3– 6.5 show the single shot crank angle resolved line of sight natural luminosity images of spray flames acquired during the combustion of ULSD and RME. The detection crank angle is displayed at the top of each image. Figure 6.3 illustrates a typical representative image of diesel spray combustion process that was aquired during the combustion of ULSD in an optical engine when operated at a swirl ratio of 1.4.

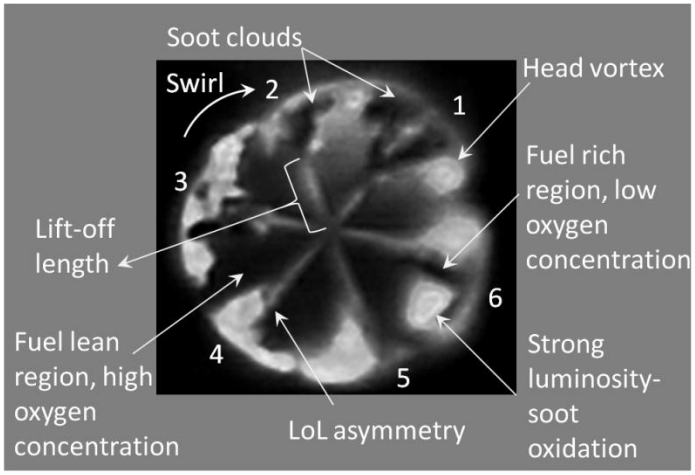

Figure 6.3. Spatial distribution of soot during combustion of ULSD.

The fuel was injected at a pressure of 1000 bar; as the spray penetrates into the combustion chamber it entrains air, vaporises and mixes with ambient air to form a reactive combustible mixture. From the high speed images it can been seen that ignition (first appearance of luminous flame) occured at about 2.16°aTDC. The flame stabilises at a distance downstream from the nozzle tip by interacting with the liquid and vapour part of the emerging fuel spray. The distance from the nozzle tip to the first appearacnce of the flame is defined as flame lift off length (FLoL). Downstream of the FLoL, closer to the cylinder wall, thick soot clouds are observed which are indicated by darker areas in the central part of the spray and the flame rolls up to form head vortices. Head vortices lead to formation of intense turbulent mixing of reaction zones with air, fuel vapour and products of combustion at that location. In these regions high levels of soot oxidation may occur as can be seen through high flame luminosity. Intensity of soot luminosity increases towards the downstream edges of the spray, indicating that in these areas higher temperature and strong soot oxidation occures. Dark areas between the jets in Fig. 6.3 represent areas of oxygen concentrations that are not effectively utilised by the fuel spray. The presence of swirl transports the flame to regions of available oxygen concentrations, which effectively enhances air utilisation and reduces soot emission. Swirl eventually results in asymmetries to spray flame as shown in Fig.6.3. Figure 6.4 illustrates the sequence of crank angle resolved single shot natural luminosity of spray flame images that were acquired for the single injection strategy for ULSD and RME. Early stages of ignition sites were detected at 2.16° aTDC, and it was observed at downstream location of the jet, closer to the cylinder wall. Subsequently in time between 3.6 and 5.04°aTDC the intensity of SNL increased and the luminous sooting flame moved towards the injector. From 6.48°aTDC onwards luminous soot was observed to occupy nearly the entire cross sectional area of the combustion chamber downstream of FLoL. For later crank angles (15.12°aTDC and

20.16°aTDC) soot luminosity was almost negligible except for some randomly appearing patches of low level soot intensities, which are indicated by arrows in the figure at these crank angles. The duration of combustion measured from the in-cylinder natural luminosity for ULSD was approximately 24.5 CAD, while for RME it was about 22.3 CAD.

Figure 6.5 shows the images of SNL acquired for ULSD and RME for double injection strategy. First injection starts at 20°bTDC and it can be seen that ignition (first visible flame luminosity) for the first injection occurs at 6.48°bTDC and 12.96°bTDC for ULSD and RME respectively. Early stages of these ignition sites were observed at the periphery of the jet, but it appears to be in the central part of the jet when viewed through the bottom of the piston window. These local ignition sites did not initiate high temperature luminous combustion as they were locally quenched, but the spray was reignited during the second injection. The early location of ignition and soot formation zones are different spatially and temporally for ULSD and RME fuel sprays. In case of ULSD the early formation of soot appears relatively closer to injector compared to RME (see Fig. 6.5, 2.16° aTDC). ULSD has higher sooting tendency than oxygenated fuels, which is related to different chemical composition of these fuel. In case of RME the soot is formed further away from the nozzle tip, closer to the cylinder wall.

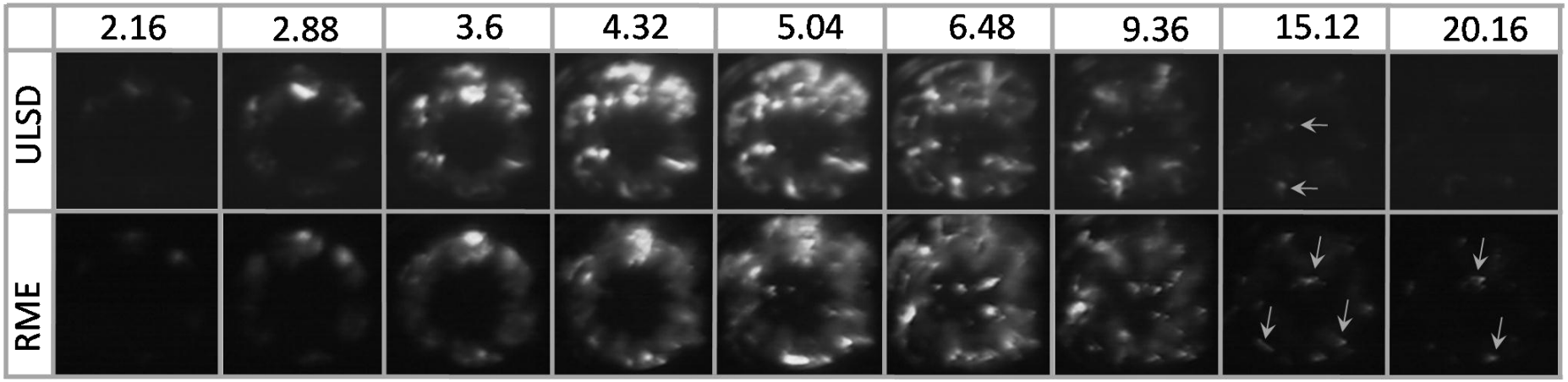

Figure 6.4. Spatial distribution of soot for single injection strategy measured for RME and ULSD. Each image is single shot raw data without corrections of intensity and top numbers indicate crank angle at which reading was taken.

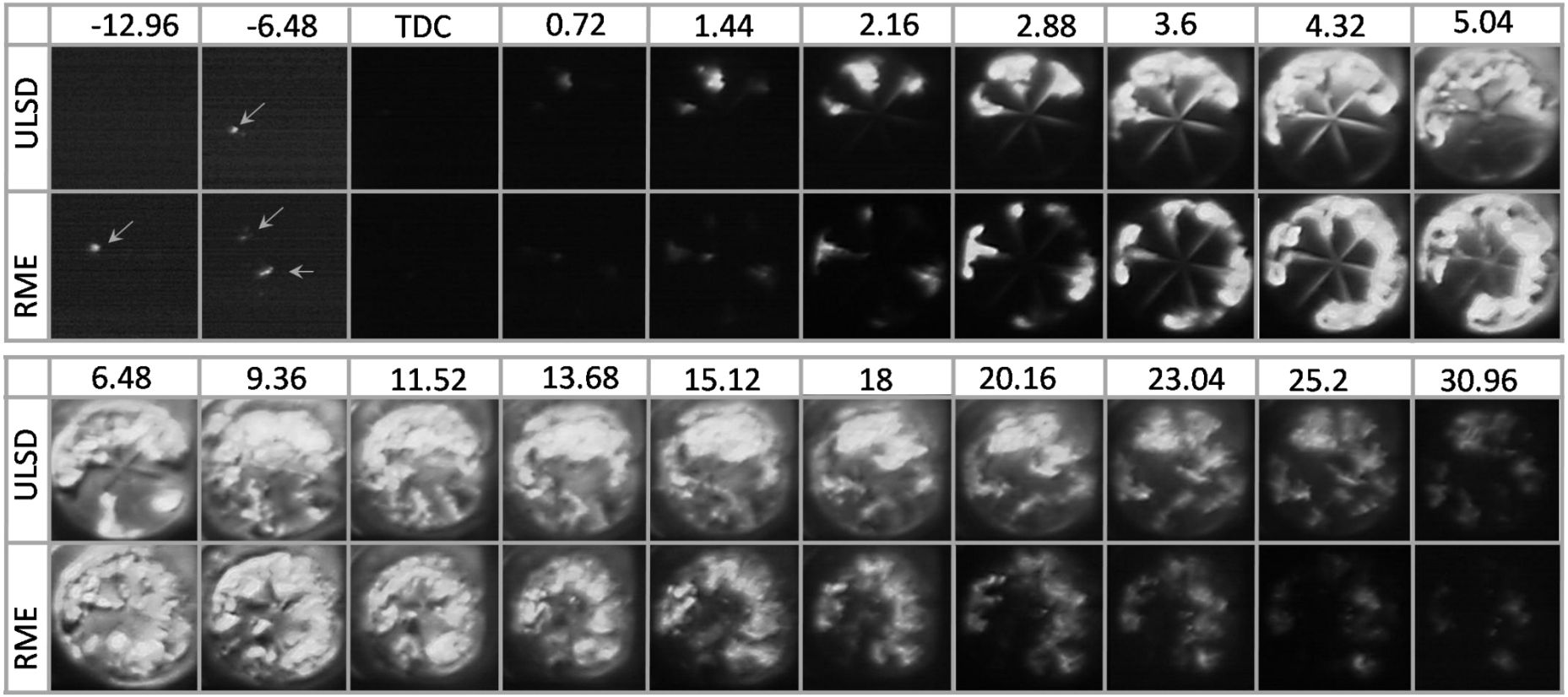

Figure 6.5. Spatial distribution of soot for double injection strategy measured for RME and ULSD during injection and later in the expansion stroke. Each image is single shot raw data without corrections of intensity and top numbers indicate crank angle at which reading was taken.

Similar type of investigation was carried out in a high pressure, high temperature vessel for diesel and oxygenated fuels [80, 82]. It has been shown that spatially the soot formation in diesel spray flames appears to be closer to the injector nozzle tip when compared to oxygenated fuels. The vapour plume after hitting the walls form vortices as described in section 6.3.2.1 and cause turbulent mixing. Closer to cylinder walls, the injected spray tends to appear in the shape of mushroom and eventually the flame then spreads out to the rest of the chamber. For first few crank angles (2.16-5.04°aTDC) the area occupied by the flame during combustion of RME seems to be greater than ULSD. For subsequent crank angles (6.48-20.16°aTDC) the luminous intensity of RME spray flame decreased faster and the area occupied by luminous soot was less compared to ULSD.

After the end of injection (from 9.36°aTDC onwards) it can be seen that the soot formed during the diffusion phase for ULSD combustion was uniformly distributed, covering most of the measurement volume. For the case of RME the central part of combustion chamber had unutilised oxygen and the observed intensity of SNL was significantly lower than ULSD. For later crank angles (e.g 25.2° aTDC) hardly any SNL was observed for RME when compared to ULSD. Figure 6.5 shows that the initial soot luminosity observed during combustion of RME occupied greater part of the combustion chamber. Subsequently its intensity decreased and the area occupied by soot luminosity was found to be smaller compared to that of ULSD. Another interesting feature of strong dissimilarities between spray-to-spray ignition and combustion was observed from the analysis of several high speed images of both ULSD and RME fuel sprays. This phenomenon is visible in Fig. 6.6, where all of these single shot images were acquired for the same operating condition at a crank angle of 3.6°aTDC but for different injection cycle.

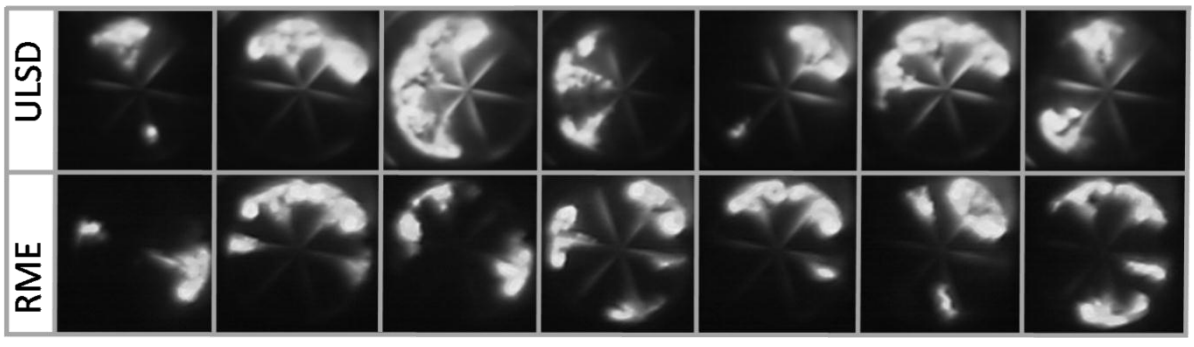

Figure 6.6. Single shot images of few injection events for 3.6°aTDC for ULSD and RME fuels.

Not all sprays were ignited in a combustion cycle; different jets tend to ignite randomly in different injection cycles and the ignition pattern was different from spray-to-spray. Presence of one, two or more non-igniting or sluggishly igniting jets within the combustion chamber

may be attributed to in-homogeneities in the in-cylinder temperature and flow field variations due to replacement of original re-entrainment bowl with a flat optical piston. Alternatively this could be the effect of spray-to-spray variation in an injection cycle caused either by asymmetric internal nozzle flow characteristics or an effect that may be present in a diesel engine due to uneven air utilisation between sprays in an injection event.
In the following sections detailed information about the variation in flame lift-off length and ignition delay for ULSD and RME will be discussed.

6.3.2.2. Lift-off length

When the fuel-air mixture in the spray reaches adequate temperature, reactions are initiated and heat is released rapidly. This phase of combustion in diesel spray is called premixed combustion. Following the premixed combustion the in cylinder temperature increase, the rich mixtures present in the fuel spray significantly influences the soot formation processes [7]. At the end of this stage, all premixed oxygen is consumed and the newly injected fuel undergoes rapid pyrolysis and further oxidation with surrounding air in the mixing-controlled phase of combustion. The most common parameter that is used for characterising the soot formation processes in spray flames is the flame lift off length (FLoL) [77, 78, 81, 120, 83]. FLoL are normally determined by measuring the distance from the tip of injector to the first appearance of OH* radicals in a spray flame, [31, 82, 120]. The mixture in the region closer to the lifted flame are premixed due to higher amount of air entrained upstream of lift-off length and this leads to lower soot production in this region. The FLoL obtained from OH* chemiluminesence are presented in Fig. 6.7.

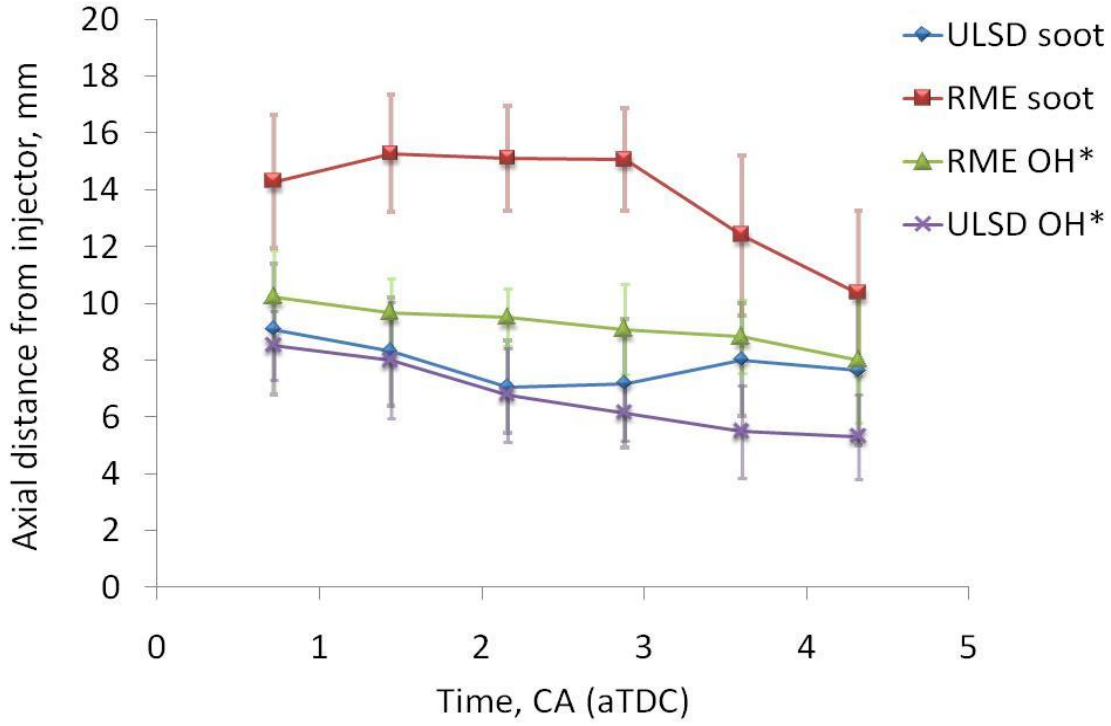

Figure 6.7. Average FLoL and SLoL calculated on the base of spray 1 for ULSD and RME fuels. Error bar corresponds to standard deviation.

The data in Fig. 6.7 was obtained by measuring the distance from the tip of injector to the nearest axial location of OH* radicals with an intensity greater than the setthreshold. The treshold intensity for FLoL determination was set at 40 on the zero to 255 intensity scale of the image (this threshold was kept the same for both fuels). Amongst other parameters, the flame lift off length is dependent mainly upon the nozzle hole diameter, injection pressure, injection velocity, ambient density, ambient temperature and fuel properties [77, 122, 123]. Additionally, based on the measured soot natural luminosity images (presented in Fig. 6.5) the distance from the tip of injector to the nearest luminous soot cloud was determined. This distance will be refered to as lift of length based soot luminosity (SLoL). FLoL and SLoL were measured for spray no. 1 (see Fig. 6.3) and their results are presented in Fig. 6.7. The average values of FLoL and SLoL are based on ten injection events and the error bar indicates the standard deviation. The spatial resolution was determined by imaging a grid of known size using the high speed camera. This enabled to get distance related to one pixel and accordingly the FLoL and SLoL were obtained.

The measured FLoL was slightly greater for RME compared to ULSD. This may suggest that the mixture distribution in RME sprays is relatively leaner compared to ULSD. Thus the flames from RME fuel sprays stabilise at a distance further from the nozzle tip compared to ULSD. Mechanism of FLoL is complex and may be related as well to fuel composition, flame

velocity, fuel velocity, nozzle diameter, ambient temperature and flame propagation [124]. For ULSD the FLoL fluctuates from 7 to 9 mm and the flame stabilises approximately at this location downstream of the nozzle tip. At the crank angle of 4.3°aTDC the FLoL for RME was 8 mm while for ULSD it was 5.3 mm. Longer FLoL in RME corresponds to greater air entrainment and this improves soot oxidation in the premixed regions of spray combustion. Additionally RME contains about 10 % oxygen which further enhances soot oxidation which results in lower emission of soot for RME compared to ULSD. For both fuels a decreasing trend in FLoL was observed as the temperature in combustion chamber increased with crank angle. Considering the SLoL, larger differences were observed between fuels, at 0.72°aTDC the SLoL for ULSD was about 9.0 mm while for RME it was about 14.3 mm.

Figure 6.8 shows the simultaneously measured OH* chemiluminescence and soot luminosity during combustion of ULSD and RME at 3.6^{o}aTDC.

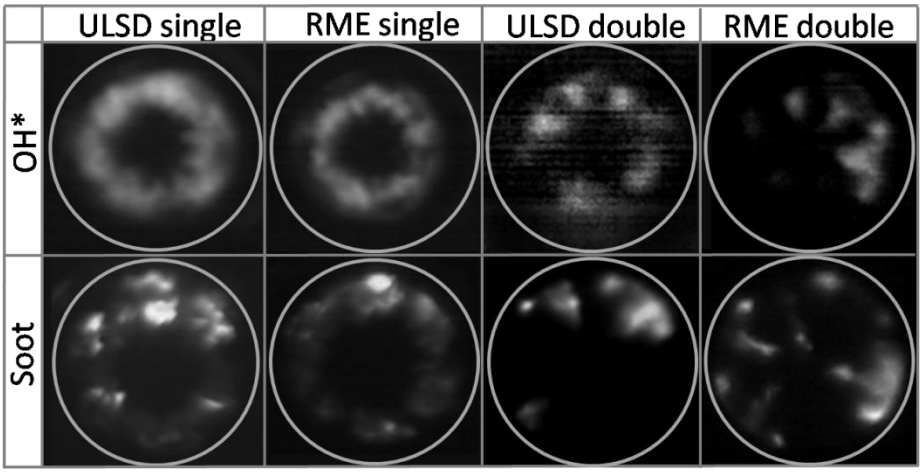

Figure 6.8. OH* chemiluminescence and soot luminosity recorded for ULSD and RME, for single and double injection strategies at 3.6ºaTDC.

The soot formation occurs behind the reaction zone where OH* radicals are found in high concentration, particularly in the spatial regions of the spray that are near stoichiometric conditions, [81].

Since RME contains more oxygen, the local stoichiometry of reactive mixture in the spray is different compared to ULSD. This causes a delay to the first appearance of soot (towards the cylinder wall), as well as reduction in soot formation and improved soot oxidation. Similar work had been carried out to study FLoL and soot inception for four different fuels in a constant volume chamber [83]. It has been shown that the time required for soot nucleation during combustion of fuel containing oxygen was greater than that of diesel, which is in line with the results presented in this work. A similar trend of longer distance from the tip of

injector to the region of first appearance of luminous flame was observed for oxygenated fuels in [82]. Besides the effect of oxygen content in the fuel, the FLoL is strongly dependent on engine operating conditions, injection strategy and the in-cylinder conditions such as temperature and pressure [77, 120]. The average in-cylinder gas temperature was about 1000 K at TDC and, this value increased further during combustion. Additionally the in-cylinder temperature for the double injection strategy was higher for ULSD compared to RME. This difference also contributes to the observed variations of the measured FLoL for these fuels.

The rate at which the reactive mixtures are consumed in a spray flame after the start of ignition are shown in and Figs. 6.9 and 6.10 for ULSD and RME fuels. This is presented in the form of area engulfed by a flame inside the combustion chamber at different crank angles, determined as the percentage of the area of the chamber that was occupied by high intensity luminous soot.

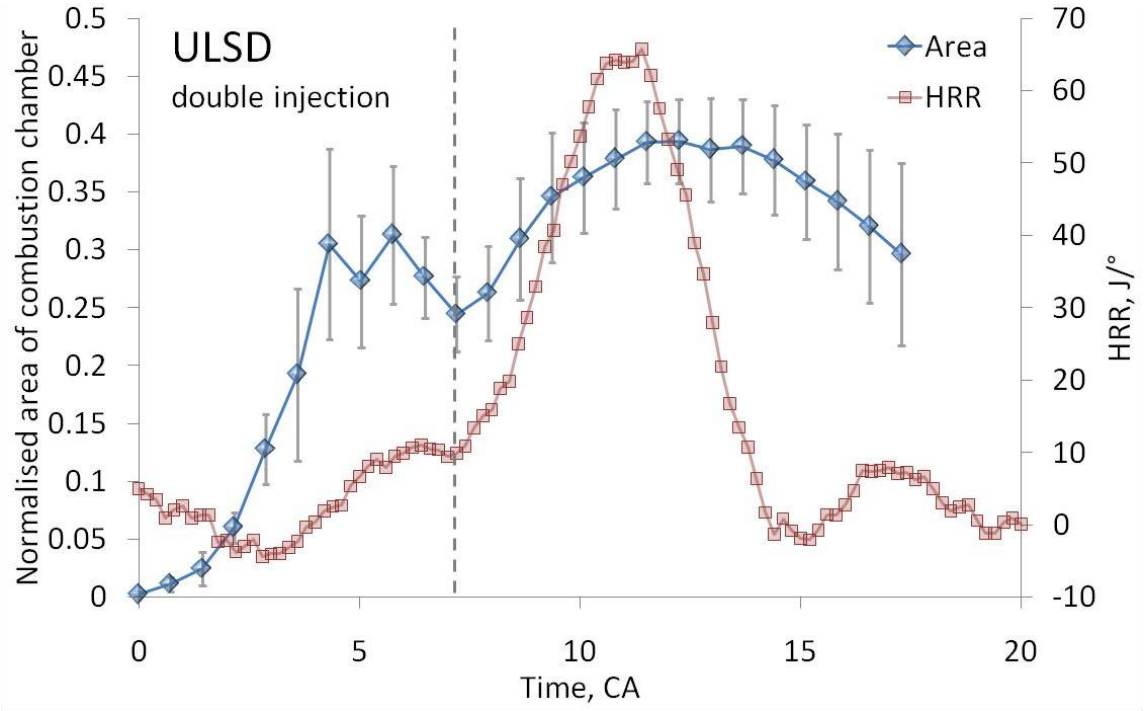

Figure 6.9. Percent of the combustion chamber occupied by the soot luminosity during combustion of ULSD (diamond symbols) plotted together with HRR (square symbols). Error bars correspond to standard deviation and dashed line show the end of the premixed and start of the mixing controlled phase of combustion.

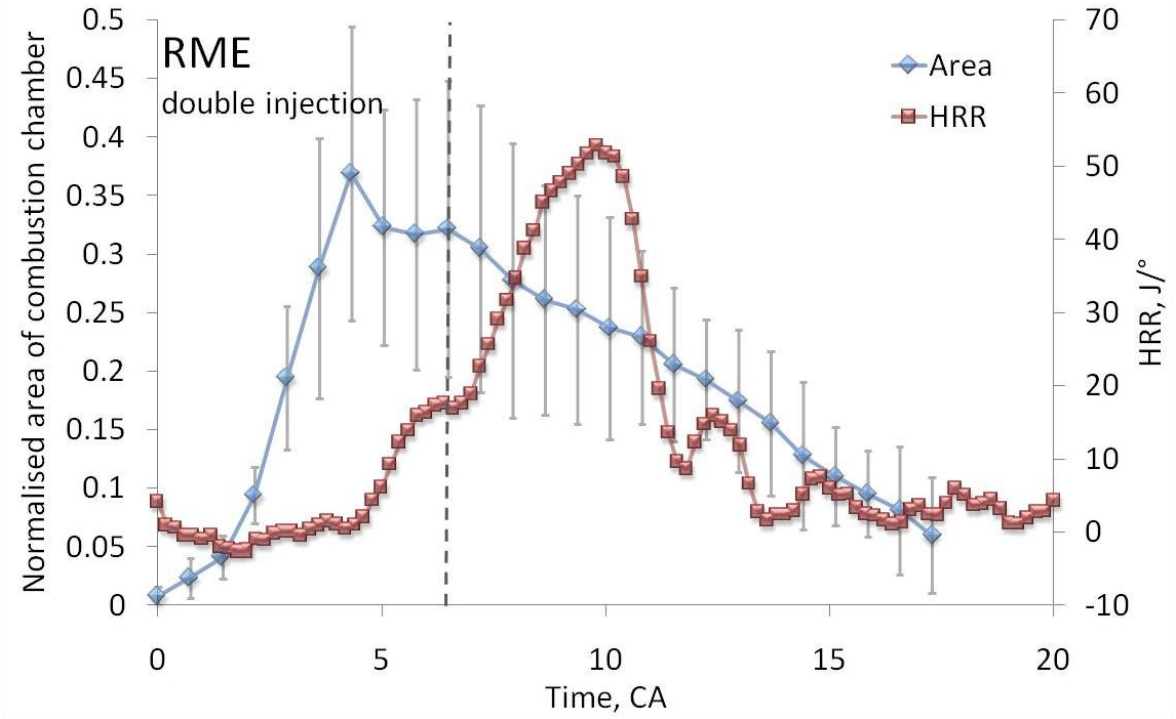

Figure 6.10. Percent of the combustion chamber occupied by the soot luminosity during combustion of RME (diamond symbols) plotted together with HRR (square symbols). Error bar corresponds to standard deviation and dashed line show the end of the premixed and start of the mixing controlled phase of combustion.

The area occupied by the flame in the combustion chamber at a given crank angle were deterimed by counting the intensity of light in the pixel that are above a certain threshold that seperates the flame luminosity from spray and other non-luminous regions. At the initial stage, when signal intensity was low, lower threshold level of 40 (on the 0 to 255 intensity scale) was used. The threshold level was increased with increasing intensity to a level of 150 to avoid reflection from cylinder walls and noise, especially when soot luminosity signal was stronger at later crank angles. The tresholds were kept at the same level for both fuels. Subsequently the number of pixels representing the area of the combustion chamber was calculated and the ratio of SNL area to the combustion chamber area provided the percent of combustion chamber occupied by luminous soot. Each data point corresponds to an averaged of over ten images, and the error bar corresponds to standard deviation.

It can be seen that RME initially occupies slightly larger area of combustion chamber in comparison to ULSD, and this area was engulfed at a relatively higher and faster rate for RME. RME flame occupies a maximum area of ~37% of combustion chamber at 4.32ºaTDC and thereafter the area occupied by flame during the remaining combustion period of this fuel decreased at a steady rate. The area occupied by the ULSD flame remained approximately at

the same level of ~30% between 4.32ºaTDC and 7ºaTDC, subsequently it increased to nearly 40% during the later part of the stoke at 11.52°aTDC and then decreased gradually. To gain more insight into the combustion behaviour of these two fuels, the heat release rate (HRR) that was calculated based on the in-cylinder pressure data was superimposed on the burn area of the spray flame. The vertical dashed line, in Fig. 6.9 and 6.10 shows the border between premixed and mixing controlled combustion that was derived from HRR. It can be seen that during the first phase of combusiton, RME releases more heat in comparison to ULSD. This is reflected in the calculated SNL area, where slightly greater area was occupied by flame during combustion of RME when compared against ULSD. At aproximately 6 to 7ºaTDC premixed phase of combustion ends. In this phase the heat release rate observed for ULSD is higher compared to RME. The area occupied by luminous sooting flame in case of ULSD increases while for RME a constant decrease was observed. As already mentioned the presence of oxygen in RME alters the local stoichiometry during entrainment and mixing process in the spray. More efficient premixing for RME (related to longer FLoL) compared to ULSD results in a generation of favourable environment for faster development of flame for RME fuels. Similar results have been reported in [125] based on the HRR analysis in a thermodyanic engine, were it was demonstrated that RME burns at a higher rate than ULSD. This image analysis revealed that the early phase of combustion proceeds quicker for RME when compared to ULSD due to oxygen enrichment of the reactive mixture. This results in a faster combustion for RME and on the contrary more of a slugish mixing controlled combustion for ULSD.

6.3.2.3. Ignition delay

Ignition delay (ID) is defined as the time from the start of injection to the start of combustion. Normally formaldehyde is used as a marker for detecting ignition in flames. In this investigation the start of combustion have been considered from the in-cylinder pressure data, natural flame luminosity and OH* chemiluminescence images. The ignition delay that was calculated from in-cylinder pressure data (see section 3.1) which provides global information, while the ID that was based on the first appearance of OH* chemiluminescence or soot luminosity measurements provides information about local. Figure 6.11 shows the plot of ignition delay calculated based on pressure, flame luminosity and OH* chemiluminescence data for ULSD and RME when operated under single and double injection strategies.

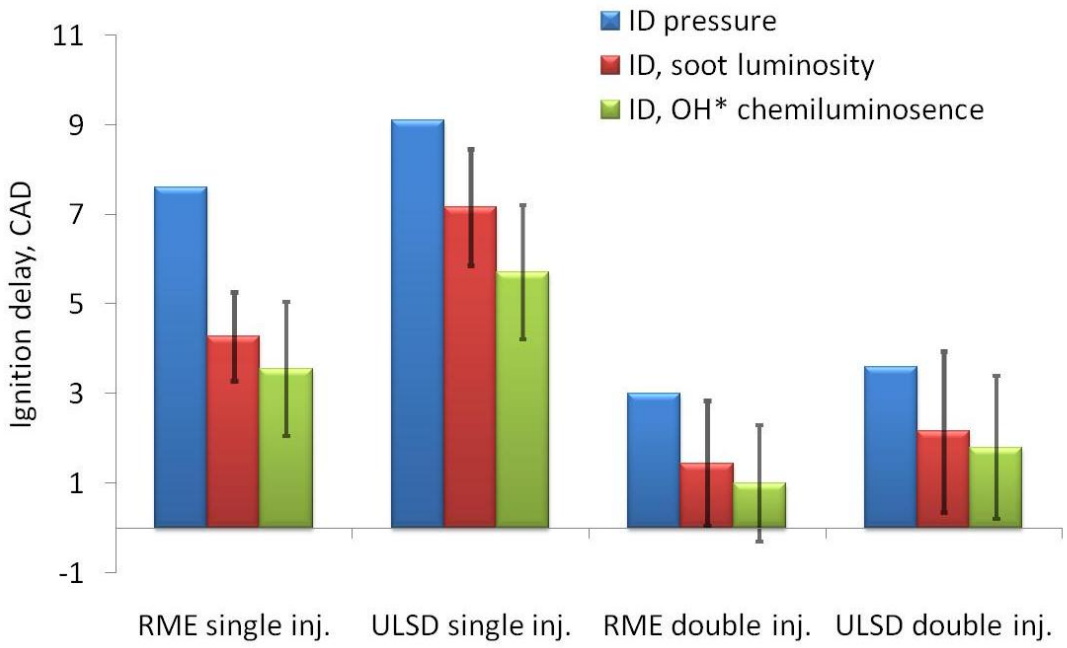

Figure 6.11. Ignition delay determined from in-cylinder pressure, soot luminosity and OH* chemiluminescence. Black lines on bars shows observed ignition after first injection for double injection strategy.

For all cases the ID that was obtained from the OH* images (first appearance of OH*) was slightly shorter than that obtained from the soot luminosity or pressure data. The OH* radicals that are detected by the camera provide information regarding the reactions that are taking place in the combustion chamber prior to soot formation. This show that hot reactions are followed by soot formation processes. The ID determined from the pressure data tend to be longer than that which was observed from OH* and natural soot luminosity images, as mentioned above this represents the global picture of the whole combustion process.

For the case of double injection strategy, the ID for both RME and ULSD was determined with respect to second injection. For this strategy significantly stronger fluctuation in ID was observed for the data from OH* chemiluminescence and soot luminosity. Injection of pilot ahead of main caused a significant effect in raising the temperature of gas in the cylinder. The variations and fluctuations to the ID derived from OH* chemiluminescence and soot luminosity for the double injection strategy are caused mainly strong local in-cylinder gas temperatures variations due to local ignition sites of pilot. The ignition delay for RME was always shorter than ULSD for both injection strategies and it is in agreement with trends reported in [31, 82], where it has been shown that fuels with higher oxygen content have shorter ID. First visible ignition for double injection strategy occurs after the first injection as indicated in Fig. 6.15 by vertical dashed line (in case of RME) and vertical solid line (in case of ULSD). The level of soot luminosity at this point was very low but still it was possible to

detect with help of an intensifier as can be seen in Fig. 6.5. Observed low luminosity areas were quickly quenched and reignited during second injection that occurred at TDC. The pilot fuel mixes with air and initiates reactions leading to formation of radicals and increase in the in-cylinder temperature. This enables the second injection to ignite easily with reduced delay.

6.3.2.4. Spatial distribution of OH* chemiluminescence

Figure 6.8 shows simultaneously measured OH* chemiluminescence and soot luminosity for ULSD and RME for single and double injection strategies at 3.6º aTDC. The intensity of OH* chemiluminescence was very low to enhance the readability the intensity was increased to 150%. It can be seen that the intensity of OH* chemiluminescence was relatively low compared to SNL for both fuels and this effect was more pronounced for double injection strategy. In this section mainly the spatial distribution of OH* radicals will be discussed and the intensity levels will be considered in section 6.3.2.5. When compared to SNL images it can be seen that OH* radicals are observed at a distance relatively closer to the nozzle tip for both fuels. It has been shown that most of OH* radicals are formed near stoichiometric conditions [83]. For the case of single injection strategy, OH* radicals are uniformly distributed during combustion for ULSD and it appears almost to be in the shape of a ring. The OH* radicals formed during the combustion of RME appears also in the form of a ring, but its distribution is less uniform when compared to ULSD. In case of double injection strategy the distribution of OH* radicals is not that uniform, the radicals are observed at the upstream location of the jet while the soot occurs at the downstream location of the same spray flames.

From the high speed images it can be seen that early stages of ignition were observed at the periphery of developing spray. As the flame starts to develop, it appears as a ring of OH* cloud within the entire combustion chamber. The OH* radicals appear to be uniformly distributed compared to sporadic distribution of soot, especially for single injection strategy.

Figure 6.12 and 6.13 are single shot images showing the spatial distribution of OH* radicals emitted from the combustion of ULSD and RME for single and double injection strategies respectively. The global distribution of OH* radicals in spray flame are similar for both fuels.

For the case of single injection the intensity of OH* chemiluminescence formed during combustion of ULSD seems to be greater when compared to RME for crank angles between 2.16°aTDC and 5.04°aTDC. For the case of RME (see Fig. 6.12, 2.16°aTDC to 3.6 °aTDC), the intensity of OH* radicals are stronger in regions closer to the nozzle tip, and the intensity of OH* gradually reduces at the external border of the ring (closer to downstream location in the flame). This gradual reduction in OH* concentration with crank angle could be mainly

due to consumption of OH* during oxidation of soot that is produced at the downstream end of the spray flame and reduction may be even stronger than derived from the image intensity because later in the stroke less soot is present causing lower signal attenuation. From 3.6°aTDC onwards the external border of the ring shaped OH* cloud (closer to cylinder wall) changes its structure after the impingement of spray flame on to the walls of the combustion chamber. This change is mainly due to the vortex roll-up and movement of the soot clouds towards the centre. The regions where the soot clouds are transported back towards the centre, from the tip of the spray flame, is indicated by arrows in Fig. 6.12. In regions where OH* cloud appears to shift slightly towards the central part of the combustion chamber correlates well with the soot luminosity images presented in Fig. 6.4. Later in the expansion stroke, after 9.36° aTDC the intensity of OH* emission decreases. Figure 6.13 shows the images of OH* chemiluminescence acquired for double injection strategy. During the early stages of combustion from 2.16° to 4.32°aTDC, the OH* radicals are observed to form along the jet. For this injection strategy higher in-cylinder temperatures were observed, this may also cause the reactions to occur earlier. For later crank angles OH* radicals are not that uniformly distributed and this could be the effect of strong spray to spray ignition and combustion fluctuations discussed in earlier sections.

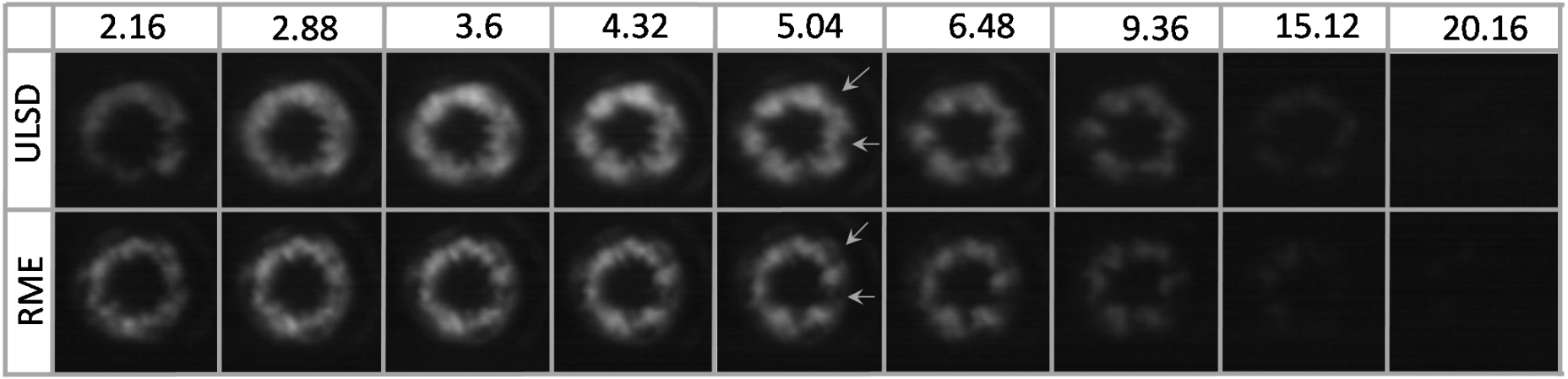

Figure 6.12. Single shot sequence of OH* chemiluminescence spatial distribution recorded for single injection strategy for ULSD and RME.

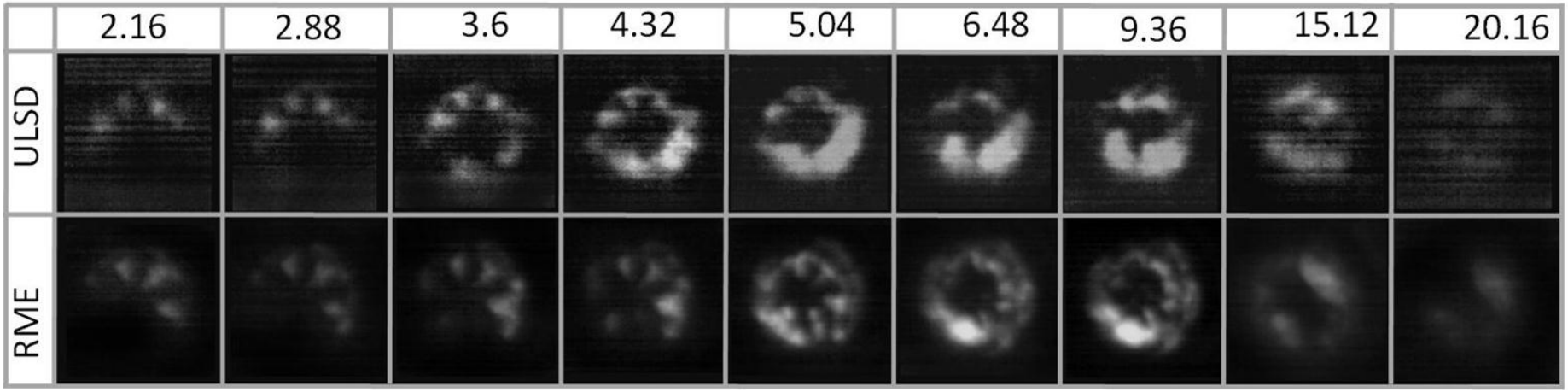

Figure 6.13. Single shot sequence of OH* chemiluminescence spatial distribution recorded for double injection strategy for ULSD and RME.

Obtained results reveal that the OH* emission generally appeared to be closer to the nozzle than the soot emission for the single injection strategy and they were more uniformly distributed compared to soot (especially for initial crank angles). For the case of double injection strategy the in-cylinder temperatures were higher due to the initiation of reactions after the first injection. Higher in-cylinder temperature leads to formation of more OH* radicals and higher soot emissions. Moreover soot will utilise OH* radicals for their oxidation, which can result in low level of observed OH* intensity. In order to compare the amount of OH* radicals during combustion of these two fuels, the OH* chemiluminescence images were spatially integrated and their results are presented in the following section.

6.3.2.5. Spatially integrated OH* chemiluminescence and soot luminosity signals

Figures 6.14 and 6.15 show spatially integrated intensities of OH* chemiluminescence and soot natural luminosity (corrected and normalised) for both ULSD and RME fuels, under single and double injection strategies.

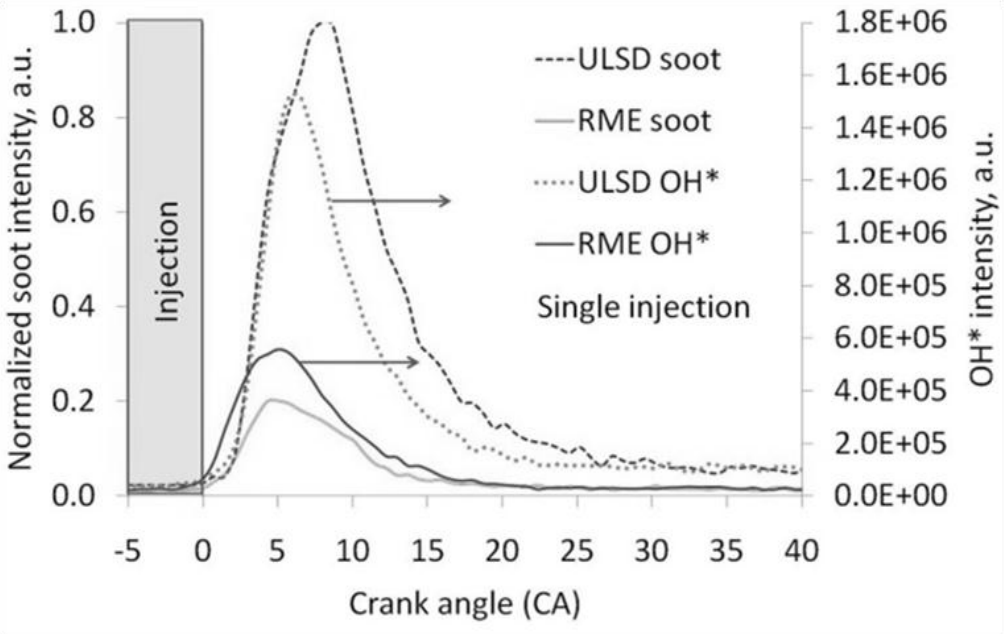

Figure 6.14. Averaged and normalized soot luminosity and raw averaged signals of OH* chemiluminescence measured for ULSD and RME for the case of single injection strategy. Grey area shows the occurrence of injection.

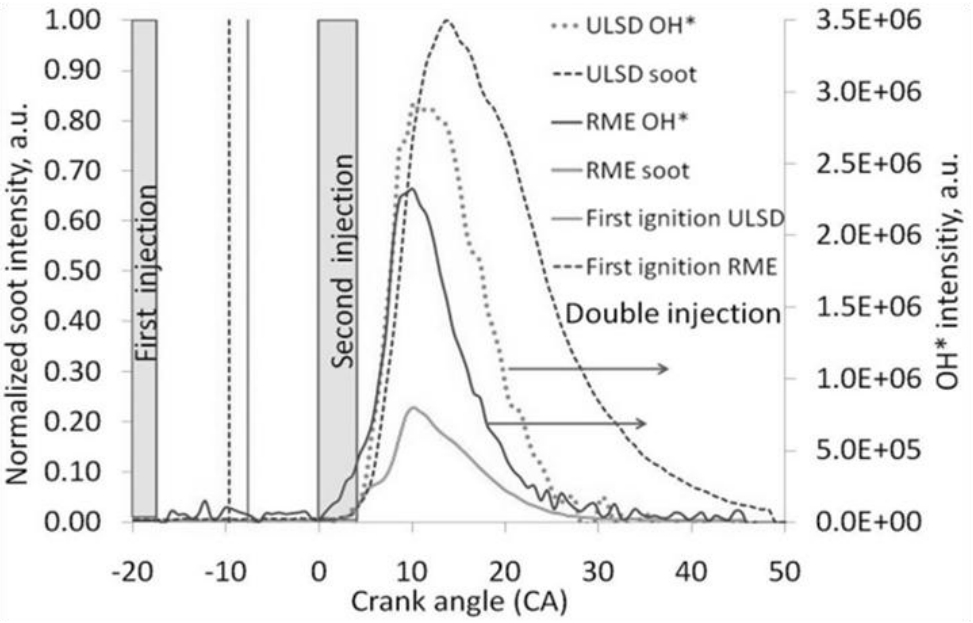

Figure 6.15. Averaged and normalized soot luminosity and raw averaged signals of OH* chemiluminescence measured for ULSD and RME for the case of double injection strategy. Grey areas indicate on injection and vertical lines show first detected ignition.

Highlighted area indicates injection events and the vertical lines, in case of double injection, show the time at which first ignition sites were detected during 2D image analysis. For the single injection strategy, it can be seen from OH* chemiluminescence and soot luminosity measurements, ignition starts earlier for RME compared to that of ULSD. These in-cylinder observations are confirming the results obtained from the in-cylinder pressure data. For the case of single injection, the incandescence intensity of ULSD was observed to peak at 8°aTDC, while for RME it peaks earlier at about 5°aTDC. The peak intensity of soot incandescence for RME was approximately 20% of ULSD. The in-cylinder soot formation rate for RME fuel was significantly reduced, and this indicates that a selection of fuel with higher oxygen content can have considerable impact on the production of in-cylinder soot. The peak intensity of OH* chemiluminescence for RME was approximately three times lower than that of ULSD. This may indicate that the in-cylinder temperatures during combustion of RME are lower compared to that of diesel and this lowers soot formation rate for RME. A high combustion temperature which may be produced by the ULSD fuel enhances the reaction kinetics, and this favours the production of soot and subsequent soot oxidation process. Intensity of soot incandescence for ULSD under double injection strategy was observed to peak at 14°aTDC, and for RME the peak was observed at 10°aTDC. The peak intensity of soot incandescence for RME was approximately 23% of the peak intensity of ULSD and the peak intensity of OH* chemiluminescence for RME was lower than that of ULSD. This

indicates that the in-cylinder combustion temperatures for ULSD are higher compared to that of RME. As previously stated, high temperature enhances the reaction kinetics favouring soot formation in ULSD fuel. Higher in-cylinder temperature also improves soot oxidation process but the lack of oxygen content in ULSD fuel leads to incomplete oxidation of soot. This results in higher amount of un-oxidised soot at the end of the combustion process. In case of RME fuel, low OH* chemiluminescence intensity compared to ULSD leads to relatively lower combustion temperatures and reduced soot formation for RME when compared to ULSD. The presence of oxygen content in fuel improves soot oxidation process for RME fuel, thus the combustion of ULSD leads to higher soot emissions compared to RME. Additionally the soot formed during the combustion of bio-diesels are easier to oxidise than the soot produced from regular diesel, a similar observations have been reported in [126].

6.3.3. Planar laser induced incandescence (PLII)

This section presents results obtained from PLII measurements. The main goal of these measurements was to compare how much soot was left in the combustion chamber after the end of luminous combustion and how soot clouds are distributed for RME and ULSD fuels.
The laser sheet was allowed to pass through the top section of combustion chamber to heat up soot particles that are left in the combustion chamber after the end of visible luminous combustion process. The incandescence from heated soot particles is detected by an ICCD camera through the piston window. Single shot, PLII images of relative soot volume fraction measured at different crank angles during the combustion of ULSD and RME fuels are shown respectively in Figure 6.16 A and B for single injection strategy.

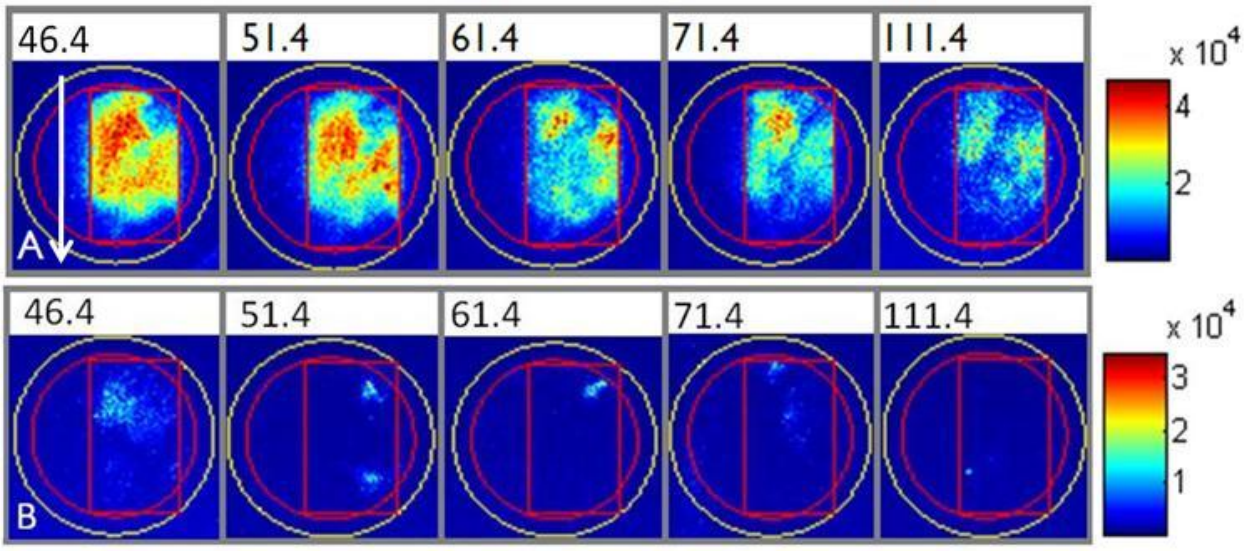

Figure 6.16. Single shot PLLI images recorded for subsequent detection crank angles (number at the top of the image) for single injection at 5ºbTDC, for A) ULSD and B) RME.

The position of the laser sheet is indicated by the red rectangle and laser is directed as indicated by the white arrow. Soot clouds present between the laser beam and the detection system may attenuate the incandescence signal. It is difficult to estimate how strong the influence of attenuation is, but the data are presented here to qualitatively understand the differences in soot processes between RME and ULSD. To minimise and to avoid piston window attenuation, window was cleaned after every engine run. The engine was operated in skip-firing mode that as well reduced the deposit of soot on piston window. Measured incandescence intensities are proportional to soot volume fraction (SVF). Images presented here provide information regarding soot present in a 3 mm thick plane across the combustion chamber. The spatial distribution of soot for the first detection crank angle of 46.4°aTDC are more uniform throughout the combustion chamber when compared to soot distribution at later crank angles. Formed soot had sufficient time to mix with ambient gases and is visible at the extremity as well as the centre of combustion chamber. The incandescence signal decreases with crank angle and it is mainly attributed to on-going soot oxidation process. In addition to this, the cylinder volume increases during expansion stroke and the soot is distributed into larger volume of the combustion chamber. In-cylinder fluid dynamics may also cause random soot transport within the combustion chamber. At later crank angles the soot distribution was sporadic in the measurements plane and this appears locally as high or low soot concentration. Looking at Fig. 6.16 and Fig. 6.17, it can be seen that for both injection strategies high levels of soot were observed for ULSD fuel in the measurement plane, being un-oxidised soot that is left after the end of luminous combustion. In Fig. 6.16 B it is clearly evident that negligible amount of soot was left after the end of luminous combustion for RME fuel for the case of single injection strategy. Low levels of soot formed during combustion of RME even led to difficulties in detecting soot incandescence. Considering the case of double injection for RME fuel (see Fig. 6.17) soot clouds were randomly distributed for the measured crank angles when compared to ULSD.

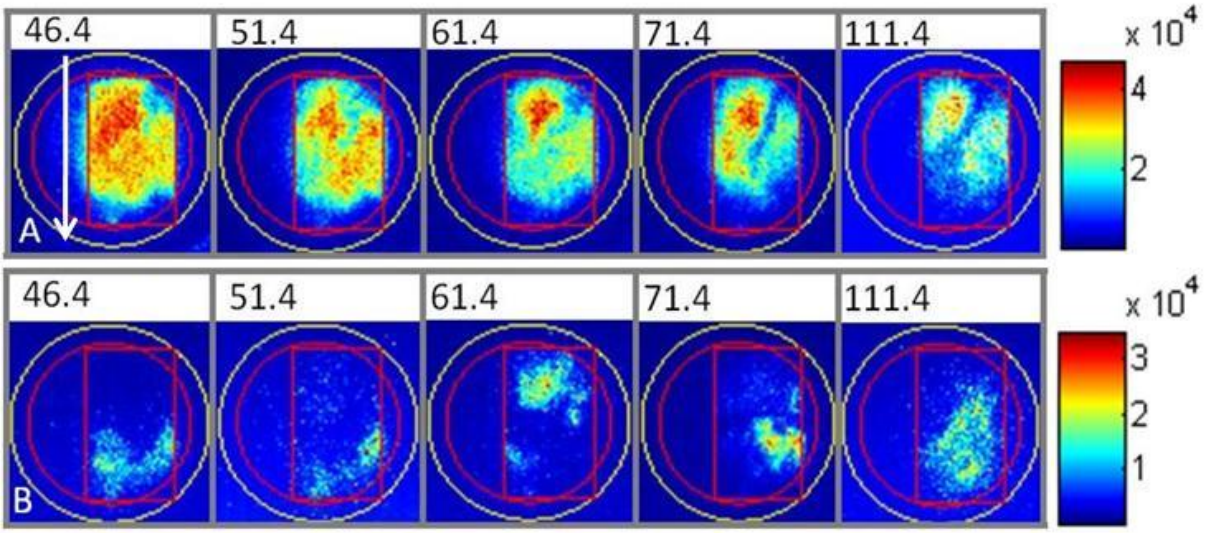

Figure 6.17. Single shot PLII images recorded for subsequent crank angles (numbers at the top of the image) for double injection, A) ULSD and B) RME.

The amount of soot emitted under double injection strategy for RME fuel was much lower than that of ULSD. Despite very weak signal, fluctuations in soot intensities were observed for RME under double injection strategy. In many cases no signal was recorded, while for some images high soot concentrations were observed locally and these shot to shot fluctuations are mainly due to in-cylinder fluid dynamics and random soot distribution within the combustion chamber. It is evident that irrespective of injection strategy, RME was producing significantly lower amount of soot compared to ULSD right from the point where the high temperature luminous combustion ends. The trend of the measured soot concentration at different crank angles for both fuels and strategies is represented in Fig. 6.18, this was obtained by taking average values of spatially integrated soot intensities detected in the probed region.

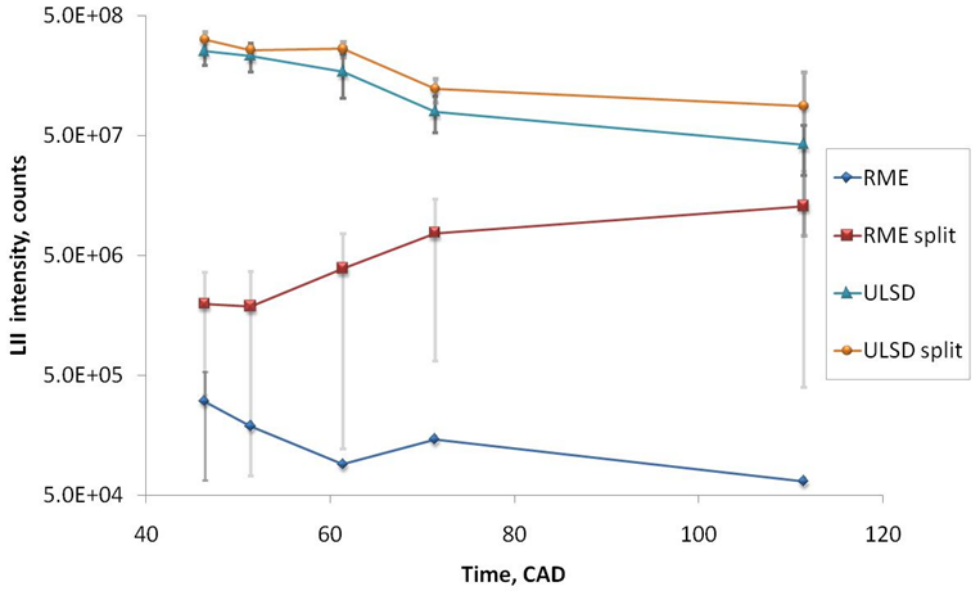

Figure 6.18. Spatially integrated PLII intensities recorded for following detection crank angle for RME and ULSD, for single and split injection. Solid points indicate on average value and error bars correspond to standard deviation.

The error bar indicates standard deviation. For all cases soot intensities detected for ULSD were greater than that for RME. Hardly any signals were recorded for RME in case of single injection suggesting that soot that is formed under these operating conditions are well oxidized. As mentioned earlier, greater LoL observed for RME caused more air entrainment. This effect is complemented by the presence of higher oxygen in fuel which resulted in better mixing and soot oxidation. All of these factors results in a relatively less amount of un-oxidised soot left in the combustion chamber after the end of luminous combustion for RME compared to that of ULSD.

6.3.4. Time-resolved laser induced incandescence (TR-LII)

In this section analysis of soot remaining in combustion chamber after the end of luminous combustion continues. The main purpose of these measurements was to look into the primary particle size and its distribution after combustion of both fuels.

TR-LII measurements were carried out in conjunction with PLII to measure simultaneously soot particle size, their size distribution and relative soot volume fraction for RME and ULSD. TR-LII measurements are point measurements were the incandescence from laser heated soot particles were recorded by two PMTs. The measured decay of soot incandescence contains information regarding soot particle sizes, size distribution, soot temperature and soot volume fraction. In order to extract particle size information from the measured LII data, theoretical modelling of TR-LII signal is essential. The LII model is based on the energy and

mass balance of soot particle when it is irradiated by a high energy laser beam. The soot particles absorbs energy from the short pulsed high energy laser beam and reaches temperatures of approximately 4000 K. Heated soot particles exchange heat with surrounding gas through the mechanism of conduction, sublimation, radiation and several other processes like annealing and oxidation. The heated soot particles exchange heat with surrounding gases and reaches ambient temperature. Under high pressure diesel engine environment, conduction was found to be a dominant mechanism of heat exchange between soot particles and the surrounding gas. In the current study, the mathematical model of TR-LII is based on the formulations used in [49, 127] The experimentally measured LII data and the theoretically derived LII signals were compared using the least square fitting procedure to get the count median diameter (called particle diameter in this work) and the distribution width. Details about the application of TR-LII measurements in optical diesel engines and data analysis are presented in [127].

6.3.4.1. Count median diameter

Figure 6.19 shows average values of count median diameter (CMD) calculated from the measured time resolved incandescence data for both fuels. Since these measurements are point measurements they may not represent the global picture of events that are occurring at that measurement crank angle.

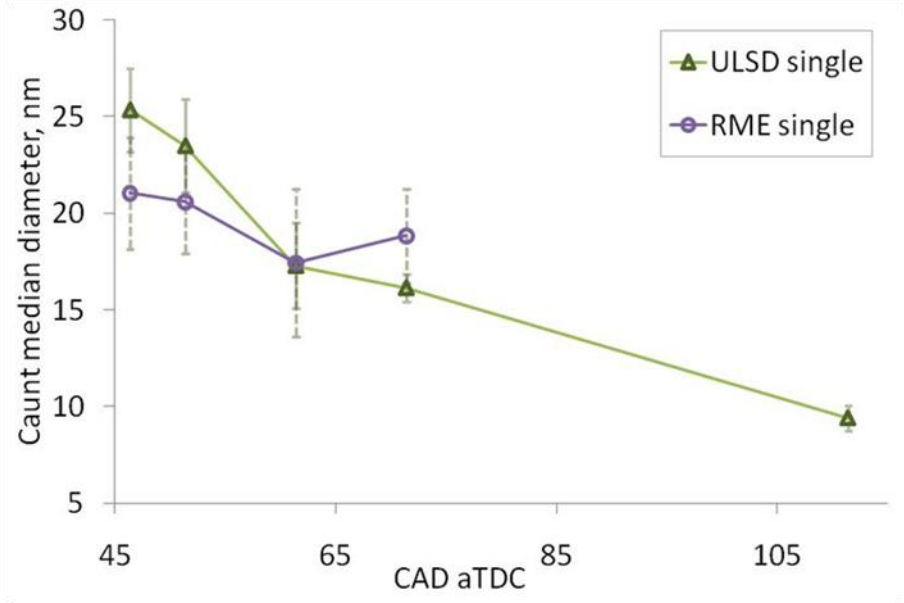

Figure 6.19. Averaged count median diameter calculated for single injection at 5°bTDC, for ULSD and RME.

A general trend of particle size decreasing with crank angle was observed for both fuels. For ULSD, the average soot particle size at 46.4°aTDC was approximately 25.3 nm, and the average size decreased with crank angle to approximately 9.4 nm at 111.4°aTDC. For the case of RME, slightly smaller average soot particle size of approximately 21.4 nm was observed at 46.4°aTDC, which decreased in size up to 51.4°aTDC and increased marginally to 18.8 nm at 71.4°aTDC. It was not possible to acquire TR-LII data for late in the expansion stroke for RME, suggesting that negligible amount of soot was present in the cylinder beyond this condition. In summary, the trends of the average values of soot particles are similar for both fuels. Slightly smaller particles were observed for RME but these differences are still within the fluctuation range. Figure 6.20 shows average values of count median diameter obtained for ULSD and RME when operated under double injection strategy and the error bars represent standard deviation.

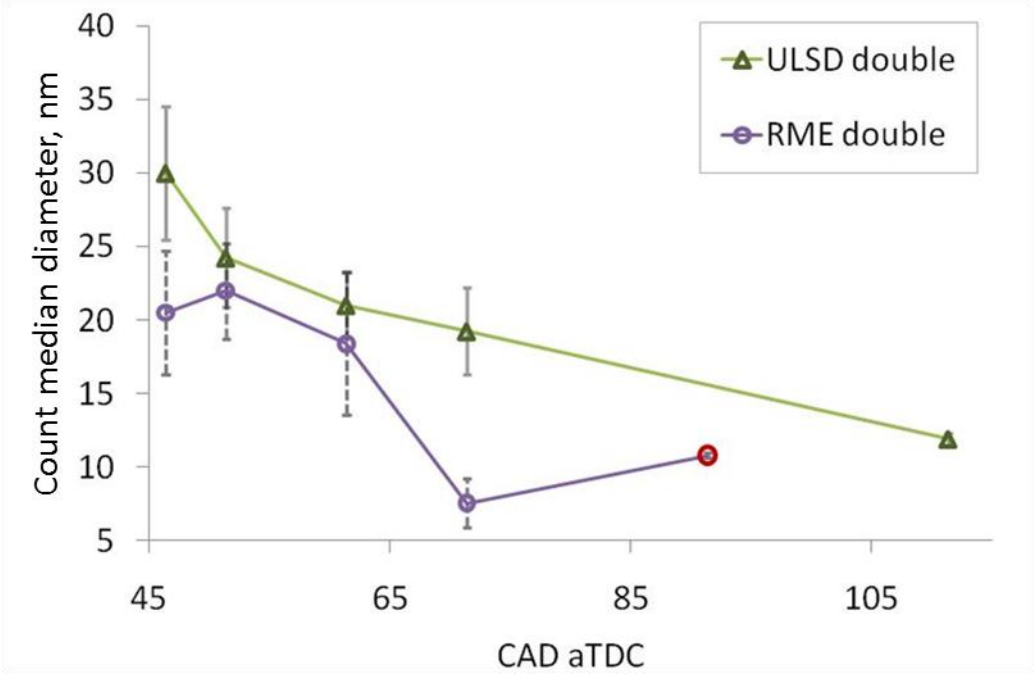

Figure 6.20. Averaged count median diameter calculated for double injection (first injection at 20°bTDC, main injection at TDC), for ULSD and RME.

A general trend of soot particle decreasing with crank angle was observed for both fuels under this injection strategy. Relatively larger size particles were observed for ULSD, the size decreased from 30 nm at 46.4°aTDC to approximately 19.2 nm at 111.4°aTDC. For RME, soot particles of approximately 20 nm and 22 nm were observed at 46.4°aTDC and 51.4°aTDC, the particle size eventually decreases to 7.5 nm at 71.4° aTDC. Since very low level of soot are left within the combustion chamber at later crank angles for RME, only few

incandescence signals were collected at 111.4° aTDC. Data presented at this crank angle for RME are based on two measurements only and the average diameter derived of these two readings is 10.8 nm. Those LII signals with low signal to noise ratio were not considered for data analysis.

6.3.4.2. Distribution width

Figures 6.21- 6.24 show the average value of geometric size distribution width obtained from measured soot particle sizes for both fuels under single and double injection strategy.

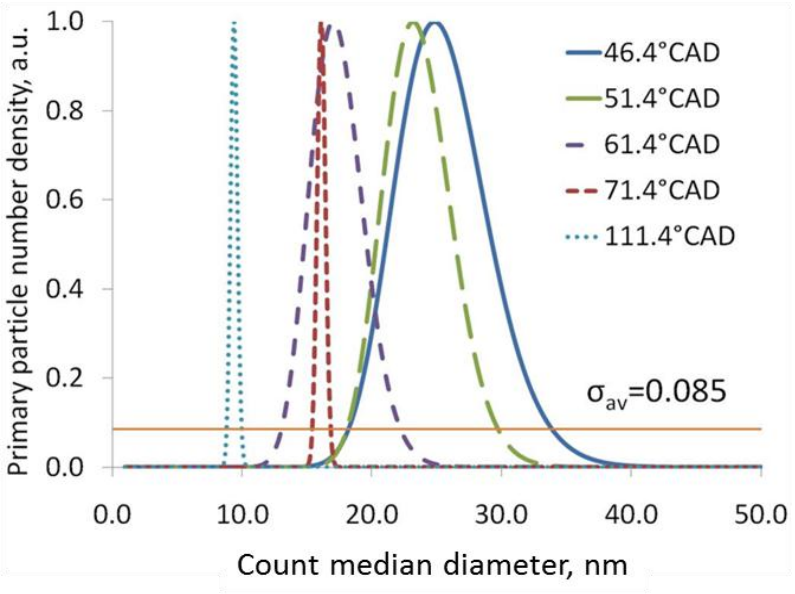

Figure 6.21. Average geometric distribution width recorded for ULSD, single injection.

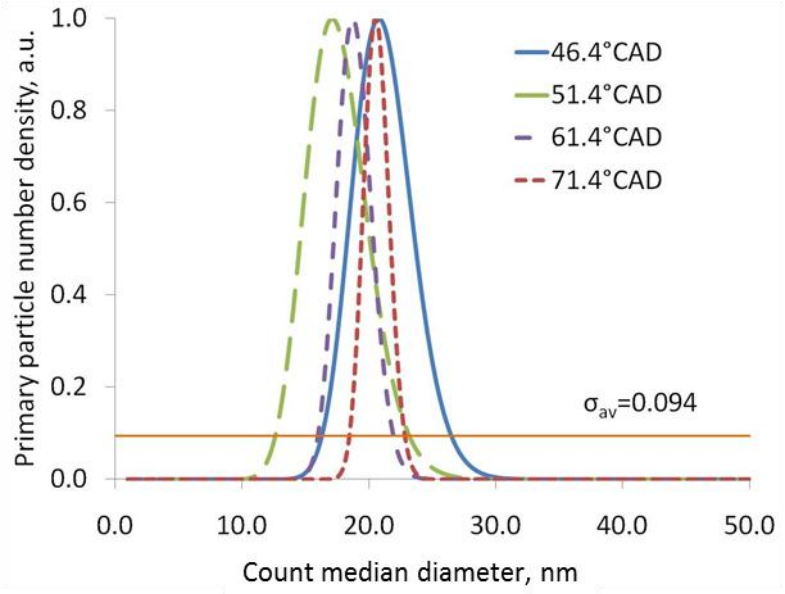

Figure 6.22. Average geometric distribution width recorded for RME, single injection.

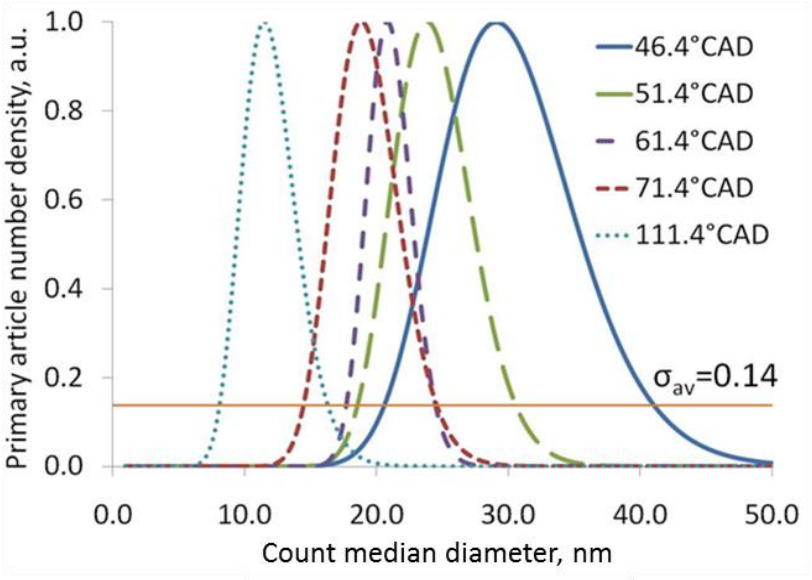

Figure 6.23. Average geometric distribution width recorded for ULSD, split injection.

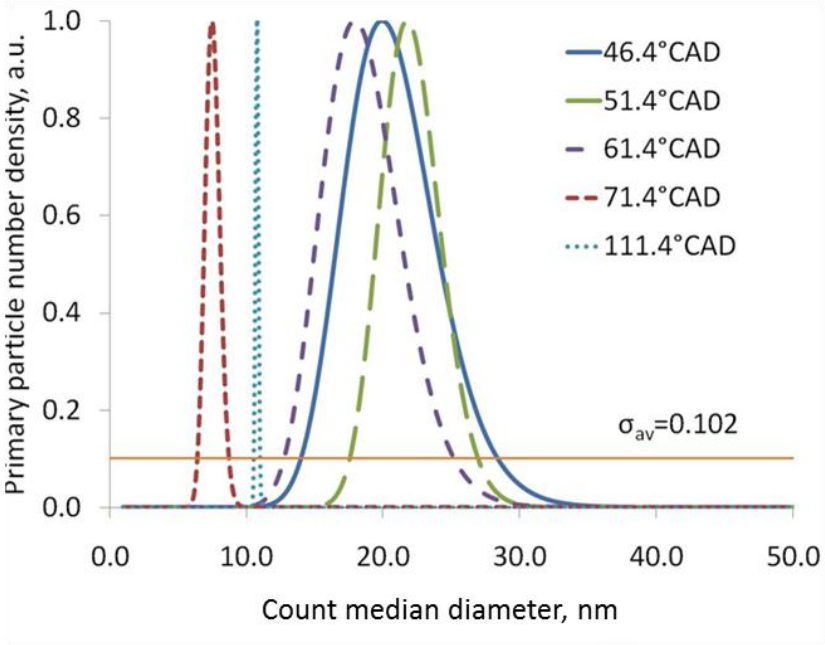

Figure 6.24. Average geometric distribution width recorded for ULSD, split injection.

Horizontal lines show average in-cylinder particle size distribution over all measured crank angles for each fuel and injection strategy. For ULSD when operated under single injection, in-cylinder particles size distribution widths are approximately in the range 0.14 – 0.11 at 46.4° aTDC and 51.4°aTDC. The size distribution width then decreased with crank angles and reached nearly a monodisperse distribution at 111.4°aTDC. In case of RME under the single injection strategy the particle size distribution decreased initially from 0.11 at 46.4°aTDC to 0.05 at 51.4°aTDC, beyond this crank angle the particle size distribution increased slightly and reached a magnitude of 0.14 at 61.4°aTDC and then decreased to approximately 0.07 at

71.4°aTDC. No clear trend can be observed for in-cylinder size distribution. Moreover as already mentioned these data are based on single point LII measurements.

For the case of double injection, the in-cylinder particle size distribution width for ULSD under most of the measured crank angles are in the range 0.17 – 0.18, however at 61.4°aTDC a minimum size distribution of 0.08 was observed. Similarly, RME also show a similar distribution width ranging from 0.10 – 0.17 for most of the measured crank angle, except for 71.4°aTDC where narrow distribution of 0.07 was observed. As previously mentioned, limited number of measurements was carried out at 111.4°aTDC and the distribution width under this condition was nearly monodisperse.

The measurements and analysis reveal that the average value of in-cylinder soot particle size distribution over all the measured crank angles are similar for ULSD and RME for the case of single injection. For the case of double injection strategy the average value of in-cylinder soot particle size distribution over all the measured crank angles for ULSD is slightly larger compared to RME. The effect of fuel on the size distribution is inconclusive. However, it can be seen that the average in-cylinder soot particle size distribution increased with the load. Thus it can be said that the average in-cylinder soot particle size distribution may be more related to equivalence ratio of the mixture than the fuel itself.

6.4. Conclusions

In-cylinder combustion and soot processes for ULSD and RME fuels were investigated in an optically accessible high speed direct injection diesel engine using high speed imaging, PLII and TR-LII measurement techniques under single and double injection strategies. The main findings of this investigation are summarised as follows:

- The magnitudes of FLoL and SLoL for RME are larger when compared to ULSD. Longer lift off length is an indication of larger entrainment of air upstream of flame lift off length. This leads to lower soot formation and improved soot oxidation for RME when compared to ULSD.
- The image analysis revealed that the early phase of combustion proceeds quicker for RME when compared to ULSD due to oxygen enrichment of the reactive mixture and it is visible in areas occupied by the flame during combustion. As a results faster combustion for RME is observed and on the contrary more of a slugish mixing controlled combustion for ULSD.
- ID determined from OH* chemiluminescence, soot luminosity and in-cylinder pressure revealed that for all cases RME has shorter ID compared to ULSD.

- Spatially integrated soot luminosity and OH* chemiluminescence images show that the crank angle resolved intensity of soot emissions as well as OH* radicals emitted during combustion of RME are lower compared to ULSD.
- PLII images confirmed that the amount of un-oxidised soot left in the cylinder after the end of visible luminous combustion is less for RME compared to ULSD.
- TR-LII results showed that RME generates soot of relatively smaller size compared to ULSD.

7. Chapter 7 - Soot luminosity and OH* chemiluminosence emission during combustion of fuels of different composition in diesel engine

7.1. Introduction

The soot, next to the NO_x is one of the most unwanted combustion products in diesel engines. The soot particulates are generated in fuel rich region from unburned fuel which due to the high temperature is pyrolised. As a result of termochemical decomposition of material, a number of molecules are formed, between them acetylenes which are identified as first precursors of soot. It is believed that soot evolves from acetylenes which are initially forming aromatic rings and eventually poliaromatic hydrocarbons (PAH). Due to the process of nucleation PAH form nuclei. Subsequently, nuclei owing to the surface growth are forming larger, primary particles, which may collide, join together and create complex structures called aggregates. Detailed description on soot formation stages is presented in section 2.2.2.2. The soot formation in diesel engine is constantly competing with soot oxidation and speed of these two processes is responsible for soot emission. Nowadays soot emissions are strictly regulated by Euro 5 and Euro 6 legislations. Fulfilment of regulations is possible by application of numerous strategies for soot reduction. Currently diesel particulate filters are widely applied [128, 129, 130, 131], however aftertreatment systems are costly. Significant work has been completed to optimize the emissions from engine. New injection strategies for improving air-mixture generation resulting in more efficient oxidation of soot are applied. High injection pressures are used together with exhaust gas recirculation (EGR) aiming in reduction of both NO_x and soot [132].

In recent years, increase in the price of oil raised interest in alternative fuels, fuels of modified composition and fuels with different additives. These fuels gained attention because of the concerns regarding greenhouse gases emissions. Another route, parallel to petroleum based fuels, are synthetic fuels. Introduced in 1925 Fisher-Tropsch synthesis was used to generate synthetic gas, from coal or natural gas, which subsequently was used for hydrocarbons production and finally was refined to diesel or gasoline fuel [9]. Synthetic fuel can be produced as well in process of gasification or hydro-cracking. Fuel obtained as a result of these processes is free of sulphur and aromatics and currently the most popular is gas-to-liquid (GTL) [125, 9]. This fuel gives possibility of simultaneous reduction of NO_x and soot

emissions especially for lower engine loads as it was reported in [125]. Unfortunately costly production of synthetic fuels has limited the use of these fuels to blends.

In current work fuel composition including (aromatics content and oxygen content) and fuel properties like cetane number will be analysed with respect to soot emission. A number of investigations considering influence of fuel composition on soot emission in diesel engines was conducted [31, 133, 134, 135]. In [136] it was suggested that oxidation of soot generated from higher aromatic fuels is easier. Soot oxidation can be improved as well by increasing local oxygen content in combustion chamber. This approach may be achieved by combining oxygenates agents with fuel. So far, different types of oxygenated hydrocarbons were analysed [137], showing that each of them improve exhaust soot emission [138, 9, 137, 139, 140]. Increase in fuel oxygen content to 30 wt% result in significant reduction in smoke emission. It was reported as well in [140] that not only oxygen content affect soot emission from diesel engine but as well chemical structure of oxygenates.

CN influences formation of in-cylinder air-fuel vapour mixture, combustion process and emissions. A high cetane number improves ignition and reduces emission of unburned species leading to higher in-cylinder temperatures. CN may also result in the smoother running of the engine. However, prompt ignition causes rich air-fuel mixture formation and this may lead to enhanced soot generation. Increase in ignition delay provides longer time for premixing fuel with air and local oxygen concentration in this mixture is higher, [31].

An oxidation characteristic of soot is related to its soot emission and may be modified by the change in fuel configuration, as it was reported in literature [80, 136, 141, 142]. Investigations aiming at the production of higher efficiency fuel, generating low emissions are gaining recently interest. In current study optical diagnostic techniques were applied for six fuels of different cetane number, aromatics and oxygen content. The main aim was to investigate how fuel composition influences in-cylinder soot emissions and relate the soot emitted during combustion with that remaining in chamber after the end of luminous combustion.

A high speed imaging technique was used to detect both OH* chemiluminescence and natural soot luminosity simultaneously, to study the soot formation and oxidation during the combustion process within the cylinder. Planar laser induced incandescence (PLII) was applied later in the stroke to study relative amount of un-oxidised soot that was left in the cylinder after the end of luminous combustion for these fuels. Experiments were carried out for single and double injection strategies. Acquired high speed images were used for determining the flame lift-off length (FLoL), area occupied by flame, ignition delay (ID), soot

and OH* chemiluminescence emitted during combustion of fuels. Spatially integrated data from the high speed soot luminosity images have shown that correlation between oxygen level in fuel and formed soot exists. Subsequently, a link between aromatics content in fuel and peak soot luminosity was studied. The flame lift off length (FLoL) and the distance at which first soot luminosity (SLoL) occurs were compared between fuels. Longer FLoL initially was measured for fuels containing aromatics and fuel containing higher levels of oxygen. Level of soot remaining in combustion chamber after the end of luminous combustion was measured using PLII technique. Similar trends of lower soot level for fuels with aromatics content and fuel with higher oxygen content were observed.

7.2. Experimental set-up

Experimental test facility presented in Fig.7.1 is composed of engine, laser and detection system.

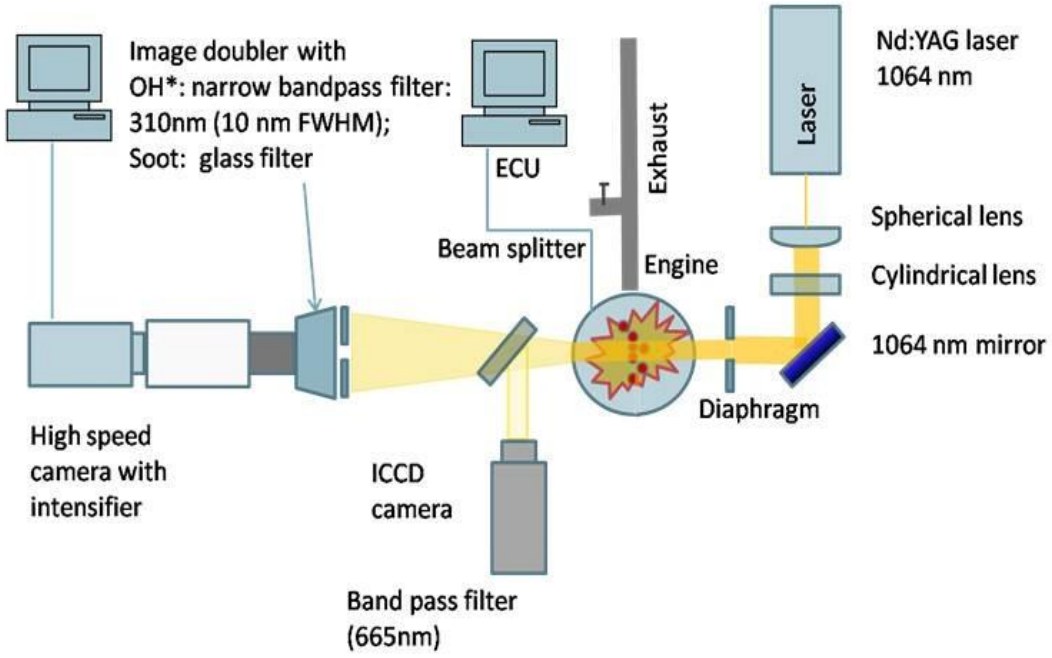

Figure 7.1. Experimental test facility.

Engine, laser and injector specification are listed in chapter 4 and detection system specifications in section 4.2 with this difference that laser fluence of 0.38 J/cm^2 was used during this test, taking into consideration energy losses on side window, lenses and mirrors. Details regarding laser fluences applied for LII measurements are reported in [127].

Before measurements engine was conditioned as described in section 4.1.6.

For high speed movies experimental set up described in section 4.2.3 was used. The image acquisition was synchronized with engine and triggered externally as explained in section 4.4.

7.3. Fuels

Measurements were done for six fuels with various aromatics, FAME, content of sulphur and cetane number CN. The main specifications of the fuels are presented in Table 7.1.

	CN	FAME, %vol	Calorific value, MJ/kg	Total hydrocarbons, % mass	S, mg/kg
Fuel 1	56.2	6.9	42.825	17.3	7
Fuel 2	44.0	6.8	42.363	37.7	7
Fuel 3	50.3	6.6	42.669	15.8	9
Fuel 4	46.2	6.7	42.154	37	14
Fuel 5	40.0	6.4	41.495	46.4	31
Fuel 6	56.0	28.5	41.233	15.9	8

Table 7.1. Properties of the fuels.

7.4. Results and discussion

7.4.1. In-cylinder pressure analysis

In cylinder pressure data for single and double injection strategy are presented in Figs.7.2 A and B respectively.

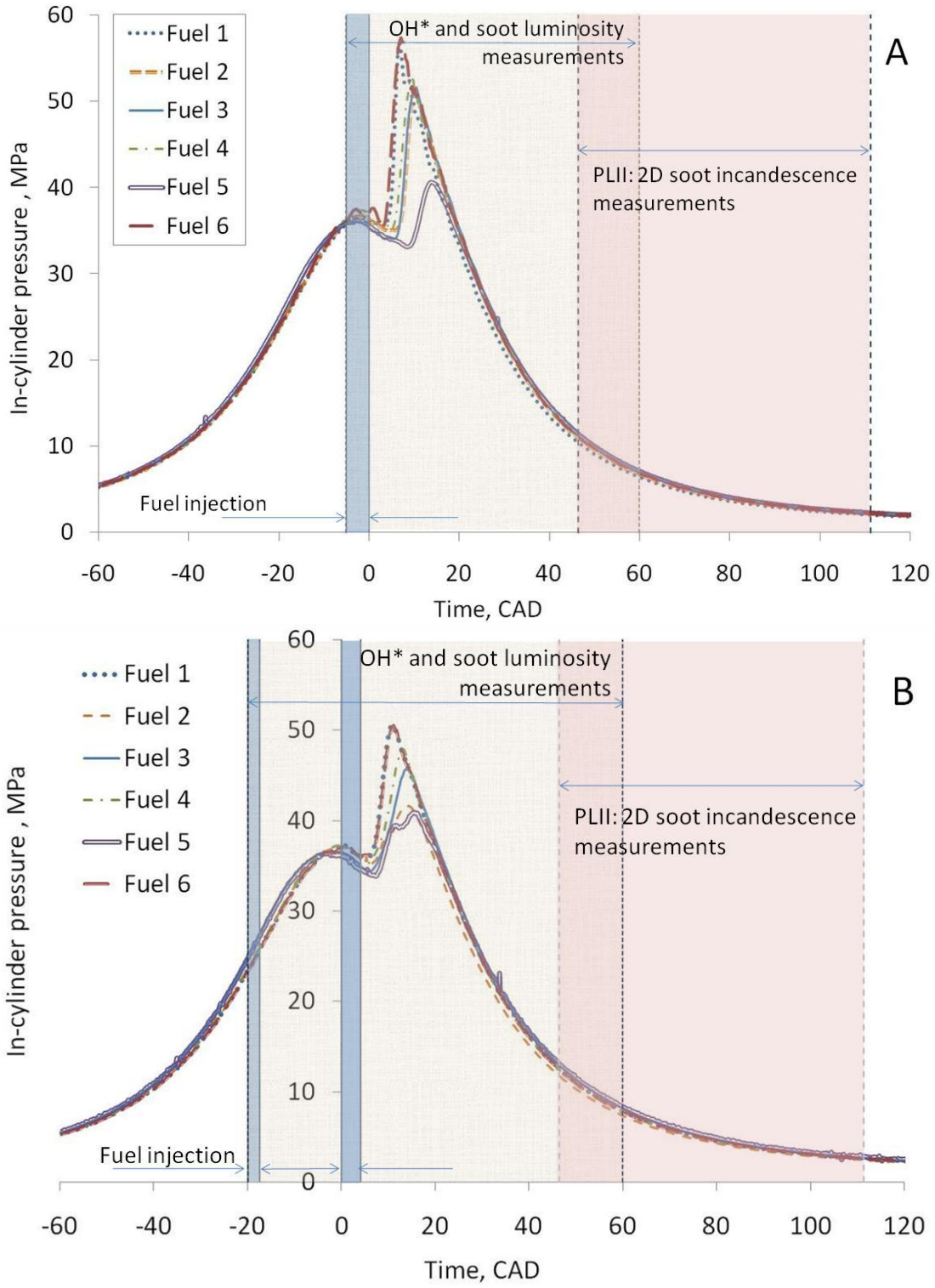

Figure 7.2. In-cylinder pressure recorded for single and double injection strategy with highlighted injection timing: A) for single injection strategy; B) for double injection strategy.

The highlighted areas in Fig. 7.2 indicate fuel injection, time where OH* chemiluminescence and soot luminosity were recorded and subsequently time where PLII readings were taken. Based on in-cylinder pressure IMEP and ID were calculated. The ID was determined by taking the difference in time between the SOC and the command for SOI. The SOC for fuels

was determined as indicated in section 3.1. The IMEP and ignition delays (ID) calculated for considered fuels are listed in Tab. 7.2.

	IMEP single, bar	ID single, CA	IMEP double, bar	ID double, CA
Fuel 1	2.8	7.6	4.0	2.6
Fuel 2	3.1	9.0	3.3	3
Fuel 3	3.4	8.2	4.1	4.4
Fuel 4	3.1	9.6	3.8	4.4
Fuel 5	3.1	12.4	3.8	2.1
Fuel 6	3.1	7.6	3.9	3

Table 7.2. Ignition delay and IMEP for single and double injection strategy based on in-cylinder pressure.

OH* chemiluminosence and soot luminosity were measured using high speed imaging from the start of injection. Later in the expansion stroke after 46.4° aTDC, soot volume fraction was measured using PLII.

For the same quantity of injected fuel, the highest peak in-cylinder pressure was observed for fuel 6 and 1, which as well ignited at the earliest stage (see Tab. 7.2). Subsequently, a slightly lower peak was measured for fuels 2, 3, 4 and the lowest peak was detected for fuel 5. This fuel as well had the longest ignition delay that may be beneficial for air/fuel mixture formation. IMEP recorded for fuels were comparable, slightly higher IMEP was measured for fuel 3.

For double injection strategy lower peak in-cylinder pressures were observed. Similarly, fuel 1 and 6 had the highest peak value followed by fuels 4, 3, 2 and 5. ID and IMEP were comparable for all fuels under this injection strategy (see Tab. 7.2).

7.4.2. Intensity analysis

Soot natural luminosity signal is a combination of incandescence signal from hot soot and chemiluminesence signal from excited gaseous species. Natural luminosity imaging is a valuable tool which may be applied for characterisation of in-cylinder processes like soot formation and oxidation. Soot incandescence as described in section 2.4.1.3 and 6.3.2 and is strongly dependent on soot temperature, its intensity increases with temperature and signal is dominated by radiation from the hottest soot. The luminosity detected by camera depends upon many factors, such as quantum efficiency of the image intensifier, detection system and its gain, adiabatic flame temperature, in-cylinder temperature and optical thickness. All these

factors have to be taken into consideration while evaluating experimental data and all these factors are discusses in section 6.3.2. During current measurements, care was taken to clean optical window regularly in order to avoid window fouling. The degree of natural luminosity signal trapping was not considered during this study. The signal trapping will be affected by soot concentration in combustion chamber and may be different for each fuel. We do not know how strong the influence of attenuation is but it will lead to underestimation of natural soot luminosity signals in combustion chamber.

7.4.2.1. Soot luminosity

Figure 7.3 A and B illustrate specially integrated incandescence signal, averaged over ten movies measured during one engine run for single and double injection strategy.

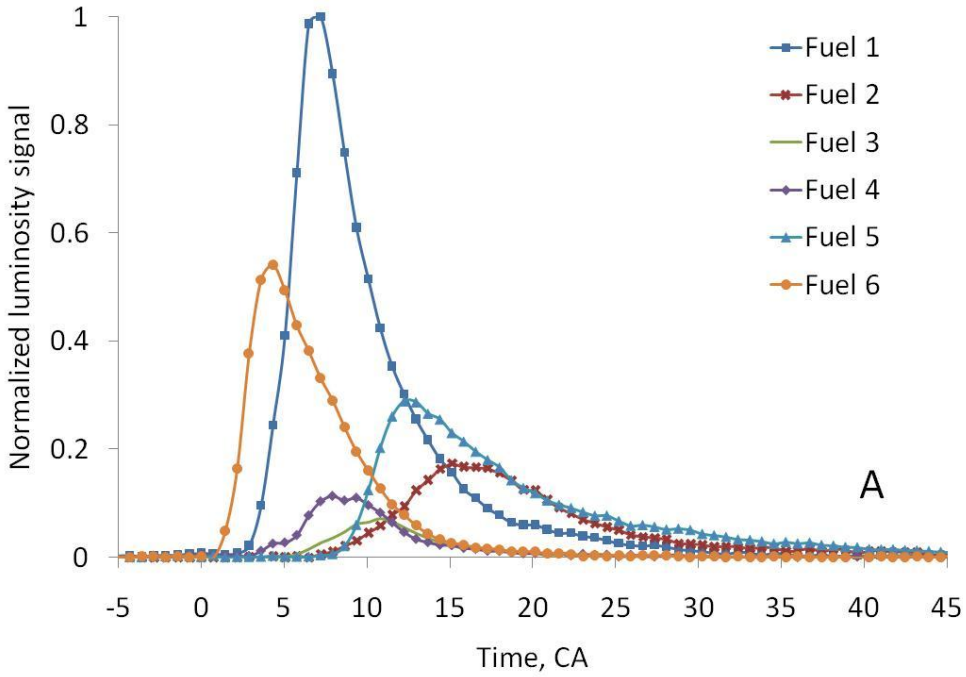

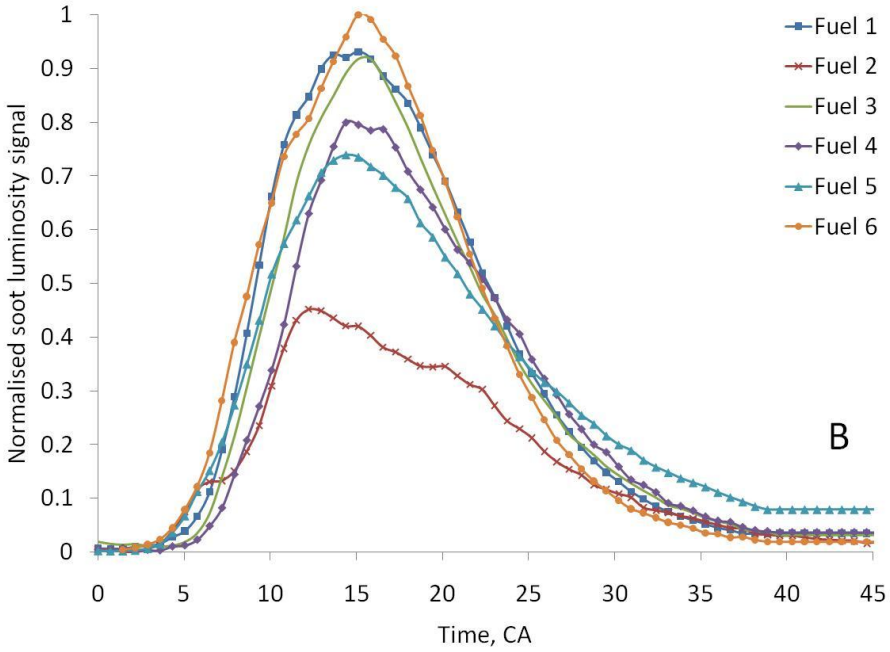

Figure 7.3. Specially integrated natural luminosity signals averaged over ten movies, recorded for single (A) and double (B) injection strategy.

Results for single injection strategy show that fuel 6 and fuel 1, of comparable cetane number (see Tab.7.1) ignite earlier than the rest of fuels. Considering these two fuels, despite very similar cetane numbers, fuel 6 ignites earlier than fuel 1 and this may be probably related to higher FAME content in fuel 6. Measured peak soot luminosity is lower for fuel 6 (approximately 55% of peak soot intensity of fuel 1) when compared to fuel 1 that may directly correspond to lower in-cylinder soot formation. As it was reported in [31, 143], oxygenated fuel may improve oxygen concentration in combustion chamber or may be preventing soot formation since oxygen replaces carbon atoms in fuel. A combination of these two processes is beneficial for soot emission. However, emission observed for single injection strategy may be affected by fuel ignitability (differences in cetane number of the fuel) that lead to differences in ID.

Soot incandescence signal measured for the rest of the fuels is lower, these fuels as well ignite later. The time for air/fuel mixture formation is longer that may lead to improved soot oxidation. The level of soot formed during combustion of fuels 3 and 4 are the lowest and strength of peak signal is approximately 10% of the maximum signal measured for fuel 1. It is quite difficult to define what exactly causes lower soot emission for these fuels. Fuels 2 and 4 have similar properties: cetane number and total aromatic content. Fuel 4 has slightly higher cetane number that may cause earlier ignition of this fuel. During combustion of fuel 5 and fuel 2 higher amount of soot were formed (approximately 15 – 30% of peak soot intensity

measured for fuel 1). This may be related to molecular structure of fuel components and aromatics content.

For double injection strategy combustion phasing is comparable and therefore it is possible to investigate effects of fuel composition. To study the impact of aromatics content on in-cylinder soot formation, maximum soot intensity was plotted against total aromatics content and is presented in Fig. 7.4.

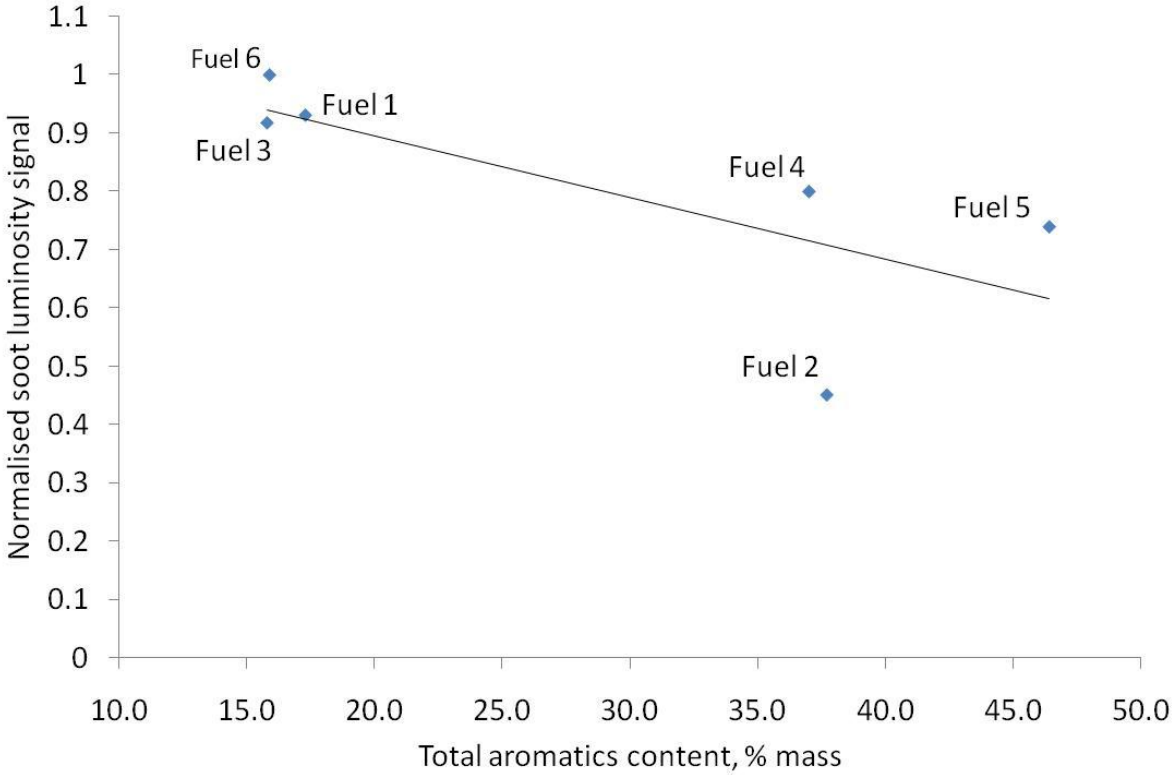

Figure 7.4. Aromatics content versus peak soot luminosity measured for double injection strategy.

As it is visible higher quantities of soot are formed during combustion of fuels with low aromatic content. About 20% to 30% less soot is formed during combustion of fuel containing doubled quantity of aromatics. We would expect that cetane number would also affect ignition delay as it was visible for single injection strategy (see Tab. 7.2, Fig. 7.3A), but in case of double injection ID is similar for all fuels. We may conclude therefore that results show the influence of aromatic content on soot emission. Similar results were presented in [136] where it was reported that morphology of soot formed during combustion of fuel with high aromatics content is less crystalline and easier to oxidize.

7.4.2.2. OH* chemiluminescence

OH* chemiluminescence represent radiation from excited molecules and is a component of soot natural luminosity. Radicals are created during reaction and are interpreted as indicator of high temperature reactions, which are initiated at certain temperature level. Formed radical is quickly consumed mainly during soot oxidation. OH* radicals are discussed in details in section 2.4.

Figure 7.5 A and B illustrate OH* chemiluminescence intensities recorded for single and double injection strategy for all measured fuels.

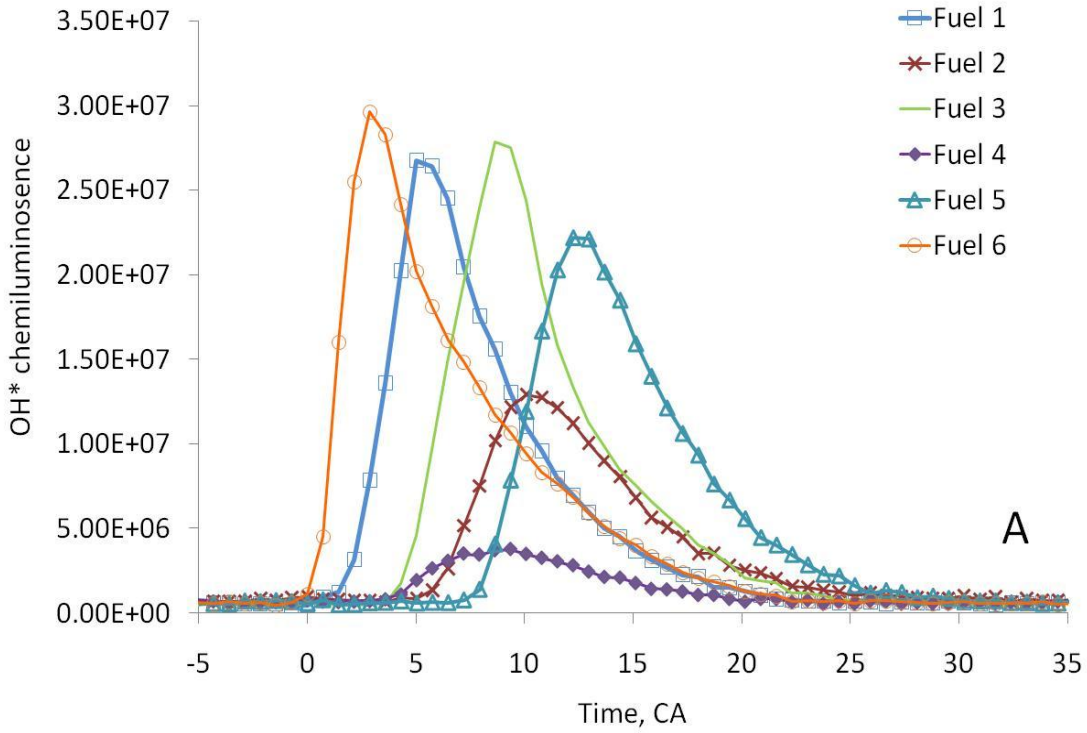

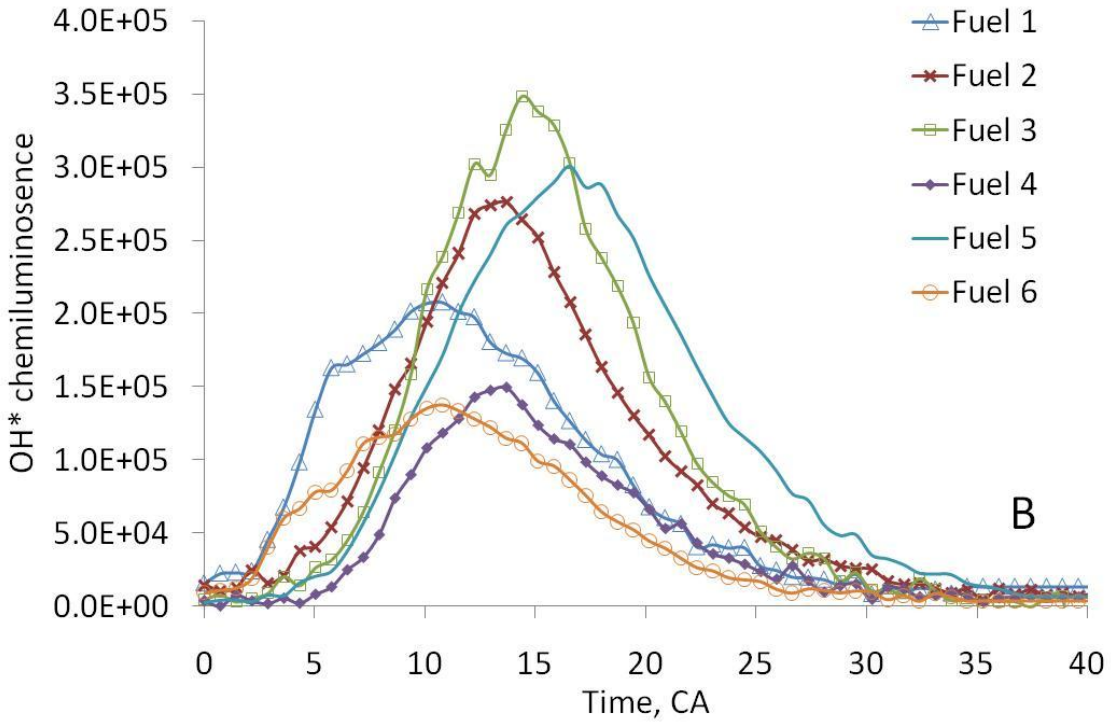

Figure 7.5. Spatially integrated OH* chemiluminescence measured for A) single and B) double injection strategy.

Clouds of OH* radicals tend to appear just before soot luminosity is visible indicating occurrence of initial chemical reactions. For single injection strategy the earliest appearance of OH* is recorded for fuel 6 and it is visible just before TDC. Similarly, chemiluminescence for fuel 1 appears second and this indicates relation between ignition delay and cetane number. The difference in peak OH* chemiluminescence intensity observed for these two fuels is not large. Subsequently, reactions for rest of the fuels start. High peak of OH* chemiluminescence was observed as well for fuel 3 but it was comparable to fuel 1 and 6. The peak intensity tends to decrease while fuel ignition occurs later in the expansion stroke and peak intensity for rest of the fuels is significantly lower. The lowest peak intensity was measured for fuel 4 despite the fact that this fuel ignites quite early and its composition is similar to fuel 2. It is not easy to assess if at this point aromatics present in fuel influence the combustion process. However, it is evident that aromatics content is related to CN. As it was visible during combustion of fuels with low aromatics content ignition occurred earlier and measured OH* chemiluminescence level for these fuels was higher. Fuels 2, 4 and 5 ignite later in the stroke and these fuels contain aromatics. Considering peak OH* chemiluminescence for these three fuels, peak intensity increases with aromatic content indicating that fuels with higher aromatics tend to produce greater quantities of OH* radicals.

As mentioned previously, for double injection strategy the differences in ignition delays between fuels are not that large suggesting that combustion will occur in similar phase. OH* radicals for this strategy appear as well slightly before first appearance of soot. The highest OH* radicals peak intensity was measured for fuel 3, 5 and 2. Fuels 1, 4 and 6 had lower peak level of radicals. For this injection strategy ignition delay effects (cetane number effects) should not be reflected that significantly in combustion characteristics and fuel composition effects should be more visible. Taking into consideration fuels with low aromatics content, (fuel 1, 6 and 3), we can see that especially fuels 1 and 6 have lower OH* peak intensity. OH* chemiluminescence level for fuel 3 is higher and it is difficult to find the reason behind this trend. Fuels 2, 3 and 5 contain more aromatics and similarly to single injection strategy, peak intensity of OH* chemiluminescence increases with aromatics content. During combustion of fuel 4 the lowest amount of OH* is generated, increasing for fuels 2 and 5.

7.4.2.3. Lift-off length

The amount of formed soot may be related to flame lift-off length (FLoL) and this relation was studied frequently in flames [80, 125, 9, 142, 144]. FLoL is determined from the distance between the tip of injector and location in the flame spray, where OH* radicals appear [144, 136, 142]. Amount of soot produced in this area depends on amount of air that enters upstream lift-off length and mixture in this region is premixed. Figure 7.6 shows results determined based on axial distance from the tip of injector to the place where first OH* radicals with an intensity greater than the set threshold appear (FLoL). The threshold intensity for FLoL determination was set at 40 on the zero to 255 intensity scale of the image (this threshold was kept the same for both fuels). The flame lift-off length is dependent on several parameters including nozzle hole, diameter, injection pressure, injection velocity, ambient density ambient temperature and fuel properties [83, 125] Similarly, based on the measured soot natural luminosity images, the distance from the tip of injector to the nearest luminous soot cloud was determined. This distance will be referred to as lift of length based on soot luminosity (SLoL). FLoL and SLoL were measured for double injection strategy since for this strategy it was possible to capture injection event and results are presented in Fig. 7.6 A and B.

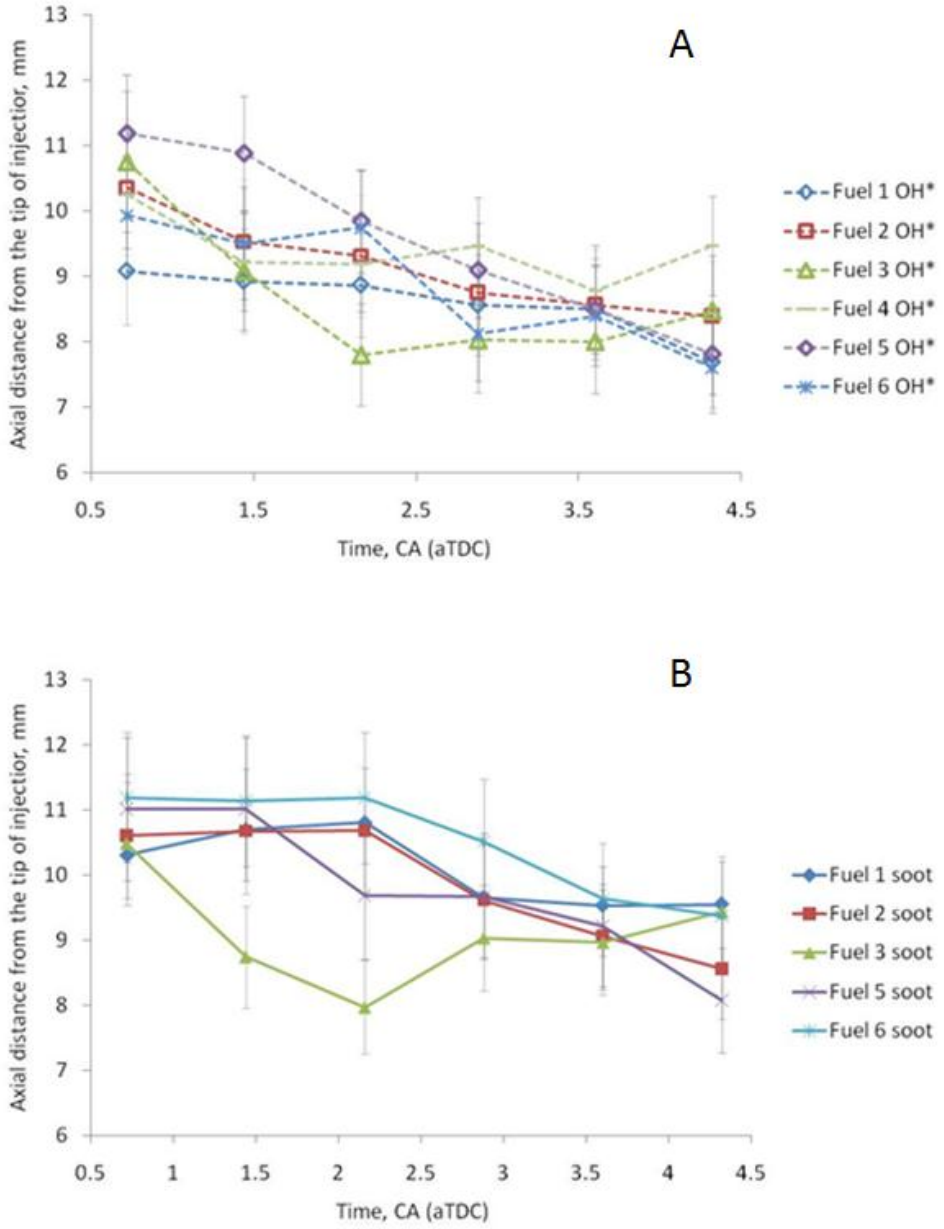

Figure 7.6. FLoL and SLoL measured for six fuel for double injection strategy.

The average values of FLoL and SLoL are calculated on the base of ten injection events. The spatial resolution was determined by imaging a grid of known size using the high speed camera. This enabled to obtain the distance related to one pixel and accordingly the FLoL and SLoL were determined.

FLoL for all fuels, for first crank angles is in the range 9 mm to approximately 11.2 mm. FLoL decreases with crank angle to ~7.5 to 9.5 mm, while temperature in combustion chamber increases. FLoL for initial crank angles is slightly greater for fuel 5 in comparison to rest of the fuels and then rapidly decreases. FLoLs for fuel 6 and 1 are initially the shortest. Comparing these fuels, fuel 6 with higher oxygen content has longer FLoL (about 1 mm

difference to fuel 1), and this is in agreement with results presented in [124] where fuel containing more oxygen has longer FLoL. Fuels with higher oxygen content tend to create different local stoichiometry causing reduction is soot formation and as well improved soot oxidation. Additionally chemical composition of fuel may influence FLoL progress. Similar work had been carried out to study FLoL and soot inception for four different fuels in a constant volume chamber [80]. It has been shown that the time required for soot nucleation during combustion of fuel containing oxygen was greater than that of diesel, which is in line with the results presented in this work. FLoL decreases with crank angle and the difference between these fuels is not visible at the later stage.

FLoLs for fuels 2, 3 and 4 are initially very similar, however later FLoL for fuel 3 rapidly decreases, FLoL for fuel 4 does not change significantly with crank angle, remaining more or less at the same level. FLoL for fuel 2 decreases slightly later in the stroke. FLoL for fuel 4 did not change radically with crank angle (variation within ~10.2 to ~9.5 mm was recorded). FLoL for fuel 3 initially was quite large ~10.8 mm but the rapidly decreased to 7.8 mm, and was the lowest from all considered fuels indicating that soot formation for this fuel will may be higher.

Considering fuels 2, 4 and 5 and comparing them to fuels with low level of aromatics we may conclude that FLoL for fuels with aromatics do not decrease that quickly (as it is visible in case of fuel 2). However, further increase in aromatics content causes that initially FLoL is larger but rapidly decreases with crank angle, as it is the most noticeable for fuel 5. Figure 7.4 shows that total aromatic content was related as well to peak in-cylinder soot level. Peak soot levels for fuels 1, 3 and 6 were higher than the rest of fuels and total aromatics content for these fuels was low. As it is visible in Fig. 7.6 A, FLoL for these fuels is shorter than for the rest of fuels indicating that during their combustion as well fuel/air mixture was not sufficiently premixed resulting in enhanced soot generation. Fuels containing higher levels of aromatics produced less soot but as well their lift-off length initially was slightly longer that allowed for higher quantities of oxygen being mixed with fuel. Mechanism of FLoL formation is complex and may be related not only to fuel composition but flame velocity, fuel velocity and flame propagation as it was reported in [124, 82]. Hence it is difficult to assess which mechanism is dominant.

In Fig. 7.6 B SLoL is presented and each point corresponds to value averaged based on ten measurements. The same global trend of SLoL decreasing with crank angle was observed, however measured SLoL is larger than FLoL for most of the cases. For first crank angles SLoL of approximately from 10.2 mm to 11.2 mm was observed for all fuels. Only SLoL for fuel 3 is significantly shorter, the soot formed during combustion of this fuel appears closer to

the tip of injector when compared to the rest of the fuels. The longest SLoL was observed for fuel 6 and very similar trend was obtained for fuels 1, 2 and 5.

7.4.3. Cetane number versus ignition delay

CN influences both combustion process and emissions especially for single injection strategy. High cetane number improves ignition and reduces emission of unburned species leading to higher in-cylinder temperatures. However, short ignition delay leads to rich air-fuel mixture formation and this may cause enhanced soot generation. Increase in ignition delay provides longer time for mixing fuel with air and local oxygen concentration in this mixture is higher improving soot emission.

Figure 7.7 shows ID for single injection strategy obtained based on in-cylinder pressure, soot luminosity and OH* chemiluminescence and for double injection strategy based on in-cylinder pressure, plotted against cetane number.

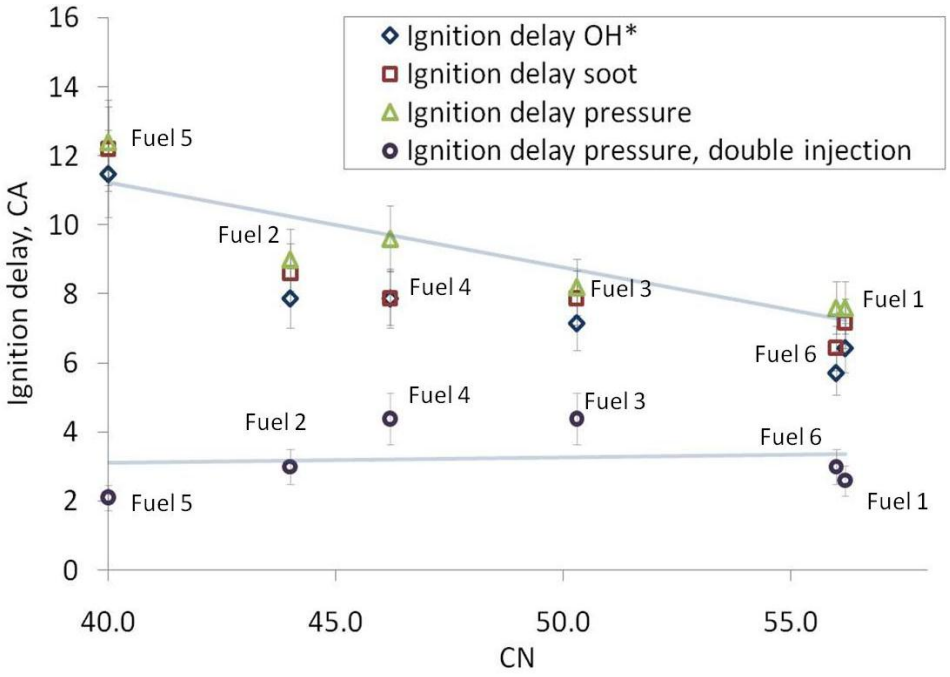

Figure 7.7. Cetane number versus ignition delay obtained based on in-cylinder pressure, OH* chemiluminosence and soot luminosity for all fuels, for single injection of 20 mg/stroke at 5º aTDC of fuel and ignition delay obtained for double injection strategy (circles).

For single injection strategy general trend of ignition delay decreasing with increasing cetane number was observed for all three methods of measurement. The trend observed here was comparable to one reported in the literature, [31].

It is visible that generally ID obtained based on OH* chemiluminescence is the shortest and is very close to ID obtained based on soot luminosity. The longest ignition delay was observed from measured in-cylinder pressure, however it should be highlighted that this ID represents

global ignition while ID determined using other two techniques indicate occurrence of local ignition. For double injection strategy, no significant fluctuations in ID were observed, all fuels were ignited in similar time (see Fig. 7.7).

7.4.4. Planar laser induced incandescence

To measured relative amount of soot left in the combustion chamber after the end of luminous combustion (in expansion stroke) planar laser induced incandescence technique (PLII) was used. The main goal of this measurement was to qualitatively understand the differences in soot processes between fuels and relate it to soot measured using high speed imaging techniques in earlier part of expansion stroke. The laser sheet used for measurements was directed through the top section of cylinder to heat up soot particles remaining in the combustion chamber (see section 4.1.1). The incandescence from heated soot particles are detected by an ICCD camera through the piston window. To minimise and to avoid piston window attenuation, window was cleaned after every engine run. The engine was operated in skip-firing mode that as well reduced the deposit of soot on piston window. Measured incandescence intensities are proportional to soot volume fraction (SVF). Single shot, PLII images of relative soot volume fraction at different crank angles during the combustion of fuels are shown respectively in Figs. 7.8 and 7.10 for single and double injection strategy. Results presented here provide information regarding soot present in a 3 mm thick plane across the combustion chamber. Position of laser sheet is indicated by red rectangle and direction by the arrow. Signal emitted by soot may be affected by the soot which is located between laser sheet and detection system causing attenuation of LII signal intensity. Effects of attenuation and signal trapping are discussed in chapters 5 and 6.

The spatial distribution of soot is measured for all fuels for single and double injection strategy at crank angles from 46.4° to 111.4°aTDC. Each image in Fig. 7.8 and 7.10 is a single shot picture of LII signal and in Figs. 7.9 and 7.11 spatially integrated LII signals averaged over 10 shots are presented. Images were selected as the most representative for each crank angle. General trend of SVF decreasing with crank angle was observed for this strategy that may indicate presence of soot oxidation. The decrease in SVF may be related as well to increasing volume of combustion chamber and soot clouds motion, as it was reported as well in [22]. The soot may spread out in larger volume that will be visible during measurements as a lower soot concentration in the laser plane.

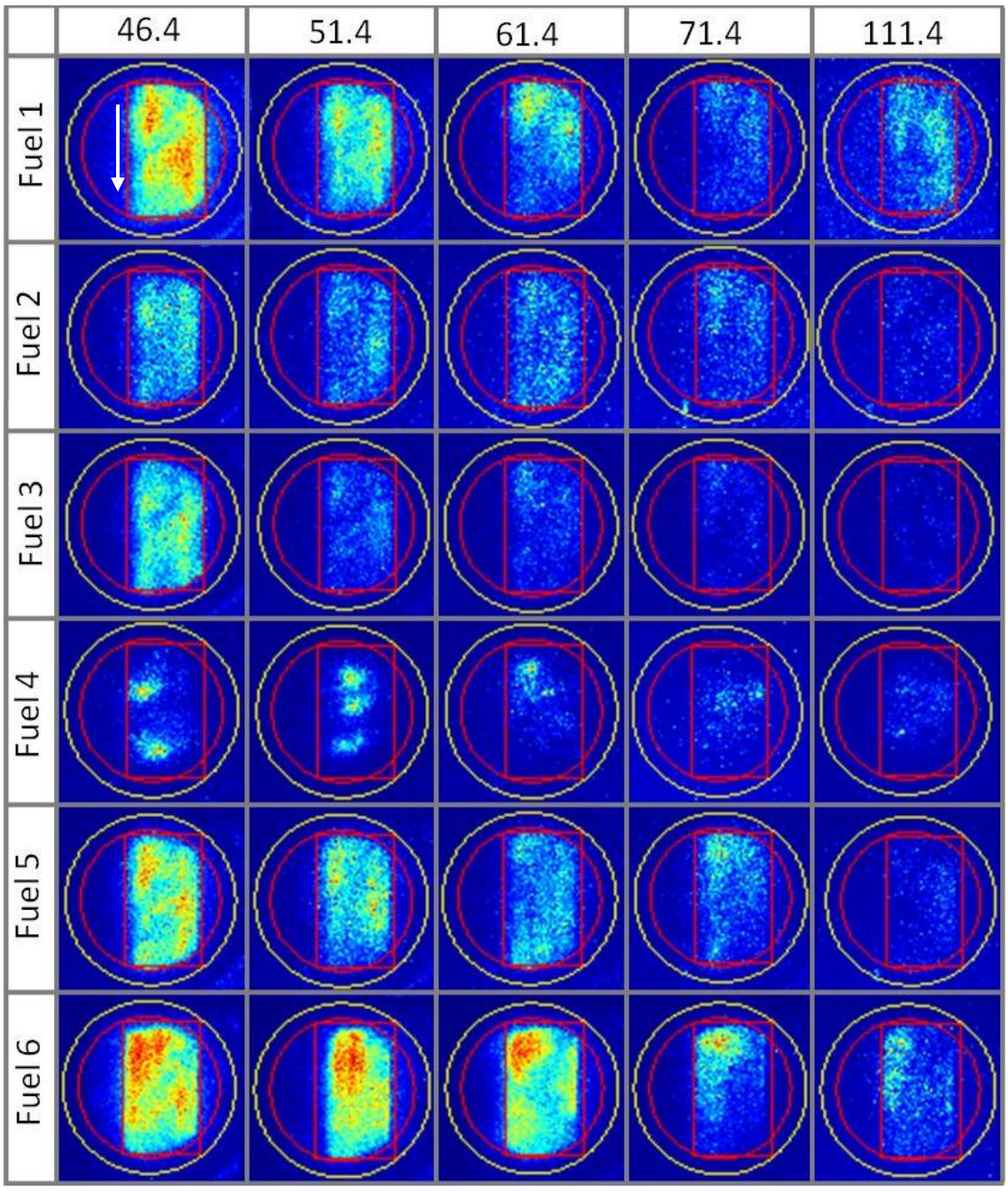

Figure 7.8. Planar laser induced incandescence for single injection strategy.

Taking into consideration results presented in Fig. 7.8, the highest soot level left after combustion was obtained for fuels 1 and 6. This corresponds to results acquired using high speed imaging, where the highest soot luminosity (amounts of soot) for single injection strategy was measured during combustion of fuel 1 and 6. Results may be related to the IDs, where for these fuels the shortest ID was measured and subsequently short FLoL was observed indicating poor air/fuel mixture formation. Considering soot distribution for these two fuels, high intensity patches that are related to areas of high soot concentrations are observed in the measurement plane. Slightly lower intensities are observed for fuel 6 when

compared to fuel 1. It is as well visible that later in the stoke distribution is more uniform and is comparable for both fuels.

Relatively high level of SVF was measured as well for fuels 3 and 5. The soot left after combustion of fuel 3 may be mostly considered as a result of short ignition delay and FLoL that may lead to insufficient air/fuel mixture formation as it was as well observed for fuels 1 and 6. However, this high level of soot is observed mostly for 46.4ºaTDC and then soot level is low. For 46.4ºaTDC soot is distributed more uniformly than for fuels 1 and 6, and high intensity patches are not visible.

Long ignition delay and FLoL were detected for fuel 5 though PLII results show high level of soot for this fuel. Results may be affected by long ID that causes the shift in soot processes which start later in the stroke as it is visible in Fig. 7.5 A leading to high soot concentrations detected later in the expansion stroke. The phase of combustion for this fuel is different than for fuels 1 and 6 and it makes the comparison difficult.

Low SVF was measured for fuel 2 and 4. It is hard to define which fuel produces lower level of soot since its distribution is different. Fuel 4 leads to formation of soot which is not uniformly distributed and in the laser plane areas of higher soot concentrations are visible especially for first three crank angles. Soot left after combustion of fuel 2 is more uniformly distributed and its level is low.

All the PLII images were spatially integrated and average values of ten readings are presented in Fig. 7.9.

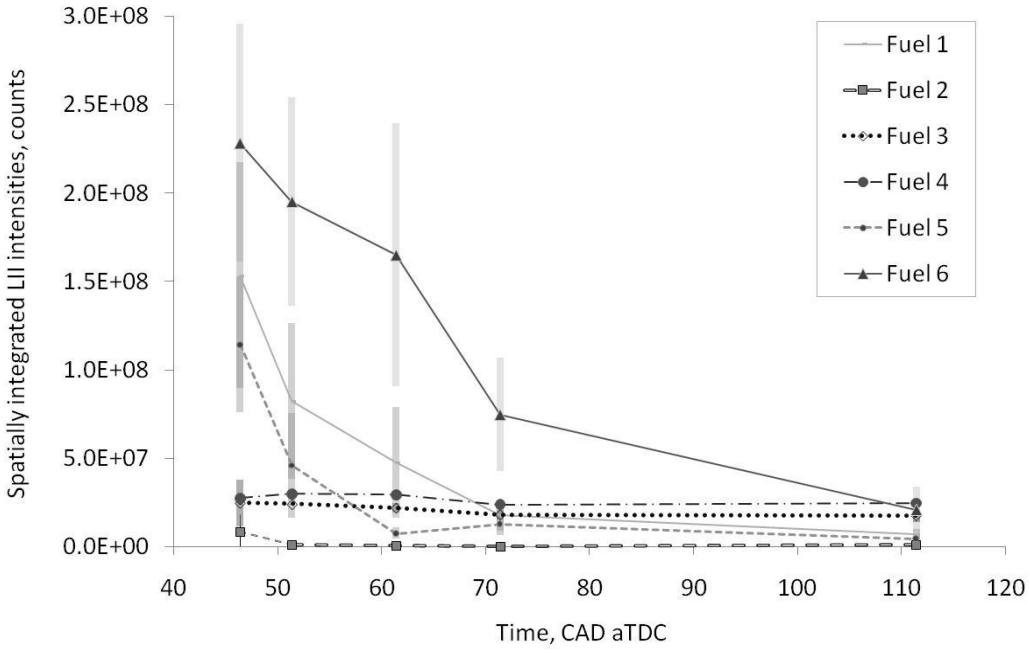

Figure 7.9. Spatially integrated planar laser induced incandescence for single injection strategy.

The trends do follow general trends reported during analysis of single shot images and here as well high soot levels were measured initially for fuels 6, 1 and 5. The SVF decreases with crank angle for these fuels and at 111.4°aTDC comparable level of soot was observed for all fuels. Soot levels measured for fuels 3, 4 and 5 are initially low and remain at this level throughout measured range of crank angles.

Figure 7.10 shows PLII images obtained for double injection strategy.

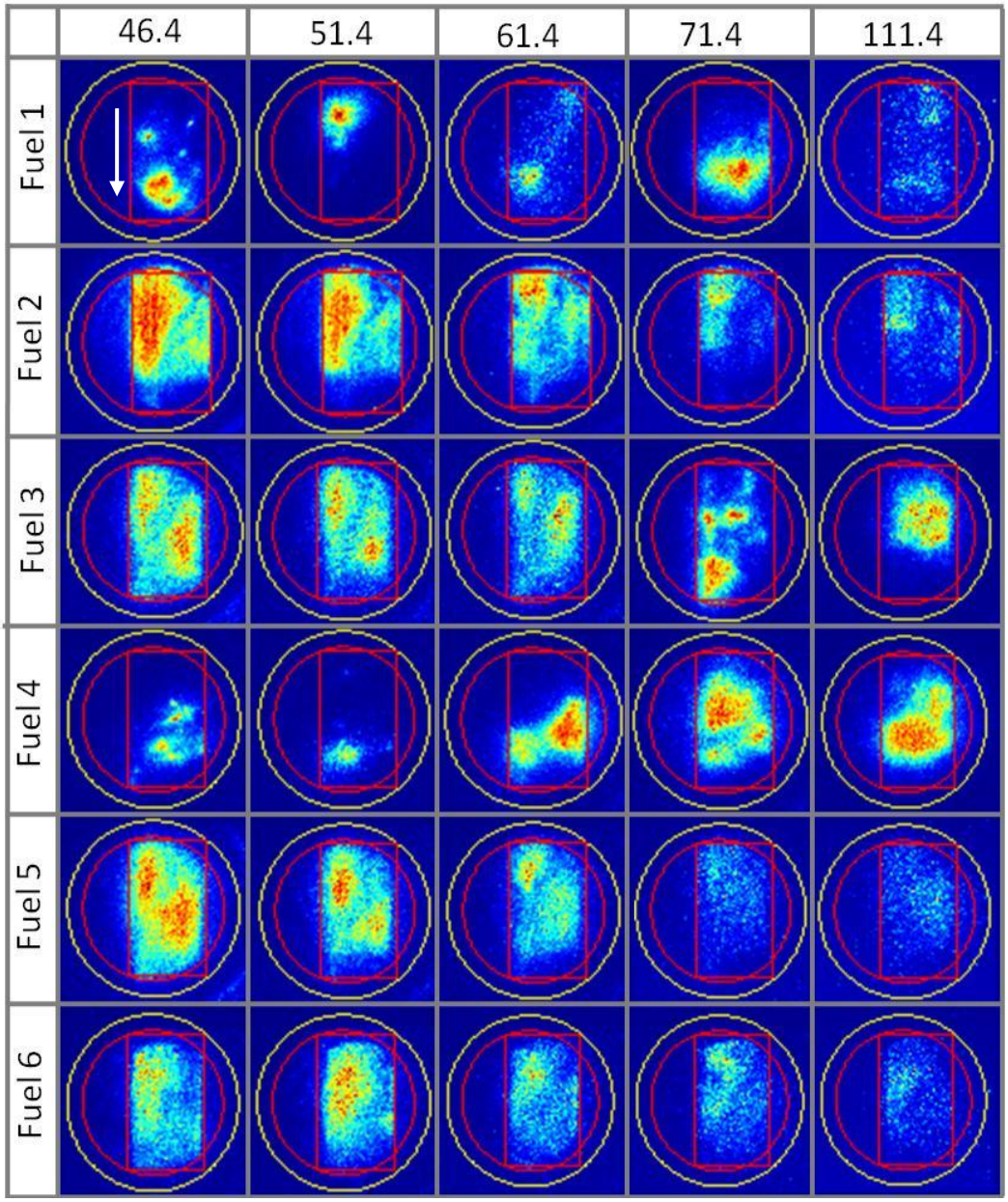

Figure 7.10. Planar laser induced incandescence for double injection strategy.

SVF decreases with crank angle only for fuels 2, 5 and 6. For rest of the fuels patches of high soot concentration appear. For this strategy, as mentioned previously, ID does not influence soot processes and it is possible to evaluate effects of fuel composition.

Following analysis from the previous sections fuels with low aromatic content: fuel 1, 3 and 6 will be considered together. PLII results presented in Fig.7.10 show that level of soot observed after combustion of fuel 3 is higher than fuel 1 and soot is more uniformly distributed considering first three crank angles (46.4 ºaTDC, 51.4 ºaTDC and 61.4 ºaTDC). For 71.4ºaTDC and 111.4 ºaTDC high intensity areas of soot were measured for this fuel. For fuel 1 small areas of high intensity soot are observed throughout all crank angles. For last detection crank angle 111.4ºaTDC soot level for fuel 1 is uniform and significantly lower than for fuel 3.There are not many differences between fuel 1 and 3. Fuel 3 has lower CN but for this injection strategy it is relevant. This fuel has slightly lower oxygen content and lower aromatics content in comparison to fuel 1. As it was reported in section 7.4.2.3., FLoL for fuel 3 was lower especially for later crank angles when compared to fuel 1, which may be one of the main reasons of trend observed here. Results acquired during high speed luminosity imaging show that peak luminosity for this fuel was quite high but very similar to fuel 1.

Results for fuel 6 show uniform soot distribution and SVF decreasing with crank angle. No high intensity zones were observed in comparison to fuels 1 and 3 that may indicate improved air/fuel mixture formation (due to longer FLoL). Considered fuel contains oxygen which has beneficial influence on soot oxidation as it was reported in [143, 145]. As mentioned previously fuel 2, 4 and 5 contain higher aromatics content. Fuels 2 and 5 show alike behaviour. Soot level is high for first 46.4 ºaTDC, 51.4 ºaTDC and 61.4 ºaTDC, significantly higher soot concentration zones are observed for fuel 2 when compared to fuel 5 of more uniformly distributed soot. For last crank angles 71.4ºaTDC and 111.4ºaTDC distribution is more even and notably lower for fuel 5. The possible relation between soot level and aromatics content was discussed previously and here further proof of influence of aromatics content is visible (fuel with higher aromatics tend to produce less soot, it is visible especially for fuel 5 which contains the highest level of aromatics). Trend observed here is strongly related to results presented in section 2.2.1 where peak soot luminosity was linked to aromatics content. Different trend was measured for fuel 4 with the least aromatics. Soot detected for initial crank angles is low and then for 61.4 ºaTDC, 71.4ºaTDC and 111.4ºaTDC areas of high soot intensities are observed for this fuel.

Spatially integrated, average PLII images for this strategy are presented in Fig. 7.11.

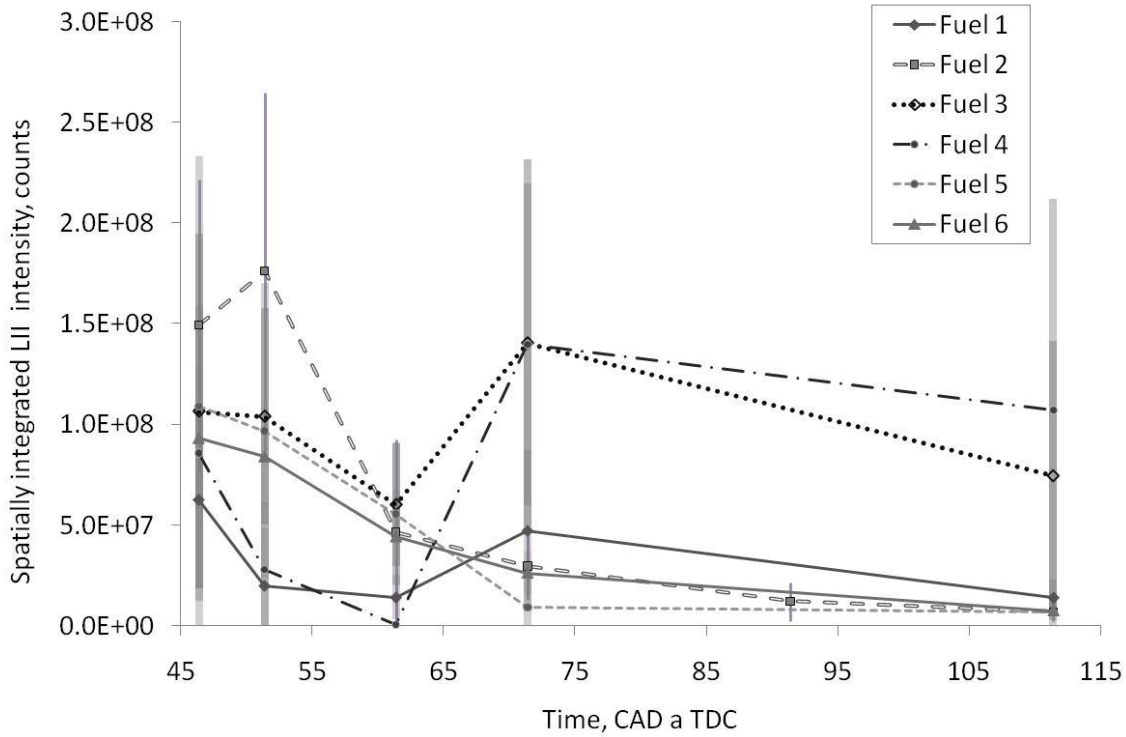

Figure 7.11. Spatially integrated planar laser induced incandescence for double injection strategy.

The trend for this strategy is not that obvious. Decrease in SVF with crank angle is observed for fuels: 5, 6 and 2. For fuels 1, 3 and 4 SVF decreases for three first crank angles and then increase in soot concentration was observed. SVF for fuel 1 however does not change that strongly like for two other fuels.

7.5. Summary and conclusions

In-cylinder combustion and soot processes for six fuels of different composition were investigated in an optically accessible high speed direct injection diesel. High speed imaging technique was used to look into soot processes from the point of fuel injection. After the end of luminous combustion soot remaining in the combustion chamber was measured using PLII technique. The main findings of this investigation are summarised as follows:

- Measurements showed that peak soot luminosity (which is proportional to soot volume fraction in combustion chamber) is dependent on fuel properties. Fuel containing oxygen tends to produce less soot.
- Peak soot luminosity may be as well related to aromatics content. Combustion of fuel with doubled quantity of aromatics resulted in about 20% to 30% decrease in soot

emission. We may conclude therefore that relation between fuel aromatic level and soot emission exists.

- During combustion of fuels with higher aromatics content higher peak intensities of OH* chemiluminescence were measured indicating that higher quantities of OH* radicals were present in combustion chamber. This was observed for single and double injection strategy.
- FLoL measured for fuel containing oxygen was longer than that for fuel without. FLoL for fuels containing aromatics tend to be longer for initial crank angles and then rapidly decreases that may contribute to amount of soot formed during combustion of these fuels.
- ID was measured using three different methods for single and double injection strategy. For single injection strategy trend of ID decreasing with CN was observed for all techniques. For double injection strategy fairly constant ID was observed showing that fuels ignite at similar time despite the differences in CN.
- For single injection strategy PLII results show that amount of soot left in the combustion chamber after the end of luminous combustion decreases for fuels with longer ID and longer FLoL. For this strategy therefore strong relation between CN and amount of produced soot was found.

  For double injection strategy SVF measured for fuel with higher oxygen content was reduced indicating presence of relation between oxygen and soot remaining in the combustion chamber. Subsequently visible influence of aromatics content in fuel on generated soot was observed where fuels with higher aromatics lead to reduced formation of soot.

8. Chapter 8 - Injection parameter dependent in-cylinder diesel soot particulate characterization by time-resolved laser induced incandescence

8.1. Introduction

In-situ optical diagnostic techniques such as time-resolved laser induced incandescence (TR-LII) have been used successfully for the characterization of nanometric size particles, for example, soot produced in diffusion and premixed flames [73, 114], soot produced during the combustion process in a heavy-duty diesel engine [52, 146, 104], for the measurement of TiO_2 nanoparticles in a flame reactor [147] and measurement of metal oxide nanoparticles from gas-to-particle synthesis [148]. In these investigations the primary particle diameters have been assumed to have a mono-dispersive particle size distribution d_{mono}, which is responsible for the temporal decay of the TR-LII signal. In a real system, combustion generated soot are in the form of primary particles which combine to form aggregates, and the primary particle distribution is often poly-dispersive rather than mono-dispersive. Recently, it has been reported [102] that the TR-LII signal also contains additional information about the poly-dispersive nature of particles that can be assumed to have a lognormal form of distribution. However, this hypothesis of a lognormal distribution yields a count median diameter d_{cmd}, which is smaller than that of the mono-dispersive particle size (d_{mono}) and is eventually dependent upon the geometric standard deviation (σ_g). Thus the assumption of a lognormal distribution erases the contribution of mono-dispersive particle size d_{mono} that is primarily responsible for the temporal decay of the TR-LII signal. This assumption also introduces complexities in determining the size distribution due to its complicated calculation procedure and non-unique solutions. In this paper the temporal decay of the laser induced incandescence (LII) signal from poly-disperse soot primary particles that are formed during the transient combustion process in a light-duty diesel engine are assumed to have a multi-lognormal particle size distribution rather than a single-lognormal distribution. The introduction of a multi-lognormal distribution into the existing LII model not only preserves the valuable parameter d_{mono} as the count median diameter $d_{1,cmd_multi}$of the first distribution, but also allows for a realistic reconstruction of the actual size distribution. The results for soot size distribution obtained from LII experiments and simulation were qualitatively compared with both published transmission electron microscopy (TEM) data and

the experimentally deduced electrical mobility spectrometer (EMS) using the proposed multi-lognormal size distribution.

8.3. Theory

The basics of TR-LII technique are presented in section 2.4.1.2 A comparison of experimentally yielded soot emission along with the theoretical LII curve yields the primary particle diameter d_{mono}. This value represents the particle size that is mainly responsible for the temporal decay of the LII signal. However, in many practical applications the probing volume in LII measurement contains a number of primary particles which are sufficient enough to represent the particle size distribution of the entire system i.e. the measured LII signal is the cumulative signal from particles of various sizes and the highest contribution comes from the primary particle size d_{mono}. It has already been reported [102] that the weighting of the signal contributions of individual particle size classes changes with time after the laser pulse. The smaller particles decay faster and therefore have a constantly decreasing influence on the total signal of the particle distribution, which results in a deviation of the LII signal from a pure exponential decay. A weighted summation of LII signals from mono-dispersive size classes calculated from the numerical integration of energy balance equation was used for estimating the signal decay of a particle ensemble to obtain the size distribution. For the reconstruction of the actual size distribution a multi-lognormal distribution is assumed in the present study and is mathematically expressed as:

$$P(r_p) = \sum_{i=1}^{n} \frac{1}{\sqrt{2\pi} r_p \sigma_i} exp\left\{ - \frac{[ln(r_p) - ln(r_{i,cmd\_multi})]^2}{2\sigma_i^2} \right\} \qquad (8.1)$$

where n indicates the total number of log-normal distribution and r_p is the radius of the particle. The parameters characterizing an individual log-normal mode i are distribution width $\sigma_i = \ln(\sigma_{g,i})$ with $\sigma_{g,i}$ being the geometric standard deviation and r_{i,cmd_multi} the count median radius. Owing to a significant increase in the number of variables for a multi-lognormal function, a simple approach of $\sigma_i = \sigma_2$ for all i >2 was employed for the purpose of reduction of variables along with the following assumption for the count median radius: $r_{i+1,cmd\_multi} = \frac{r_{i,cmd\_multi}}{\xi}$ where ξ is the divisible factor. The fitting of the theoretically obtained signal $LII(t)$ (see section 3.3.4) of a particle ensemble to the experimentally measured LII data was achieved by the variation of distribution-width σ_i, visible factor ξ and the count median radius r_{i,cmd_multi} of the first distribution (starting from the largest particle) to satisfy the following conditions: (a) $r_{i,cmd\_multi} = r_{mono} = \frac{d_{mono}}{2}$ and (b) minimum χ^2 for the

comparison of the experimental LII signal to the theoretical signal, which is defined as $\chi^2 = \sum_{a=1}^{N}\left(LII_{exp}(a) - LII_{theo}(a)\right)^2$ where $LII_{exp}(a)$ and $LII_{theo}(a)$ are the measured and calculated LII signal intensity values. Note that the above two conditions are satisfied only at a unique value of the variables and as divisible factor ξ is a function of the total number of lognormal distribution *n*, unique values were obtained for ξ, which is approximated by $\xi \cong 1 + \frac{2.5}{n^2 - 2.75}$ where $2 \leq n \leq 6$ and for $n = 1$, $\xi = 1$. The expression for the divisible factor "ξ" comes from a data set created by fitting number of times the LII temporal decay with different "n" value, as the two conditions for fitting are satisfied only at unique values of divisible factor, the ξ values were repeated for the same "n", finally the data set was fitted to a single-pole Sellmeier equation, and the coefficients were obtained by a regression fit. Moreover, distribution-width $\sigma_1$was obtained by fitting the LII temporal decay for satisfying the above two conditions and assuming $\sigma_2 \sim \sigma_{single-lognormal}$, which eventually resulted in a unique size distribution. For example, Fig. 8.1A shows a theoretically calculated LII signal for a primary particle radius r_{mono} of 60 nm at an ambient pressure of 25 bars and temperature of 1600 K.

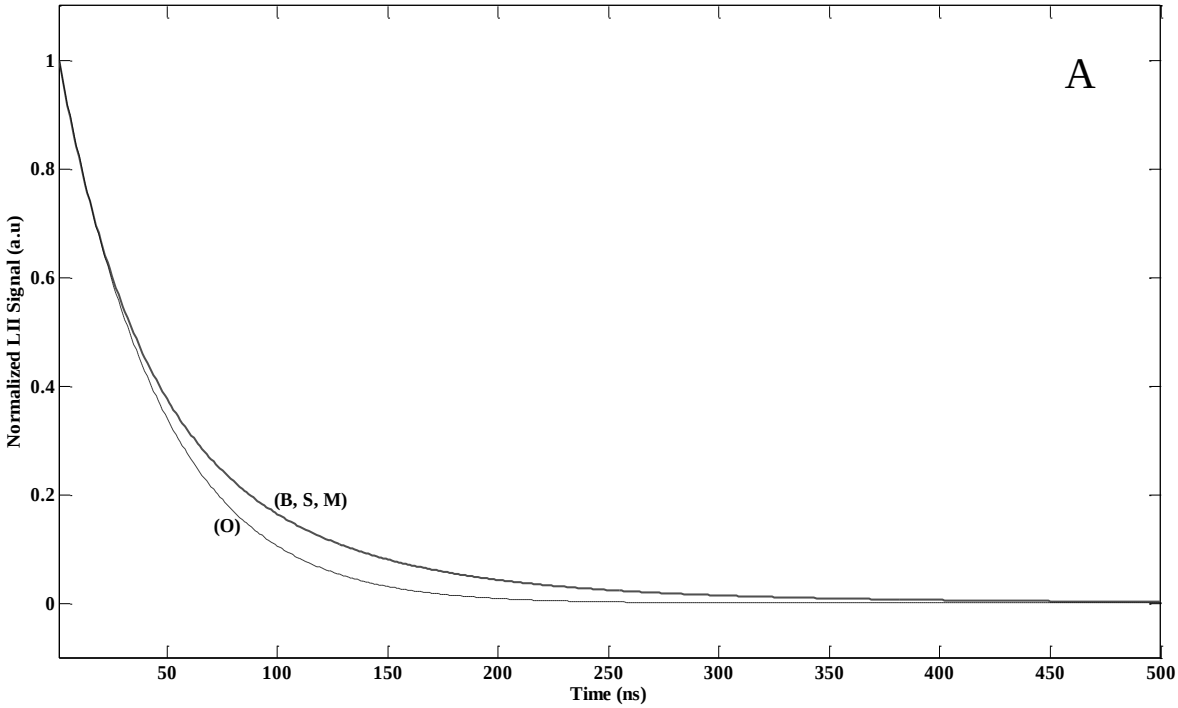

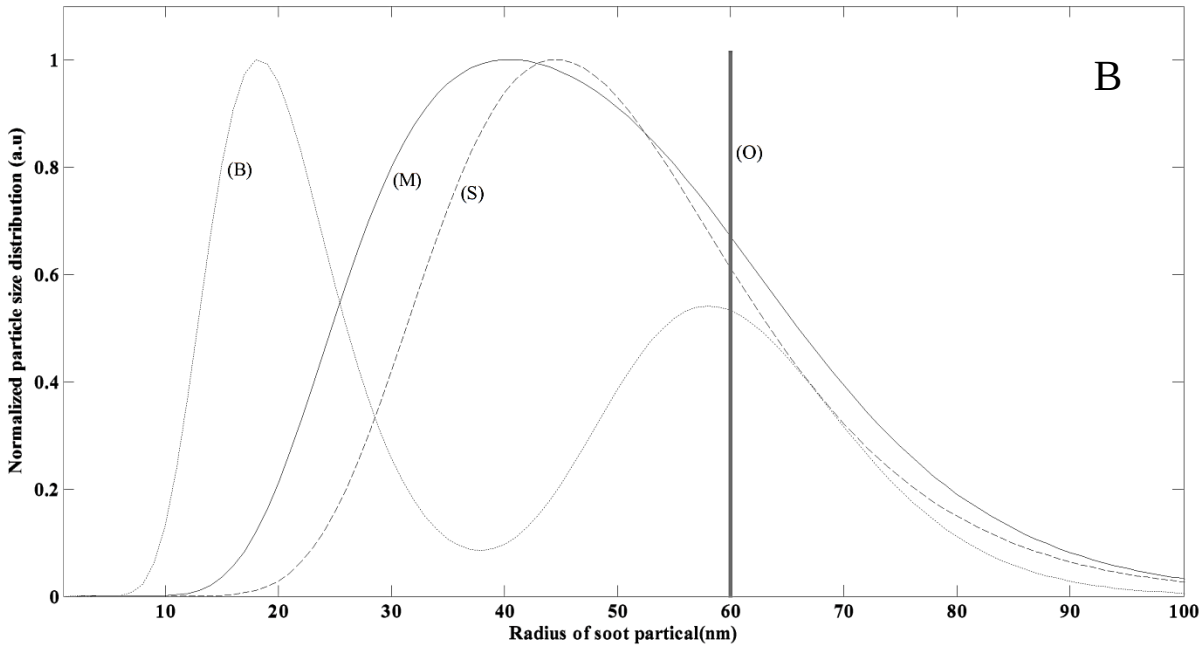

Figure 8.1. A : Theoretically calculated LII signal for a primary particle radius of 60 nm. The dashed line (O) is the modelled LII signal decay for a mono-dispersive size distribution. The solid lines (B, S, M) are the theoretically calculated LII decay for a single-lognormal (S) n=1, bi-model (B) n=2 and multi-lognormal (M) n=4, respectively. B: The corresponding size distribution. Dashed line (S) is the distribution for n=1. The line (B) for n=2 and solid line (M) for n=4, respectively.

The initial temperature of the particle was assumed to be 3800 K, taking into account a small contribution of sublimation in the process. The dashed line (O) corresponds to the decay of the thermal radiation if a mono-dispersive size distribution is assumed. The solid lines (B, S, M) are the theoretically calculated LII decay for a single-lognormal (S) n= 1, bi-model (B) n= 2 and multi-lognormal (M) n= 4, respectively. The Fig. 8.1 B shows the corresponding size distribution. For a single-lognormal distribution n=1, shown by the dashed line (S), a distribution-width of n= 0.3 and the resulting mean count radius r_{cmd} was computed as 48 nm. However, the same LII signal was reproduced for a multi-lognormal distribution with n= 2 as well as n= 4. In case of n= 2, shown in the insert by dotted line (B), the above mentioned two condition were satisfied only for distribution widths of σ_1= 0.18, σ_2= 0.3 and ξ= 3, thus resulting in a unique size distribution with r_{1,cmd_multi}= 60 nm and r_{2,cmd_multi}= 20 nm. Similarly, for n= 4 shown by the solid line (M) in the insert, the unique variables satisfying the two conditions were σ_1= 0.23, σ_2= 0.32 and ξ= 1.2, which results in a mean radius of r_{1,cmd_multi}= 60 nm, r_{2,cmd_multi}= 50 nm, r_{3,cmd_multi}= 41.6 nm and r_{4,cmd_multi}= 34.7 nm. Note that the average count median particle radius for a multi-lognormal distribution

(M) (n= 4) is slightly less than the count median particle radius for a single-lognormal distribution (S) even though the distribution differs significantly. Figure 8.2 shows the contributions of individual particle size classes in an ensemble towards the evolution of the LII signal.

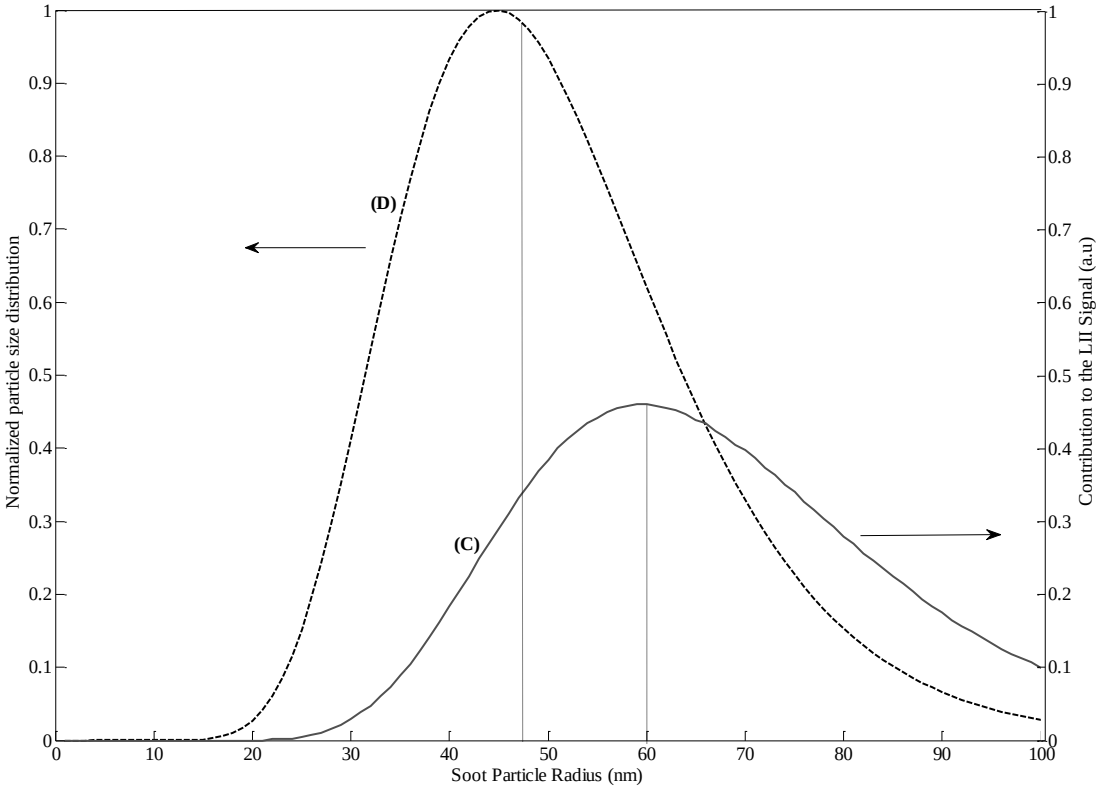

Figure 8.2. The contributions of individual particle size classes in an ensemble towards the evolution of the LII signal. Dashed curve (D) is the reconstructed size distribution for a single-lognormal particle ensemble and solid line (C) is the contribution to the LII signal.

The dashed curve (D) is the reconstructed size distribution for a single-lognormal particle ensemble. Although the count median particle radius r_{cmd} for σ= 0.3 is 48 nm, the highest contribution to the LII signal comes from the primary particle radius r_{mono} of 60 nm, the solid curve (C). Thus from Figs. 8.1 and 8.2 it is clear that a multi-lognormal particle size distribution can also be assumed for the reconstruction of a particle size distribution due to its repeatability of the same LII signal decay as for a single-lognormal distribution. In order to verify this, both in-cylinder TR-LII measurements and the exhaust soot particle size measurements were carried out in a high-speed diesel engine.

8.4. Experiments

The TR-LII technique was applied in a single cylinder, optically accessible diesel engine described in section 4.2.1. The pulse energy was adjusted and set to 42 mJ for the LII

experiments, which corresponds to a laser fluence of 0.13 J/cm^2 taking into account the losses due to the front window. The detection system was arranged orthogonal to the laser beam direction. A broadband antireflection (AR) coated plano-convex lens of focal length *f*= 150 mm was used to direct the LII signal to the photomultiplier tubes (PMT) via a 50% beam splitter (EBS1). Two band-pass filters of wavelength 700 nm (FB700) and 400 nm (FB400) were used to limit the radiation to a narrow spectral range (FWHM = 10 nm). The signals were recorded by a digital storage oscilloscope Tektronix (TDS 3034, 300 MHz) at a sampling rate of 2.5 GS/s.

8.5. Application of multi-lognormal soot particle size distribution

Figure 8.3 shows the evolution of the experimental signal (Exp) along with the theoretical curve (O) and (S, M) at the crank angle of 47◦ after TDC.

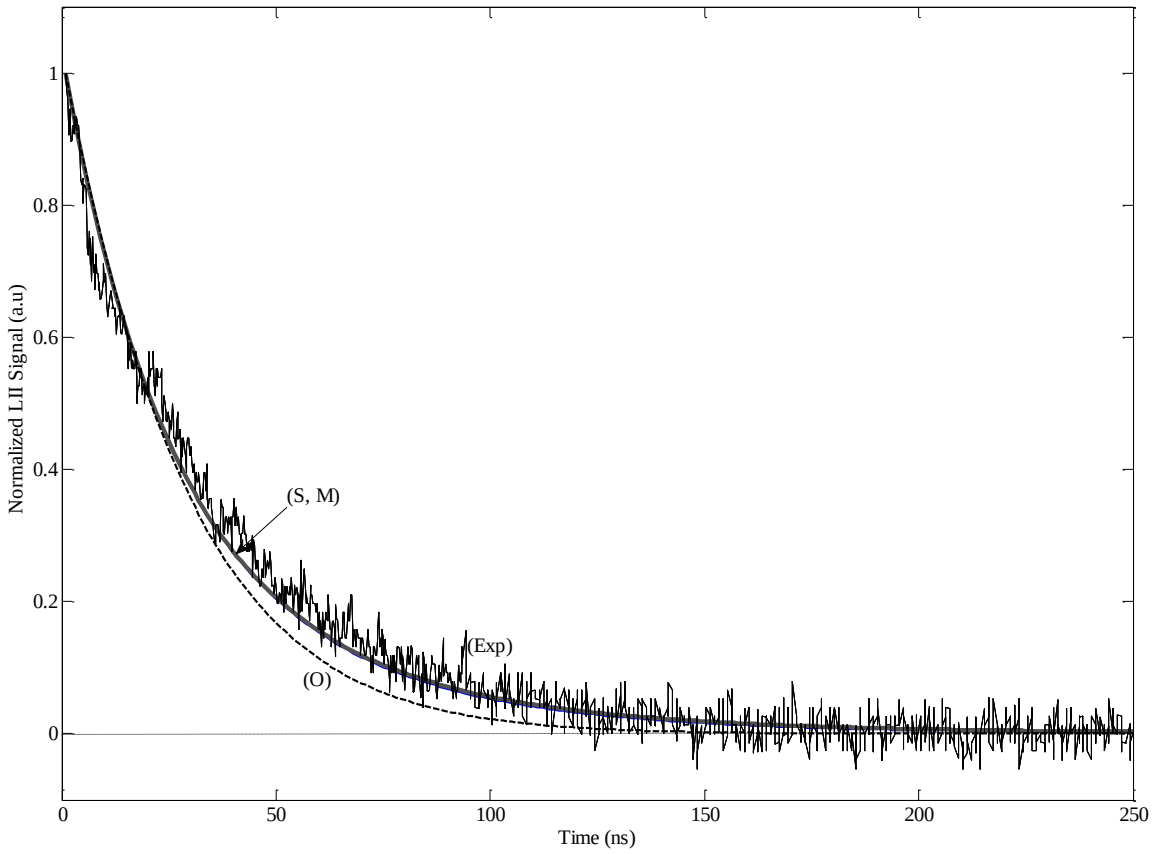

Figure 8.3. The evolution of the experimental signal (Exp) along with the theoretical curve (O) and (S, M) at 47° CA after TDC. The line (O) is the calculated LII signal assuming a mono-dispersive size distribution and the solid lines (S, M) are the calculated LII signal for single-lognormal (*n*=1) and multi-lognormal (*n*=4) particle size distribution.

The ambient pressure p_g and temperature T_g were calculated from the in-cylinder pressure data and were 9 bar and 1300 K, respectively. Figure 8.4 shows χ^2 as a function of the initial soot temperature, which was calculated from the comparison of experimental LII trace with the modelled trace.

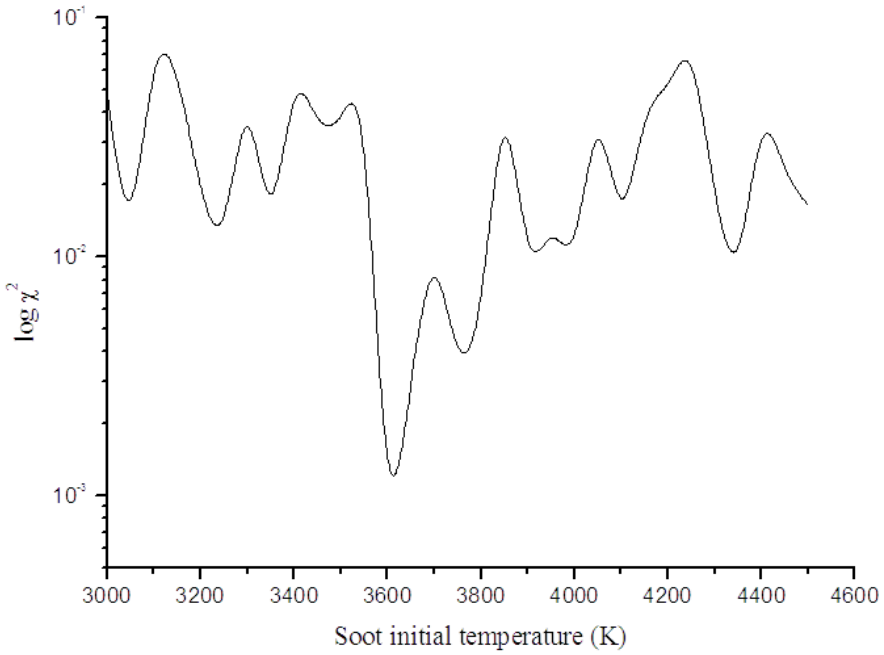

Figure 8.4. χ^2 as a function of the initial soot temperature calculated for the comparison of the experimental LII trace at a crank angle of 47°after TDC with the modelled trace.

The initial temperature of 3600 K that was obtained from the χ^2 map was used to calculate the mono-dispersive particle size r_{mono} of 42 nm viathe model described in the previous section. As shown in Fig. 8.3, the experimental curve (Exp) is not a pure exponential decay curve as compared to the theoretically calculated mono-dispersive curve (O) and shows the contribution from other size particles in the ensemble. Thus a size distribution was reconstructed assuming both single (n = 1) as well as multi-lognormal (n = 4) distribution as shown in Fig. 8.5.

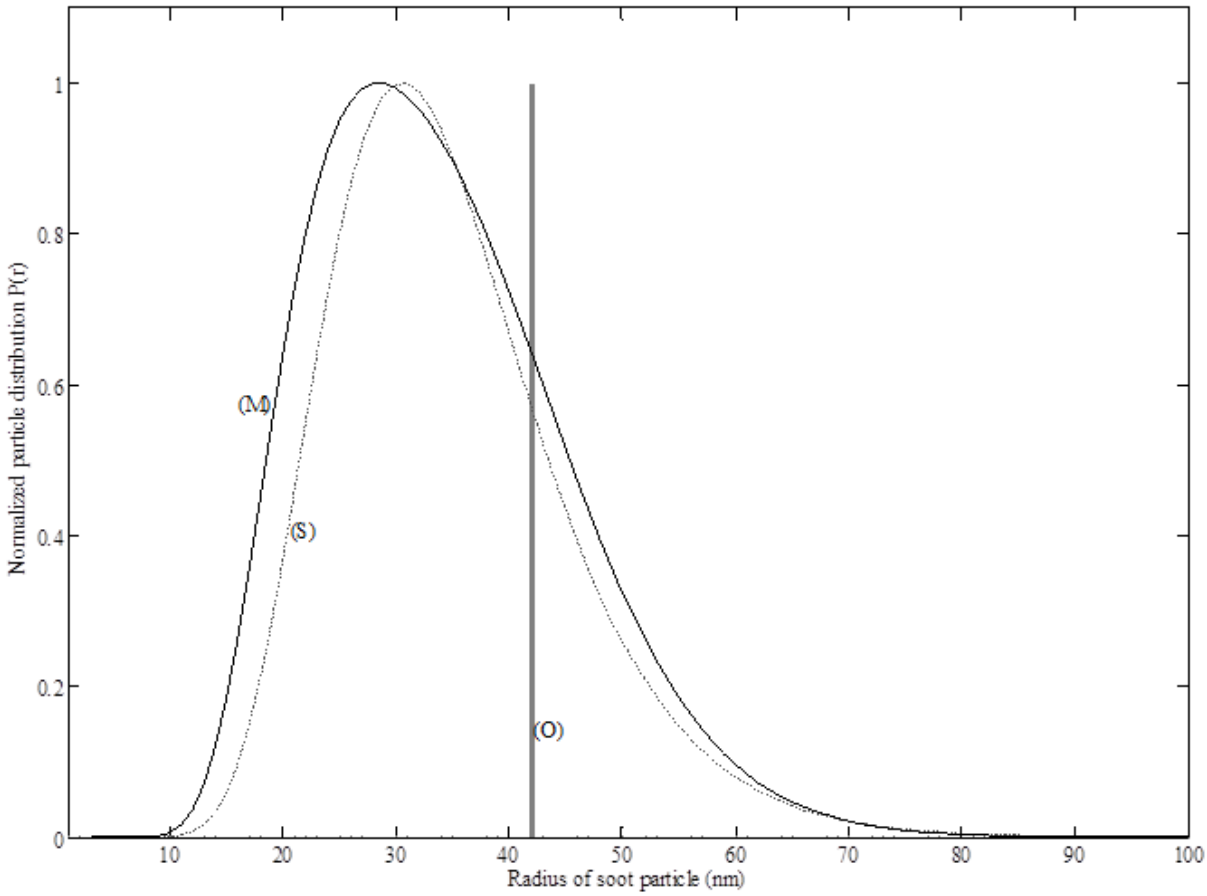

Figure 8.5. Reconstructed particle size distribution assuming both single-lognormal (n=1) (dotted line (S)) as well as multi-lognormal (n=4) (Solid line (M)) distribution for the experimental LII signal at 47°aTDC.

For a single-lognormal distribution (n = 1) the best fit was produced for a distribution width of σ = 0.27 and the count median radius r_{cmd} of 35 nm and is shown by the dotted line (S). However, for a multi-lognormal distribution (n = 4), the same LII signal was reproduced (see solid line (M) in Fig. 8.3) but reconstructed a different distribution (solid line (M)) as shown in Fig. 8.5. The unique variables satisfying the above mentioned two conditions were σ_1 = 0.22, σ_2 = 0.28 and ξ = 1.18, which results in a count median radius of r_{1,cmd_multi} =42 nm, r_{2,cmd_multi}= 35.6 nm, r_{3,cmd_multi}= 30.2 nm and r_{4,cmd_multi}= 25.5 nm, thus preserving the valuable parameter r_{mono} as the count median radius r_{1,cmd_multi}.To establish credibility of the reconstructed size distribution assuming a multi-lognormal distribution (n = 4), the LII signal was again reproduced for different values of "n" satisfying the above mentioned two conditions. The size distributions are shown in Fig.8.6, where the curves (S), (B), (T), (Q) and (H) are the reconstructed particle size distribution for n = 1, 2, 3, 4 and 6, respectively. Note that the distributions for n >3 converge towards a typical size distribution and remain stable

for any increase in total number of lognormal distribution "*n*", which indicates that a realistic size distribution can be safely assumed for $n>3$.

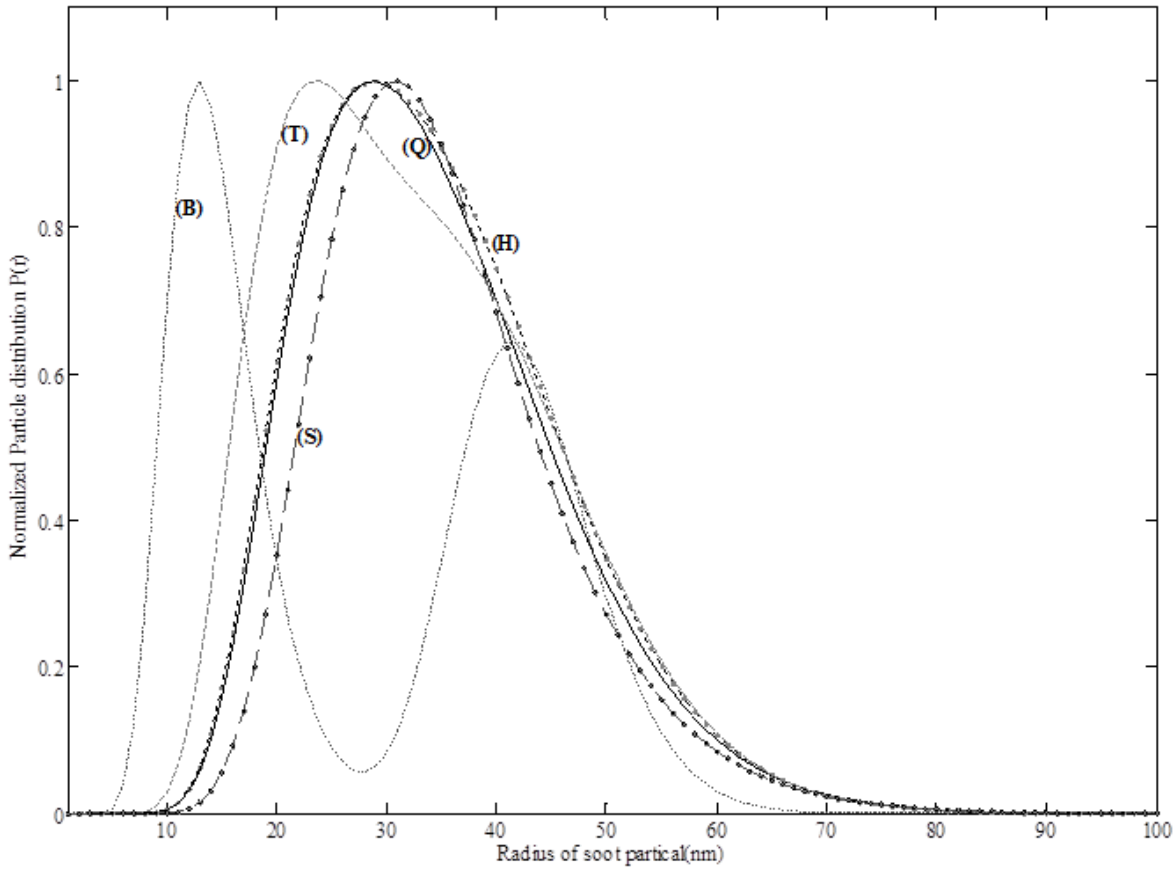

Figure 8.6. Reconstructed particle size distribution from the experimental LII signal at 47° aTDC. The curves (S), (B), (T), (Q) and (H) are particle size distribution for n = 1, 2, 3, 4 and 6, respectively.

Apart from these experiments, exhaust soot particle size distribution measurements were carried out independently by an electrical mobility spectrometer for the verification of multi-lognormal soot size distribution. A differential mobility analyser (DMA) was used to separate the particle sizes based on their electrical mobility, which determines the drift velocity of charged particles under the influence of electric field. After classification, the number concentration of particles in the output sample flow was determined by a Faraday-cup electrometer (FCE). An integrated closed-loop mixing tube diluter was used for sampling aerosols from the engine exhaust to the EMS system to provide the exhaust particulate size distribution (see section 4.6 for more details). The EMS system was installed at the exhaust of a 4 cylinder, 2.0 litre direct injection diesel engine. Ultra low sulphur diesel (ULSD) fuel was used in the experiments. The injecting pressure was maintained at 800 bars with a constant speed of 1500 rpm. Figure 8.7 shows the experimental data for the exhaust soot particle size

distribution generated by EMS along with the theoretically obtained single-lognormal and multi-lognormal distribution fitting using multi-dimensional non-linear regression.

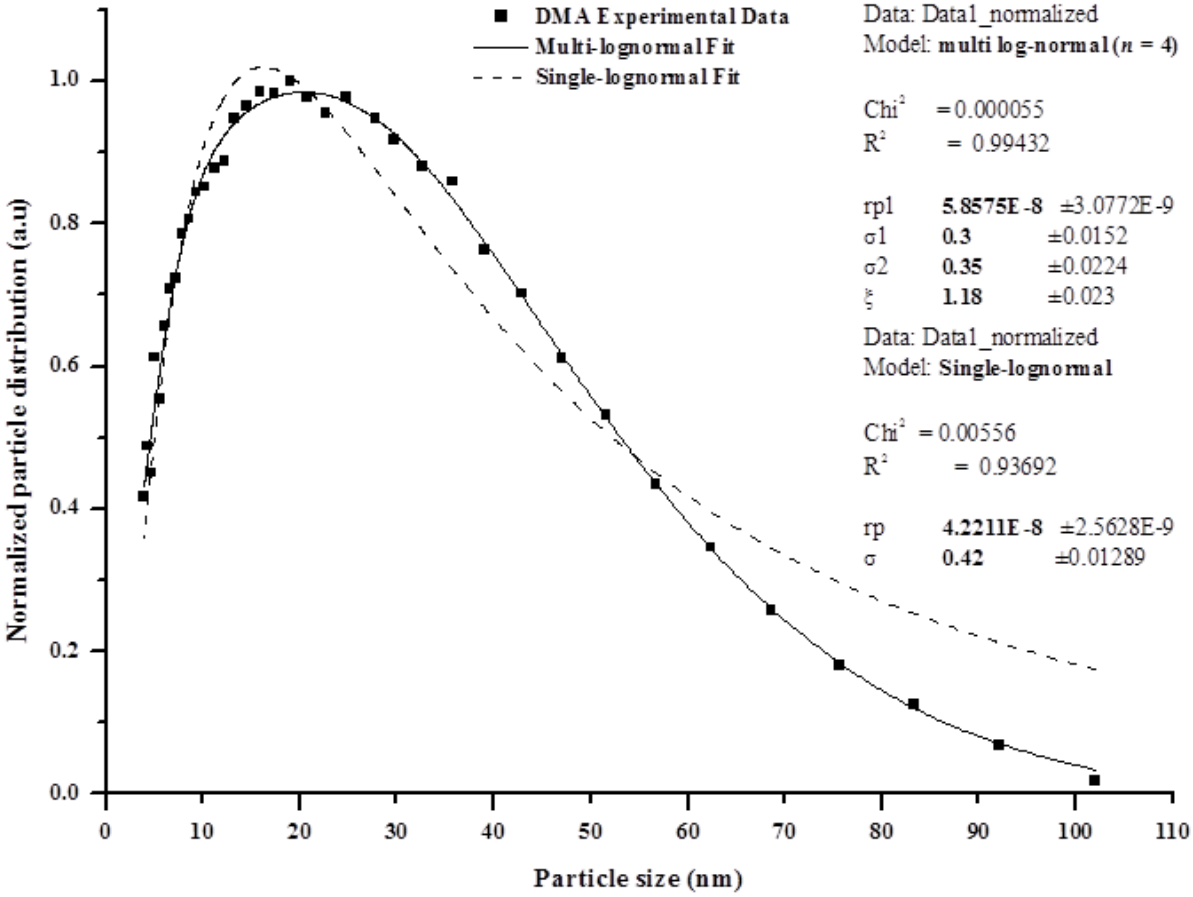

Figure 8.7. The experimental results (•) for the particle size distribution obtained by electrical mobility spectrometer (EMS) along with multi-dimensional non-linear regression fits. The solid line is the theoretical fit assuming a multi-lognormal function (n=4) and the dashed line is the theoretical fit assuming a single-lognormal function (n=1).

The dotted line in Fig. 8.7 shows the fitting of a single-lognormal particle size distribution function, whereas the solid line assumes a multi-lognormal size distribution (n = 4) function, which provides a relatively good agreement with the experimental data compared to single lognormal size distribution. To further verify the validity of a multi-lognormal size distribution, the model was compared with the published TEM data given by S. Dankers and A. Leipertz [102] and is shown in Fig. 8.8. The solid line (M) is the size distribution that was reconstructed by assuming a multi-lognormal distribution with n = 4, and is in agreement with the published TEM data.

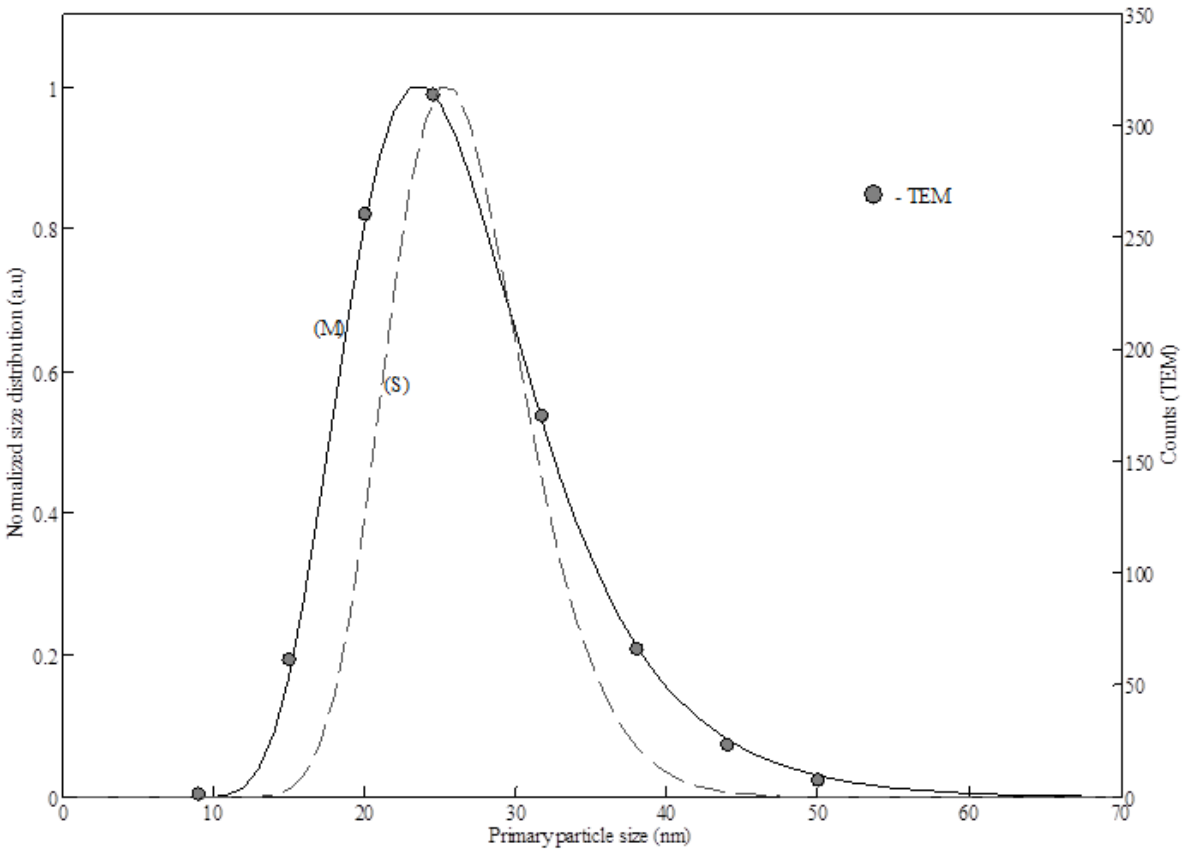

Figure 8.8. Comparison of a multi-lognormal size distribution with the published transmission electron microscopy (TEM) data. (•) are the published TEM values [104], Solid line (M) is the reconstructed particle size distribution assuming a multi-lognormal (n=4) distribution and the dashed line (S) is the single-lognormal (n=1) size distribution with a count median diameter d_{cmd}. = 27.2nm and σ = 0.175.

The parameters satisfying the conditions were σ_1= 0.26, σ_2= 0.2 and ξ= 1.16. The count median diameter of the first distribution r_{1,cmd_multi} was deduced as 32nm (which is the same as the mono-dispersive primary particlesize d_{mono}). This value is in good agreement with the published LII data of d_{cmd}= 27.2 nm, if a reverse calculations done for a single-lognormal distribution (S) with a distribution-width of σ = 0.175. It could be seen that the average count median particle diameter for a multi-lognormal distribution (M) (n = 4) is ~1.5 nm less than the count median particle diameter for a single-lognormal distribution (S) as published in [102]. All these results obtained from different soot size measurement techniques show the effectiveness of a multi-lognormal size distribution in describing the polydispersive nature of soot along with a realistic reconstruction of size distribution applied for time-resolved laser induced incandescence.

8.6. Conclusion

In summary, a multi-lognormal particle size distribution with $n > 3$ was shown to reconstruct a realistic soot size distribution instead of a single-lognormal distribution. Using time-resolved laser induced incandescence (TR-LII) a mono-dispersive soot particle size r_{mono} of 42 nm was deduced for a crank angle of 47°aTDC. The mono-dispersive size was preserved while reconstructing the particle size distribution assuming a multi-lognormal size distribution ($n = 4$). Experimental results from an electrical mobility spectrometer (EMS) also shows a better fit for a multi-lognormal size distribution compared to a single-lognormal distribution. Further verification of the multi-lognormal particle size distribution was shown by comparing the reconstructed size distribution for $n = 4$ with the published transmission electron microscopy (TEM) data. Good agreement has been established between the published TEM data with the proposed distribution. These results show that the soot size distribution in engines is better represented by a multi-lognormal size distribution compared to a mono-dispersive or a single-lognormal size distribution.

9. Chapter 9 - Conclusions and recommendation for future work

9.1. Introduction

During recent years, a significant increase in the European diesel car market was observed and a further increase is expected. Diesel engines, however, suffer from high emissions of NO_x and PM which are strictly regulated by latest emission directives. The work presented here focuses mainly on the characterisation of soot emission from the combustion of standard diesel fuel as well as ULSD, RME and fuels of different composition in a diesel engine. In order to understand soot processes more extensively, in-cylinder optical diagnostics like TR-LII, PLII, high speed imaging were used and fuel properties e.g. oxygen and aromatics content were investigated. The presented results can be used to support the models for soot formation and oxidation in diesel engines. They provide information regarding changes in soot processes depending on fuel composition. An attempt was made to determine in-cylinder soot particle size, distribution and soot volume fraction for a number of fuels and understand the reason for the variations in measured soot. Finally, changes to the mathematical model were made by assuming that multi-lognormal particle size distribution is present in the combustion chamber. The main findings from this research are discussed in following sections.

9.2. Measurement of in-cylinder soot particles and their distribution in an optical HSDI diesel engine using Time Resolved Laser Induced Incandescence (TR-LII)

The study presented in chapter 5 revealed that TR-LII can be used as a powerful tool for characterization of in-cylinder soot in diesel engines. In current work, the results obtained from point measurements in a single cylinder optical diesel engine are presented and challenges and uncertainties encountered during measurements and data analysis are highlighted. Quantitative in-cylinder information about particle sizes and their distribution aid in understanding the mechanisms of soot formation and oxidation under different engine conditions and for various fuel types. TR-LII technique helped in obtaining information about the in-cylinder particle sizes and their distribution in the combustion chamber. Strong cycle to cycle fluctuations showed that soot particles are randomly distributed and transported within the cylinder. Analysis of LII signals revealed that initially soot particles of small and large

diameters contribute to the signal and in the later part of LII decay, contribution from larger soot particles is observed.

Excessive noise in the signal emitted from soot in the engine lead to difficulties in signal analysis. The fitting function can be trapped in a local minimum causing errors on the derived soot particle size and their distribution. Time resolved LII measurements revealed a general trend of the soot particle sizes decreasing with crank angle due to the oxidation. A slight increase in particle size was observed later in the stroke due to soot agglomeration. It was also found that injection timing does not influence particle size. However, the relationship between particle size and injected fuel quantity was observed. Measurements show that later in expansion stroke, a well-defined soot particle size distribution is present. General trend of SVF decreasing with crank angle was detected for the majority of engine operating conditions. A higher amount of soot was measured for early injection timings (10°bTDC and 5°bTDC). Less soot was observed for injection at TDC where a long ignition delay helped premixing of fuel and air.

9.3. Characterization of in-cylinder combustion and soot processes for RME and ULSD fuels in a single cylinder optical diesel engine

In-cylinder combustion and soot processes for ULSD and RME were investigated using TR-LII as well as PLII and high speed imaging techniques in chapter 6. Two injection strategies of single and double injection were applied during these measurements. Based on high speed images, the magnitudes of FLoL and SLoL were determined. Longer FLoL and SLoL were measured for RME in comparison to ULSD indicating larger entrainment of air upstream of flame lift off length for RME fuel. This leads to lower soot formation and improved soot oxidation for RME when compared to ULSD. ID determined from OH* chemiluminescence, soot luminosity and in-cylinder pressure revealed that for all cases RME has shorter ID compared to ULSD. The level of soot measured using high speed imaging during combustion of RME was lower than for ULSD and the trend was confirmed by results obtained from PLII. The amount of un-oxidized soot left in the combustion chamber after the end of visible combustion was as well lower for RME. For this fuel, soot particle of smaller sizes were detected when compared to ULSD.

9.4. Soot luminosity and OH* chemiluminosence emission during combustion of fuels of different composition in diesel engine

In-cylinder combustion and soot processes for six fuels of different composition were investigated using high speed imaging and PLII technique and applying single and double injection strategy. Results obtained during measurements are presented in chapter 7. It was found that the peak soot luminosity obtained using high speed imaging depends on fuel properties. Lower soot levels were observed for fuels with higher oxygen content. The relationship between the peak soot luminosity and aromatics content was evident, with the combustion of fuel with doubled the quantity of total aromatics leading to decrease in soot emission by approximately 20% to 30%. During this investigation, longer FLoL was measured for fuels with higher oxygen content. The fuel containing aromatics had longer FLoL at initial crank angles and then a rapid decrease was observed. ID was measured using three different methods for single and double injection strategies and was analysed with respect to the CN of fuel. For the single injection strategy, trends of ID decreasing with CN were observed for all techniques. For the double injection strategy, a fairly constant ID was observed showing that fuels ignite at similar time despite the differences in CN. PLII measurements applied for single injection strategy revealed that amount of soot left in the combustion chamber after the end of luminous combustion decreases for fuels with longer ID and longer FLoL. For this strategy a strong relation between CN and amount of produced soot was found. SVF measured for double injection strategy was lower for fuels with higher oxygen content or fuels with higher aromatics content.

9.5. Injection parameter dependent in-cylinder diesel soot particulate characterization by time-resolved laser induced incandescence

A multi-lognormal particle size distribution discussed in chapter 8 was introduced in the existing mathematical model for a characterisation and realistic reconstruction of the size distribution in the combustion chamber. Detailed theoretical analysis of multi-lognormal size distribution along with its application to the experimentally measured soot particle size is validated in this work. It was found that a multi-lognormal particle size distribution reconstructs a realistic soot size distribution instead of a single-lognormal distribution. Further verification of the multi-lognormal particle size distribution was shown by comparing the reconstructed size distribution with the published transmission electron microscopy (TEM) data. Good agreement has been established between the published TEM data with the proposed distribution. The results show that the soot size distribution in engines is better

represented by a multi-lognormal size distribution compared to a mono-dispersive or a single-lognormal size distribution.

9.6. Recommendation for future work

The work presented here focuses on soot measurements in an optical diesel engine. Due to the engine design, TR-LII and PLII were measured later in the stroke providing useful data for soot oxidation characterisation. It would be desirable to extend the current study and perform measurements for earlier crank angles, from the point of fuel injection, where soot formation processes for these fuels are taking place. For further work, application of thermophoretic sampling and acquisition of TEM images for considered fuels will allow for comparisons of soot particle sizes in exhaust gases with those measured in combustion chamber using TR-LII. This would provide validation of primary particle sizes and will identify changes which the particulates undergo during transport from the cylinder to the tailpipe. Additionally, it would be useful to perform TR-LII measurements for the considered six fuels in order to determine soot particle sizes.

In the current study, the influence of injection timing and engine load on measured soot diameters was considered. It would be advantageous to extend these measurements and investigate further influence on later injection timing, injection pressure and addition of exhaust gas recirculation on measured particulate size, distribution and soot volume fraction.

Further development of the mathematical model is as well advised, where the method for optimisation can be improved by application of genetic algorithm which will lead to significant reduction of computational time for fitting experimental and theoretical LII curve.

References

[1] Internal Combustion Engine Handbook, SAE, (2004).

[2] Rajput R.K., Internal Combustion Engines, Laxmi Publications, (2005).

[3] http://knowledgepublications.com, (14.07.2012).

[4] Heywood J.B., Internal Combustion Engines Fundamentals, McGraw-Hill Co, New York, (1988).

[5] http://www.cdxetextbook.com/engines/engines.html, (14.07.2012).

[6] Encyclopaedia Britannica 2007.

[7] Dec J.E., "A conceptual model of DI diesel combustion based on laser sheet imaging", SAE 970873, (1997).

[8] Flynn, P. F., Durrett, R.P., Hunter, G.L., zur Loye, A.O., Akinyemi, O.C., Dec, J.E,, Westbrook, C.K., "Diesel Combustion: An Integrated View Combining Laser Diagnostics, Chemical Kinetics, and Empirical 'Validation"', Society of Automotive Engineers publication, SAE 1999-01-0509, (1999).

[9] Euro 6 standards: Commission Regulation (EC) No 715/2007 of the European Parliament and the Council of 20 June, (2007).

[10] http://europa.eu/, (14.07.2012).

[11] Stone R., "Introduction To Internal Combustion Engines", MacMillan Press LTD, (1999).

[12] Pott, P., "Chirurgical Observations", Vol 3. London: Hawes L., Clarke W. , Collins R., London, 177-83, (1775).

[13] Barfknecht, T.R. , "Toxicology of soot", Prog.Energy Combust. Sci. Vol. 9, pp. 199-237 (1983).

[14] Kotin, P., Falk, H. L., Mader, P., Arehs T. M., A M A Arch Ind Hyg Occup Med., 9, 153 (1954).

[15] Mauderly J.L. "An evolution of perspectives: summary of the Third Colloquium on Particulate Air Pollution and Human Health", Durham, North Carolina, June 6-8, 1999. Inhalation Toxicology 2000; 12 (Suppl 1):7-12.

[16] Bockhorn, H., "Soot Formation in Combustion, Mechanisms and Models"; Springer Series in Chemical Physics; Springer-Verlag: Berlin, (1994).

[17] Tree, D. R., Svensson, K. I., “Soot processes in compression ignition engines”, Progress in Energy and Combuston Scienc, Vol. 33, pp. 272-309, (2007).

[18] Haynes B.S., Wagner H.GG., “Soot formation”, Prog. Energy Combust SCI , 7:229-73, (1981).

[19] Bartok W., Sarofim A.F., “Fossil Fuel Combustion: A Source Book”, ISBN-10: 0471847798, New York: Wiley, (1991).

[20] Kennedy I.M., “Models of soot formation and oxidation”, Prog. Energy Combust. Sci. Vol. 23, pp. 95-132, (1997).

[21] Singh S., Reitz R.D. , Musculus P.B., Lachaux T. , “Validation of engine combustion models against detailed in-cylinder optical diagnostics data for heavy duty compression-ignition engine”, In. J. Eng. Res. 8:97-126, (2006).

[22] Epping K., Aceves S., Bechtold R. , Dec J. , “The potential of HCCI Combustion for High Efficiency and Low Emissions”, SAE 2002-01-1923, (2002).

[23] Christensen, M., Johansson, B., Einewall, P., “Homogeneous Charge Compression Ignition (HCCI) Using Iso-octane, Ethanol and Natural Gas -A Comparison with Spark Ignition Operation", SAE 972874, (1997).

[24] Kawano D., Suzuki H., Ishii H., Goto Y., Odaka M., Murata Y., Kusaka J., Daisho Y., “Ignition and Combustion Control of Diesel HCCI”, SAE 2005-01-2132, (2005).

[25] A Report to the U.S. Congress, Homogeneous Charge Compression Ignition (HCCI) Technology, (2001).

[26] Zhao H., “HCCI and CAI engines for the automotive industry”, Woodhead Publishing, (2006).

[27] Tsurushima T., Harada A., Iwashiro Y., Enomoto Y., Asaumi Y. , Aoyagi Y., “Thermodynamic Characteristics of Premixed Compression Ignition Combustions”, SAE 2001-01-1891, (2001).

[28] Neely G.D., Sasaki S., Huang Y., Leet J.A., Stewart D.W., “New Diesel Emission Control Strategy to Meet US Tier 2 Emissions Regulations”, SAE 2005-01-1091, (2005).

[29] Ashgriz N., Springer, “Technology & Engineering, Handbook of Atomization and Sprays: Theory and Applications”, (2011).

[30] Alriksson M. , Denbratt I., “Low Temperature Combustion in a Heavy Duty Diesel Engine Using High Levels of EGR”, SAE 2006-01-0075, (2006).

[31] Klein-Douwel R.J.H., Donkerbroek A.J., van Vliet A.P., Boot M.D., Somers L.M.T., Baert R.S.G., Dama N.J., ter Meulen J.J., “Soot and chemiluminescence in diesel combustion of bio-derived, oxygenated and reference fuels”, Proc. Comb. Inst. 32, 2817–2825, (2009).

[32] http://europa.eu/legislation_summaries/internal_market/single_market_for_ goods/motor_vehicles/interactions_industry_policies/l28077_en.htm, (17.07.2012).

[33] Schäfer F., van Basshuysen R., “Reduced Emissions and Fuel Consumption in Automobile Engines”, ISBN 3-211-82718-8, Springer-Verlag, Wien, New York, (1995).

[34] Ajav E.A., Singh B., Bhattacharya T.K., “Experimental study of some performance parameters of a constant speed stationary diesel engine using ethanol–diesel blends as fuel”, Volume 17, Issue 4, p. 357-365, Biomass and Bioenergy, (1999).

[35] Bang-Quan He, Shi-Jin Shuai, Jian-Xin Wang, Hong He, “The effect of ethanol blended diesel fuels on emissions from a diesel engine”, Volume 37, Issue 35, Pages 4965-4971,Atmospheric Environment, (2003).

[36] http://www.biofuels-platform.ch/en/infos/production.php, (11.07.2014).

[37] Nakajima T., Nishiumi R., Kitano K., Sakata I., Clark R., “Improvement of DI Diesel System by Utilizing GTL Fuel Specifications”, Review of Automotive Engineering 30 219-225, (2009).

[38] Griesemann J-C., “Biomass to liquid (BTL) diesel fuel. Sourcing, stakes and enablers”, P. Duret, X. Montagne (Eds.) and Editions Technip, Paris, pp. 21-25, (2004).

[39] Kerker M., “The Scattering of Light and Other Magnetic Properties”, Academic, New York, USA, (1969).

[40] Aronsson, U., Chartier, C., Horn, U., Andersson, Ö. et al., "Heat Release Comparison Between Optical and All-Metal HSDI Diesel Engines," SAE Technical Paper 2008-01-1062, 2008, doi:10.4271/2008-01-1062, (2008).

[41] Childs P. R. N., “Practical temperature measurement”, ISBN 0 7506 5080, Elsevier Science, (2001).

[42] Weeks R.W, Duley W.W., "Aerosol-Particle Sizes from Light Emission During Excitation by TEA CO_2 Laser Pulses", J. Appl. Phys. Vol.45, pp.4661-4662, (1974).

[43] Melton L.A., "Soot diagnostics Based on Laser Heating", Appl. Optics, vol. 23, pp.2201-2208, (1984).

[44] Dash C.J., "Continuous-Wave Probe Laser Investigation of Laser Vaporization of Small Soot Particles in a Flame", Appl. Optics, vol. 23, pp. 2209-2215, (1984).

[45] Dash C.J., "Spatially Resolved Soot-Absorption Measurements in Flames Using Laser Vaporization of Particles", Optics Lett., vol.9, pp.214-216, (1984).

[46] Roth P., Filippov A.V., "In Situ Ultrafine Particle Sizing by a Combination of Pulsed Laser Heat up and Particle Thermal Emission", J. Aerosol Sci., vol. 27, pp. 95-104, (1996).

[47] Filippov A.V., Marcus M.W., Roth P., In-Situ Characterization of Ultrafine Particles by Laser-Induced Incandescence: Sizing and Particle Structure Determination, J. Aerosol Sci., vol. 30, pp. 71-87, (1999).

[48] Daun K.J., Stagg B.J., Liu F., Smallwood G.J., Snelling D.R., "Determining aerosol particle size distribution using time-resolved laser-induced-incandescence", Applied Physics B, Vol. 87, pp. 363-372, (2007).

[49] Kock B. F., Eckhardt T., Roth P., "In-cylinder sizing of Diesel particles by time-resolved laser-induced incandescence (TR-LII)," Proc. Combust. Inst. 29, 2775-2781, (2002).

[50] Michelsen H.A., Liu F., Kock B.F., Bladh H., Boiarciuc A., Charwath M., Dreier T., Hadef R., Hofmann M., Reimann J., "Modelling laser-induced incandescence of soot: a summary and comparison of LII models", Appl. Phys. B 87, 503-521, (2007).

[51] Ryser R., Gerber T., Dreier T., "Soot particle sizing during high-pressure Diesel spray combustion via time-resolved laser-induced incandescence", Combust. Flame 156, 120-129, (2009).

[52] Dec J.E., zur Loye A.O., Siebers D.L., "Soot Distribution in a DI Diesel Engine Using 2-D Laser Induced Incandescence Imaging", SAE Trans., vol.100, pp. 277-288, no. 910224, (1991).

[53] Dec J.E., "Soot Distribution in a DI Diesel Engine Using 2-D Imaging of Laser Induced Incandescence, Elastic Scattering and Flame Luminosity", SAE-92011 of the

SAE Technical Paper Series, Society of Automotive Engineers, Warrendale, PA. (1992).

[54] Hofeldt D.L., "Real –Time Soot Concentration Measurement Techniques for Engine Exhaust Streams", SAE Transactions, 102, J. Fuels Lubric., Sec. 4, pp-45-57, (1993).

[55] Pinson J.A., Mitchell D.L., Santoro R.J., Litzinger T.A., "Quantitative Planar Soot Measurements in a D.I. Diesel Engine Using Laser-Induced Incandescence and Light Scattering", SAE 932650, SAE International Fall Fuels and Lubricants Meeting and Exposition , Philadelphia, October 18-21, Society of Automotive Engineers, Warrendale, PA. (1993).

[56] Shaddix C.R., Harrington J.E., Smyth K.C., "Quantitative Measurements of Enhanced Soot Production in a Flickering Methane/Air Diffusion Flame", Combust.Flame, vol. 99, pp. 723-732, (1994).

[57] der Wal V., Weiland K.J., " Laser-Induced Incandescence Development and Characterization Towards a Measurements of Soot-Volume Fraction", Appl. Phys. B, vol.59, pp. 445-452, (1994).

[58] Goulay F., Schrader P.E., Nemes L., Dansson M.A., Michelsen H.A., " Photochemical interferences for laser-induced incandescence of flame-generated soot", Proceedings of the Combustion Institute 32,963–970, (2009).

[59] Dreier T., Bougie B., Dam N., Gerber T., "Modelling of time resolved laser-induced incandescence transient for particle sizing in high-pressure spray combustion environments: a comparative study", Appl. Phys. B 83, 403-411, (2006).

[60] Schulz C., Kock B.F., Hofmann M., Michelsen H., Will S., Bougie B., Suntz R., Smallwood G, "Laser-induced incandescence: recent trends and current questions"Appl. Phys. B 83, 333-354, (2006).

[61] Hofmann M., Bessler W.G., Shulz C., Jander H., "Laser-induced incandescence for soot diagnostics at high pressures", Appl. Opt. 42, 2052-2062, (2003).

[62] Liu F., Daun K. J., Snelling D. R., Smallwood G. J., "Heat conduction from a spherical nano-particle: status of modeling heat conduction in laser-induced incandescence", Appl. Phys. B 83, 355-382, (2006).

[63] Boiarciuc A., Foucher F., Mounaim-Rousselle C., "Soot volume fractions and primary particle size estimate by means of the simultaneous two-color-time-resolved and 2D laser-induced incandescence", Appl. Phys. B 83, 413-421, (2006).

[64] Ni T., Gupta S.B., Santoro R.J., Symp. (Int.), "Suppression of soot formation in ethene laminar diffusion flames by chemical additives", Combust. 25, 585-592, (1994).

[65] Val R.L.V., Jensen K.A., "Laser-Induced Incandescence: Excitation Intensity", Appl. Opt. 37, 1607-1616, (1998).

[66] Braun-Unkhoff M., Chrysostomou A., Gutheil E., Frank P., Lückerath R., Sticker W.. "Experimental and numerical study on soot formation in laminar high-pressure flames", Combustion and Flame, pages 1565–1572, (1998).

[67] Angrill O., Geitlinger H., Streibel T., Suntz R., Bockhorn H. , "Influence of exhaust gas recirculation on soot formation in diffusion flames", Proc. Combust. Inst. 28, 2643-2649, (2000).

[68] Cignoli F., De Iuliis S., Manta V., Zizak G., "Two-Dimensional Two-Wavelength Emission Technique for Soot Diagnostics", Appl. Opt. 40, 5370-5378, (2001).

[69] Bougie B., Ganippa L. C., van Vliet A.P., Meerts W.L., Dam N.J., ter Meulen J.J., "Soot particulate size characterisation in a heavy-duty diesel engine for different engine loads by laser-induced incandescence", Proc. Combust. Inst. 31, 685-691, (2007).

[70] Kock B. F., Tribalet B., Schulz C., Roth P., "Two-color time-resolved LII applied to soot particle sizing in the cylinder of a Diesel engine", Combust. Flame 147, 79-92, (2006).

[71] Lapuerta M., Martos F., Herreros J., "Effect of engine operating conditions on the size of primary particles composing diesel soot agglomerates", Aero. Sci. 38, 455-466, (2007).

[72] Park, J. "A Study on Time Resolved Laser Induced Incandescence Analysis Method for the Measurements of Primary Particle Size in Diesel Exhaust". JSME International Jurnal Series B, 4, Vol. 49, (2009).

[73] Will S., Schraml S., Leipertz A., "Two-Dimensional Soot-Particle Sizing by Time-Resolved Laser-Induced Incandescence", Optics Lett., vol. 20, pp. 2342-2344, (1995).

[74] Kosaka H., Aizawa T., Kamimoto T., "Two-dimensional imaging of ignition and soot formation processes in a diesel flame", Int. Jou. of Eng. Res., (2005).

[75] Knox K.J., "Light-Induced Processes in Optically-Tweezed Aerosol Droplets", ISBN 978-3-642-16347-0, (2011).

[76] Merola S.S., Vaglieco B.M., “Analysis on Common Rail diesel engine combustion process by optical diagnostics”, IstitutoMotori-CNR , Napoli –Italy.

[77] Pickett L.M., Siebers D.L., “Soot in Diesel Fuel Jets: Effects of Ambient Temperature, Ambient Density, and Injection Pressure”, submitted to Combust. Flame, (2003).

[78] Pickett L.M., Siebers D.L., “Injection Pressure and Orifice Diameter Effects on Soot in DI Diesel Fuel Jets,” Conference on Thermo-fluid Dynamic Processes in Diesel Engines, Valencia, Spain, (2002).

[79] Musculus M. P., Dec J. E., Tree D. R., “Effects of Fuel Parameters and Diffusion Flame Lift-off on Soot Formation in a Heavy-Duty DI Diesel Engine”, SAE Paper 2002-01-0889, (2002).

[80] Mueller C. J., Martin G. C., “Effect of oxygenated compounds on combustion and soot evolution in a DI diesel engine: broadband natural luminosity imaging”. SAE Paper 2002-01-1631, (2002).

[81] Siebers, D.L., Higgins, B., “Flame Lift-off on Direct-Injection Diesel Sprays under Quiescent Conditions”, SAE Paper 2001-01-0530, (2001).

[82] Pickett L.M., Siebers D. L., “Fuel Effects on Soot Processes of Fuel Jets at DI Diesel Conditions”, SAE 2003-01-3080, (2003).

[83] Pickett L.M., Siebers D. L, “Soot formation in diesel fuel jets near the lift-off length”, International Journal of Engine Research, vol. 7, no. 2, 103-130, (2006).

[84] McQuarrie D.A., Simon J.D., “Physical chemistry: a molecular approach”, University Science Books, , ISBN 978-0-935702-99-6, (1997).

[85] Dec, Coy, “OH Radical Imaging in a DI Diesel Engine and the Structure of the Early Diffusion Flame”, SAE Paper No. 96083, (1996).

[86] Zhao, H., Ladommatos, N., “A Guide to Measurement of Flame Temperature and Soot Concentration in Diesel Engines Using the Two-Colour Method Part 1: Theory” SAE Paper 941956, (1994).

[87] Kittelson D.B., Watts W.F, Johnson J.P., “On-road and laboratory evaluation of combustion aerosols - Part1: Summary of diesel engine results”, Aerosol Science, 37 913-930, (2006).

[88] Mathis U., Ristimaki J., Mohr M., Keskinen J., Ntziachristos L., Samaras Z., Mikkanen P., ”Sampling Conditions for the measurement of Nucleation Mode

particles in the Exhaust of a Diesel Vehicle", Aerosol Science and Technology, 38, 1149-1160, (2004).

[89] Kittelson D.B., Johnson J., Watts W., Wei Q.,Drayton M., Paulsen D., Bukowiecki N., " Diesel Aerosol Sampling in the Atmosphere", SAE, 200-01-2212, (2000).

[90] Ronkko, T., Virtanen, A., Vaaraslahti, K., Keskinen, J., Pirjola, L., Lappi, M., "Effect of dilution conditions and driving parameters on nucleation mode particles in diesel exhaust: Laboratory and on-road study", Atmospheric Environment, 40: 2893-2901, (2006).

[91] Jung, H., Kittelson, D.B., Zachariah, M.R., "The Influence of Engine Lubricating Oil on Diesel Nanoparticle Emissions and Kinetics of Oxidation", SAE International, 2003-01-3179: 408-412, (2003).

[92] van der Wal, R. L. and Tomasek, A. J., "Soot nanostructure: Dependence upon synthesis conditions", Combust. Flame, vol. 136, no. 1-2, pp. 129-140, (2004).

[93] Hirschfelder J.O., Curties C.F., Bird R.B., "Molecular theory of gases and liquids" J.Wiley &Sons, (1954).

[94] Williams M.M.R., Loyalka S.K., "Aerosol Science Theory and Practice: With Special Application to the Nuclear Industry", Pergamon Press.Oxford, New York, (1991).

[95] Michelsen H. , "Understanding and predicating the temporal response of laser – induced incandescence from carbonaceous particles", JCP 118 (15), 7012-7045, (2003)

[96] Snelling D.R., Liu F., Smalwood G.J., Gulder Ö.L., " Evaluation of the nanoscale heat and mass transfer model for LII" , In: Proc. NHTC 2000-12132 25. 36. (2000).

[97] Bladh H., Bengtson P.-E., "Characteristics of laser-induced incandescence from soot in studies of a time-dependent heat- and mass- transfer model" Appl. Phys. B 78 (2), 381-388, (2004).

[98] Kuhlmann S.-A., Reimann J., Will S., "On heat conduction *between* laser-heated *nanoparticles* and a surrounding gas", Aerosol Science 37, 1696 – 1716, (2006).

[99] McCoy, B. J., & Cha, C.Y. , "Transport phenomena in the rarefied gas transport regime", Chemical Engineering Science, 29, 381–388, (1974).

[100] Schittkowski T., Mewes B., Bruggemann D., “Laser Induced Incandescence and Raman measurements in sooting methane and ethylene flames”, 4 (11), 2063-2071, (2002).

[101] Fuchs N. A., “The mechanics of aerosols”, Pergamon Press, Oxford, UK, (1964).

[102] Dankers S., Leipertz A., “Determination of Primary Particle Size Distributions from Time-Resolved Laser-Induced Incandescence Measurements”, Appl. Opt. 43, 3726-3731, (2004).

[103] Liu F., Smallwood G.J., Snelling D.R, “Effect of Primary Particle Diameter and Aggregate Size Distribution on the Temperature of Soot Particles Heated by Pulsed Lasers”, Journal of Quantitative Spectroscopy & Radiative Transfer 93, 301–312, (2005).

[104] Bougie B., Ganippa L.C., Dam N.J., ter Meulen J.J., “On particulate characterisation in a heavy-duty Diesel engine by time-resolved laser-induced incandescence”, Appl. Phys. B 83, 477-485, (2006).

[105] Will S., Schraml S., Bader K., Leipertz A., ”Performance Characteristics of Soot Primary Particle Size Measurements by Time-Resolved Laser-Induced”, Appl. Opt. 37, 24, (1998).

[106] Reimann J., Kuhlmann S.-A., Will S., “2D aggregate sizing by combining laser-induced incandescence (LII) and elastic light scattering (ELS)”, Appl. Phys. B, 583-592, (2009).

[107] http://www.oceanoptics.com/products/hl2000.asp, (25.11.2012)

[108] Krishnan S. S., Lin K.-C., Faeth G. M., J., “Optical Properties in the Visible of Overfire Soot in Large Buoyant Turbulent Diffusion Flames”, Heat Transf. 122, 517, (2000).

[109] de Iuliis S., Migliorini F., Cignoli F., Zizak G., “Peak soot temperature in laser-induced incandescence measurements”, Appl. Phys. B 83, 397-402, (2006).

[110] Krishnan S. S., Lin K.C., Faeth G.M., “Extinction and Scattering Properties of Soot Emitted from Buoyant Turbulent Diffusion Flames”, J. Heat Transf. 123, 331, (2001).

[111] http://learn.hamamatsu.com/articles/photomultipliers.html , (14.07.2012).

[112] Tree D. R., Svensson K.I., “Soot Processes in Compression Ignition Engines”, Prog.Energy Combust. Sci. 33, 272-309, (2007).

[113] Krüger V., Wahl C., Hadef R. , Geigle K. P., Stricker W., Aigner M., "Comparison of laser-induced incandescence method with scanning mobility particle sizer technique: the influence of probe sampling and laser heating on soot particle size distribution", Meas. Sci. Tech. 16 1477-1486, (2005).

[114] Bockhorn H., Geitlinger H., Jungfleisch B., Lehre T., Schön A., Streibel T., Suntz R., "Progress in characterization of soot formation by optical methods", Phys. Chem. Chem. Phys., 3780–3793, (2002).

[115] Park J., Ryoo H. R., Chun H.S., Song S., Hahn J.W., Chun K.M., JSME Int. J. Series B 49, 1-7, (2006).

[116] Banerjee S., Menkiel B., Ganippa L.C., "Multi-lognormal soot particle size distribution for time-resolved laser induced incandescence in diesel engines" Appl. Phys. B 96 571, (2009).

[117] Neoh K.G., Howard J.B., Sarofim A.F, Twentieth Symposium (International) on Combustion, The Combustion Institute, 951-957, (1984).

[118] Josling T., Blandford D., Earley J., International Food & Agricultural Trade Policy Council, IPC Position Paper September (2010).

[119] Fujimoto H., Kurata K., Asai G., Senda J., "OH Radical Generation and Soot Formation/Oxidation in DI Diesel Engine", SAE 982630, (1998).

[120] Pickett L.M., Siebers D. L., Idicheria C.A., "Relationship Between Ignition Processes and the Lift-Off Length of Diesel Fuel Jets", SAE 2005-01-3843, (2005).

[121] Kosaka H., Nishigaki T., Kamimoto T., Harada S., "A Study on Soot Formation and Oxidation in an Unsteady Spray Flame via Laser Induced Incandescence and Scattering Techniques", SAE 952451 (1995).

[122] Som S., Ramirez A.I., Longman D. E., Aggarwal S. K, "Effect of nozzle orifice geometry on spray, combustion, and emission characteristics under diesel engine conditions ", Fuel 90, 1267–1276, (2011).

[123] Pickett, L.M., Siebers, D.L, J. Eng. Gas Turbines Power 127, 1, 187, (2005).

[124] Vanquickenborne L., Tiggelen V., "The stabilisation mechanism of lifted diffusion flames", Combustion Flame 10:59-69, (1966).

[125] Czerwinski, Y. Zimmerli, T. Neubert, A. Heitzer, M.Kasper, "Injection, Combustion and (Nano) Particle Emissions of a Modern HD-Diesel Engine with GTL, RME and ROR", SAE 2007-01-2015, (2007).

[126] Lapuerta M., Armas O., Rodríguez-Fernández J., "Effect of Biodiesel Fuels on Diesel Engine Emissions", Progr.Energy and Combust.Sci. 34:198, 223, (2008).

[127] Menkiel B., Donkerbroek A., Uitz R., Cracknell R., Ganippa L., "Measurement of in-cylinder soot particles and their distribution in an optical HSDI diesel engine using Time Resolved Laser Induced Incandescence (TR-LII)" , Accepted for publication in Combustion and Flame, CNF-D-11-00172R1.

[128] Johnson, T.V., "Diesel Emission Control in Review", SAE 2008-01-0069, (2008).

[129] Warren J.P.,"Diesel Aftertreatment Systems: 2004-2007, A Cost Assessment", SAE 2001-01-1948, (2001).

[130] Krämer M., Abthoff J., Duvinage F., Ruzicka N., Krutzsch B., Liebscher T., "Possible Exhaust Gas Aftertreatment Concepts for Passenger Car Diesel Engines with Sulphur-free Fuel", SAE 1999-01-1328, (1999).

[131] Graves R. L., SAE, "Review of Diesel Exhaust Aftertreatment Programs", 1999-01-2245, (1999).

[132] Maiboom, X. Tauzia, J.-F.Hétet, "Experimental study of various effects of exhaust gas recirculation (EGR) on combustion and emissions of automotive direct injection diesel engine", Energy, Vol. 33, pp. 22-34, (2008).

[133] Yehliu K. , Boehman A. L. , Armas O., "Emissions from different alternative diesel fuels operating with single and split fuel injection", Fuel 89, 423–437, (2010).

[134] Kouremenos D. A , Hountalas D. T., Kouremenos A. D., "Experimental Investigation of the Effect of Fuel Composition on the Formation of Pollutants in Direct Injection Diesel Engines", SAE 1999-01-0189, (1999).

[135] Mitchell K., Steere D. E, Taylor J. A., Manicom B., Fisher J.E., Sienicki E. J., C. Chiu, Williams P., "Impact of Diesel Fuel Aromatics on Particulate, PAH and Nitro-PAH Emissions", SAE 942053, (1994).

[136] Uitz R., Cracknell R., Jansma H., Makkee M., "Impact of Diesel Fuel Composition on Soot Oxidation Characteristics", SAE 2009-01-0286, (2009).

[137] Miyamoto N., Ogawa H, Nurun N. Md., Obata K., Arima T., "Smokeless, Low NOx, High Thermal Efficiency and Low Noise Diesel Combustion with Oxygenated Agents as Main Fuel", SAE No.980506, (1998).

[138] Schönborn A., Ladommatos N., Williams J., Allan R., Rogerson J.,"Effects on diesel combustion of the molecular structure of potential syntetic bio-fuel molecules", SAE International, 2007-24-0125, (2007).

[139] Yanfeng, L. Shenghua, G. Hejun, H.Tiegang, Z. Longbao, "A new diesel oxygenate additive and its effects on engine combustion and emissions". Appl. Therm. Eng. Vol. 27, pp. 202-207, (2007).

[140] Mueller Ch. J., William J. P., Picketn L. M., Siebers D.L., Westbrook Ch. K., "Effects of Oxygenates on Soot Processes in DI Diesel Engines: Experiments and Numerical Simulations", SAE 2003-01-1791, (2003).

[141] Boot M.D., Frijters P.J.M., Klein-Douwel R.J.H, Baert R.S.G., "Oxygenated Fuel Composition Impact on Heavy-Duty Diesel Engine Emissions", SAE International, 2007-01-2018, (2007).

[142] Song J., Alam M., Boehman A.L., Kim U., "Examination of the oxidation behaviour of biodiesel soot", Combustion and Flame, Vol. 146, pp. 589-604, (2006).

[143] Tinsdale M., Price P., Chen R., "The Impact of Biodiesel on Particle Number, Size and Mass Emissions from a Euro4 Diesel Vehicle", SAE 2010-01-0796, (2010).

[144] Kirchen P., Obrecht P., Boulouchos K., Bertola A., "Exchaust-Stream and In-Cylinder Measurements and Analysis of the Soot Emissions From a Common Rail Diesel Engine Using Two Fuels", Journal of Engineering for Gas Turbines and Power, Vol. 132, 112804-1, (2010)

[145] Williams P.T., Bart K.D., Andrews G.E., "The relation between polycyclic aromaticcompounds in diesel fuels and exhaust particulates", Fuel 65, pp. 1150–1158, (1986).

[146] Bougie B., Ganippa L.C., Van Vliet A.P., Meerts W.L., Dam N.J., ter Meulen J.J., "Laser-induced incandescence particle size measurements in a heavy-duty diesel engine", Combust. Flame 145, 635, (2006).

[147] S. Maffi, F. Cignoli, C. Bellomunno, S. De Iuliis, G. Zizak, "Spectral effects in laser induced incandescence application to flame-made titania nanoparticles", Spectrochim. Acta Part B: At. Spectrosc. 63, 202, (2008).

[148] T. Lehre, R. Suntz, H. Bockhorn, Proc. Combust, "Time-resolved two-color LII: size distributions of nano-particles from gas-to-particle synthesis", Inst. 30, 2585, (2005).

Publications

1. Measurement of in-cylinder soot particles and their distribution in an optical HSDI diesel engine using Time Resolved Laser Induced Incandescence (TR-LII), B. Menkiel, A. Donkerbroek, R. Uitz, R. Cracknell, L.C. Ganippa, Combustion and Flame, Volume 159, Issue 9, September 2012, Pages 2985–2998.
2. Multi-lognormal soot particle size distribution for time-resolved, laser induced incandescence in diesel engines, S. Banerjee, B. Menkiel, L.C. Ganippa, Appl Phys B DOI 10.1007/s00340-009-3589-6.
3. European Combustion Meeting 2011: In-cylinder Soot Formation and Oxidation for Diesel and RME Fuels in an Optical Single Cylinder HSDI Diesel Engine, B. Menkiel, A. Donkerbroek, R. Uitz, R. Cracknell, L.C. Ganippa, Proceedings of the European Combustion Meeting 2011.
4. 8th International Symposium Towards Clean Diesel Engines-TCDE 2011, Experimental Investigation on In-cylinder Soot Formation and Oxidation for Diesel and RME Fuels in an Optical Single Cylinder HSDI Diesel Engine, B. Menkiel, A. Donkerbroek, R. Uitz, R. Cracknell, L.C. Ganippa.